



water

Wastewater Treatment by Adsorption and/ or Ion-Exchange Processes for Resource Recovery

Edited by

Xanel Vecino and Mònica Reig

Printed Edition of the Special Issue Published in *Water*

Wastewater Treatment by Adsorption and/or Ion-Exchange Processes for Resource Recovery

Wastewater Treatment by Adsorption and/or Ion-Exchange Processes for Resource Recovery

Editors

Xanel Vecino

Mònica Reig

MDPI • Basel • Beijing • Wuhan • Barcelona • Belgrade • Manchester • Tokyo • Cluj • Tianjin



Editors

Xanel Vecino
Chemical Engineering
Universidad de Vigo
Vigo
Spain

Mònica Reig
Chemical Engineering
Universitat Politècnica de
Catalunya
Barcelona
Spain

Editorial Office

MDPI
St. Alban-Anlage 66
4052 Basel, Switzerland

This is a reprint of articles from the Special Issue published online in the open access journal *Water* (ISSN 2073-4441) (available at: www.mdpi.com/journal/water/special_issues/adsorption_water_resource).

For citation purposes, cite each article independently as indicated on the article page online and as indicated below:

LastName, A.A.; LastName, B.B.; LastName, C.C. Article Title. <i>Journal Name</i> Year , Volume Number, Page Range.
--

ISBN 978-3-0365-3926-3 (Hbk)

ISBN 978-3-0365-3925-6 (PDF)

© 2022 by the authors. Articles in this book are Open Access and distributed under the Creative Commons Attribution (CC BY) license, which allows users to download, copy and build upon published articles, as long as the author and publisher are properly credited, which ensures maximum dissemination and a wider impact of our publications.

The book as a whole is distributed by MDPI under the terms and conditions of the Creative Commons license CC BY-NC-ND.

Contents

About the Editors	vii
Preface to "Wastewater Treatment by Adsorption and/or Ion-Exchange Processes for Resource Recovery"	ix
Xanel Vecino and Mònica Reig Wastewater Treatment by Adsorption and/or Ion-Exchange Processes for Resource Recovery Reprinted from: <i>Water</i> 2022 , <i>14</i> , 911, doi:10.3390/w14060911	1
Asma Hanif, Shaukat Ali, Muhammad Asif Hanif, Umer Rashid, Haq Nawaz Bhatti and Muhammad Asghar et al. A Novel Combined Treatment Process of Hybrid Biosorbent–Nanofiltration for Effective Pb(II) Removal from Wastewater Reprinted from: <i>Water</i> 2021 , <i>13</i> , 3316, doi:10.3390/w13233316	5
Andrea Martínez-Arcos, Mònica Reig, José Manuel Cruz, José Luis Cortina, Ana Belén Moldes and Xanel Vecino Evaluation of Calcium Alginate-Based Biopolymers as Potential Component of Membranes for Recovering Biosurfactants from Corn Steep Water Reprinted from: <i>Water</i> 2021 , <i>13</i> , 2396, doi:10.3390/w13172396	21
X. Vecino, M. Reig, C. Valderrama and J. L. Cortina Ion-Exchange Technology for Lactic Acid Recovery in Downstream Processing: Equilibrium and Kinetic Parameters Reprinted from: <i>Water</i> 2021 , <i>13</i> , 1572, doi:10.3390/w13111572	39
Vicenç Martí, Irene Jubany, David Ribas, José Antonio Benito and Berta Ferrer Improvement of Phosphate Adsorption Kinetics onto Ferric Hydroxide by Size Reduction Reprinted from: <i>Water</i> 2021 , <i>13</i> , 1558, doi:10.3390/w13111558	59
Oriol Gibert, César Valderrama, María M. Martínez, Rosa Mari Darbra, Josep Oliva Moncunill and Vicenç Martí Hydroxyapatite Coatings on Calcite Powder for the Removal of Heavy Metals from Contaminated Water Reprinted from: <i>Water</i> 2021 , <i>13</i> , 1493, doi:10.3390/w13111493	75
Sami Ullah, Altaf Ur Rahman, Fida Ullah, Abdur Rashid, Tausif Arshad and Eva Viglašová et al. Adsorption of Malachite Green Dye onto Mesoporous Natural Inorganic Clays: Their Equilibrium Isotherm and Kinetics Studies Reprinted from: <i>Water</i> 2021 , <i>13</i> , 965, doi:10.3390/w13070965	93

About the Editors

Xanel Vecino

Xanel Vecino is a Chemical Engineering Ph.D. Nowadays, she is working as a postdoc researcher at the Chemical Department of the Universidad de Vigo (Spain) and collaborating with the Resource Recovery and Environmental Management (R2EM) group of the Chemical Department of the Universitat Politècnica de Catalunya (Spain).

Her research is mainly focused on the integration of adsorption and membrane processes (e.g., diffusion dialysis or electrodialysis) for the treatment, separation and recovery of added-value products from agro-industrial wastes. Indeed, she is the principal investigator of her own Spanish JIN project, named BIOMEM: "Recovery of biosurfactants from corn steep waters by membrane processes".

Mònica Reig

Mònica Reig is a Chemical Processes Engineering Ph.D. Nowadays, she is working as adjunct professor and as a postdoc researcher at the Resource Recovery and Environmental Management (R2EM) group of the Chemical Department of the Universitat Politècnica de Catalunya (Spain).

Her research is mainly focused on resource recovery, valorisation and added-value products extraction by membrane techniques (e.g., electrodialysis, nanofiltration, membrane contactors) from wastewater and agro-waste residues. Indeed, she is actively involved on a European H2020 Project, named SEA4VALUE: Development of radical innovations to recover minerals and metals from seawater desalination brines.

Preface to “Wastewater Treatment by Adsorption and/or Ion-Exchange Processes for Resource Recovery”

The triple-R model (reduce, reuse, and recycle) is the essential concept of the circular economy. Due to population growth, the recovery of added-value products from wastes has become a challenge. Wastewaters of different origin (urban, industrial, mining, textile, distillery, and microbial culture, among others) are rich in energy, water, and nutrient sources that can be recovered and reused within a circular economy framework. Recently, wastewater treatment plants have been converted into biofactories, since they can convert waste into new products (water, nutrients, fertilizers, biomethane, electricity, heat, etc.) with a minimal environmental impact. In this context, adsorption and ion-exchange, as well as the integration of both processes, have been proposed as promising technologies for the treatment of wastewaters for resource recovery. Therefore, the aim of this Special Issue, entitled “Wastewater Treatment by Adsorption and/or Ion-Exchange Processes for Resource Recovery”, is to promote these two processes as innovative and environmentally friendly alternatives for the recovery of secondary raw materials from by-products or waste streams. These processes could improve the environmental, economic, and social impacts of the currently used wastewater treatment techniques.

Xanel Vecino and Mònica Reig

Editors

Editorial

Wastewater Treatment by Adsorption and/or Ion-Exchange Processes for Resource Recovery

Xanel Vecino ^{1,2,*}  and Mònica Reig ^{1,2} 

¹ Chemical Engineering Department, Escola d'Enginyeria de Barcelona Est (EEBE), Campus Diagonal-Besòs, Universitat Politècnica de Catalunya (UPC)-BarcelonaTECH, C/Eduard Maristany 10-14, 08930 Barcelona, Spain; monica.reig@upc.edu

² Barcelona Research Center for Multiscale Science and Engineering, Chemical Engineering Department, Escola d'Enginyeria de Barcelona Est (EEBE), Campus Diagonal-Besòs, 08930 Barcelona, Spain

* Correspondence: xanel.vecino@upc.edu

Nowadays, resource recovery is a trending topic following the circular economy schemes proposed by the European Union. The main idea is to recover as much as resources from wastewater or other residues, realizing the “waste to product” concept. In this sense, adsorption and ion-exchange processes are environmental, eco-friendly and non-expensive technologies that can achieve this aim. For that reason, this Special Issue is centered on wastewater treatment by adsorption and/or ion-exchange processes for resource recovery.

Six full research articles are published in this Special Issue. Although the authors are mostly Spanish and mainly from the Chemical Engineering Department of Universitat Politècnica de Catalunya, the published articles covered the removal and recovery of several compounds/minerals from water and wastewater, with worldwide interest. Specifically, the removal/recovery of organic dyes, phosphates, heavy metals, biosurfactants, Pb(II) or lactic acid has been studied using different sorbents or resins, including commercials and natural ones.

For instance, an international research group formed by researchers from different Chemical Departments of Pakistan, Malaysia, Saudi Arabia, Poland and Greece studied a hybrid biosorbent process for heavy-metal-polluted water, followed by a nanofiltration step. Indeed, the main objective of the work was the removal of Pb(II) from wastewater. In this case, a maximum biosorption capacity of 365.9 mg/g was achieved, following the Langmuir isotherm model. Moreover, different desorption agents were studied, acetic acid being the optimal one for hybrid biosorbent regeneration. Finally, a nanofiltration step was used to increase the remediation effectiveness, even when treating wastewater with high Pb(II) concentrations. All in all, authors concluded that the integration of the hybrid biosorbent and nanofiltration techniques resulted in a low-cost and attractive process for the removal of Pb(II) from wastewater [1].

This Special Issue also contains another work related to bioconcepts. In this case, two research groups from two Chemical Departments from Spanish universities collaborate with CETaqua, a Spanish Water Technology Center, to recover biosurfactants from an agro-food stream through a novel and sustainable method. Thus, calcium-alginate-based polymers were evaluated for use in the recovery of biosurfactant in corn steep water. The results showed that, although biosurfactants from corn steep water have other competing compounds (such as inorganic solutes and biomolecules), calcium-alginate-based biopolymers had an adsorption capacity around 50 mg/g, recovering around 50% of the biosurfactants. Then, the authors concluded that it would be possible to formulate green membranes based on calcium-alginate-based polymers for a sustainable recovery of biosurfactants from aqueous streams [2].

Regarding organic compounds, some of the previous Spanish authors published another article of this Special Issue, reporting the recovery of lactic acid by commercial ion-exchange resins. This topic could be of interest in the bio-refinery field and different

Citation: Vecino, X.; Reig, M.

Wastewater Treatment by Adsorption and/or Ion-Exchange Processes for Resource Recovery. *Water* **2022**, *14*, 911. <https://doi.org/10.3390/w14060911>

Received: 4 March 2022

Accepted: 10 March 2022

Published: 15 March 2022

Publisher's Note: MDPI stays neutral with regard to jurisdictional claims in published maps and institutional affiliations.



Copyright: © 2022 by the authors. Licensee MDPI, Basel, Switzerland. This article is an open access article distributed under the terms and conditions of the Creative Commons Attribution (CC BY) license (<https://creativecommons.org/licenses/by/4.0/>).

industrial sectors, such as the cosmetic, food or pharmaceutical industries. The study was focused on the determination of the optimal operational parameters for the adsorption (e.g., pH, solid/liquid ratio, contact time) and desorption (e.g., regenerant agent, contact time, solid/liquid ratio) steps. For that, a Box–Behnken factorial design and the response surface methodology were used, as well as isotherm and kinetic models. The authors concluded that the best option was to use the A100 resin for the adsorption/desorption process, using the feed water at pH 4, with a solid/liquid ratio of 0.15 g/mL for 1 h (adsorption step) and using NaOH 0.1 M for 30 min, with a solid/liquid ratio of 0.15 mg/mL (desorption step). All in all, the Langmuir isotherm and pseudo-second-order kinetic model fit the results, which were able to recover 85% of the lactic acid, achieving a desorption capacity of around 4.5 mg/g [3].

Moreover, Spanish researchers from the Universitat Politècnica de Catalunya and the Technological Center Eurecat published two articles in this Special Issue [4,5]. The first manuscript [4] was focused on the reduction of granular ferric hydroxide (GFH) to improve phosphate adsorption kinetics. In that case, two methods were used: ball milling and ultra-sonication. With the first one, it was possible to reduce the GFH from 0.5–2 mm to 0.1–2 µm and achieve a total disaggregation of its structure, whereas the ultra-sonication system allowed only a partial disaggregation and a final size of 2–50 µm. Experimental isotherm data were fitted properly to the Langmuir model, while kinetic tests were correlated with the pseudo-second-order model. Finally, it was concluded that the application of both methods for GFH reduction increased the kinetic constant in contrast with the virgin GFH, thus enhancing the phosphate adsorption rate. On the other hand, the aim of the second manuscript [5] was the removal of heavy metals (mainly Zn and Cu) from contaminated wastewater by hydroxyapatite (HAP)-based particles. In that case, HAP was synthesized by a cost-efficient route: the combination of natural solid calcite and a phosphate solution. Kinetic and isotherm experiments were carried out by the synthesized HAP, and the sonication effect was compared. The results showed that the synthesized HAP with calcite particles has a high Zn and Cu removal capacity (34.97 mg/g for Zn and 60.24 mg/g for Cu). In addition, sonication tests demonstrated that Zn removal was enhanced but Cu removal was not.

Finally, one more article was published by researchers from Pakistan, Slovakia and Iran focused on wastewater treatment by the adsorption of malachite green dye onto mesoporous natural inorganic clays (NICs) [6]. Several operational parameters of the batch adsorption process were studied, such as dye concentration, contact time, the amount of NICs or the solution pH. Equilibrium isotherms and kinetic studies fit properly to the Langmuir and pseudo-first-order kinetic models, respectively. Moreover, the authors concluded that NICs with high surface areas and high aqueous solution pH were favorable for the adsorption process, indicating that NICs can be effective adsorbents for the removal of dye from aqueous solutions.

As a summary of this Special Issue, it can be concluded that sustainable, green, low-cost, attractive and efficient adsorption and ion-exchange processes can be used for resource recovery from wastewater.

Funding: This research received no external funding.

Data Availability Statement: Not applicable.

Acknowledgments: The guest editors are grateful to all the authors that contributed to this Special Issue.

Conflicts of Interest: The guest editors declare no conflict of interest.

References

1. Hanif, A.; Ali, S.; Hanif, M.A.; Rashid, U.; Bhatti, H.N.; Asghar, M.; Alsalme, A.; Giannakoudakis, D.A. A Novel Combined Treatment Process of Hybrid Biosorbent–Nanofiltration for Effective Pb(II) Removal from Wastewater. *Water* **2021**, *13*, 3316. [CrossRef]
2. Martínez-Arcos, A.; Reig, M.; Cruz, J.M.; Cortina, J.L.; Moldes, A.B.; Vecino, X. Evaluation of Calcium Alginate-Based Biopolymers as Potential Component of Membranes for Recovering Biosurfactants from Corn Steep Water. *Water* **2021**, *13*, 2396. [CrossRef]

3. Vecino, X.; Reig, M.; Valderrama, C.; Cortina, J.L. Ion-Exchange Technology for Lactic Acid Recovery in Downstream Processing: Equilibrium and Kinetic Parameters. *Water* **2021**, *13*, 1572. [CrossRef]
4. Martí, V.; Jubany, I.; Ribas, D.; Benito, J.A.; Ferrer, B. Improvement of Phosphate Adsorption Kinetics onto Ferric Hydroxide by Size Reduction. *Water* **2021**, *13*, 1558. [CrossRef]
5. Gibert, O.; Valderrama, C.; Martínez, M.M.; Darbra, R.M.; Moncunill, J.O.; Martí, V. Hydroxyapatite Coatings on Calcite Powder for the Removal of Heavy Metals from Contaminated Water. *Water* **2021**, *13*, 1493. [CrossRef]
6. Ullah, S.; Rahman, A.U.; Ullah, F.; Rashid, A.; Arshad, T.; Viglašová, E.; Galamboš, M.; Mahmoodi, N.M.; Ullah, H. Adsorption of Malachite Green Dye onto Mesoporous Natural Inorganic Clays: Their Equilibrium Isotherm and Kinetics Studies. *Water* **2021**, *13*, 965. [CrossRef]

Article

A Novel Combined Treatment Process of Hybrid Biosorbent–Nanofiltration for Effective Pb(II) Removal from Wastewater

Asma Hanif ^{1,2}, Shaukat Ali ², Muhammad Asif Hanif ^{2,*}, Umer Rashid ^{3,*} , Haq Nawaz Bhatti ², Muhammad Asghar ⁴, Ali Alsalmeh ⁵  and Dimitrios A. Giannakoudakis ^{6,7} 

¹ Department of Chemistry, Government College Women University, Faisalabad 38000, Pakistan; asmarana_hanif@yahoo.com

² Department of Chemistry, University of Agriculture, Faisalabad 38040, Pakistan; shaukatchemist@hotmail.com (S.A.); haq_nawaz@uaf.edu.pk (H.N.B.)

³ Institute of Nanoscience and Nanotechnology (ION2), Universiti Putra Malaysia, Serdang 43400, Selangor, Malaysia

⁴ Department of Biochemistry, University of Agriculture, Faisalabad 38040, Pakistan; mabajwapk@yahoo.com

⁵ Chemistry Department, College of Science, King Saud University, Riyadh 1145, Saudi Arabia; aalsalme@ksu.edu.sa

⁶ Institute of Physical Chemistry, Polish Academy of Sciences, Kasprzaka 44/52, 01-224 Warsaw, Poland; dagchem@gmail.com

⁷ Department of Chemistry, Aristotle University of Thessaloniki, 54124 Thessaloniki, Greece

* Correspondence: drmuhammadasifhanif@gmail.com (M.A.H.); dr.umer.rashid@gmail.com (U.R.); Tel.: +60-3-9769-7393 (U.R.)

Citation: Hanif, A.; Ali, S.; Hanif, M.A.; Rashid, U.; Bhatti, H.N.; Asghar, M.; Alsalmeh, A.; Giannakoudakis, D.A. A Novel Combined Treatment Process of Hybrid Biosorbent–Nanofiltration for Effective Pb(II) Removal from Wastewater. *Water* **2021**, *13*, 3316. <https://doi.org/10.3390/w13233316>

Academic Editors: Xanel Vecino and Mónica Reig

Received: 24 September 2021

Accepted: 8 November 2021

Published: 23 November 2021

Publisher's Note: MDPI stays neutral with regard to jurisdictional claims in published maps and institutional affiliations.

Abstract: The untreated effluents discharged by different industries, such as metallurgy, fertilizers, pesticide, leather, mining, electroplating, surface finishing, aerospace, and electroplating, have increased the risk of the contamination of bodies of water by heavy metals. Herein, hybrid biosorbent–nanofiltration processes for Pb(II) removal from wastewater was studied. The hybrid biosorbent was prepared from date seed waste and *Ganoderma lucidum*. Hybrid biosorbent characterization was performed by SEM and FTIR. SEM micrographs showed that the HB surface is irregular. For the adsorption studies, various sorption parameters were optimized. The maximum biosorption capacity of immobilized heat-inactivated hybrid biosorbent was 365.9 mg/g, with the Langmuir isotherm model to present the best fit. Desorption experiments were conducted for regenerating immobilized heat-inactivated hybrid biosorbent for three consecutive cycles using different desorption agents, with acetic acid to be the optimum. Going a step further, nanofiltration was also applied as a post-treatment process to elevate the remediation effectiveness for wastewater of high Pb(II) initial concentrations. The reasonably low cost and high removal of Pb(II) make hybrid biosorbent–nanofiltration processes a prosperous and potentially attractive hybrid approach against heavy-metal-polluted wastewater.

Keywords: hybrid biosorbent; desorption; thermodynamic; nanofiltration



Copyright: © 2021 by the authors. Licensee MDPI, Basel, Switzerland. This article is an open access article distributed under the terms and conditions of the Creative Commons Attribution (CC BY) license (<https://creativecommons.org/licenses/by/4.0/>).

1. Introduction

For wastewater management, strict environmental rules are developed in many countries [1]. Among the plethora of potential pollutants that wastewaters can contain, toxic heavy metals (HMs) are assumed to be major pollutants due to their existence in ground, marine, industrial, and even treated wastewater in low concentrations [2,3]. Heavy metal ions in wastewater must be regulated and their concentration retained at lower than established values. Rampant anthropogenic activities result in the excessive release of metals in water systems. Being non-biodegradable, inorganic heavy metal ions cause health risks to living biota even at low concentrations [4]. Due to their accumulation tendency and persistence, heavy metals lead to toxicity and complications in living organisms and environments. Pb (II) is a hazardous environmental pollutant. Upon insertion to human

body, it can limit the oxygen-carrying capacity of red blood cells and cause harmful effects to the hearing, nervous system, and kidneys. In drinking water, the maximum allowable level of lead is 15 µg/L according to EPA [5].

Different processes for heavy metal removal are available, among which electrolysis, evaporation, ion exchange, adsorption, and coagulation–flocculation are the most used ones [6,7]. However, these techniques have several demerits, such as high chemical requirements (such as expensive organic solvents, which produce side-polluted wastes), high operational costs, and in various cases low efficiency. The development of economical water treatment techniques, which will be more environmentally friendly and in general more practical in real-life application than the traditional methods, is always an open research and development goal. A modern strategy towards the development of effective technologies has led to hybrid processes, advanced chelating materials, enhanced membrane filtration, and specific adsorbents in the production of reclaimed water. The use of appropriate biological methods for the uptake of wastewater pollutants includes bioaccumulation and biosorption. Biosorption is the sequestering of organic or inorganic pollutants by active or dead/inactive biomass. Bioaccumulation refers to intracellular accumulation of pollutant [8].

Various pressure-driven membrane filtration systems such as nanofiltration (NF), microfiltration, ultrafiltration, and reverse osmosis have become popular treatment technologies for wastewater. Among these approaches, nanofiltration is comparatively the newest wastewater treatment process. The characteristics of NF membranes are between ultrafiltration and reverse osmosis [9]. NF membranes are used for water purification due to higher flux, lower operational pressure, less energy consumption, lower monovalent ions rejection, and higher rejection of divalent ions. Therefore, NF process can be extensively used in the retention of dyes [10], treatment of drinking and industrial wastewater [11], and removal of micropollutants [12].

Considering all the aforementioned, the goal of this work was to explore the potential of using simple and cost-effective biosorbent and nanofiltration membranes to treat wastewater containing Pb(II) using immobilized hybrid biosorbent–nanofiltration processes.

2. Materials and Methods

2.1. Chemicals

All the chemicals were purchased from Sigma-Aldrich and Merck. Stock Pb(II) solution was prepared by dissolving 1.60 g of lead nitrate in 1 L DDW. The required solutions were prepared by diluting metal stock solution. A total of 1M NaOH/ HCl was used to adjust the pH of solutions.

2.2. Hybrid Biosorbent Preparation and Characterization

The date seed waste (A2) left after oil extraction was collected from the Nano and Biomaterials Laboratory, Department of Chemistry, University of Agriculture, Faisalabad-Pakistan. The date seed waste was washed twice with distilled water and then oven dried at 60 °C to obtain constant mass and stored in sealed plastic box. *Ganoderma lucidum* (A1) was preserved by sub culturing on PDA plates and stored at 4 °C for further study. The desired amount of growth medium was prepared in conical flasks. The fungal inoculums were prepared from properly grown, uncontaminated slants. The inoculum media for *Ganoderma lucidum* were prepared following compositions given in the literature [13]. A total of 1M NaOH/ HCl was used to adjust the pH of media at 4.5. Conical flasks containing 100 mL of growth medium were sterilized by autoclaving at 121 °C for 15 min. After cooling to a lower temperature (≈40 °C), spores of *Ganoderma lucidum* were aseptically added to the growth medium and incubated in an orbital shaker (120 rpm) at 30 °C for 7 days. After the incubation period, homogenous suspensions of *Ganoderma lucidum* spores were formed.

The pre-weighed, oven-dried date seed waste was transferred to Erlenmeyer flasks containing growth medium and autoclaved for 15 min at 121 °C. Then, 5.0 ± 0.025 mL *Ganoderma lucidum* mycelium suspension was added to these flasks and agitated at 100 rpm,

for 7 days at 30 °C. After seven days, *Ganoderma lucidum* biomass was found growing on the date seed waste to produce a hybrid biosorbent (HB). The dry weight of A1 within A2 was calculated as the weight difference of A2 before and after A1 growth on it, when dried at 70 °C overnight [14].

The hybrid biomass (HB) was autoclaved at 121 °C for 15 min and then oven dried for 72 h at 70 °C to obtain heat-inactivated hybrid biosorbent (HI HB). The material was crushed by means of a food processor (Moulinex, France) and U.S. A standard sieve was used for sieving. The fraction with 50 mesh size was selected for further studies and stored in sealed plastic box. Two per cent Na-alginate was used to immobilize the heat-inactivated hybrid biosorbent (HI HB). To dissolve sodium alginate, the solution was heated and then cooled down. Then, 1g/100 mL of HI HB was mixed with the above solution to obtain a homogeneous mixture, which was taken in a burette and introduced into 0.1M CaCl₂·2H₂O solution. The prepared beads were washed twice and stored in 0.05M CaCl₂·2H₂O [15].

The surface morphologies of samples were analyzed by SEM (FEI Quanta 400F electron microscope), and the chemical characteristics of hybrid biosorbent were interpreted by FTIR Agilent N630, with the samples prepared as KBr discs.

2.3. Biosorption Studies

The immobilized HI HB potential for Pb(II) biosorption was determined in batch mode (Figure 1). The effects of pH (2–4.5), biosorbent dose (0.05–0.3 g/L), initial metal ion concentration (25–400 ppm), and temperature (30–70 °C) were checked by varying one parameter, while keeping other parameters constant. The effects of the presence of Mg⁺², Al⁺³, Cu⁺², and Zn⁺² on the adsorption capacity of immobilized HI HB in binary system for Pb(II) were also studied. The concentration of lead ions was fixed at 100 ppm, while the concentration of other metal ions was varied from 25 to 400 ppm. Blank solutions without hybrid biosorbent were run in parallel at the same conditions. The samples were shaken at 120 rpm for a specific duration using an orbital shaking incubator (PA250/25H). Atomic absorption measurements were performed using a Varian AA240, GTA 120 instrument to determine lead concentration in solutions. The removal capacity was determined using the following equation:

$$q_e = \frac{(C_o - C_e)V}{W}$$

where C_o and C_e (mg/L) denote the initial and equilibrium metal ion concentration, respectively, V (L) is the volume of the solution, and W (g) is the amount of HB used [16].

2.4. Biosorption Isotherm Models

The equilibrium adsorption data were fitted to the following isotherms according to equations given in the literature, including: Freundlich model [17], Langmuir model [18], Temkin [17], and Harkins and Jura [19], to determine the adsorption mechanism for Pb (II) removal by hybrid biosorbent.

2.5. Biosorption Thermodynamics

The study of thermodynamic parameters is essential to determine the orientation and feasibility of an adsorptive reaction. The thermodynamic behavior of metal ions' biosorption using immobilized HI HB can be estimated by various thermodynamic parameters, such as change in free energy (ΔG), entropy (ΔS) and enthalpy (ΔH) using equations given in the literature [20].

2.6. Desorption

After biosorption experiments, Pb(II) ions were desorbed from the hybrid matrix. Three sorption/regeneration cycles for immobilized HI HB were conducted using various eluents. Sorption of metal ions was performed at optimum pH by adding 0.05 g hybrid biosorbent in 100 mg/L Pb (II) solution at 30 °C for 3 h. After the solution was filtered and dried, the metal ions loaded immobilized HI HB into the oven at 60 °C. Then, the dried

biomass was shaken with 0.1M HCl, HNO₃, acetic acid, and EDTA. Desorption efficiency (%) was estimated using following equation:

$$\text{Desorption efficiency (\%)} = \frac{q_{de}}{q_{ad}} \times 100$$

Combined Treatment

Hybrid Biosorbent treatment

Nanofiltration treatment

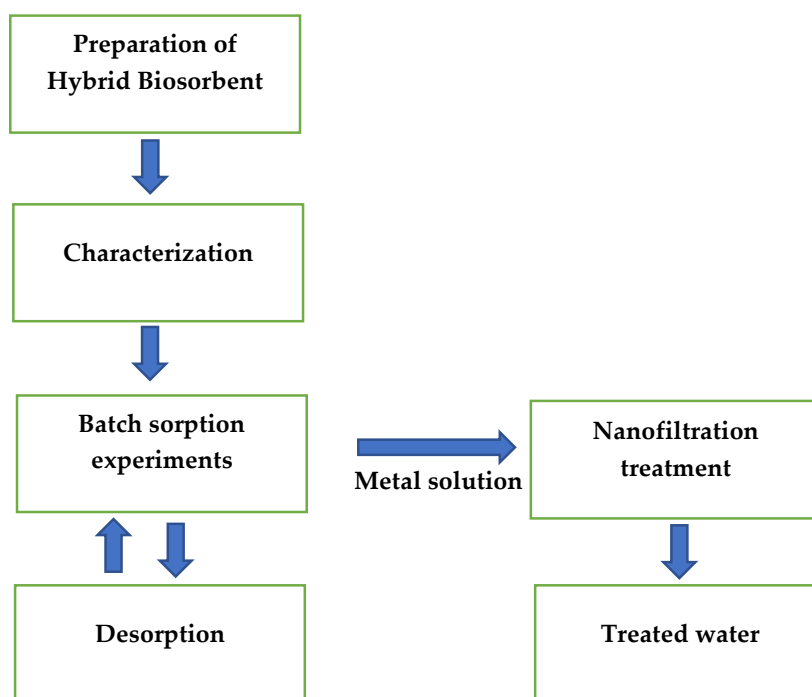


Figure 1. Schematic design of hybrid biosorbent–nanofiltration process.

2.7. Nanofiltration

Wastewater was treated through integrated processes by adsorption as a pretreatment, with nanofiltration (NF) as a post-treatment in this study. A commercially available NF membrane was used. After adsorptive removal using immobilized HI HB, the lead ions were subjected to the NF membrane unit. The main properties of the NF membrane are summarized in Table 1.

Table 1. Characteristics of NF membrane.

Parameters	Nanofiltration
Membrane type	Flat sheet
Material	PA (polyamide)
Membrane area	0.006 m ²
Pressure	5 bar

Membrane Filtration Experiments

For removal studies, a dead-end NF unit was utilized. The NF unit consisted of a reservoir, a membrane module, and a high-pressure pump. This NF unit was operated at a pressure of 5 bar. The membrane was immersed in deionized water before being used in any experiment and pressurized at 5 bar for 1 h to prevent compression effects

and to determine leak tightness. In these experiments, after adsorptive removal, metal ion solutions were pumped out of the membrane module. The influence of important process parameters such as pH, temperature and initial metal ion concentration upon lead ions removal was estimated. The percentage removal was calculated through the following relationship:

$$\% \text{ Removal} = \frac{(C_i - C_f)}{C_i} \times 100 \quad (1)$$

2.8. Statistical Analysis

All the experiments were performed in triplicate. The results were analyzed statistically by applying regression analysis.

3. Results and Discussion

3.1. Biosorption Study

3.1.1. Characterization

The morphological uniqueness of biosorbents can be evaluated using SEM. The SEM micrograph of hybrid biosorbent (HB) is shown in (Figure 2a), where all the morphological characteristics were taken at $5000\times$ magnification. The SEM micrograph of HB before biosorption revealed an irregular, rough, and porous surface. Such a structure significantly enlarges the available adsorptive surface, which results in increased binding capabilities of Pb(II) ions (Figure 2b). Therefore, HB is more conducive for the adsorption process. After biosorption of metals and dyes the pores are filled with sorbate ions on the surface of the biosorbents [21,22].

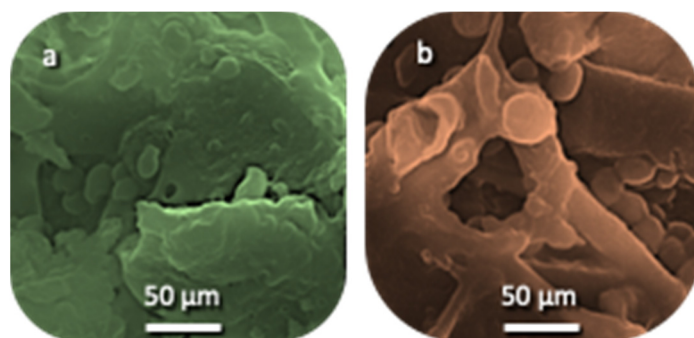


Figure 2. (a) SEM micrograph of hybrid biosorbent (HB). (b) SEM micrograph of HB loaded with Pb(II) ions.

The Fourier transform infrared spectroscopic study reveals important information about the chemical environment of biomaterials responsible for sorption. The spectrum of HB shows a strong and broad unbounded O-H stretching band centered at 3349 cm^{-1} . The peaks at 2924 and 2853 cm^{-1} were due to C-H symmetric and asymmetric stretching vibrations. The peak observed at 1735 cm^{-1} corresponds to C=O stretching vibration due to non-ionic -COOH groups. The peak at 1507 cm^{-1} corresponds to the amide II band of protein peptide bonds. In addition, the peak at 1032 cm^{-1} is attributable to the C-N and C-O bonds (Figure 3) [23]. This indicates that the hydroxyl and carboxyl groups of HB participated in the Pb(II) ions biosorption by sharing or exchanging electrons among sorbent and sorbate.

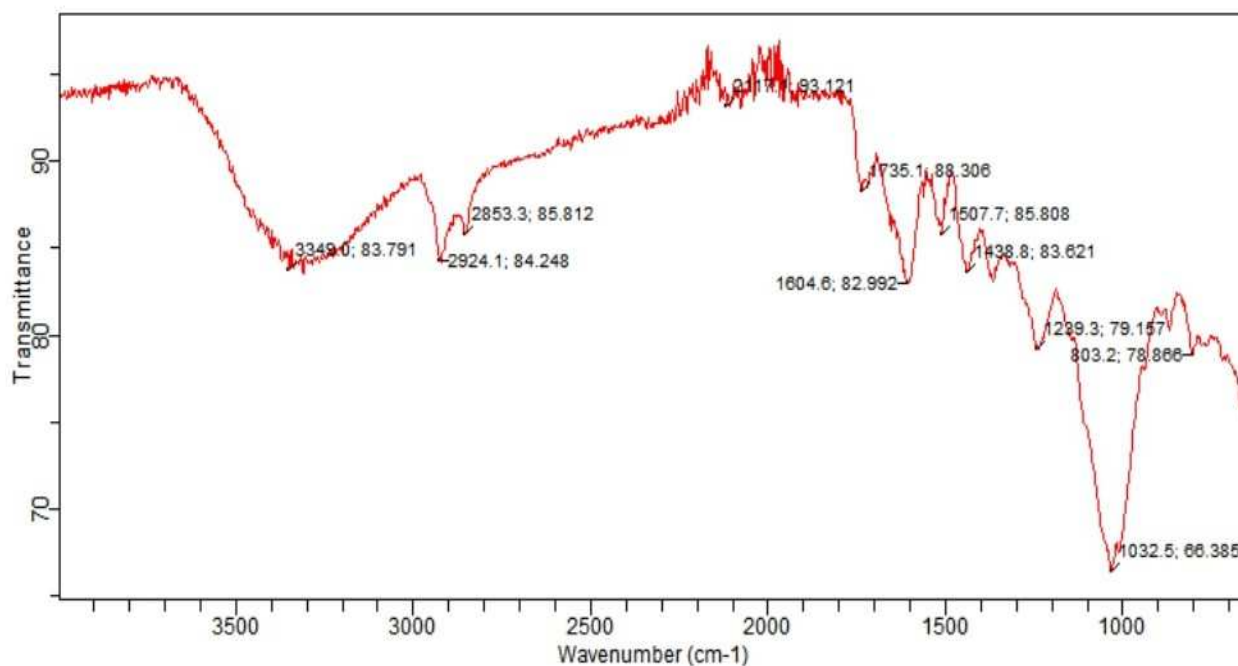


Figure 3. FTIR spectra of hybrid biosorbent (HB).

3.1.2. Batch Study

The different pH binding profiles for these components can be explained based on the different chemical interactions of each species with the adsorbent's surface. The influence of the initial pH (2–4.5) on Pb (II) adsorption was determined at 30 °C by fixing the initial metal ion concentration at 100 mg/L and 0.05 g/L biosorbent dose. The maximum removal of Pb (II) ions was found as 365.9 mg/g at pH 4.5 by immobilized heat-inactivated hybrid biosorbent (Figure 4). The lower uptake of metal ions in stronger acidic conditions (pH 2–4) by hybrid biosorbent can be ascribed to the large number of hydrogen or/and hydronium ions competing with Pb (II) ions for the binding at sorption sites of biosorbent, as has been reported by other authors [24,25]. The concentration of H⁺ decreased with the increase in pH, leading to an increased uptake of lead ions [26]. The increase in the rate of adsorption with increasing pH was due to a combination of various effects: (i) less ionic competition due to metal binding sites' deprotonation, (ii) at higher pH values, decrement in solubility of heavy metal ions. However, precipitation occurs at higher pH (>7.0) due to the increased concentration of hydroxyl ions in the medium [27].

The adsorption capacity can be strongly affected by the biosorbent dosage [28]. To determine the biosorbent dosage effect on adsorption, optimum adsorption conditions were determined for better biosorption. The influence of biosorbent dosage on the removal efficiency of hybrid biosorbent against Pb(II) was examined in the range of 0.05–0.3 g/L, when pH (4.5), metal ion concentration (100 mg/L), and temperature (30 °C) were kept constant (Figure 5). The results presented in Figure 5 indicate that the equilibrium biosorption capacity for metal ions decreased when the immobilized HI HB dosage increased. The uptake capacity of hybrid biosorbent decreased with the increase in biomass dosage, whereas the reverse was true for percentage removal. The maximum metal ion removal was observed at 0.05 g/L. It was noticed that the removal efficiency (both as an absolute value or expressed as per adsorbent mass) of the hybrid biomass was a function of biomass amount. The metal ions' removal declined with the increase in biomass dose. The decremental trend of Pb(II) ions' removal by the increase in the utilized biomass is due to poor utilization and the agglomeration of biomass at a higher dosage leading to a lower extent of available adsorption sites [29]. This observation clearly suggested that maximum adsorption sets in after a particular biomass dose, thus, the ratio of ions bound to hybrid biosorbent to free ions became constant even when more biomass was added [30]. The selection of such

a biomass concentration when both metal uptake capacity and percentage removal have suitable high values is practically very important, since the optimization of the minimum desired amount has a direct positive effect on the cost.

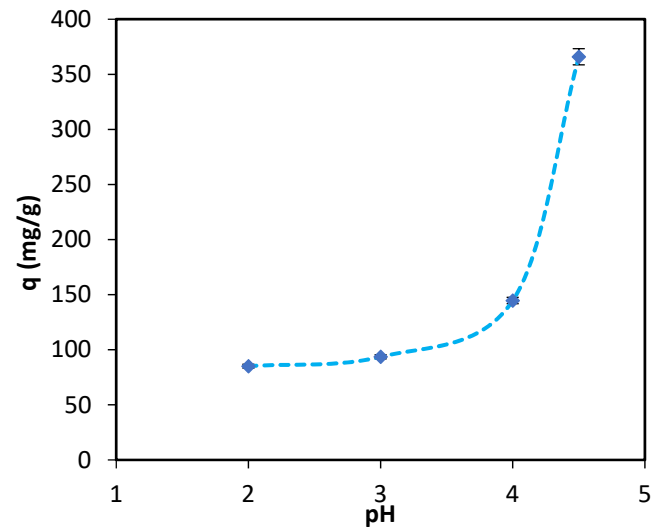


Figure 4. Effect of pH on the Pb(II) ions' removal by immobilized heat-inactivated hybrid biosorbent (HI HB).

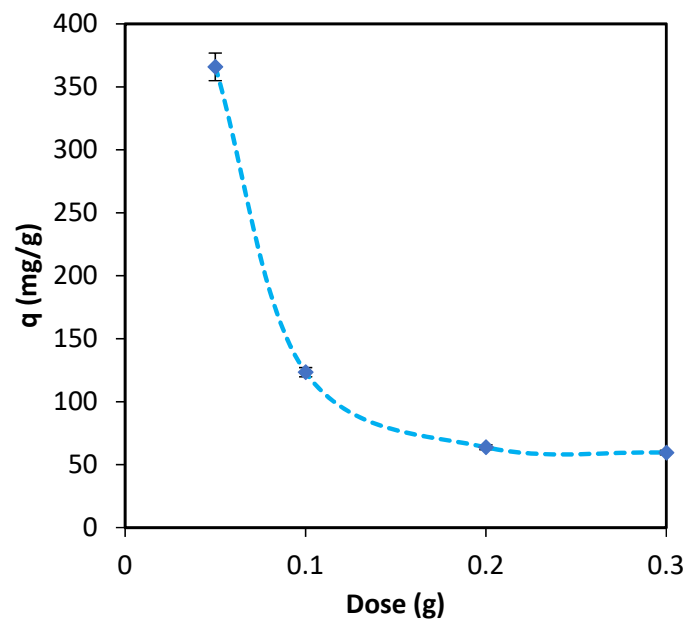


Figure 5. Effect of biosorbent dose on the removal of Pb(II) ions by immobilized HI HB.

The effect of initial Pb(II) concentration (25–400 mg/L) on adsorption efficiency of immobilized HI HB was studied at an optimum pH (4.5) and biosorbent dose (0.05 g) (Figure 6). It was observed that the adsorbed amount increased almost linearly as Pb(II) concentration increased up to 100 mg/L and remained stable for higher Pb(II) concentrations. The high initial metal ion concentration suggests an initial force to overcome pollutant mass transfer resistances between solid and aqueous phases. The incremental trend of adsorption at low initial Pb(II) concentration might be due to increased electrostatic interactions. The number of adsorbed metal ions was higher at high initial metal concentrations than at lower concentrations, because more binding sites were free for interaction [27]. At higher concentrations, the vacant sites of hybrid biosorbent became less, and sorption sites rapidly saturated due to constant amounts of adsorbent.

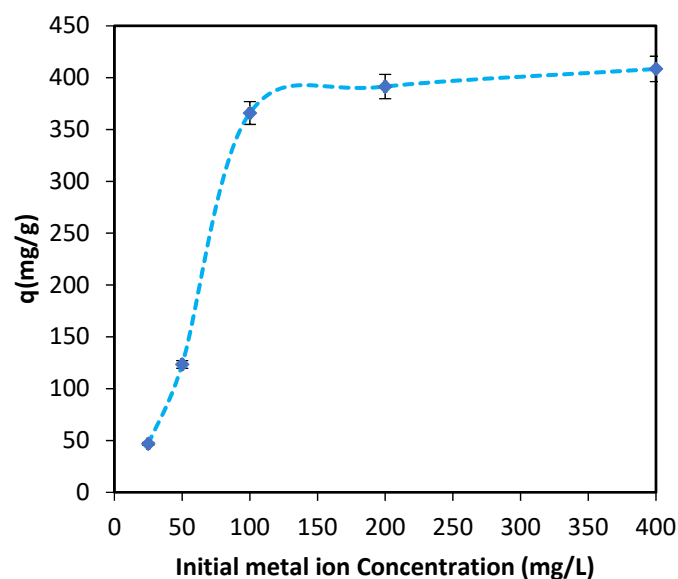


Figure 6. Effect of initial concentration on the removal of Pb(II) ions by immobilized HI HB.

Temperature change has an effect on adsorption capacity. The effect of temperature on Pb(II) removal using immobilized HI HB was investigated at five different temperatures; the results are shown in Figure 7. Adsorption capacity was at a maximum at 30 °C, then decreased steadily with an increase in temperature. The adsorption capacity decreased because the adsorptive forces responsible for Pb(II) biosorption on immobilized HI HB became weaker at higher temperatures. This might be due to the deactivation of sorption sites of biosorbent at high temperatures, which leads to decreased biosorption [31]. A similar trend was reported for Congo red uptake by surface-modified bentonite [32], and Direct Blue 106 dye adsorption onto pomegranate peels [33].

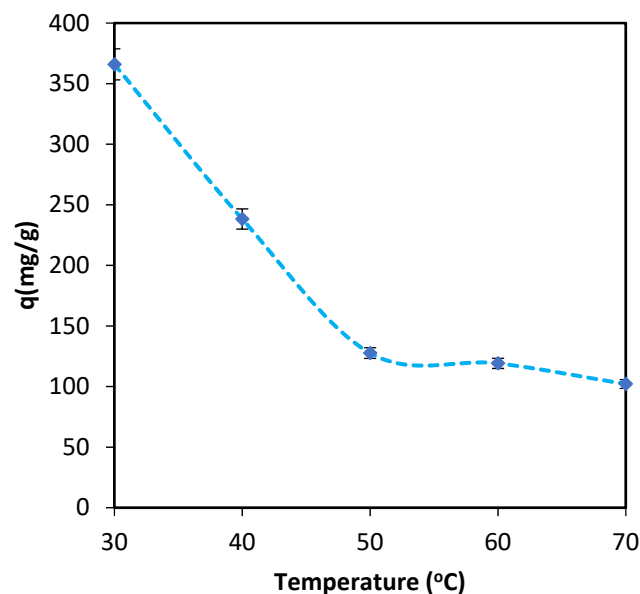


Figure 7. Effect of temperature on the removal of Pb(II) by immobilized HI HB.

3.1.3. Biosorption Isotherms

Different models of isotherms were studied to determine crucial remediation parameters and to have a better comparison with various other parameters reported in the literature materials. More precisely, four isothermal equations were used to study the adsorption process: Temkin, Langmuir, Freundlich, and Harkins–Jura, with all the calcu-

lated parameters shown in Table 2. The adsorption data (at 30 °C) fit well to the Langmuir isotherm ($R^2 = 0.993$) and were significantly close in value to experimental and calculated maximum capacity. Low values of R^2 in the case of the Temkin and Harkins–Jura isotherm model fittings suggested that experimental data for Pb(II) removal were not fitted satisfactorily. In addition, a poor fit to the Freundlich model was also observed. Even though the extraction of specific outcomes for the extent of fitting of the models should be very careful, it can be considered in general based on the above results that a monolayer of adsorption, but also a more heterogeneous adsorption process, took place.

Table 2. Equilibrium modeling of data for the uptake of Pb(II) ions by immobilized HI HB.

Parameters Derived from Isotherm Models	Values
Langmuir	
q_m Calculated (mg/g)	500
q_m Experimental (mg/g)	408.9
b	0.02
R^2	0.993
Freundlich	
K_F	38.90
n	4.20
R^2	0.821
Temkin	
A	5.25
B	0.009
R^2	0.717
Harkins–Jura	
A	25.64
B	3.84
R^2	0.590

3.1.4. Adsorption Thermodynamics

To evaluate the thermodynamic viability of the sorption process and to confirm its nature, different thermodynamic parameters were calculated for Pb(II) adsorption onto immobilized HI HB. The negative value of ΔH° (Table 3) indicates the exothermic nature of the adsorption process. The negative value of ΔS° suggests that the process is enthalpy driven. It also shows a decrease in randomness during Pb(II) biosorption onto immobilized HI HB [34].

Table 3. Thermodynamic parameters for the uptake of Pb(II) ions by immobilized HI HB.

Temperature (K)	ΔG° (kJ/mol)	ΔH° (kJ/mol)	ΔS° (Jmol ⁻¹ K ⁻¹)
303	33.4		
313	34.5		
323	35.6	−38.9	−110.3
333	36.7		
343	37.8		

3.1.5. Competitive Adsorption

A competitive adsorption process was studied to check the effect of other heavy metal ions on Pb(II) ion adsorption (Figure 8). The results demonstrate that as the concentration of the co-cations was increased from 25 to 400 mg/L in solution, immobilized HI HB adsorption capacity decreased. The adsorption capacity of immobilized HI HB decreased from 365.90 mg/g to 143.24 mg/g for the Pb(II) in the Pb(II) + Cu(II) binary system at 100 mg/L. In a binary solution, the sorption of primary metal was inhibited by the presence of secondary metal on the immobilized HI HB. However, copper ions have a stronger inhibitory effect during the sorption of lead as compared to the inhibitory effect of zinc in the adsorption of lead. The overall metal (Pb + Cu) sorbed from binary metal solution always remained lower than individual metal solutions by biosorbent. This indicates a competition between Cu(II), Zn (II), and Pb(II) for common binding sites on immobilized HI HB.

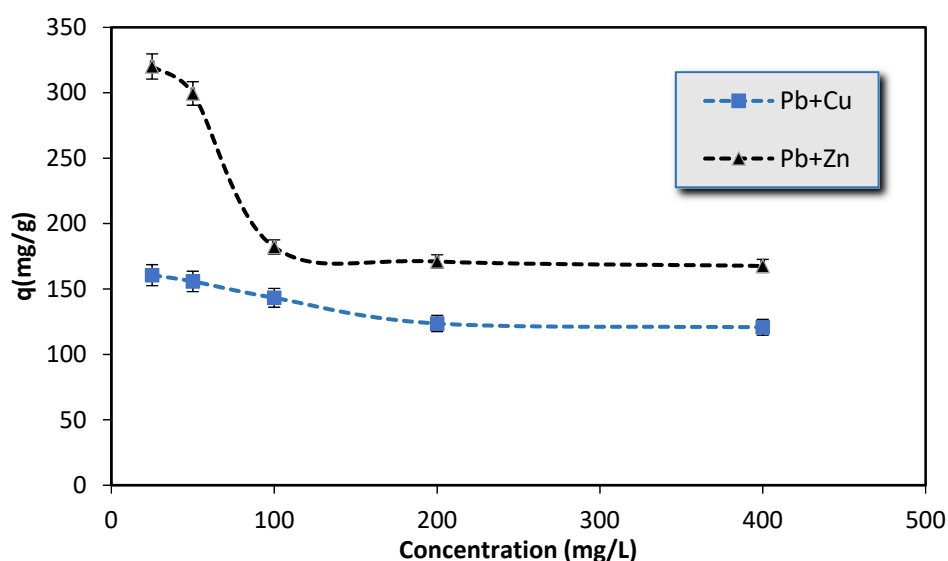


Figure 8. Effect of Cu(II) and Zn(II) concentrations on Pb(II) uptake by immobilized HI HB.

Several co-metal ions are always present in industrial wastewater. The adsorption of any metal depends upon metal chemistry, affinity for binding sites, and the presence of other metal ions in its vicinity. In this view, the effect of light metal ions such as Mg^{2+} and Al^{3+} on the uptake of lead ions by immobilized HI HB was evaluated (Figure 9). In general, metals with a higher atomic weight, ionic size, electronegativity, and electrode potential tend to exhibit a greater affinity for sorption [35]. The light atomic weight co-metal ions with greater charge competed/interfered more with the uptake of lead ions by immobilized HI HB and the competition for adsorption sites on biomass was in the following order $Al^{3+} > Mg^{2+}$.

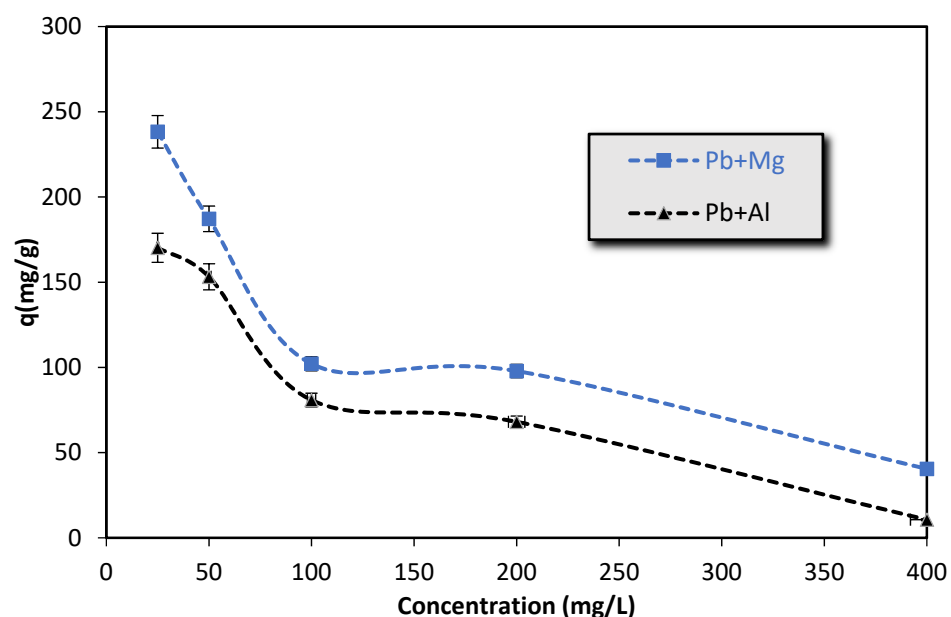


Figure 9. Effect of Mg²⁺ and Al³⁺ concentrations on Pb(II) uptake by immobilized HI HB.

3.1.6. Desorption

In developing a novel adsorbent for real-life applications, its reusability efficiency is vital. Thus, immobilized HI HB was reused in two successive adsorption–desorption cycles for Pb(II) during the current work. The Pb(II)-loaded immobilized HI HB was recovered using 0.1M EDTA, HCl, HNO₃, and acetic acid. The biomass regeneration efficiency of immobilized HI HB-loaded Pb(II) was in the following order: acetic acid < nitric acid < hydrochloric acid < EDTA. The highest metal recovery was 86.4% using acetic acid during the first cycle (Figure 10). On the other hand, the experimental data with EDTA revealed that this regenerating solution was unsuitable to recover metal ions from the sorbent in the next cycle. EDTA was not used in the second cycle because immobilized HI HB changed to an amorphous form after the first desorption cycle. The highest metal recovery was 54.43% and 33.5% using acetic acid after the second and third cycles respectively.

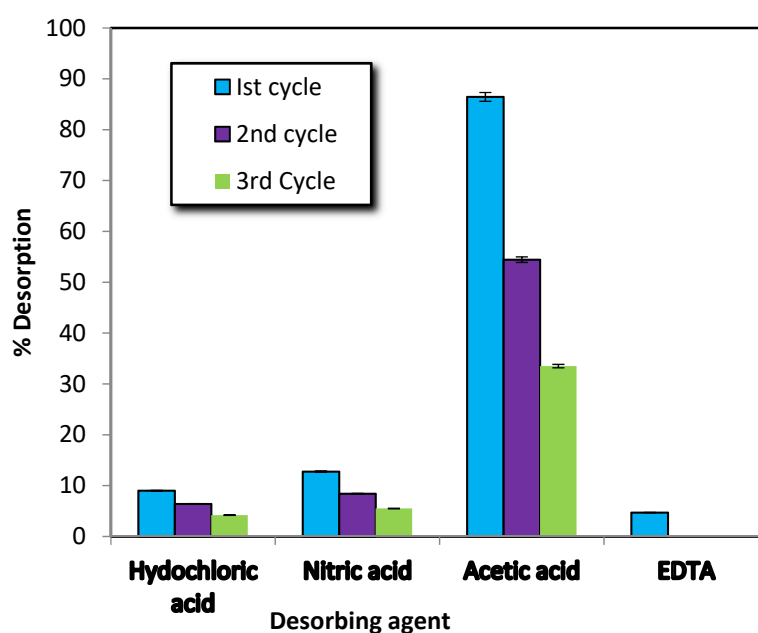


Figure 10. Desorption of Pb(II) ions from immobilized HI HB in three consecutive sorption–desorption cycles.

3.2. Nanofiltration Study

Parameters Affecting the Performance of NF Membrane

In the present study, wastewater is treated through adsorption, in combination with nanofiltration (NF) as a post-treatment process. The important operating parameter affecting the performance of flat sheet polyamide (PA) NF membrane is pH. Solution pH is an important factor in membrane-based processes, because it can affect a membrane's charge and therefore its rejection properties. The separation of ions by NF is achieved both by size exclusion and by electrical interactions between ions in feed aqueous solution and charged NF membranes [36,37]. Figure 11 presents the influence of pH on percentage removal of Pb(II) by PA nanofiltration membrane. It was found that the metal removal was very high across the whole pH range investigated. The results show that, in most cases, increasing pH from 2 to 5 enhanced the removal efficiency of metals >60% [38]. The positively charged ions, for example heavy metal ions, are rejected partly based on molecular weight. The nanofiltration membrane's performance is affected by pH in more than one way. NF membranes are charged due to functional groups' presence and their dissociation. At a higher or neutral pH, the functional groups (i.e., sulfonic group or carboxylic groups) present on the NF membrane's surface are negatively charged but lose their charge at an acidic pH. At a low pH, most RO and NF membranes had lower rejections. The solubility of ions changes by changing the pH and, therefore, the dissociation states of ions also change [39].

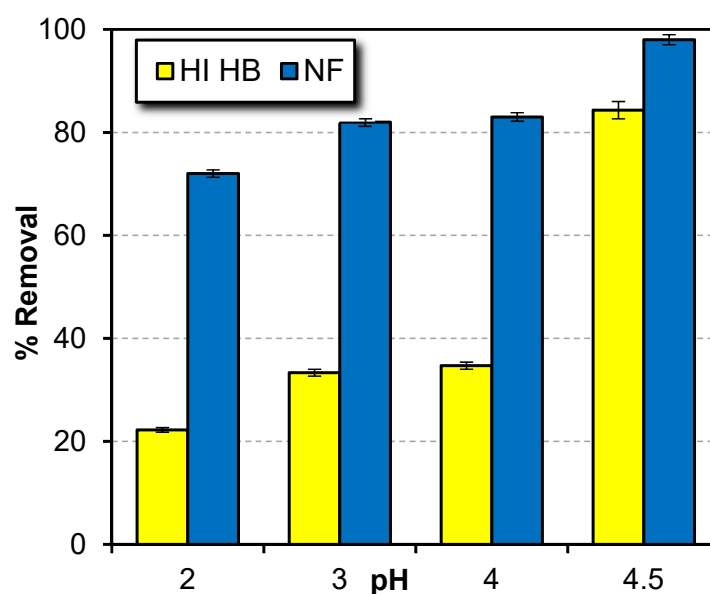


Figure 11. Influence of feed pH on Pb(II) ions' removal using immobilized HI HB and NF.

The effect of initial Pb(II) concentration (25, 50, and 100 mg/L) was studied keeping the applied pressure constant (results shown Figure 12). Very high percentage removal values (>90%) were obtained for all the above-mentioned initial concentrations. The metal removal with the use of NF was >95% in all cases, showing that NF membrane has very good separation properties.

The percentage Pb(II) removal was additionally evaluated as a function of temperature, as shown in Figure 13. It was observed that the Pb(II) percentage removal decreases with the increase in temperature, since removal at 30 °C is >98 % while at 70 °C it is 80%. This can be linked to the fact that the NF membrane flux increased due to a decrease in viscosity when the temperature was increased. However, the rejection by NF membranes is not considerably dependent on temperature [39,40] in comparison to batch removal experiments with immobilized HI HB.

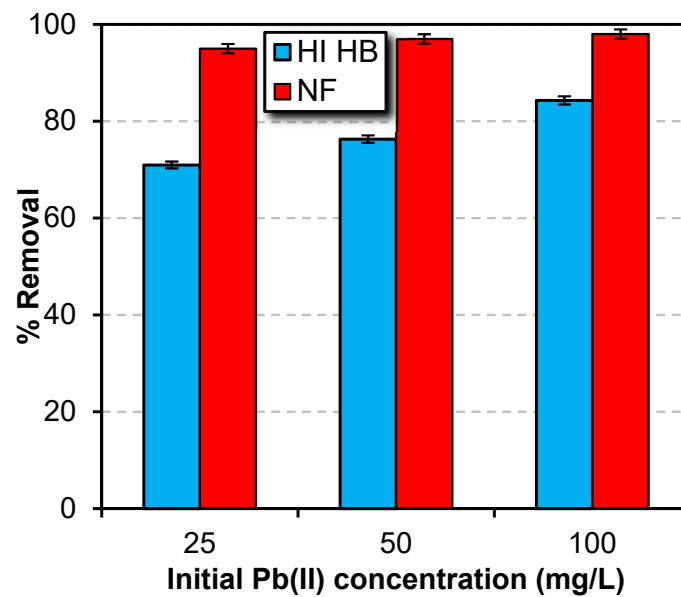


Figure 12. Influence of feed concentration on Pb(II) ions removal using immobilized HI HB and NF.

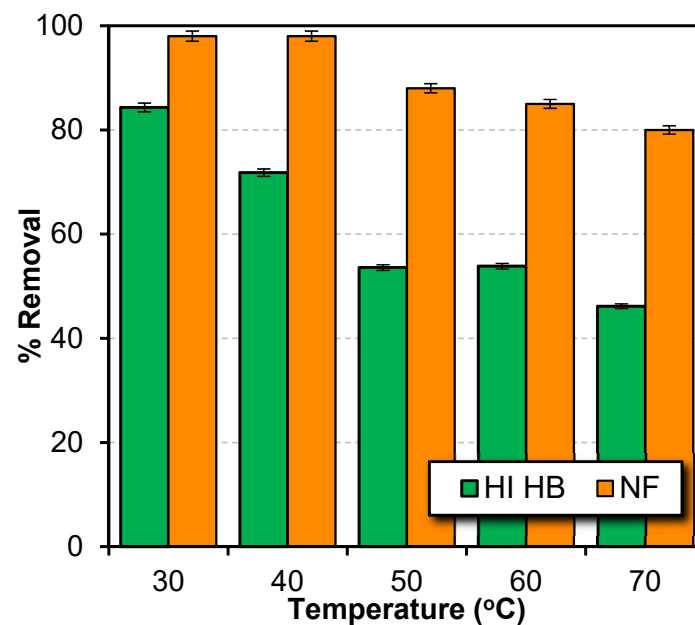


Figure 13. Influence of temperature on Pb(II) ions removal using immobilized HI HB and NF.

4. Conclusions

This research work attempted to combine two technologies, namely (bio)sorption and nanofiltration, towards wastewater treatment. In order to elevate the sorptive efficiency, the strategy of hybrid bio-sorbent was followed by combining two bio-sorbents. The maximum biosorption capacity (365.9 mg/g at 100 mg/L initial Pb(II) concentration) reported in this work is higher than that of various previously used biomaterials. The uptake of Pb(II) from aqueous solutions by hybrid biosorbent would be an addition to the list of high-metal-uptake-capacity biomaterials. The Langmuir isotherm model presents the best fitting. Different divalent metal ions' presence significantly decreased the adsorption capacity of immobilized HI HB. The FTIR results indicate the involvement of hydroxyl and carboxylic groups in the biosorption process. SEM micrographs showed that the HB surface is irregular and rough. Such a surface significantly enlarges the available surface of hybrid biosorbent, which results in increased binding capabilities of metal ions. Nanofiltration as a post treatment after adsorptive removal further increased the percentage removal of

metal ions. The main concluding remarks in this work are that the combination of the two treatments, the hybrid biosorbent and nanofiltration process, resulted in the removal of almost 98% of lead ions, providing better results than each technique separately.

Author Contributions: Conceptualization, M.A.H. and U.R.; data curation, A.H., S.A., H.N.B., M.A. and U.R.; formal analysis, A.H., M.A.H. and U.R.; funding acquisition, U.R., M.A.H. and A.A.; investigation, M.A., D.A.G. and U.R.; methodology, M.A.H., U.R. and D.A.G.; project administration, M.A.H., U.R. and A.A.; resources, M.A.H. and U.R.; visualization, M.A.H. and U.R.; writing—original draft, D.A.G., M.A.H., A.H. and U.R.; writing—review and editing, D.A.G., U.R., A.A. and M.A.H. All authors have read and agreed to the published version of the manuscript.

Funding: The authors are thankful to the Higher Education Commission of Pakistan for providing funding (17-5(2Ps1-301)/HEC/Sch-Ind/2012) to conduct the present study. The APC is funded by Universiti Putra Malaysia (UPM), Malaysia.

Institutional Review Board Statement: Not applicable.

Informed Consent Statement: Not applicable.

Data Availability Statement: Not applicable.

Acknowledgments: The authors extend their thanks to the Researchers Supporting Project (Ref: RSP-2021/78), King Saud University (Riyadh, Saudi Arabia).

Conflicts of Interest: The authors declare no conflict of interest.

References

1. Chai, W.S.; Cheun, J.Y.; Kumar, P.S.; Mubashir, M.; Majeed, Z.; Banat, F.; Ho, S.-H.; Show, P.L. A review on conventional and novel materials towards heavy metal adsorption in wastewater treatment application. *J. Clean. Prod.* **2021**, *296*, 126589. [CrossRef]
2. Seliem, M.K.; Mobarak, M.; Selim, A.; Mohamed, E.; Halfaya, R.A.; Gomaa, H.K.; Anastopoulos, I.; Giannakoudakis, D.A.; Lima, E.C.; Bonilla-Petriciolet, A. A novel multifunctional adsorbent of pomegranate peel extract and activated anthracite for Mn (VII) and Cr (VI) uptake from solutions: Experiments and theoretical treatment. *J. Mol. Liq.* **2020**, *311*, 113169. [CrossRef]
3. Giannakoudakis, D.A.; Anastopoulos, I.; Barczak, M.; Antoniou, E.; Terpiłowski, K.; Mohammadi, E.; Shams, M.; Coy, E.; Bakandritsos, A.; Katsoyiannis, I.A. Enhanced uranium removal from acidic wastewater by phosphonate-functionalized ordered mesoporous silica: Surface chemistry matters the most. *J. Hazard. Mater.* **2021**, *413*, 125279. [CrossRef] [PubMed]
4. Yargıç, A.Ş.; Şahin, R.Y.; Özbay, N.; Önal, E. Assessment of toxic copper (II) biosorption from aqueous solution by chemically-treated tomato waste. *J. Clean. Prod.* **2015**, *88*, 152–159. [CrossRef]
5. Black, R.; Sartaj, M.; Mohammadian, A.; Qiblawey, H.A. Biosorption of Pb and Cu using fixed and suspended bacteria. *J. Environ. Chem. Eng.* **2014**, *2*, 1663–1671. [CrossRef]
6. Abatal, M.; Anastopoulos, I.; Giannakoudakis, D.A.; Olguin, M. Carbonaceous material obtained from bark biomass as adsorbent of phenolic compounds from aqueous solutions. *J. Environ. Chem. Eng.* **2020**, *8*, 103784. [CrossRef]
7. Liakos, E.V.; Rekos, K.; Giannakoudakis, D.A.; Mitropoulos, A.C.; Fu, J.; Kyzas, G.Z. Activated porous carbon derived from tea and plane tree leaves biomass for the removal of pharmaceutical compounds from wastewaters. *Antibiotics* **2021**, *10*, 65. [CrossRef] [PubMed]
8. Qiu, B.; Tao, X.; Wang, H.; Li, W.; Ding, X.; Chu, H. Biochar as a low-cost adsorbent for aqueous heavy metal removal: A review. *J. Anal. Appl. Pyrolysis* **2021**, *155*, 105081. [CrossRef]
9. Qasem, N.A.; Mohammed, R.H.; Lawal, D.U. Removal of heavy metal ions from wastewater: A comprehensive and critical review. *NPJ Clean Water* **2021**, *4*, 1–15. [CrossRef]
10. Riera-Torres, M.; Gutiérrez-Bouzán, C.; Crespi, M. Combination of coagulation–flocculation and nanofiltration techniques for dye removal and water reuse in textile effluents. *Desalination* **2010**, *252*, 53–59. [CrossRef]
11. Gherasim, C.-V.; Mikulášek, P. Influence of operating variables on the removal of heavy metal ions from aqueous solutions by nanofiltration. *Desalination* **2014**, *343*, 67–74. [CrossRef]
12. Van der Bruggen, B.; Vandecasteele, C. Removal of pollutants from surface water and groundwater by nanofiltration: Overview of possible applications in the drinking water industry. *Environ. Pollut.* **2003**, *122*, 435–445. [CrossRef]
13. Hanif, A.; Bhatti, H.N.; Hanif, M.A. Removal of zirconium from aqueous solution by *Ganoderma lucidum*: Biosorption and bioremediation studies. *Desalination Water Treat.* **2015**, *53*, 195–205. [CrossRef]
14. Saravanan, A.; Kumar, P.S.; Yaashikaa, P.; Karishma, S.; Jeevanantham, S.; Swetha, S. Mixed biosorbent of agro waste and bacterial biomass for the separation of Pb (II) ions from water system. *Chemosphere* **2021**, *277*, 130236. [CrossRef] [PubMed]
15. Sayin, F.; Akar, S.T.; Akar, T.; Celik, S.; Gedikbey, T. Chitosan immobilization and Fe₃O₄ functionalization of olive pomace: An eco-friendly and recyclable Pb²⁺ biosorbent. *Carbohydr. Polym.* **2021**, *269*, 118266. [CrossRef]

16. Pavithra, S.; Thandapani, G.; Sugashini, S.; Sudha, P.; Alkhamis, H.H.; Alrefaei, A.F.; Almutairi, M.H. Batch adsorption studies on surface tailored chitosan/orange peel hydrogel composite for the removal of Cr (VI) and Cu (II) ions from synthetic wastewater. *Chemosphere* **2021**, *271*, 129415. [CrossRef]
17. Dada, A.; Olalekan, A.; Olatunya, A.; Dada, O. Langmuir, Freundlich, Temkin and Dubinin–Radushkevich isotherms studies of equilibrium sorption of Zn²⁺ onto phosphoric acid modified rice husk. *IOSR J. Appl. Chem.* **2012**, *3*, 38–45.
18. Langmuir, I. The adsorption of gases on plane surfaces of glass, mica and platinum. *J. Am. Chem. Soc.* **1918**, *40*, 1361–1403. [CrossRef]
19. Harkins, W.D.; Jura, G. An adsorption method for the determination of the area of a solid without the assumption of a molecular area, and the area occupied by nitrogen molecules on the surfaces of solids. *J. Chem. Phys.* **1943**, *11*, 431–432. [CrossRef]
20. Torab-Mostaedi, M.; Ghassabzadeh, H.; Ghannadi-Maragheh, M.; Ahmadi, S.; Taheri, H. Removal of cadmium and nickel from aqueous solution using expanded perlite. *Braz. J. Chem. Eng.* **2010**, *27*, 299–308. [CrossRef]
21. Kumar, B.; Smita, K.; Sánchez, E.; Stael, C.; Cumbal, L. Andean Sacha inchi (*Plukenetia volubilis* L.) shell biomass as new biosorbents for Pb²⁺ and Cu²⁺ ions. *Ecol. Eng.* **2016**, *93*, 152–158. [CrossRef]
22. Alencar, W.S.; Acayanka, E.; Lima, E.C.; Royer, B.; de Souza, F.E.; Lameira, J.; Alves, C.N. Application of *Mangifera indica* (mango) seeds as a biosorbent for removal of Victazol Orange 3R dye from aqueous solution and study of the biosorption mechanism. *Chem. Eng. J.* **2012**, *209*, 577–588. [CrossRef]
23. Petrović, M.; Šoštarić, T.; Stojanović, M.; Milojković, J.; Mihajlović, M.; Stanojević, M.; Stanković, S. Removal of Pb²⁺ ions by raw corn silk (*Zea mays* L.) as a novel biosorbent. *J. Taiwan Inst. Chem. Eng.* **2016**, *58*, 407–416. [CrossRef]
24. Amini, M.; Younesi, H.; Bahramifar, N. Biosorption of U (VI) from aqueous solution by *Chlorella vulgaris*: Equilibrium, kinetic, and thermodynamic studies. *J. Environ. Eng.* **2013**, *139*, 410–421. [CrossRef]
25. Galedar, M.; Younesi, H. Biosorption of ternary cadmium, nickel and cobalt ions from aqueous solution onto *Saccharomyces cerevisiae* cells: Batch and column studies. *Am. J. Biochem. Biotechnol.* **2013**, *9*, 47. [CrossRef]
26. Zhou, K.; Yang, Z.; Liu, Y.; Kong, X. Kinetics and equilibrium studies on biosorption of Pb (II) from aqueous solution by a novel biosorbent: *Cyclosorus interruptus*. *J. Environ. Chem. Eng.* **2015**, *3*, 2219–2228. [CrossRef]
27. Hajahmadi, Z.; Younesi, H.; Bahramifar, N.; Khakpour, H.; Pirzadeh, K. Multicomponent isotherm for biosorption of Zn (II), CO (II) and Cd (II) from ternary mixture onto pretreated dried *Aspergillus niger* biomass. *Water Resour. Ind.* **2015**, *11*, 71–80. [CrossRef]
28. Pirbazari, A.E.; Saberikhah, E.; Kozani, S.H. Fe₃O₄–wheat straw: Preparation, characterization and its application for methylene blue adsorption. *Water Resour. Ind.* **2014**, *7*, 23–37. [CrossRef]
29. Hanif, M.A.; Nadeem, R.; Bhatti, H.N.; Ahmad, N.R.; Ansari, T.M. Ni (II) biosorption by *Cassia fistula* (Golden Shower) biomass. *J. Hazard. Mater.* **2007**, *139*, 345–355. [CrossRef] [PubMed]
30. Saifuddin, M.N.; Kumaran, P. Removal of heavy metal from industrial wastewater using chitosan coated oil palm shell charcoal. *Electron. J. Biotechnol.* **2005**, *8*, 43–53.
31. Aksu, Z.; Isoglu, I.A. Use of agricultural waste sugar beet pulp for the removal of Gemazol turquoise blue-G reactive dye from aqueous solution. *J. Hazard. Mater.* **2006**, *137*, 418–430. [CrossRef] [PubMed]
32. Toor, M.; Jin, B. Adsorption characteristics, isotherm, kinetics, and diffusion of modified natural bentonite for removing diazo dye. *Chem. Eng. J.* **2012**, *187*, 79–88. [CrossRef]
33. Amin, N.K. Removal of direct blue-106 dye from aqueous solution using new activated carbons developed from pomegranate peel: Adsorption equilibrium and kinetics. *J. Hazard. Mater.* **2009**, *165*, 52–62. [CrossRef]
34. Akar, S.T.; Özcan, A.S.; Akar, T.; Özcan, A.; Kaynak, Z. Biosorption of a reactive textile dye from aqueous solutions utilizing an agro-waste. *Desalination* **2009**, *249*, 757–761. [CrossRef]
35. Sağ, Y.; Akcael, B.; Kutsal, T. Ternary biosorption equilibria of chromium (VI), copper (II), and cadmium (II) on *Rhizopus arrhizus*. *Sep. Sci. Technol.* **2002**, *37*, 279–309. [CrossRef]
36. Mohammad, A.W.; Teow, Y.; Ang, W.; Chung, Y.; Oatley-Radcliffe, D.; Hilal, N. Nanofiltration membranes review: Recent advances and future prospects. *Desalination* **2015**, *356*, 226–254. [CrossRef]
37. Verma, B.; Balomajumder, C.; Sabapathy, M.; Gumfekar, S.P. Pressure-Driven Membrane Process: A Review of Advanced Technique for Heavy Metals Remediation. *Processes* **2021**, *9*, 752. [CrossRef]
38. Askari, N.; Farhadian, M.; Razmjou, A.; Hashtroodi, H. Nanofiltration performance in the removal of dye from binary mixtures containing anthraquinone dyes. *Desalination Water Treat.* **2016**, *57*, 18194–18201. [CrossRef]
39. Abhang, R.; Wani, K.; Patil, V.; Pangarkar, B.; Parjane, S. Nanofiltration for recovery of heavy metal ions from waste water—a review. *Int. J. Res. Environ. Sci. Technol.* **2013**, *3*, 29–34.
40. Chai, X.; Chen, G.; Po-Lock, Y.; Mi, Y. Pilot scale membrane separation of electroplating waste water by reverse osmosis. *J. Membr. Sci.* **1997**, *123*, 235–242. [CrossRef]

Article

Evaluation of Calcium Alginate-Based Biopolymers as Potential Component of Membranes for Recovering Biosurfactants from Corn Steep Water

Andrea Martínez-Arcos¹, Mònica Reig² , José Manuel Cruz¹ , José Luis Cortina^{2,3} , Ana Belén Moldes¹  and Xanel Vecino^{1,*} 

- ¹ Chemical Engineering Department, Campus As Lagoas-Marcosende, School of Industrial Engineering—CINTECX, University of Vigo, 36310 Vigo, Spain; andrea.martinez.arcos@uvigo.es (A.M.-A.); jmcruz@uvigo.es (J.M.C.); amoldes@uvigo.es (A.B.M.)
- ² Barcelona Research Center for Multiscale Science and Engineering, Chemical Engineering Department, Campus Diagonal-Besòs, Escola d'Enginyeria de Barcelona Est, Universitat Politècnica de Catalunya, 08930 Barcelona, Spain; monica.reig@upc.edu (M.R.); jose.luis.cortina@upc.edu (J.L.C.)
- ³ CETaqua, Carretera d'Esplugues 75, 08940 Cornellà de Llobregat, Spain
- * Correspondence: xanel.vecino@uvigo.es; Tel.: +34-986-130-190

Abstract: Corn steep water (CSW) is a complex agro-food stream that is used as a source of cost-competitive biosurfactants, since they are produced spontaneously in the steeping process of corn, avoiding production costs. Nevertheless, the extraction of biosurfactants from CSW using sustainable processes is still a challenge. Consequently, the use of calcium alginate membranes could present a novel and sustainable technology for recovering biosurfactants from aqueous streams. Therefore, the aim of this work is to evaluate calcium alginate-based biopolymers, without and with the presence of grape marc as an additive, as a key component of membranes for the recovery of biosurfactants in corn steep water. Biosurfactants are present in CSW, together with other inorganic solutes and biomolecules, such as organic acids, sugars, cations, anions as well as metals. Hence, the competition of these mentioned compounds for the active sites of the calcium alginate-based biopolymers was high. However, they showed a good adsorption capacity for biosurfactants, recovering around $55 \pm 2\%$ and $47 \pm 1\%$, of biosurfactants from CSW using both calcium alginate-based biopolymers, with and without biodegraded grape marc. Regarding adsorption capacity, it was 54.8 ± 0.6 mg biosurfactant/g bioadsorbent for the biopolymer containing grape marc, and 46.8 ± 0.4 mg biosurfactant/g bioadsorbent for the calcium alginate-based biopolymer alone. Based on these results, it could be postulated that the formulation of green membranes, based on calcium alginate-based polymers, could be an interesting alternative for the recovery of biosurfactants from aqueous streams including CSW.

Keywords: corn stream; surface-active compounds; eco-adsorbents; green membranes; resource recovery

Citation: Martínez-Arcos, A.; Reig, M.; Cruz, J.M.; Cortina, J.L.; Moldes, A.B.; Vecino, X. Evaluation of Calcium Alginate-Based Biopolymers as Potential Component of Membranes for Recovering Biosurfactants from Corn Steep Water. *Water* **2021**, *13*, 2396. <https://doi.org/10.3390/w13172396>

Academic Editor: Antonio Zuorro

Received: 10 August 2021

Accepted: 30 August 2021

Published: 31 August 2021

Publisher's Note: MDPI stays neutral with regard to jurisdictional claims in published maps and institutional affiliations.



Copyright: © 2021 by the authors. Licensee MDPI, Basel, Switzerland. This article is an open access article distributed under the terms and conditions of the Creative Commons Attribution (CC BY) license (<https://creativecommons.org/licenses/by/4.0/>).

1. Introduction

Corn steep water (CSW) is a fermented stream obtained as a by-product in the wet-milling corn industry, when the corn is steeping under acid conditions (pH = 4), high temperatures (45–52 °C) and in presence of SO₂(g) and lactic acid bacteria or *Bacillus* [1]. CSW is commonly used in biotechnology processes as a low-cost source of nitrogen [2–4] as well as an ingredient in animal feed due to its nutritional properties [5,6]. However, CSW has been proposed as a direct source of biosurfactants due to the presence of lactic acid bacteria, which are producers of this type of surface-active compounds [1,7,8]. In fact, it has recently been isolated and identified that *Aneurinibacillus aneurinilyticus* is the main biosurfactant-producing *Bacillus* strain in CSW [9].

Biosurfactants are microbial surfactants produced by microorganisms that not only have similar or equal properties than their chemical homologous (e.g., reduce surface tension, emulsifying properties, solubilizing, and stabilizing agent, among others), but are also very promising and interesting substances, since they are composed of natural structures (lipids, proteins, and carbohydrates) compatible with the composition of cell membranes [10–13]. Several carbon sources as well as energy are used for microorganisms to grow. The combination of carbon sources (e.g., agro-food products or wastes) with insoluble substrates (e.g., hydrocarbons, oils) facilitates the intracellular diffusion and the biological production of diverse substances, such as biosurfactants [12]. Hence, the synthesis of biosurfactants is a growth-dependent production and frequently arises in resting microbial cell systems [13]. In addition, microorganisms can produce biosurfactants with different molecular structures and characteristics (e.g., surface activity), being a combination of a hydrophobic chain (e.g., fatty acids) with a hydrophilic moiety (e.g., carbohydrates, peptides, amino acids, alcohols, so on) [12]. Regarding their chemical composition, there are low-molecular-weight biosurfactants, like glycolipids, lipopeptides, and flavolipids, and high-molecular-weight biosurfactants, such as polysaccharides, proteins, lipopolysaccharides, lipopolysaccharides, and lipoproteins [11]. Nevertheless, the biosurfactants commercialized at the moment are produced in controlled fermentation processes, which make them non-cost competitive with chemically produced surfactants. Hence, the industrial application of biosurfactants is limited by their high production cost due to the complex recovery and purification stages [10–13]. For that reason, in a context of a circular economy, the use of streams generated in agro-food industries like CSW, where biosurfactants are produced spontaneously, it is an interesting alternative to obtain cost-competitive and value-added biosurfactants, increasing the market opportunities for these secondary raw materials.

The ionic charge, water solubility and location of the surface-active sites (e.g., intracellular, extracellular, or cell-bound) of biosurfactant molecules define the required processing stages needed for their recovery. Therefore, there are several techniques that can be applied for the selective separation and recovery of biosurfactants such as acid precipitation (e.g., acidic solutions, ammonium sulfate solutions and in non-aqueous media), crystallization, chromatographic separation, adsorption, among others, with the liquid-liquid extraction the most commonly used [14]. In fact, for the moment, the recovery of biosurfactants from CSW has been achieved by liquid-liquid extraction with organic solvents. For instance, chloroform or ethyl acetate are used depending on the final application of the biosurfactant, as they are extracellular surface-active compounds [7]. Otherwise, the adsorption onto granular activated carbon [15–18] or ion-exchange resins [19] has also been studied for biosurfactant recovery. The adsorption process is an *in situ* technique that has certain advantages, such as that it allows the reuse of the adsorbent during several cycles without decreasing adsorption efficiency and avoids the use of organic solvents. Additionally, biosurfactants can be desorbed from the solid adsorbent using typically an aqueous pH buffer solution due to their lipophilic properties [15,16,19,20]. Despite this, new processes have been developed to recover biosurfactants based on cost-effective and environmentally friendly *in situ* downstream processing approaches. Examples are foam fractionation and membrane technology [20–22]. With regard to membrane technology, ultrafiltration membranes have been remarkably applied for the recovery and purification of glycolipid and lipopeptide biosurfactants [23–26].

From a sustainable point of view, there is an effort to develop more green membranes using biodegradable polymers such as alginate. Specifically, sodium alginate is a natural polysaccharide obtained from the cell wall of brown algae and is an unbranched binary copolymer of 1-4 linked β -D-mannuronic acid and α -L-guluronic acid. The combination of these blocks determines the physical and chemical properties of this polymer [27]. For instance, Aburabie et al. [28] developed calcium alginate-based membranes by crosslinking sodium alginate in calcium chloride aqueous solution, for green organic solvent nanofiltration application to test the retention or permeation of dyes and vitamin B12 in methanol.

In view of the aforementioned information, the aim of this work is to evaluate calcium alginate-based biopolymers, without or with the presence of biodegraded grape marc, for the recovery of biosurfactants from corn steep water by adsorption processes as a previous step to their use as potential materials in the manufacture of green membranes, and their subsequent use in the recovery of these biomolecules. It should be highlighted that this is the first time that biosurfactants from corn steep water have been recovered by liquid-solid processes without the use of organic solvents.

2. Materials and Methods

2.1. Corn Steep Water

The corn steep water (CSW) was provided by the FeedStimulants company (Zoetermeer, The Netherlands; Lot No. CSL-201811; Reg. No. NI214247). CSW, containing 50% of solids (*m/v*), was diluted in distilled water up to 50 g/L, and then it was centrifugated (Hettich Rotina 380R), at 5000 rpm and 4 °C for 30 min, for solid removal.

The characterization of the CSW, before and after adsorption processes, was carried out by using infrared spectroscopy and mass spectrophotometry analysis.

2.1.1. Fourier-Transform Infrared Spectroscopy (FTIR)

A pellet was obtained after pressing 1 mg of the lyophilized sample with 10 mg of potassium bromide. After that, the infrared absorption analysis was carried out with a Nicolet 6700 FTIR system (Thermo Fisher Scientific, Waltham, MA, USA). The spectra were recorded with a resolution of 4 cm⁻¹ and wavenumber range between 400 and 4000 cm⁻¹.

2.1.2. Electrospray Ionization Mass Spectrometry (ESI-MS)

Electrospray ionization mass spectrometry/collision-induced dissociation (ESI-MS/CID) was used to characterize the corn stream. For that, 1 mg of the lyophilized sample was diluted in Milli-Q water and volatilized under vacuum. Then, a current of electrons was used to ionize the molecules, and the fragmentation pattern was recorded on a Mass Spectrometer Bruker FTMS APEXIII (Bruker, Billerica, MA, USA) in positive mode.

2.2. Calcium Alginate-Based Biopolymers

The biopolymers were formulated using 2% sodium alginate, whereas biopolymers in combination with other biomaterial (e.g., grape marc) was formulated with 2% sodium alginate (*m/v*) and 2% biodegraded grape marc (*m/v*). Calcium alginate-based biopolymers were formulated using water as a solvent and calcium chloride solution (0.58 mol/L) as a crosslinking agent. Furthermore, grape marc was obtained from local winery industries and subjected to a spontaneous biodegradation of the organic matter following the protocol described previously [29,30].

Biopolymers Morphology Characterization

The biopolymers were washed with sodium cacodylate 0.1 mol/L buffer and fixed with 2.5% of glutaraldehyde in cacodylate 0.1 mol/L buffer for 2–4 h at 4 °C. Following this, the samples of biopolymer were introduced in 1% OsO₄ in cacodylate 0.1 mol/L buffer during for 1 h at 4 °C. Dehydration was carried out with ethanol using a different graded series (30%–15 min; 50%–2 × 15 min; 70%–2 × 15 min; 80%–2 × 15 min; 90%–2 × 15 min; 100%–3 × 15 min). Then, samples were dried at the chamber of a critical point dryer (Baltec CPD030, Rambouillet, France) using liquid CO₂. Dried samples were cut with liquid N₂, covered with gold (Emitech K550X, Dubai, United Arab Emirates) and observed using a digital microscope with a DeltaPix camera (Infinity X21) as well as a scanning electron microscope (SEM) (JEOL JSM 6700F FEG) operating at an acceleration voltage of 5.0 kV for secondary-electron imaging (LEI).

2.3. Adsorption Studies

Adsorption experiments were carried out in 250 mL Erlenmeyer flasks placed in an orbital shaker (IKA KS 4000 ic control) at 150 rpm and 25 °C. The CSW/biopolymer ratio used was 1:1 (v/v). Samples were removed after 24 h, once the equilibrium was reached, for analysis of biosurfactant extract and other inorganic solutes and biomolecules. Experiments were carried out in triplicate.

Adsorption Removal and Capacity Determination

Equation (1) was used to determine the percentage of inorganic solutes and biomolecules removed from the corn steep water, whereas Equation (2) was used to calculate the adsorption capacity q_e (mg/g) of calcium alginate-based biopolymers [31]:

$$C_{\text{removed}}(\%) = \frac{C_0 - C_t}{C_0} \cdot 100 \quad (1)$$

where C_0 and C_t (mg/L) are the concentration of inorganic solutes and biomolecules in CSW initially and at a fixed time t , respectively.

$$q_e \left(\frac{\text{mg}}{\text{g}} \right) = \frac{(C_0 - C_e) \cdot V}{W} \quad (2)$$

where C_0 and C_e (mg/L) are the initial and equilibrium concentrations of inorganic solutes and biomolecules in the corn steep water, respectively, V (L) is the volume of the CSW used during adsorption experiments and W (g) is the mass of biopolymer (expressed as g of initial sodium alginate).

2.4. Extraction of Biosurfactants from Corn Steep Water

For comparative purposes, the lipopeptide biosurfactant extract was obtained by liquid-liquid extraction from CSW, using a ratio chloroform/CSW of 2:1 (v/v), at a temperature of 56 °C, for 60 min and at an agitation speed of 150 rpm. After extraction, the biosurfactant was separated from the chloroform by rotary evaporation (Buchi R-210, Flawil, Switzerland) at a pressure of 474 mbar and 60 °C, following the methodology proposed by Vecino et al. [7]. This biosurfactant extract was used as a control to determine the quantity of biosurfactant present in the initial CSW and after adsorption processes.

Surface Activity and Critical Micellar Concentration Determination

The presence of biosurfactants in the CSW (liquid samples) was observed by surface tension measurements using a Krüss K20 EasyDyne tensiometer with a 1.9 cm platinum Wilhelmy plate (Krüss GmbH, Hamburg, Germany). Additionally, the critical micellar concentration (CMC) of lyophilized initial CSW and lyophilized samples after adsorption processes as well as the lipopeptide biosurfactant extract, from the CSW using liquid-liquid extraction, were determined after several dilutions in deionized water. The concentration above which micelles are formed is defined as the CMC. Below the CMC, surface tension in aqueous solution decreases. Once the CMC is reached, surface tension remains more or less constant. Therefore, it is possible, under the CMC, to linearly relate the surface tension with the concentration of biosurfactant [1]. In this case, a calibration curve under the CMC from the biosurfactant extract obtained by liquid-liquid extraction is used to extrapolate the surface tension of liquid samples, before and after adsorption processes, in order to determine the biosurfactant concentration. All determinations were carried out in triplicate.

2.5. Measurement of Other Inorganic Solute and Biomolecules from Corn Steep Water

The determination of other inorganic solutes and biomolecules from CSW (liquid samples) such as organic acids, sugars as well as total organic carbon (TOC), total nitrogen

(TN), anions, cations, and metal ions before and after adsorption processes, were carried out as follows:

2.5.1. TOC and TN

The Analytik Jena 3100 Multi N/C Analyzer was used to determine the carbon and nitrogen content of aqueous samples. The determination was carried out by thermocatalytic decomposition (oxidation) of the samples at 950 °C as it allows the quantitative determination of even poorly oxidizable carbon and nitrogen components.

2.5.2. Anions, Organic Acids and Sugars

The determination and quantification of the anion, organic acids and sugars were carried out by ion chromatography with the DIONEX ICS-3000 equipment. For anion determination, a Metrosep A Supo 5 column (250 × 4 mm Metrohm) with carbonate-bicarbonate buffer solution in a mobile phase at 0.7 mL/min and conductivity as detector were used. For organic acid determination, an IonPac AS11-HC column (250 × 4 mm Dionex) with 50 mM NaOH solution as a mobile phase at 1.0 mL/min and conductivity as detector were applied. For sugar determination, a CarboPac PA1 column (250 × 4 mm Dionex) with 150 mM NaOH solution as a mobile phase at 1.0 mL/min and amperometric as a detector were utilized.

2.5.3. Cations and Metals

Cations and metals were determined and quantified by inductively coupled plasma emission spectroscopy (Optima 4300DV de PerKin Elmer, Waltham, MA, USA). Prior to ICP-OES analyses, samples were filtered (0.2 µm) and acidified with 2% HNO₃.

3. Results and Discussion

3.1. Corn Steep Water Composition

The composition of CSW results in the extraction of water-soluble components during the steeping step of corn, as shown in Table 1. The CSW is mainly composed of carbon (around 37%) and nitrogenous (about 7%) components (elemental analysis data not shown), being the total carbon from organic sources. Regarding organic acids, lactic acid is the most predominant one (6.7 g/L), followed by the phytic acid (3.1 g/L) and acetic acid (2.8 g/L). Monosaccharides, like glucose (0.3 g/L) and arabinose (0.2 g/L), as well disaccharides such as sucrose (0.04 g/L) are part of the CSW composition. Physiologically relevant ions such as chloride, phosphate, sulphate, ammonium, calcium, boron, iron, potassium, magnesium, sodium, manganese, zinc, and silicon, were detected in CSW at substantial quantities. Among them, potassium (0.8 g/L) and phosphate (0.5 g/L) are the most significant; while aluminum, chromium, copper, cobalt, and nickel are the less represented. Hull and Montgomery [32] suggested that the high amount of inorganic phosphate in CSW could be due to in part to being a product of dephosphorylation of myo-inositol phosphates.

The above composition agrees with the composition analyzed by Hull et al. [33] at various times during the steeping of corn and from four different industrial processes. However, the novelty of this composition is the concentration of biosurfactant. This bioactive compound is present in a concentration of 2 g/L, based on the CMC data of biosurfactant extracted from con steep water by liquid-liquid extraction with chloroform (see Figure S1). This finding, related with the use of CSW as a direct source of biosurfactants, and its uses have been previously patented and published by Vecino et al. [1,7,34]. Nowadays, depending on the industrial application of the biosurfactant extract from CSW, an organic solvent is proposed for the extraction process. However, the possibility of using a liquid-solid extraction process by calcium alginate-based biopolymers to recover biosurfactants from CSW has not been considered until now.

Table 1. Chemical composition of diluted (20 times) raw corn steep water used in this study after solid removal.

Component	Concentration (mg/L)
Biosurfactant extract	2007 ± 39
Total organic carbon	5613 ± 45
Total nitrogen	1655 ± 21
Lactic acid	6714 ± 394
Acetic acid	2822 ± 1
Formic acid	4.9 ± 0.7
Phytic acid	3141 ± 3
Arabinose	204 ± 5
Glucose	287 ± 10
Sucrose	41 ± 3
Chloride	163 ± 3
Phosphate	511 ± 16
Sulphate	242 ± 8
Ammonium	183 ± 4
Calcium	3.6 ± 0.2
Aluminum	0.1 ± 0.005
Boron	0.7 ± 0.03
Chromium	0.03 ± 0.001
Copper	0.07 ± 0.003
Iron	3.1 ± 0.1
Cobalt	ND *
Potassium	847 ± 45
Magnesium	301 ± 15
Sodium	183 ± 1
Manganese	1.5 ± 0.1
Nickel	0.09 ± 0.005
Zinc	4.9 ± 0.2
Silicon	8.0 ± 0.4

ND * = below the limit of quantification (0.01 mg/L).

3.2. Calcium Alginate-Based Biopolymers Characterization

The macro view as well as the SEM images of the calcium alginate-based biopolymers formulated without (Figure 1a,c,e) shows and with the presence of grape marc (Figure 1b,d,f) are shown in Figure 1. Figure 1a,b show the macro view images of the calcium alginate-based biopolymers. The presence of the biodegradable material (e.g., grape marc) can be observed in Figure 1b through black dot visualization. Figure 1c,d shows the external morphology of biopolymers at 300× magnification; whereas Figure 1e,f shows the internal morphology of biopolymers at 1000× magnification. Taking into account the images above, it can be observed that the calcium alginate-based biopolymer in the presence of grape marc is a heterogeneous biopolymer; while the biopolymer composed of by alginate is a homogeneous biopolymer. Both biopolymers have rough surfaces, but the polymer with grape marc has a rougher surface (see Figure 1c,d). The morphology observed, in the case of biopolymer of alginate tunned with grape marc, is in concordance with the characterization of this biopolymer in previous studies [30].

3.3. Calcium Alginate-Based Biopolymers Performance in Liquid-Solid Process to Recover Biosurfactants from Corn Steep Water

In this study, two types of calcium alginate-based biopolymers were formulated without and with the presence of grape marc for the recovery of biosurfactants in CSW. Table 2 shows the removal percentage of the inorganic solutes and biomolecules, that comprise CSW, after adsorption process for a contact time for 24 h (e.g., equilibrium was attained), using alginate biopolymer and alginate biopolymer with grape marc.

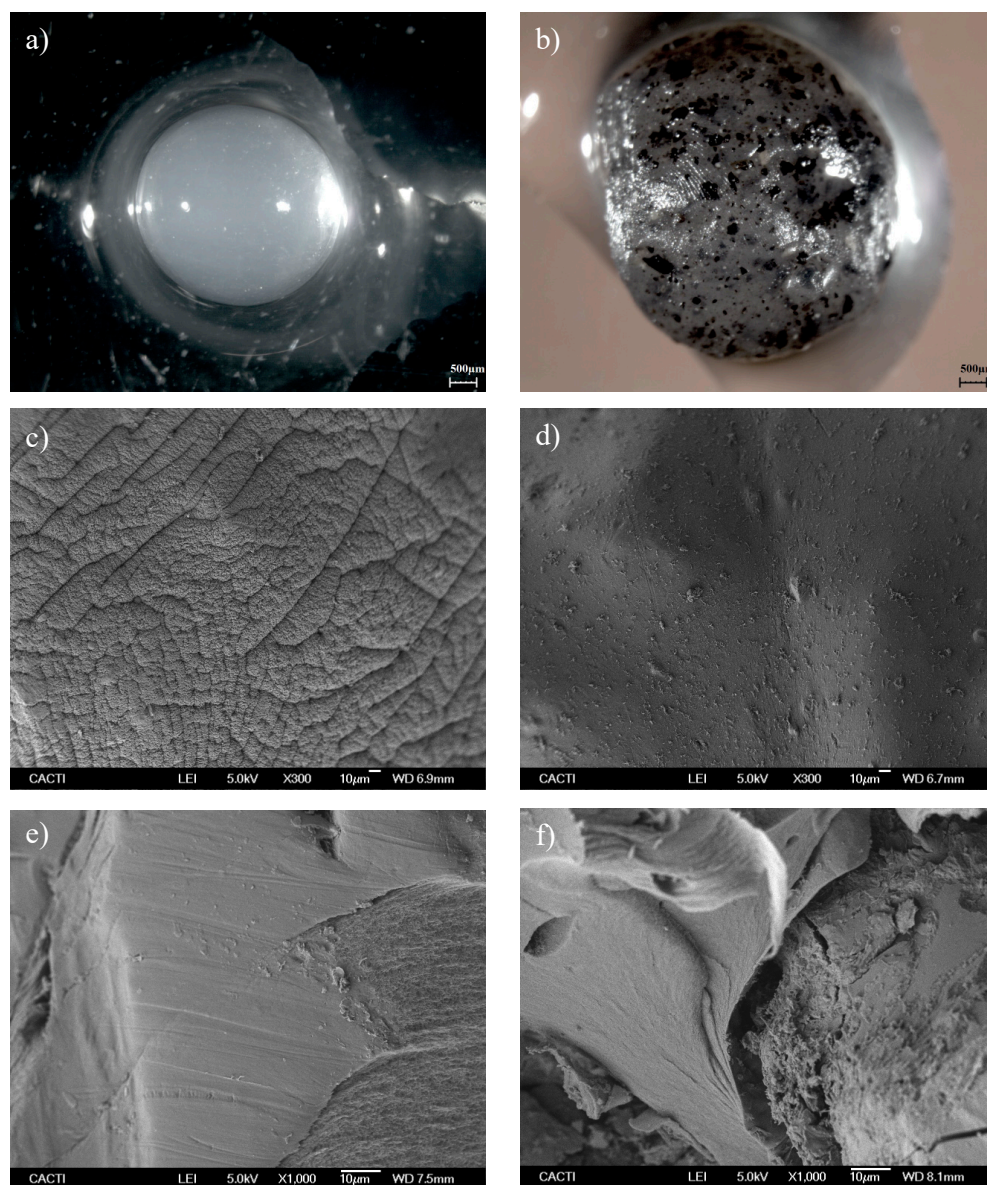


Figure 1. Macro view and SEM micrographs of alginate-based biopolymers: (a,c,e) from the biopolymer composed only for alginate, and (b,d,f) from the biopolymer with alginate and grape marc.

The biopolymer that only contains alginate presented a high capacity for the elimination of organic acids and sugars from the CSW, with a maximum removal for acetic acid (100%) and glucose (98.5%), respectively. For almost all ions, metals as well as biosurfactant extract, the percentage of removal was about 50%, except for boron (40.4%) and silicon (39.2%). On the other hand, the alginate-based biopolymer tunned with grape marc, also showed good elimination rates for the same families, organic acids, and sugars, but for other types. For instance, the highest percentage of elimination was for lactic acid (99%) and for all the sugars tested this was greater than 99%. Moreover, this biopolymer had obtained good removal of metals such as iron (98.5%) and zinc (96.8%) as well as for cations, like manganese (90.4%), and anions, such as phosphate (75%). However, the amount of biosurfactant extract eliminated was of 55%.

Table 2. Removal of some inorganic solutes and biomolecules (%) with the calcium alginate-based biopolymers after 24 h of equilibration time.

Component	Alginate Biopolymer (%)	Alginate Biopolymer with Grape Marc (%)
Biosurfactant	46.6 ± 1.5	54.6 ± 1.5
Total organic carbon	36.7 ± 0.5	48.8 ± 0.1
Total nitrogen	42.7 ± 2.4	57.5 ± 0.2
Lactic acid	50.0 ± 1.6	99.0 ± 0.1
Acetic acid	100 ± 0.1	83.8 ± 2.6
Formic acid	73.7 ± 4.3	69.1 ± 3.9
Phytic acid	72.7 ± 0.1	82.6 ± 1.7
Arabinose	88.5 ± 0.6	99.2 ± 0.1
Glucose	98.5 ± 0.6	99.4 ± 0.2
Sucrose	92.5 ± 1.8	99.8 ± 0.1
Phosphate	59.1 ± 1.1	75.1 ± 0.5
Sulphate	48.5 ± 2.2	42.0 ± 1.0
Ammonium	44.0 ± 1.4	27.1 ± 1.5
Boron	40.4 ± 0.8	8.8 ± 0.4
Iron	77.0 ± 0.1	98.5 ± 0.1
Potassium	49.2 ± 0.5	54.9 ± 0.4
Magnesium	45.8 ± 0.2	66.0 ± 0.3
Manganese	62.2 ± 0.2	90.4 ± 0.7
Zinc	58.9 ± 1.4	96.8 ± 0.2
Silicon	39.2 ± 0.4	10.1 ± 0.5

Overall, the combination of calcium alginate-based biopolymer with grape marc provided better results in comparison with only calcium alginate biopolymer; except for boron and silicon, where only the alginate biopolymer offered greater affinity for these compounds. The initial hypothesis is supported by the fact that grape marc possesses lower adsorption capacity for these elements than calcium alginate, which reduces the adsorption capacity for boron and silicon. When the bio-adsorbent is formulated with sodium alginate, the active surface sites for adsorption are based only in the calcium alginate-based polymer, whereas when the bioadsorbent is formulated with sodium alginate (2%) plus grape marc (2%), the active surface sites, for adsorption, based on calcium alginate, were lower, since the latter biopolymer has a lower percentage of alginate, with respect to the total composition, than the former. Additionally, the adsorption of biosurfactant extract was not greatly influenced by the type of biopolymer since there was only around 8% difference between them. Indeed, it is important to remark that this is a multi-adsorption mechanism, occurring simultaneously with physical and/or chemical adsorption and ion-exchange processes. Moreover, the corn stream is composed of several inorganic solutes and biomolecules that interact between them, adding more complexity to the adsorption process. However, in a previous study [30], a calcium alginate-based biopolymer tunned with grape marc was evaluated for the removal of color in wastewater. It was observed that the adsorption process followed a pseudo-second order kinetic model (heterogeneous process). In addition, in another physicochemical study with a bio-based adsorbent made from grape marc [35], the physical control of the sorption stage was well- described by the Freundlich isotherm.

Biodegraded grape marc entrapped in calcium alginate beads has been previously tested as an eco-adsorbent. For instance, Perez-Ameneiro et al. evaluated the use of a biopolymer based on grape marc entrapped in calcium alginate beads for the removal of pigments from an agro-industrial effluent [30] or dye compounds from winery wastewater [35] as well as to remove micronutrients from winery effluents in order to avoid eutrophication [36]. Additionally, an alginate-based polymer with grape marc has also been tested as an eco-adsorbent for removal of copper (II) from aqueous streams [37]; for adsorption of binary mixtures of dyes [38]; and for the removal of cyanide and transition metals from industrial electroplating process waters [39]. Nevertheless, it should be highlighted that this type of biopolymer has never been tested to recover biosurfactants present in corn steep water.

In the case study of micronutrients [36], the calcium alginate-based biopolymer with grape marc removed most of the TN, NH_4^+ and NO_3^- existing in the vinasses (wastewater from winery industry) and about 60% of Mg, P, K, and total carbon. Similar results were obtained in the current study, with 66% of Mg, 75% of P, 55% of K and 49% of TOC. It is important to note that in the corn steep water, the concentration of Mg and P was almost ten times more, being double for K and around six times more for the total carbon than vinasses.

On the other hand, the adsorption capacities for the inorganic solutes and biomolecules tested using calcium alginate-based biopolymers, after 24 h of equilibration time, are displayed in Table 3.

Table 3. Adsorption capacity (mg/g) of some inorganic solutes and biomolecules with the calcium alginate-based biopolymers after 24 h of adsorption process.

Component	Alginate Biopolymer (mg/g)	Alginate Biopolymer with Grape Marc (mg/g)
Biosurfactant	46.8 ± 0.4	54.8 ± 0.6
Total organic carbon	102.9 ± 1.3	136.9 ± 0.1
Total nitrogen	35.3 ± 2.0	47.6 ± 0.1
Lactic acid	167.9 ± 5.4	332.4 ± 0.1
Acetic acid	141.1 ± 0.2	118.2 ± 3.7
Phytic acid	114.2 ± 0.2	129.7 ± 2.7
Arabinose	9.0 ± 0.1	10.1 ± 0.1
Glucose	14.1 ± 0.1	14.3 ± 0.1
Sucrose	1.9 ± 0.1	2.0 ± 0.1
Phosphate	15.1 ± 0.3	19.2 ± 0.1
Sulphate	5.9 ± 0.3	5.1 ± 0.1
Ammonium	4.0 ± 0.1	2.5 ± 0.1
Potassium	20.8 ± 0.2	23.3 ± 0.2
Magnesium	6.9 ± 0.1	9.9 ± 0.1

The maximum adsorption capacity was achieved for lactic acid with both biopolymers, which was 167.9 and 332.4 mg/g for the calcium alginate-based biopolymer without and with grape marc, respectively. This maximum capacity is followed by the capacity for acetic acid (141.1 mg/g) and phytic acid (114.2 mg/g) in the case of the biopolymer alone with alginate; and this order of adsorption capacity value is reversed in the biopolymer containing grape marc: phytic acid with 129.7 mg/g and acetic acid with 118.2 mg/g. Additionally, both biopolymers presented high capacity for TOC between 102.9 mg/g (alginate) and 136.9 mg/g (alginate plus grape marc); and the capacity of TN was 35.3 and 47.6 mg/g for the alginate biopolymer and the alginate biopolymer tunned with grape marc, respectively. Concerning the biosurfactant adsorption capacity, both biopolymers showed values of 46.8 and 54.8 mg/g for the alginate biopolymer and the alginate biopolymer tunned with grape marc, respectively. For the other inorganic solutes and biomolecules, that compose the CSW, the calcium alginate-based biopolymers provided adsorption capacities values below 24 mg/g.

Depending on the solute and its concentration, the capacity of calcium alginate-based biopolymer, tunned with grape marc, changes substantially. For example, in the study of pigment removal from vinasses [30], the capacity of the biopolymer varied between 0.28 and 0.76 mg/g as a function of the initial dye concentration (8.8 to 24.7 mg/L). Also, in the case of mixtures of dyes [38], the adsorption capacity was 2.47 and 2.22 mg/g for methylene blue and methyl red, respectively, using calcium alginate-based biopolymer with grape marc; whereas, the biopolymer based only in calcium alginate achieved capacity values lower than 2 mg/g. These capacities are very low compared to those obtained in this work. However, the biopolymer capacities for metal ions were higher. Pérez-Cid et al. [39] concluded that calcium alginate hydrogel beads can be considered a bioadsorbent with a high capacity to remove free cyanide (1177 mg/g) and transition metals (Ni, Cu and

Zn as follows 107.3, 39.5 and 1.52 mg/g, respectively) in electroplating streams. In this case, the introduction of composted grape marc in the calcium alginate bead formulation did not produce significant improvements in the adsorption capacity. Comparatively, the Zn adsorption capacity, achieved in the current work, was higher 23.9 mg/g, but the initial concentration of zinc in the corn stream was around ten times less and also lower quantity of adsorbent was used (the CSW/biopolymer ratio used was 1:1 (v/v) vs. the wastewater/bioadsorbent ratio used was 1.5:1 (v/v)) than in the previous study. Otherwise, the maximum adsorption capacity was reached by using the calcium alginate-based biopolymer with grape marc for copper (II) removal from sulfate solutions [37]. In this study, the adsorption capacity value was around 1800 mg/g after 5 min of contact time, while it increased to 2785 mg/g at the highest concentration assessed (0.15 mol/L) and at the maximum extraction times (20 min).

3.4. Characterization of Corn Steep Water before and after Adsorption Processes

The corn steep waters were characterized based on CMC, FTIR and ESI-MS analysis. Raw corn steep liquor possesses a CMC of 10–15 g/L depending on the provider company, providing minimum surface tension values to water between 36.6 and 46.7 mN/m [1]. However, these results are not comparable with those obtained in this work since the corn steep water has been centrifuged (for solids removal) and lyophilized. Thus, in the current work the CMC of the corn steep water, as shown in Figure 2, was 0.46 g/L, reaching a minimum surface tension of 54.5 ± 0.2 , observing that solids increased the CMC of raw corn steep liquor, although they provide a higher reduction of surface tension in water.

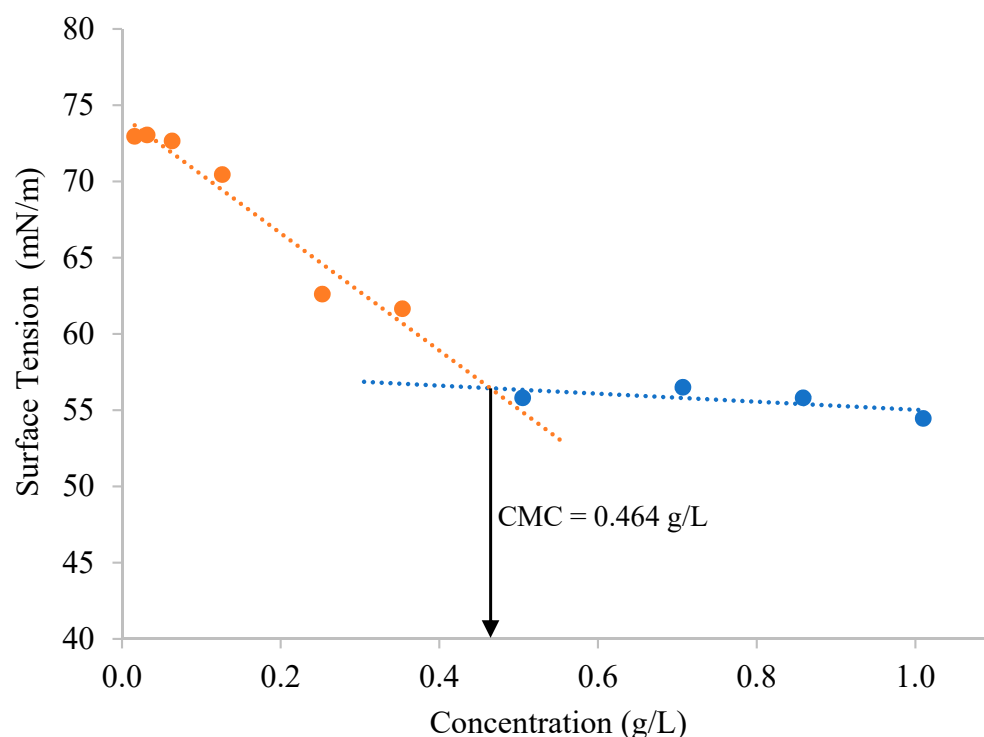


Figure 2. Critical micellar concentration (CMC) of corn steep water before adsorption processes.

The concentration at which the micellization starts is known as CMC. At this concentration not only the micelles are made, but also the lower surface tension value of the solution is achieved [40]. Thus, after the adsorption processes, with the calcium alginate-based biopolymers, the CMC values increased almost two-fold, being 0.99 and 1.15 g/L for the biopolymer based on calcium alginate and calcium alginate tunned with grape marc, respectively; whereas the minimum surface tension remained constant (54.2–55.3 mN/m). In this case, although the minimum surface tension value had been kept constant, an increase in CMC implies that a higher amount of biosurfactant extract is needed to reach

this value of surface tension. Therefore, the corn steep water reduced its surfactant capacity, since the biosurfactant extract is adsorbed by these calcium alginate-based biopolymers. Thus, CMC results are in concordance with the percentage removal of the biosurfactant as a function of the type of biopolymer (see Table 2). Therefore, greater capacities for biosurfactants obtained with the biopolymers, involved higher CMC values for the treated corn steep water. Although the presence of biosurfactants in those streams treated with calcium alginate polymer tunned with grape marc was lower.

On the other hand, Figure 3 shows the FTIR spectra of the initial corn steep water (grey line) as well as the corn streams after adsorption processes with the calcium alginate-based biopolymers (orange and blue lines). Also, it was used to determine the similarities of the corn stream before and after the adsorption processes.

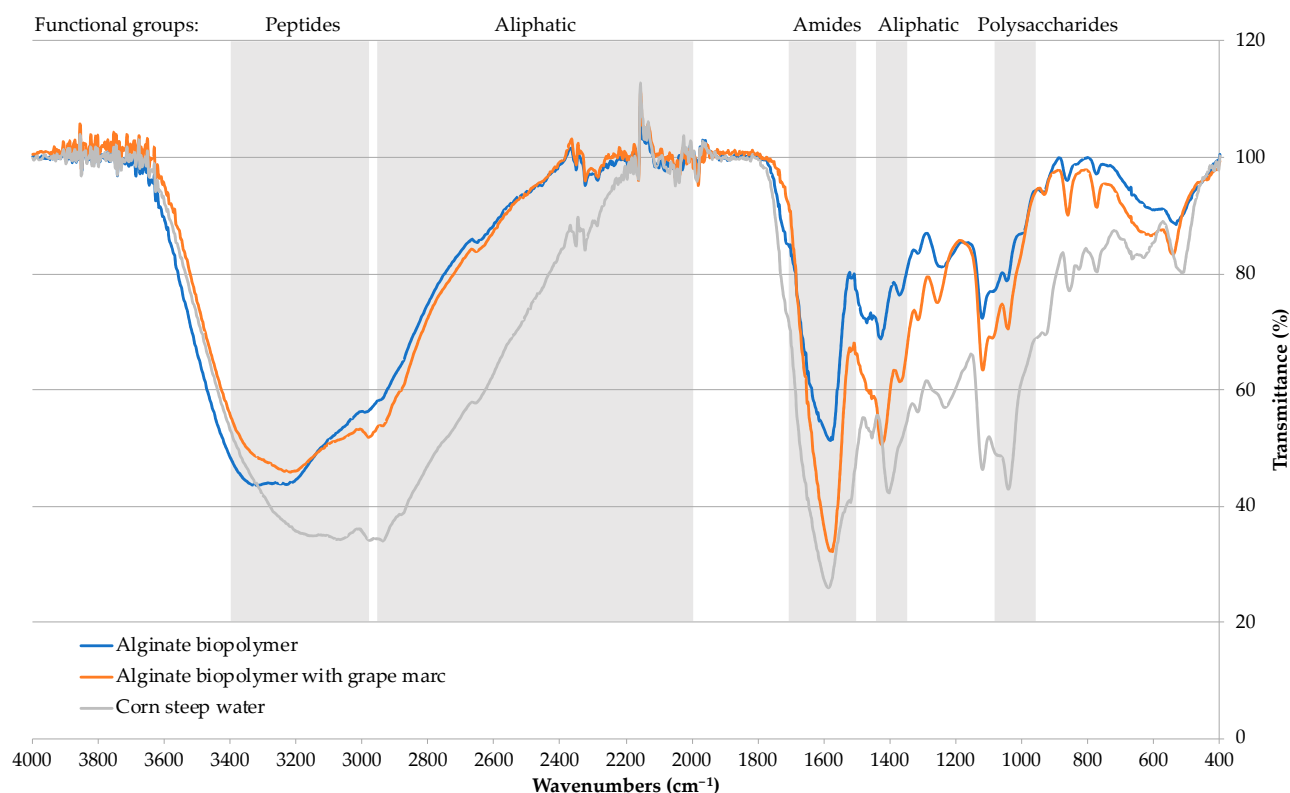


Figure 3. FTIR spectra of corn steep water before and after adsorption processes with calcium alginate-based biopolymers.

The FTIR spectrum of the biopolymer only with alginate is in concordance with the results of characterization carried out by Aburabie et al. [28], where the absorption region of stretching vibrations of O–H bonds (3344 cm^{-1}) in calcium alginate membranes was narrower and more elongated than sodium alginate solution; while the C–O stretching vibration (1080 and 1021 cm^{-1}) decreased in calcium alginate membranes.

In general terms, the bands of corn stream that are affected, after the adsorption process, correspond to the functional groups of proteins, lipids, and polysaccharides. The characterization was as follows: (i) the wavenumbers between 3400 and 3000 cm^{-1} corresponded with the peptide groups resulting from O–H and N–H stretching; (ii) bands around 3000 and 2000 cm^{-1} as well as 1400 cm^{-1} related to the presence of C–H stretching corresponding to aliphatic chains (CH_2 and CH_3 groups) of fatty acids; (iii) the bands C=O bond at 1640 cm^{-1} (amide I bond) and N–H bonds at 1540 cm^{-1} (amide II bond) indicated the presence of protein-related weakness; and iv) the band around 1000 cm^{-1} denoted the presence of polysaccharides, conforming the C–O stretch vibration [41,42].

The bands of the three main functional groups (proteins, lipids, and polysaccharides) are decreased after the adsorption process with both calcium alginate-based biopolymers. This is confirmed by the degree of similarity of the initial corn stream before and after

adsorption processes, which was 69.6% and 72.1% for the biopolymer alone with alginate or alginate tunned with grape marc, respectively between 400–4000 cm^{-1} . It would be expected that the corn steep treated with the alginate-based biopolymer tunned with grape marc would be more different from the initial corn steep, since the removal rates for most of the inorganic solutes and biomolecules were higher than those obtained after treating the corn steep water with the biopolymer only based on calcium alginate (see Table 2). Additionally, the biosurfactant extract obtained from corn steep liquor is a lipopeptide [1]; therefore, observing the protein band, it would be expected that the biopolymer with grape marc would produce a greater reduction in the band of corn steep water, due to the higher removal percentage of biosurfactant achieved in comparison with the biopolymer only formulated with calcium alginate (around 55% vs. 47%). This finding could be due to the fact that the calcium alginate-based biopolymer tunned with grape marc provided nitrogen to corn steep water, since grape marc is a biodegradable material with the following composition: 3.9% N, 42.7% C and 5.5% H [30].

Moreover, the ESI-MS analysis allowed us to corroborate the adsorption of certain inorganic solutes and biomolecules such as the biosurfactant by the biopolymers under evaluation. Figure 4 shows the natural molecular masses of the bioactive molecules present in the raw corn steep as well as those present in the corn steep water after adsorption treatment with the calcium alginate-based biopolymers. The following signals were detected in raw corn steep water: at 175, 219, 263, 330, 423, 493, 570, 659, 806, 879, 966 as well as signals between 1200–1300 m/z . Some of them, for instance 879, were m/z also detected in the biosurfactant extract obtained from corn steep liquor, after the liquid-liquid extraction process, in previous studies [43]. In fact, the biomarker observed at 879 m/z (and at 617 m/z) was derived from the fragmentation of the signal observed at 933 m/z , with signals compatible with the presence of lipopeptide biosurfactants [43]. Additionally, Li et al. [44] suggested that the presence of triglycerides, diglycerides and monoglycerides could be signals below 800 m/z . Ma et al. [45] detected, in the ESI-MS/MS spectrum, at 441 m/z , several surfactin precursors. Nevertheless, in the biosurfactant extract from CSW, obtained after liquid-liquid extraction with organic solvents, this signal could correspond to the presence of phenolic compounds [46,47].

Otherwise, signals within the range of 800 and 1200 m/z are mass biomarkers of biosurfactant precursors produced by *Bacillus* strains widely described in lipopeptide analyses [44,48–50]. Thus, the masses higher than 800 m/z relatively disappeared from the ESI spectrum, in treated corn steep water, corroborating that part of the biosurfactant extract was trapped by the calcium alginate-based biopolymers.

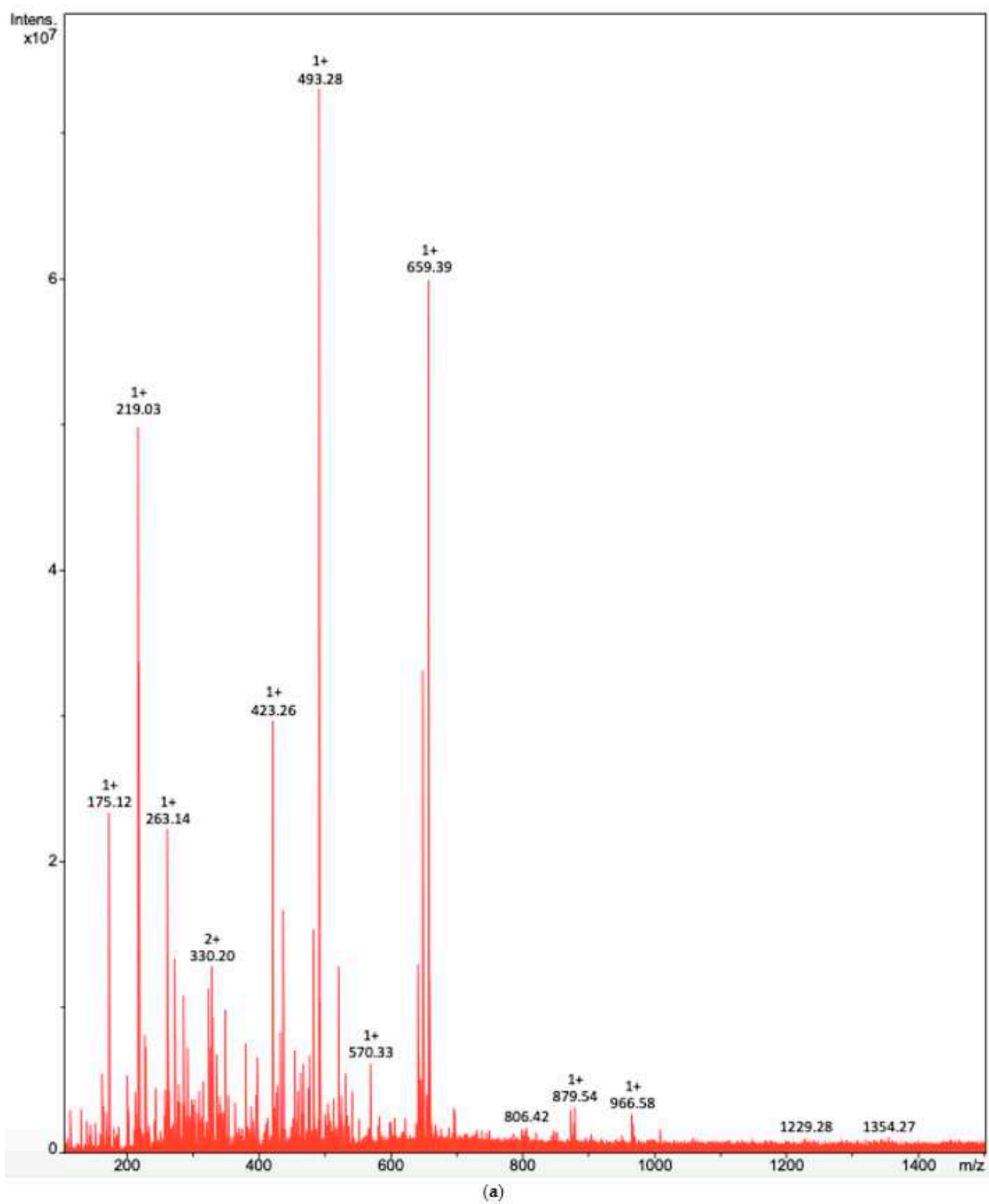


Figure 4. Cont.

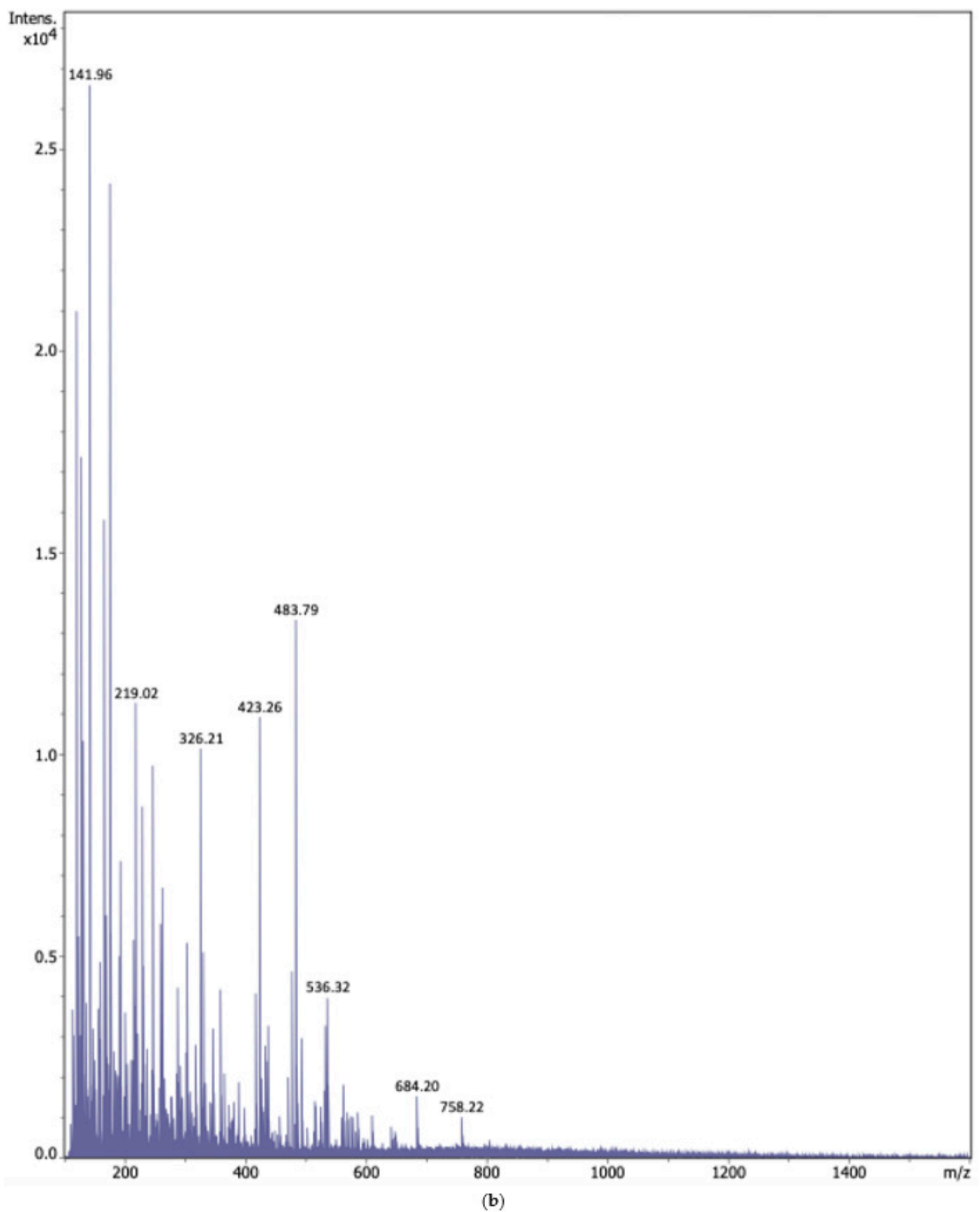


Figure 4. Cont.

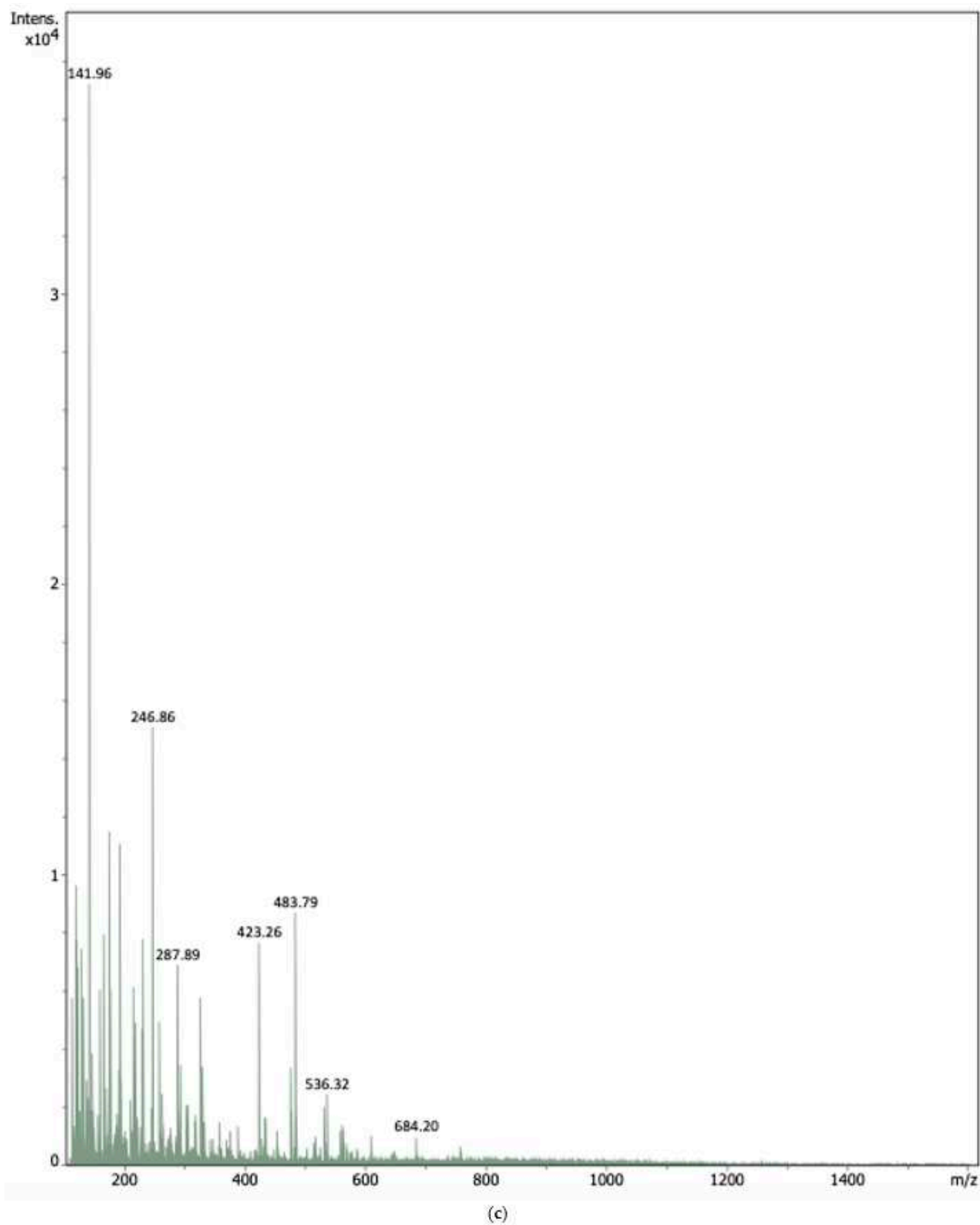


Figure 4. ESI spectra of raw corn steep water (a) and corn stream after adsorption process with the calcium alginate-based biopolymers, only alginate (b) and alginate tunned with grape marc (c).

4. Conclusions

Corn steep water is an interesting secondary stream obtained from the corn industry and is used as a direct source of biosurfactants. However, nowadays, the recovery of biosurfactants using sustainable processes is a challenge. Thus, this work is a first attempt at recovering biosurfactants from CSW by a liquid-solid process using calcium alginate-based biopolymers, without or with an additive (e.g., biodegraded grape marc). The results achieved showed that calcium alginate-based biopolymers possess an enormous potential to enhance the capabilities of membranes prepared from green materials. Based on the results obtained in this work, several scenarios can be proposed for the use of these biopolymers: i) as a polishing step before biosurfactant recovery to remove impurities such as organic acids, sugars as well as cations, metals, and anions from CSW; and ii) as a recovery step for biosurfactant extract since about 50% is removed. Overall, it could be highlighted that it is possible to recover biosurfactants, avoiding organic solvents, with biodegradable materials. Although more studies are needed in order to design the alginate-based membranes, as well as the eluent used for the desorption process.

Supplementary Materials: The following are available online at <https://www.mdpi.com/article/10.3390/w13172396/s1>, Figure S1: Critical micellar concentration (CMC) of biosurfactant extract obtained from corn steep water after liquid-liquid extraction with chloroform.

Author Contributions: Conceptualization, A.M.-A., M.R., J.M.C., J.L.C., A.B.M. and X.V.; methodology, A.M.-A.; validation, A.M.-A., J.M.C., A.B.M. and X.V.; formal analysis, A.M.-A., A.B.M. and X.V.; investigation, A.M.-A., M.R., J.M.C., J.L.C., A.B.M. and X.V.; resources, J.M.C. and A.B.M.; Writing—Original draft preparation, X.V.; Writing—Review and editing, A.M.-A., M.R., J.M.C., J.L.C., A.B.M. and X.V.; visualization, J.L.C., A.B.M. and X.V.; supervision, A.B.M. and X.V.; project administration, X.V.; funding acquisition, X.V. All authors have read and agreed to the published version of the manuscript.

Funding: This research was funded by the Spanish Ministry of Science and Innovation under the project PID2019-103873RJI00/AEI/10.13039/501100011033, and by the Xunta de Galicia under the project GPC-ED431B 2020/17.

Institutional Review Board Statement: Not applicable.

Informed Consent Statement: Not applicable.

Data Availability Statement: The data presented in this study is available on request from the corresponding author.

Conflicts of Interest: The authors declare no conflict of interest.

References

- Vecino, X.; Barbosa-Pereira, L.; Devesa-Rey, R.; Cruz, J.M.; Moldes, A.B. Study of the Surfactant Properties of Aqueous Stream from the Corn Milling Industry. *J. Agric. Food Chem.* **2014**, *62*, 5451–5457. [CrossRef]
- Rivas, B.; Moldes, A.B.; Domínguez, J.M.; Parajó, J.C. Development of Culture Media Containing Spent Yeast Cells of *Debaryomyces Hansenii* and Corn Steep Liquor for Lactic Acid Production with *Lactobacillus Rhamnosus*. *Int. J. Food Microbiol.* **2004**, *97*, 93–98. [CrossRef]
- Gudiña, E.J.; Fernandes, E.C.; Rodrigues, A.I.; Teixeira, J.A.; Rodrigues, L.R. Biosurfactant Production by *Bacillus Subtilis* Using Corn Steep Liquor as Culture Medium. *Front. Microbiol.* **2015**, *6*, 1–7. [CrossRef]
- Wang, G.; Shi, B.; Zhang, P.; Zhao, T.; Yin, H.; Qiao, C. Effects of Corn Steep Liquor on β -Poly(l-Malic Acid) Production in *Aureobasidium Melanogenum*. *AMB Express* **2020**, *10*, 1–10. [CrossRef] [PubMed]
- Azizi-Shotorkhoft, A.; Sharifi, A.; Mirmohammadi, D.; Baluch-Gharaei, H.; Rezaei, J. Effects of Feeding Different Levels of Corn Steep Liquor on the Performance of Fattening Lambs. *J. Anim. Physiol. Anim. Nutr.* **2016**, *100*, 109–117. [CrossRef] [PubMed]
- Ullah, Z.; Yousaf, M.; Shami, M.M.; Sharif, M.; Mahrose, K. Effect of Graded Levels of Dietary Corn Steep Liquor on Growth Performance, Nutrient Digestibility, Haematology and Histopathology of Broilers. *J. Anim. Physiol. Anim. Nutr.* **2018**, *102*, e395–e402. [CrossRef] [PubMed]
- Vecino, X.; Barbosa-Pereira, L.; Devesa-Rey, R.; Cruz, J.M.; Moldes, A.B. Optimization of Liquid-Liquid Extraction of Biosurfactants from Corn Steep Liquor. *Bioprocess. Biosyst. Eng.* **2015**, *38*, 1629–1637. [CrossRef] [PubMed]
- López-Prieto, A.; Martínez-Padrón, H.; Rodríguez-López, L.; Moldes, A.B.; Cruz, J.M. Isolation and Characterization of a Microorganism That Produces Biosurfactants in Corn Steep Water. *CyTA-J. Food* **2019**, *17*, 509–516. [CrossRef]

9. López-Prieto, A.; Rodríguez-López, L.; Rincón-Fontán, M.; Cruz, J.M.; Moldes, A.B. Characterization of Extracellular and Cell Bound Biosurfactants Produced by *Aneurinibacillus Aneurinilyticus* Isolated from Commercial Corn Steep Liquor. *Microbiol. Res.* **2021**, *242*, 126614. [CrossRef]
10. Marchant, R.; Banat, I.M. Biosurfactants: A Sustainable Replacement for Chemical Surfactants? *Biotechnol. Lett.* **2012**, *34*, 1597–1605. [CrossRef]
11. Marchant, R.; Banat, I.M. Microbial Biosurfactants: Challenges and Opportunities for Future Exploitation. *Trends Biotechnol.* **2012**, *30*, 558–565. [CrossRef]
12. Santos, D.K.F.; Rufino, R.D.; Luna, J.M.; Santos, V.A.; Sarubbo, L.A. Biosurfactants: Multifunctional Biomolecules of the 21st Century. *Int. J. Mol. Sci.* **2016**, *17*, 401. [CrossRef]
13. Jimoh, A.A.; Lin, J. Biosurfactant: A New Frontier for Greener Technology and Environmental Sustainability. *Ecotoxicol. Environ. Saf.* **2019**, *184*, 109607. [CrossRef]
14. Desai, J.D.; Banat, I.M. Microbial Production of Surfactants and Their Commercial Potential. *Microbiol. Mol. Biol. Rev.* **1997**, *61*, 47–64. [CrossRef]
15. Dubey, K.V.; Juwarkar, A.A.; Singh, S.K. Adsorption-Desorption Process Using Wood-Based Activated Carbon for Recovery of Biosurfactant from Fermented Distillery Wastewater. *Biotechnol. Prog.* **2005**, *21*, 860–867. [CrossRef] [PubMed]
16. Liu, T.; Montastruc, L.; Gancel, F.; Zhao, L.; Nikov, I. Integrated Process for Production of Surfactin. Part 1: Adsorption Rate of Pure Surfactin onto Activated Carbon. *Biochem. Eng. J.* **2007**, *35*, 333–340. [CrossRef]
17. Montastruc, L.; Liu, T.; Gancel, F.; Zhao, L.; Nikov, I. Integrated Process for Production of Surfactin. Part 2. Equilibrium and Kinetic Study of Surfactin Adsorption onto Activated Carbon. *Biochem. Eng. J.* **2008**, *38*, 349–354. [CrossRef]
18. Carmen dos Santos Mendes de Oliveira, A.; da Silva Bezerra, M.; de Araujo Padilha, C.E.; Melchuna, A.M.; de Macedo, G.R.; dos Santos, E.S. Recovery of Rhamnolipids Produced by *Pseudomonas Aeruginosa* Using Acidic Precipitation, Extraction, and Adsorption on Activated Carbon. *Sep. Sci. Technol.* **2013**, *48*, 2852–2859. [CrossRef]
19. Chen, H.L.; Lee, Y.S.; Wei, Y.H.; Juang, R.S. Purification of Surfactin in Pretreated Fermentation Broths by Adsorptive Removal of Impurities. *Biochem. Eng. J.* **2008**, *40*, 452–459. [CrossRef]
20. Jauregi, P.; Kourmentza, K. Membrane filtration of biosurfactants. In *Separation of Functional Molecules in Food by Membrane Technology*; Elsevier Inc.: Amsterdam, The Netherlands, 2019; pp. 79–112. ISBN 9780128150566.
21. Diaz De Rienzo, M.A.; Kamalanathan, I.D.; Martin, P.J. Comparative Study of the Production of Rhamnolipid Biosurfactants by *B. Thailandensis* E264 and *P. Aeruginosa* ATCC 9027 Using Foam Fractionation. *Process. Biochem.* **2016**, *51*, 820–827. [CrossRef]
22. Najmi, Z.; Ebrahimipour, G.; Franzetti, A.; Banat, I.M. In Situ Downstream Strategies for Cost-Effective Bio/Surfactant Recovery. *Biotechnol. Appl. Biochem.* **2018**, *65*, 523–532. [CrossRef]
23. Juang, R.S.; Chen, H.L.; Chen, Y.S. Membrane Fouling and Resistance Analysis in Dead-End Ultrafiltration of *Bacillus Subtilis* Fermentation Broths. *Sep. Purif. Technol.* **2008**, *63*, 531–538. [CrossRef]
24. Chen, H.L.; Chen, Y.S.; Juang, R.S. Flux Decline and Membrane Cleaning in Cross-Flow Ultrafiltration of Treated Fermentation Broths for Surfactin Recovery. *Sep. Purif. Technol.* **2008**, *62*, 47–55. [CrossRef]
25. De Andrade, C.J.; de Andrade, L.M.; Rocco, S.A.; Sforça, M.L.; Pastore, G.M.; Jauregi, P. A Novel Approach for the Production and Purification of Mannosylerythritol Lipids (MEL) by *Pseudozyma Tsukubaensis* Using Cassava Wastewater as Substrate. *Sep. Purif. Technol.* **2017**, *180*, 157–167. [CrossRef]
26. Vicente, R.; de Andrade, C.J.; de Oliveira, D.; Ambrosi, A. A Prospection on Membrane-Based Strategies for Downstream Processing of Surfactin. *Chem. Eng. J.* **2021**, *415*, 1–9. [CrossRef]
27. Dalheim, M.; Omtvedt, L.A.; Bjørge, I.M.; Akbarzadeh, A.; Mano, J.F.; Achmann, F.L.; Strand, B.L. Mechanical Properties of Ca-Saturated Hydrogels with Functionalized Alginate. *Gels* **2019**, *5*, 23. [CrossRef] [PubMed]
28. Aburabie, J.H.; Puspasari, T.; Peinemann, K.V. Alginate-Based Membranes: Paving the Way for Green Organic Solvent Nanofiltration. *J. Memb. Sci.* **2020**, *596*, 117615. [CrossRef]
29. Moldes, A.B.; Vázquez, M.; Domínguez, J.M.; Díaz-Fierros, F.; Barral, M.T. Evaluation of Mesophilic Biodegraded Grape Marc as Soil Fertilizer. *Appl. Biochem. Biotechnol.* **2007**, *141*, 27–36. [CrossRef] [PubMed]
30. Perez-Ameneiro, M.; Vecino, X.; Barbosa-Pereira, L.; Cruz, J.M.; Moldes, A.B. Removal of Pigments from Aqueous Solution by a Calcium Alginate-Grape Marc Biopolymer: A Kinetic Study. *Carbohydr. Polym.* **2014**, *101*, 954–960. [CrossRef]
31. Perez-Ameneiro, M.; Vecino, X.; Cruz, J.M.; Moldes, A.B. Wastewater Treatment Enhancement by Applying a Lipopeptide Biosurfactant to a Lignocellulosic Biocomposite. *Carbohydr. Polym.* **2015**, *131*, 186–196. [CrossRef]
32. Hull, S.R.; Montgomery, R. Myo-Inositol Phosphates in Corn Steep Water. *J. Agric. Food Chem.* **1995**, *43*, 1516–1523. [CrossRef]
33. Hull, S.R.; Yang, B.Y.; Venzke, D.; Kulhavy, K.; Montgomery, R. Composition of Corn Steep Water during Steeping. *J. Agric. Food Chem.* **1996**, *44*, 1857–1863. [CrossRef]
34. Moldes, A.B.; Cruz, J.M.; Devesa, R.; Vecino, X. Method for Separating the Surfactants Present in the Washing Liquors of Corn, and Uses. Patent WO2014044876A1, 27 March 2014.
35. Perez-Ameneiro, M.; Vecino, X.; Cruz, J.M.; Moldes, A.B. Physicochemical Study of a Bio-Based Adsorbent Made from Grape Marc. *Ecol. Eng.* **2015**, *84*, 190–193. [CrossRef]
36. Perez-Ameneiro, M.; Vecino, X.; Vega, L.; Devesa-Rey, R.; Cruz, J.M.; Moldes, A.B. Elimination of Micronutrients from Winery Wastewater Using Entrapped Grape Marc in Alginate Beads. *CYTA-J. Food* **2014**, *12*, 73–79. [CrossRef]

37. Bustos, G.; Calvar, S.; Vecino, X.; Cruz, J.M.; Moldes, A.B. Industrial Symbiosis Between the Winery and Environmental Industry Through the Utilization of Grape Marc for Water Desalination Containing Copper (II). *Water Air Soil Pollut.* **2018**, *229*, 1–11. [CrossRef]
38. Ndiaye, B.; Bustos, G.; Calvar, S.; Vecino, X.; Cruz, J.M.; Moldes, A.B.; Pérez-Cid, B. Selective Adsorption Capacity of Grape Marc Hydrogel for Adsorption of Binary Mixtures of Dyes. *Water Air Soil Pollut.* **2020**, *231*, 1–14. [CrossRef]
39. Pérez-Cid, B.; Calvar, S.; Moldes, A.B.; Manuel Cruz, J. Effective Removal of Cyanide and Heavy Metals from an Industrial Electroplating Stream Using Calcium Alginate Hydrogels. *Molecules* **2020**, *25*, 5183. [CrossRef]
40. Moldes, A.; Vecino, X.; Rodríguez-López, L.; Rincón-Fontán, M.; Cruz, J.M. Biosurfactants: The use of biomolecules in cosmetics and detergents. In *New and Future Developments in Microbial Biotechnology and Bioengineering*; Rodrigues, A.G., Ed.; Elsevier: Amsterdam, The Netherlands, 2020; pp. 163–185. ISBN 9780444643018.
41. Vecino, X.; Barbosa-Pereira, L.; Devesa-Rey, R.; Cruz, J.M.; Moldes, A.B. Optimization of Extraction Conditions and Fatty Acid Characterization of *Lactobacillus Pentosus* Cell-Bound Biosurfactant/Bioemulsifier. *J. Sci. Food Agric.* **2015**, *95*, 313–320. [CrossRef] [PubMed]
42. Andrade, R.F.S.; Silva, T.A.L.; Ribeaux, D.R.; Rodriguez, D.M.; Souza, A.F.; Lima, M.A.B.; Lima, R.A.; Alves Da Silva, C.A.; Campos-Takaki, G.M. Promising Biosurfactant Produced by *Cunninghamella Echinulata* UCP 1299 Using Renewable Resources and Its Application in Cotton Fabric Cleaning Process. *Adv. Mater. Sci. Eng.* **2018**, *2018*, 1–12. [CrossRef]
43. Rodríguez-López, L.; Rincón-Fontán, M.; Vecino, X.; Cruz, J.M.; Moldes, A.B. Extraction, Separation and Characterization of Lipopeptides and Phospholipids from Corn Steep Water. *Sep. Purif. Technol.* **2020**, *248*, 117076. [CrossRef]
44. Li, J.; Deng, M.; Wang, Y.; Chen, W. Production and Characteristics of Biosurfactant Produced by *Bacillus Pseudomycoloides* BS6 Utilizing Soybean Oil Waste. *Int. Biodeterior. Biodegrad.* **2016**, *112*, 72–79. [CrossRef]
45. Ma, Y.; Kong, Q.; Qin, C.; Chen, Y.; Chen, Y.; Lv, R.; Zhou, G. Identification of Lipopeptides in *Bacillus Megaterium* by Two-Step Ultrafiltration and LC–ESI–MS/MS. *AMB Express* **2016**, *6*, 1–15. [CrossRef]
46. LeClere, S.; Schmelz, E.A.; Chourey, P.S. Phenolic Compounds Accumulate Specifically in Maternally-Derived Tissues of Developing Maize Kernels. *Cereal Chem.* **2007**, *84*, 350–356. [CrossRef]
47. Rodríguez-López, L.; Vecino, X.; Barbosa-Pereira, L.; Moldes, A.B.; Cruz, J.M. A Multifunctional Extract from Corn Steep Liquor: Antioxidant and Surfactant Activities. *Food Funct.* **2016**, *7*, 3724–3732. [CrossRef] [PubMed]
48. Chen, Y.; Liu, S.A.; Mou, H.; Ma, Y.; Li, M.; Hu, X. Characterization of Lipopeptide Biosurfactants Produced by *Bacillus Licheniformis* MB01 from Marine Sediments. *Front. Microbiol.* **2017**, *8*, 1–11. [CrossRef] [PubMed]
49. Béchet, M.; Caradec, T.; Hussein, W.; Abderrahmani, A.; Chollet, M.; Leclère, V.; Dubois, T.; Lereclus, D.; Pupin, M.; Jacques, P. Structure, Biosynthesis, and Properties of Kurstakins, Nonribosomal Lipopeptides from *Bacillus* spp. *Appl. Microbiol. Biotechnol.* **2012**, *95*, 593–600. [CrossRef] [PubMed]
50. Hathout, Y.; Ho, Y.P.; Ryzhov, V.; Demirev, P.; Fenselau, C. Kurstakins: A New Class of Lipopeptides Isolated from *Bacillus Thuringiensis*. *J. Nat. Prod.* **2000**, *63*, 1492–1496. [CrossRef]

Article

Ion-Exchange Technology for Lactic Acid Recovery in Downstream Processing: Equilibrium and Kinetic Parameters

X. Vecino ^{1,2,3,*}, M. Reig ^{1,2,†}, C. Valderrama ^{1,2} and J. L. Cortina ^{1,2,4}

¹ Chemical Engineering Department, Escola d'Enginyeria de Barcelona Est (EEBE), Universitat Politècnica de Catalunya (UPC)-BarcelonaTECH, C/Eduard Maristany 10-14, Campus Diagonal-Besòs, 08930 Barcelona, Spain; monica.reig@upc.edu (M.R.); jose.luis.cortina@upc.edu (J.L.C.)

² Barcelona Research Center for Multiscale Science and Engineering, Campus Diagonal-Besòs, 08930 Barcelona, Spain; cesar.alberto.valderrama@upc.edu

³ Chemical Engineering Department, School of Industrial Engineering—CINTECX, University of Vigo, Campus As Lagoas-Marcosende, 36310 Vigo, Spain

⁴ Water Technology Center (CETAQUA), Carretera d'Esplugues, 75, 08940 Cornellà de Llobregat, Spain

* Correspondence: xanel.vecino@upc.edu or xanel.vecino@uvigo.es; Tel.: +34-934016184 or +34-986812215

† These authors contributed equally to the work.

Abstract: The downstream processing for the separation and purification of lactic acid is a hot research area in the bio-refinery field due to its continuous growing market in different sectors, such as the food, cosmetic and pharmaceutical sectors. In this work, the use of ion-exchange technology for lactic acid recovery is proposed. For that, four anion exchange resins with different polymer structures and functional groups were tested (A100, MN100, A200E and MP64). The sorption process was optimized by the Box–Behnken factorial design, and the experimental data obtained in the sorption process were analyzed by using the response surface methodology and fitted at different isotherms and kinetics models. Moreover, regenerant type, contact time and solid/liquid ratio were evaluated in the desorption process. Results showed that the best resin for lactic acid removal was A100, at pH = 4, with a resin/lactic acid solution ratio of 0.15 g/mL during a maximum of 1 h, achieving 85% of lactic acid removal. Moreover, equilibrium data sorption of lactic acid onto A100 resin was fitted by a Langmuir isotherm and by a kinetic model of a pseudo-second order. In addition, in the desorption process, it was established that a resin/regenerant ratio of 0.15 g/mL during 30 min with 0.1 M of NaOH solution provided the best results (4.45 ± 0.08 mg/g).

Keywords: organic acid; circular economy; optimization process; bio-economy; response surface methodology

Citation: Vecino, X.; Reig, M.; Valderrama, C.; Cortina, J.L. Ion-Exchange Technology for Lactic Acid Recovery in Downstream Processing: Equilibrium and Kinetic Parameters. *Water* **2021**, *13*, 1572. <https://doi.org/10.3390/w13111572>

Academic Editors: Goen Ho and Alexandra B. Ribeiro

Received: 7 April 2021

Accepted: 31 May 2021

Published: 2 June 2021

Publisher's Note: MDPI stays neutral with regard to jurisdictional claims in published maps and institutional affiliations.



Copyright: © 2021 by the authors. Licensee MDPI, Basel, Switzerland. This article is an open access article distributed under the terms and conditions of the Creative Commons Attribution (CC BY) license (<https://creativecommons.org/licenses/by/4.0/>).

1. Introduction

Lactic acid is an alpha-hydroxy acid with dual functional groups, is considered both an alcohol and an acid and has an asymmetric carbon that confers optical activity. It can be found in two optically active forms, levorotatory L (+)-lactic acid and dextrorotatory D (−)-lactic acid, or in racemic form, which is a mixture of L (+)-lactic acid and D (−)-lactic acid [1]. The ratio of each isomer confers different physical properties to the final product, which makes enantiomeric purity a crucial factor for the industrial production of lactic acid, such as in the manufacture of biodegradable plastics and polymers such as polylactic acid [1,2].

Regarding lactic acid production, it can be mainly obtained by two routes:

- i. chemical synthesis from non-renewable sources, such as coal, petroleum products and natural gas. In this case, it is mainly based on the hydrolysis of lactonitrile by strong acids, but it can also include base-catalyzed degradation of sugars, oxidation of propylene glycol, hydrolysis of chloropropionic acid, oxidation of propylene by nitric acid and reaction of acetaldehyde, carbon monoxide and water at high temperatures and pressures [2,3]; and secondly by

- ii. fermentation, from different renewable substrates, such as starchy materials (e.g., corn, maize, rice, rye, wheat, potato, barley and cassava), lignocellulosic biomass (from agricultural, agro-industrial and forestry sources), microalgae, food waste (e.g., vegetables, meat, etc.) and glycerol [4]. Low temperatures, low energy consumption, better environmental concerns and high purity are some of the advantages of the fermentative route over chemical synthesis [5]. Consequently, 90% of lactic acid production is done by fermentation, since pure lactic acid can be obtained, whereas the chemical synthesis it always gives a racemic mixture [6]. Moreover, the fermentation route is considered a “bio-refinery” alternative, which relies within the circular economy approach.

Furthermore, lactic acid is a worldwide consolidated bioproduct. The industrial interest of lactic acid is widespread, as it is used in different sectors, such as the food and pharmaceutical industries, especially the L (+)-lactic acid isomer; meanwhile, the D (−)-lactic acid isomer is considered harmful to humans and can cause acidosis or decalcification in high doses [4,6–9]. For instance, lactic acid presents a large demand share in the food industry (35%) as an acidulant, due to its mild acid taste compared to other acids used in food, and as a preservative in olives and pickled vegetables. It is also used as a flavoring agent, pH regulator and inhibitor of residual bacteria in food processing, such as in candies, breads, soft drinks, beer and other products. Moreover, it is an essential ingredient in fermented foods, such as yogurt, butter and canned vegetables. In the pharmaceutical industry, lactic acid is used in implants, pills, dialysis, surgical sutures and controlled drug-release systems; meanwhile, in the cosmetic industry, lactic acid is used in the manufacture of hygiene and aesthetic products due to its moisturizing, antimicrobial and rejuvenating properties on the skin, as well as in oral hygiene products [1,9].

On the other hand, although the market of lactic acid is constantly growing, its production by fermentation presents two main bottlenecks: (i) the cost of carbon sources and (ii) the cost of sterilization and downstream separation and purification processes [3,10]. The former limitation can be solved by using low-cost and renewable substrates as mentioned above, but they must be saccharificated by physicochemical and enzymatic treatments before use them as a carbon source [11]. The conventional lactic acid recovery is carried out by chemical precipitation. Nowadays, several techniques have been reported on the separation of lactic acid produced in the fermentation broth without precipitation such as diffusion dialysis, solvent extraction, direct distillation, liquid surfactant membrane extraction, adsorption, chromatographic methods, ultrafiltration, reverse osmosis, drying or electrodialysis with monopolar and bipolar membranes [12]. Among them, ion-exchange technology, using resins, can be proposed to recover lactic acid from fermentation media, improving the later weakness; since it is an in situ recovery technique with potential to not only recover lactic acid but also release product inhibition [13].

The recovery of lactic acid obtained by fermentation media or from synthetic solutions has been studied by different authors over the years [14–29]. In these studies, the most commonly used resin was Amberlite IRA 400 [16–18,23,27,28]. The IRA 400 is a gel-type strong base resin, with quaternary ammonium groups. For instance, Moldes et al. [16,18] tested four ion-exchange resins types (Amberlite IRA 900, IRA 400, IRA 96 and IRA 67) for lactic acid recovery from simultaneous saccharification and fermentation (SSF) media. Among them, Amberlite IRA 400 and IRA 900, both strong anion exchange resins, showed the highest capacities for lactic acid recovery. Moreover, the Amberlite IRA 400 resin was selected for intermittent lactic acid separation in a typical SSF process, in which pretreated wood was saccharified by cellulases in the presence of *Lactobacillus delbrueckii* [16]. Weak anion exchange resins, such as IRA 96 [16,18,24,27] and IRA 67 [16,18,27,29], were also used. For instance, Ahmad et al. [29] proposed the extraction of lactic acid from the fermentation broth by a weak anion exchanger, Amberlite IRA 67, followed by a cation exchanger, Amberlite IR 120. They observed that the maximum adsorption capacity of lactic acid (150 mg/g) was observed with weak anion resin at an initial pH of 3. Lastly, other resins found in the literature for lactic acid recovery were Indion 850, Indion 860, Indion 810,

Indion 190 (the first two resins are weak base macroporous and the last two are strong base microporous) [21] and resins from Chinese companies (such as D314, D311 and 331 from Anhui Sanxing Resin Technology Co. (Hochi, Anhui, China); 313, D301 and D319 from Suqing Group (Jinagsu, China); D302 and 201 × 4 from Nansen Hangzhou Water Treatment Equipment Co. (Hangzhou, China) [25]; D354, D380, D941, D396 and D293 from Zhengzhou Qinshi Science and Technology Development Co. (Henan, China); and resins D301, D315, 335, D201 and 717 from Shanghai Zhenhua Technology Development Co. (Shanghai, China) [26]).

In view of the aforementioned, the aim of this study is to evaluate novel types of anionic exchange resins for the lactic acid recovery: one strong base with quaternary ammonium groups gel-type resin (A200E), one weak base containing tertiary amine groups resin with macroporous structure (A100), a weak base macroporous resin containing mixtures of quaternary ammonium and tertiary amine groups (MP64) and a free base macroporous hyper-crosslinked resin containing tertiary amine groups (MN100) in order to evaluate the sorption of lactic acid from water. It should be highlighted that this is the first time that these resins have been evaluated for the recovery of lactic acid. First, sorption optimization was carried out by surface response methodology, being the pH, resin/lactic acid solution ratio and contact time the independent variables. Then, the lactic acid sorption was fitted by different isotherm and kinetic models. Finally, the desorption process was also evaluated changing the type of regenerant, contact time and resin/regenerant ratio.

2. Materials and Methods

2.1. Reagents

Synthetic solutions were prepared by mimicking fermentation media with L (+)-lactic acid ($C_3H_6O_3$, 85%) purchased from Sigma-Aldrich. Hydrochloric acid (HCl, 37%) was used for resin conditioning and sodium hydroxide (NaOH, 98%) was used for pH adjustment and desorption step, both were supplied by Panreac (Barcelona, Spain). Moreover, sodium hydrogen carbonate ($NaHCO_3$, 99% from Fluka (Madrid, Spain)), anhydrous sodium carbonate (Na_2CO_3 , 99.8% from Panreac (Barcelona, Spain)) and methanesulfonic acid (CH_4O_3S , 99% from Sigma-Aldrich (Madrid, Spain)) were used as reagents in the analytical chromatography analysis.

2.2. Resins

The anion exchange resins used in this work consisted of A100, MN100 and A200E from Purolite Ltd. (Barcelona, Spain) and MP64 supplied by Lanxess Co. (Cologne, Germany). Before their use, all resins were converted into Cl^- form by washing the resin sequentially with 1 M HCl solution during 1 h, and then distilled water until pH = 7. Table 1 shows the main characteristics of the resins.

Table 1. Resins properties tested in this work.

Resin	Type	Functional Group (Capacity)	Ionic Form	Matrix	Reference
A100	Weak base macroporous	Tertiary amine (1.3 eq./L)	Free base	Polystyrene crosslinked with divinylbenzene	[30]
MN100	Free base macroporous	Tertiary amine (0.1 eq./L)	Free base	Hyper-crosslinked polystyrene-divinylbenzene	[31]
A200E	Strong base gel	Quaternary ammonium (1.3 eq./L)	Cl^-	Polystyrene crosslinked with divinylbenzene	[32]
MP64	Weak base macroporous	Tertiary/quaternary amine (1.3 eq./L)	Free base/ Cl^-	Polystyrene	[33]

2.3. Resin Selection

Batch experiments were carried out with two different lactic acid concentrations (1 and 10 g/L) at $\text{pH} > \text{pK}_a$ lactic acid (about 6) and four resins (A100, MN100, A200E and MP64) (Barcelona, Spain), using a resin/solution ratio of 0.1 (1 g: 10 mL, *w/v*) during 24 h in an overhead shaker (Heidolph Reax 2 from Sigma-Aldrich (Madrid, Spain)). After the sorption process, resins were desorbed with 1 M NaOH at the same ratio as adsorption process during 24 h.

2.4. Sorption Process Optimization by Box–Behnken Design

In order to evaluate the optimal sorption capacity and removal efficiency of lactic acid, a Box–Behnken factorial design was applied [34,35]. For that, an incomplete 3^3 factorial design was established to obtain theoretical models that define the most favorable conditions for the removal of lactic acid by using the selected resin. The independent variables selected were pH of the lactic acid solution (x_1), resin/solution ratio (x_2) and contact time (x_3); the dependent variables were the adsorption capacity (y_1), percentage of lactic acid removal (y_2), desorption capacity (y_3), and percentage of lactic acid recovery (y_4). The 15 experiments established by the factorial design were carried out in an overhead shaker by fixing the lactic acid concentration at 1 g/L. Table 2 shows the variation range established for the independent variables selected, which were codified between -1 and 1 in order to limit the influence of their magnitudes.

Table 2. Independent and dependent variables used in the Box–Behnken factorial design.

Independent Variables			
	Units	Range of Variation	
pH	-	4–8	
Resin/solution ratio	g/mL	0.05–0.15	
Contact time	h	1–9	
Dimensionless, coded independent variables			
	Nomenclature	Definition	Range of variation
pH	x_1	$(x_1 - 6)/2$	$(-1, 1)$
Resin/solution ratio	x_2	$(x_2 - 0.10)/0.05$	$(-1, 1)$
Contact time	x_3	$(x_3 - 5)/4$	$(-1, 1)$
Dependent Variables			
	Nomenclature	Units	
Adsorption capacity	y_1	mg/g	
Lactic acid removal	y_2	%	
Desorption capacity	y_3	mg/g	
Lactic acid recovery	y_4	%	

The desorption process for the 15 experiments was carried out with 1 M NaOH, at the same solid/liquid ratio and contact time as for the adsorption process tested.

2.4.1. Sorption Isotherms Models

Different isotherms were used to study the sorption process at the equilibrium condition as described in previous works [36]. For instance, the Langmuir isotherm is described by Equations (1) and (2) [37], the Freundlich isotherm by Equation (3) [38], the Dubinin–Radushkevich isotherm by Equations (4) and (5) [39] and the Temkin isotherm by Equations (6) and (7) [40]. All of these equations have been used in this work in order to evaluate the isotherm model that fitted better under the optimal operational conditions previously predicted by the Box–Behnken model. This equilibrium study was carried out by using different initial concentrations of lactic acid, namely 10, 6, 4, 2, 1, 0.5 and 0.1 g/L, and a contact time of 24 h, taking into account the optimal pH and resin/lactic acid solution ratio obtained in the previous stage with the design model.

$$\frac{1}{q_e} = \frac{1}{q_m K_L C_e} + \frac{1}{q_m} \quad (1)$$

$$R_L = \frac{1}{1 + K_L C_0} \quad (2)$$

$$\ln q_e = \log K_F + \frac{1}{n} \ln C_e \quad (3)$$

$$\ln q_e = \ln q_m - \beta \left[RT \ln \left(1 + \frac{1}{C_e} \right) \right]^2 \quad (4)$$

$$E = \sqrt{\frac{1}{2\beta}} \quad (5)$$

$$q_e = B_1 \ln K_T + B_1 \ln C_e \quad (6)$$

$$B_1 = \frac{RT}{b} \quad (7)$$

In these equations, q_e (mg/g) is the resin capacity at equilibrium and q_m (mg/g) is the maximum theoretical capacity that can be reached; C_0 (mg/L) and C_e (mg/L) are the initial and equilibrium lactic acid concentration in the aqueous phase, respectively; K_L (mg/L) is the Langmuir equilibrium constant and R_L is a dimensionless equilibrium parameter; K_F (L/g) is related to the adsorption capacity, and n is associated with the sorption intensity (g/L). In addition, $(\text{mol}^2/\text{J}^2)$ is a constant related to the sorption energy, R (8.314 J/mol K) is the ideal gas constant; T (298.15 K) is the temperature of sorption; and E (kJ/mol) is the mean free energy of adsorption per molecule of adsorbate when transferred to the surface of the solid from infinity in solution. Finally, K_T (L/mg) is the equilibrium binding constant (maximum binding energy); B_1 (J/mol) is related to the heat of sorption; R is the universal gas constant (8.314 J/mol K); T is the temperature at 298 K; and b is the Temkin isotherm constant.

2.4.2. Adsorption Kinetic Models

In addition, at the optimal operational conditions predicted by the Box–Behnken model, a kinetic study was carried out and the experimental data obtained were adjusted to four kinetic models described in previous works [41,42]. The pseudo-first order kinetic model is described by Equation (8) [43], the pseudo-second-order kinetic model by Equation (9) [44], Chien–Clayton kinetic model by Equation (10) [45] and intraparticle diffusion model by Equation (11) [46]. In this work, the kinetic study was developed by using different contact times, namely 0, 2, 4, 6, 8, 10, 12, 14, 20, 30, 40, 50, 60 and 90 min, and an initial lactic acid concentration of 1 g/L at the optimal pH and resin/lactic acid solution ratio obtained in the previous stage with the design model.

$$\log(q_e - q_t) = \log q_e - \frac{K_1}{2.303} t \quad (8)$$

$$\frac{t}{q_t} = \frac{1}{K_2 q_e^2} + \frac{1}{q_e} t \quad (9)$$

$$q_t = \frac{1}{\beta} \ln(\alpha\beta) + \frac{1}{\beta} \ln t \quad (10)$$

$$q_t = K_p t^{0.5} + C \quad (11)$$

In these equations, q_e (mg lactic acid/g resin) and q_t (mg lactic acid/g resin) are the amount of adsorbed lactic acid at equilibrium and at a defined time t (min), respectively; K_1 (1/min) is the rate constant of pseudo-first-order adsorption; K_2 (g/mg min) is the equilibrium rate constant of pseudo-second-order sorption; α (min mg/g) is the initial sorption rate; β (g/mg) is related to the extent of surface coverage and activation energy for chemisorption; K_p is the intraparticle diffusion rate constant (mg/g min^{0.5}); and C is the intercept (mg/g), and it is related to the thickness of the boundary layer.

2.5. Desorption Process Optimization

Desorption step was evaluated by changing (i) the type and concentration of regenerant: NaOH (0.1, 0.5 and 1 M), ethanol (0.1, 0.5 and 1 M) and equimolar mixture of NaOH/ethanol (0.1, 0.5 and 1 M); (ii) the contact times of 2, 4, 6, 8, 10, 12, 14, 20, 30, 40, 50, 60 and 90 min, as well as 2, 4, 6, 8 and 24 h; and (iii) the resin/regenerant ratio (w:v, g/mL) at 0.075, 0.15 and 0.3. Table 3 shows the experimental design to evaluate the type and concentration of the regenerant, contact time and ratio in the desorption process of lactic acid, fixing the adsorption conditions predicted by the Box–Behnken model.

Table 3. Study of the desorption process changing the type and concentration of regenerant, contact time and the solid/liquid ratio.

Sorption Process			Desorption Process		
Initial Lactic Acid (g/L)	Solid/Liquid Ratio (g/mL)	Contact Time	Ratio Solid/Liquid (g/mL)	Contact Time	Parameter Tested
1	0.15	30 min	0.15	30 min	Type and concentration of the regenerant Contact time Solid/liquid ratio in desorption
			0.15	2 min–24 h	
			0.075–0.3	30 min	

2.6. Data Analysis

Sorption and desorption capacities were calculated following the procedure described elsewhere [47]. The resin sorption capacity (q_{ads} , mg lactic acid/g resin) was calculated by Equation (12), and Equation (13) was applied to determine the percentage of lactic acid removed from the solution:

$$q_{ads} \text{ (mg/g)} = \frac{(C_0 - C_e) \cdot V_{solution}}{\text{resin mass}} \quad (12)$$

$$\text{Sorption (\%)} = \frac{(C_0 - C_e)}{C_0} \cdot 100 \quad (13)$$

where C_0 is the initial concentration of the lactic acid (mg/L), C_e is the lactic acid at the end of sorption (equilibrium) (mg/L), $V_{solution}$ is the volume of lactic acid solution used for sorption (L) and resin mass is the amount of resin mass used for the experiments (g).

On the other hand, the resin desorption capacity (q_{des} , mg lactic acid/g resin) is described by Equation (14):

$$q_{des} \text{ (mg/g)} = \frac{C_e \cdot V_{regenerant}}{\text{resin mass}} \quad (14)$$

where C_e is the lactic acid concentration at the end of desorption process (mg/L), $V_{regenerant}$ is the volume of regenerant (e.g., NaOH) used for desorption (L) and mass resin is the amount of mass resin used for the experiments (g).

Consequently, the percentage of lactic acid recovery can be established by the relationship between adsorption capacity and desorption capacities of the resin. This parameter (lactic acid recovery percentage, %) was calculated by Equation (15):

$$\text{Recovery (\%)} = \frac{q_{des}}{q_{ads}} \cdot 100 \quad (15)$$

where q_{des} is the desorption capacity (mg/g) and q_{ads} is the sorption capacity (mg/g), described in Equations (14) and (12), respectively.

2.7. Analytical Methodology

Lactic acid was determined by cationic and anionic chromatography systems (Dionex ICS-1000 and ICS-1100, respectively) supplied by Thermo-Fisher Scientific (Barcelona, Spain). Both devices were controlled by Chromeleon chromatographic software from the same company. Moreover, a CS16 column ($5 \times 250 \text{ mm}^2$) and an AS23 column

(4 × 250 mm²) with their precolumns (CG16 (5 × 50 mm²) and AG23 (4 × 50 mm²)) (Dionex, Barcelona, Spain) were used for cation and anion determination and quantification, respectively. The mobile phase used for each system was 0.03 M CH₄O₃S for cation equipment and 0.8 mM NaHCO₃ and 4.5 mM Na₂SO₃ for anion apparatus. Before ion chromatography analyses, the samples were filtered by using a 0.22 μm filter.

2.8. Statistical Analysis

Triplicate experiments were performed in order to increase the accuracy of the results. Thus, data are reported as the mean ± standard deviation of triplicate determinations. Data were subjected to analysis of variance (Fisher's F-test and Student's *t*-test) performed by using the excel statistical software package. Significant differences were assessed at $p < 0.05$.

Moreover, the experimental data obtained in the sorption process were analyzed by using the response surface method with Design-Expert[®] Version 12 (Stat-Ease, Inc., Minneapolis, MN, USA) by fitting the results obtained to a quadratic function shown in Equation (16):

$$y = \beta_0 + \beta_1 x_1 + \beta_2 x_2 + \beta_3 x_3 + \beta_{12} x_1 x_2 + \beta_{13} x_1 x_3 + \beta_{23} x_2 x_3 + \beta_{11} x_1^2 + \beta_{22} x_2^2 + \beta_{33} x_3^2 \quad (16)$$

where y is the dependent variable of each experiment (adsorption capacity, lactic acid removal, desorption capacity and lactic acid recovery); β_i represents the regression coefficients, which were calculated from experimental data by performing multiple regressions, using the least-squares method; and x_i represents the independent variables of this study (pH, solid/liquid ratio and contact time).

3. Results and Discussion

3.1. Ion-Exchange Resins Screening for Lactic Acid Extraction

For the selection of the anion exchange resin, the results of the sorption capacity and percentage of lactic acid extracted were obtained in relation to the sorption process (represented in Figure 1a,b, respectively). On the other hand, for the desorption process, desorption capacity and percentage of lactic acid recovery were calculated and plotted in Figure 1c,d, respectively. For each resin, initial concentrations of 1 and 10 g/L of lactic acid were tested.

The sorption capacity was 5.6 ± 0.3 mg/g (average) for all anion exchange resins tested at 1 g/L of lactic acid, whereas it increased up to from 34.3 mg/g, using the MN100 resin, to 57.5 mg/g for A100 resin. The same behavior was observed for the desorption capacity, being a minimum desorption capacity of 4.0 ± 0.4 mg/g (average) for 1 g/L of lactic acid and a maximum of 39.1 mg/g at 10 g/L for A100 resin. Although at 10 g/L of lactic acid, both sorption and desorption capacities varied slightly according to the type of resins, they were not significantly different ($p > 0.05$).

Regarding to the lactic acid extraction, A100, MN100 and A200E resins provided the maximum value of $81.3 \pm 1.2\%$ (average) at 1 g/L. At 10 g/L of lactic acid, A100 and A200E resins achieved values about 50–60%, whereas the lactic acid extraction value decreased up to $36.5 \pm 1.7\%$ (average), using the MN100 and MP64 resins. This fact may be due to the fact that the former resins are made of a polystyrene crosslinked with divinylbenzene matrix, while the latter resins are only based on a polystyrene matrix.

Finally, the lactic acid recovery was practically the same, $67 \pm 6.1\%$ (average), regardless of the concentration of lactic acid used (1 or 10 g/L). Although, there were no significant differences between the resins evaluated ($p > 0.05$), the resin that reported the best recovery values, for both concentrations of lactic acid, was the A100 resin. Therefore, only this resin was used in the following assays.

To our knowledge, the resins tested in this work were not studied for lactic acid sorption/desorption previously. For instance, resins A100, MN100 and MP64 have been applied for the recovery of metals [48], halogenated compounds [49], aurocyanide extraction [50], natural organic matter [51,52], dissolved organic matter removal [53] and humic substances removal [54], but no for lactic acid recovery.

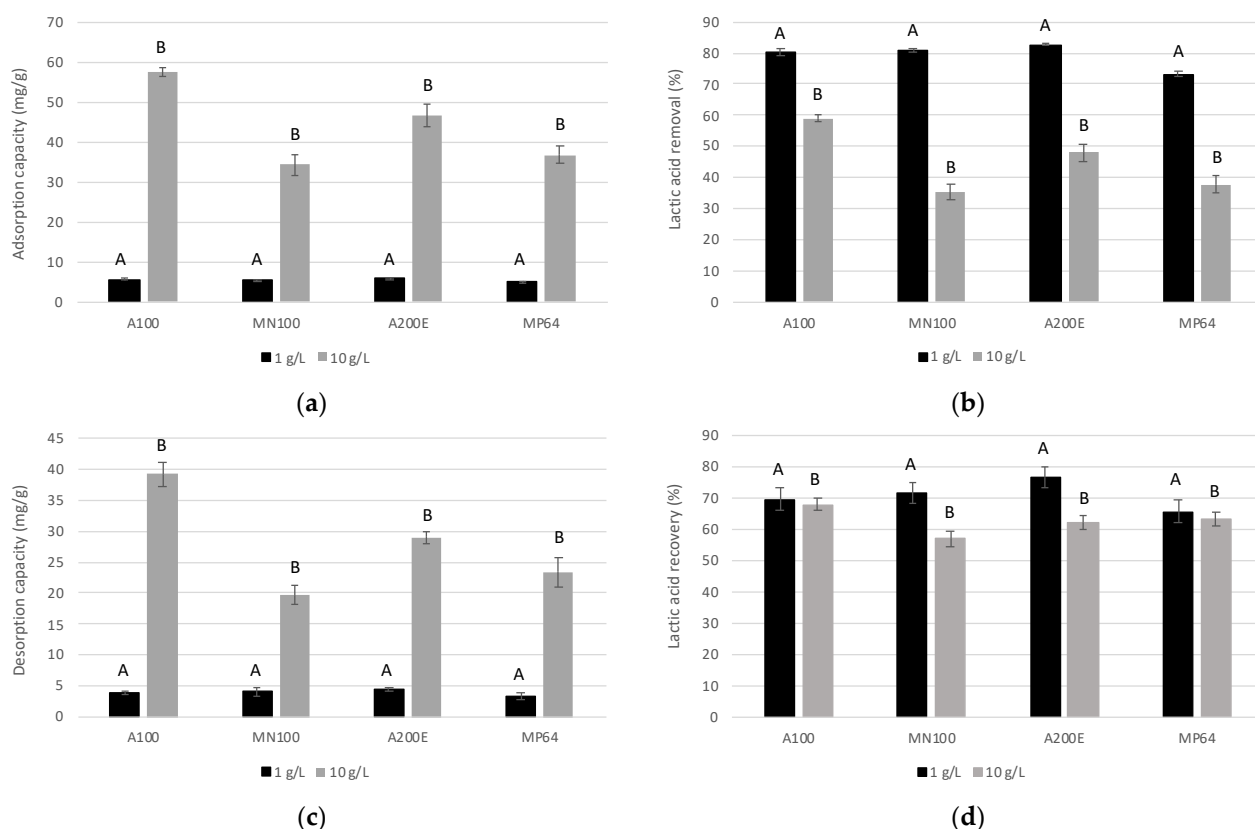


Figure 1. Resin selection based on (a) sorption capacity, (b) lactic acid removal, (c) desorption capacity and (d) lactic acid recovery at 1 and 10 g/L of initial lactic acid concentration. Different letters at the same lactic acid concentration indicate significant differences ($p < 0.05$).

However, the removal efficiency of lactic acid as function of different lactic acid concentrations was also studied by other authors, by using other resins. For example, Luongo et al. [27] observed that lactic acid removal efficiency decreased from 68% to 27% at the same time as the initial lactic acid concentration increased from 1.4 to 18.0 g/L, using Amberlite IRA 900 resin at 30 °C. Moreover, Amberlite IRA 400 showed a significant decrease from 71% to 32% in the lactic acid removal efficiency at the same temperature, when increasing the initial lactic acid concentration. Instead, the weak anionic resins, Amberlite IRA 96 and Amberlite IRA 67, showed minimal changes in the removal efficiencies at the tested initial lactic acid concentrations. Similarly, in this work, lactic acid removal and recovery decreased when increasing the initial lactic acid concentration from 1 to 10 g/L (Figure 1b,d). Otherwise, adsorption and desorption capacities increased when testing higher initial lactic acid concentration (Figure 1a,c).

3.2. Optimization of Sorption Process for Lactic Acid Recovery Using Response Surface Methodology

The set of experimental conditions assayed (expressed as coded variables) and the experimental data obtained for the dependent variables y_1 to y_4 are shown in Table 4.

As can be seen in Table 4, the maximum lactic acid removal value from the Box–Behnken factorial design was 85.3% (Experiment 8), achieved with pH = 4 (low value), ratio 0.15 g/mL (high value) and contact time of 5 h (intermediate value).

In regards with capacities, both sorption and desorption, Experiment 1 (pH 4, ratio 0.05 g/mL and time 5 h) presented better results than Experiment 8 (pH 4, ratio 0.15 g/mL and time 5 h). The only difference between these two experiments was their solid/liquid ratio, where Experiment 1 was carried out with a ratio of 0.5 g: 10 mL, while Experiment 8 with a ratio of 1.5 g: 10 mL, meaning that the later test did not have enough lactic acid solution for a larger amount of resin. Furthermore, a clear positively trend, based on sorption capacity, can be seen when the solid/liquid ratio tested was the lower. Therefore,

experiments with a ratio of 0.05 g/mL were best suited to sorb and desorb lactic acid in a more efficient manner, with a sorption capacity range between 21 and 28 mg lactic acid/g resin and a desorption capacity range between 17 and 20 mg lactic acid/g resin.

Table 4. Coded independent variables (pH (x_1), solid/liquid ratio (x_2), contact time (x_3)) values considered in this study and experimental results obtained for all dependent variables: sorption capacity (y_1), removal of lactic acid (y_2), desorption capacity (y_3) and recovery of lactic acid (y_4).

Experiment	Independent Variables (Coded)			Dependent Variables			
	x_1	x_2	x_3	y_1	y_2	y_3	y_4
1	−1	−1	0	27.89	68.50	20.22	72.52
2	0	0	0	13.90	73.39	11.47	82.52
3	−1	0	1	16.62	82.30	12.33	74.22
4	0	0	0	13.80	72.75	11.23	81.39
5	1	0	−1	13.26	63.67	11.57	87.26
6	0	−1	1	22.49	59.24	18.79	83.55
7	1	0	1	13.45	64.97	11.83	88.01
8	−1	1	0	11.54	85.27	8.79	76.18
9	0	0	0	13.72	72.35	11.93	86.97
10	0	−1	−1	22.72	59.74	19.08	83.97
11	0	1	1	9.71	76.77	8.04	82.85
12	−1	0	−1	15.60	76.62	12.78	81.94
13	0	1	−1	9.66	76.52	8.15	84.35
14	1	1	0	10.19	73.32	8.13	79.78
15	1	−1	0	21.73	52.19	17.76	81.72

On the other hand, the experiment at conditions of pH 8, ratio 0.1 g/mL and contact time of 9 h (corresponding to Experiment 7) presented the highest recovery percentage, reaching 88% of the lactic acid recovery. Compared to the Experiment 8 (at pH 4, ratio 0.15 g/mL and contact time of 5 h), 76% of lactic acid was recovered, but the former experiment (Experiment 7) was developed at a higher pH, with a lower solid/liquid ratio and with a longer contact time. Under the above conditions, Experiment 7 reported better results than Experiment 8 due to the fact that a such high pH, it had more lactate ions in the solution than Experiment 8, which a pH 4 was very close to the $pK_{a(298K)}$ of lactic acid (HL/L^-) (3.86).

In the case of percentage of lactic acid extracted, the pH (x_1) and the solid/liquid ratio (x_2) were the only statistically significant variables ($p < 0.05$), while the contact time effect was negligible. For that, the variation of the lactic acid extraction percentage for the abovementioned independent variables (pH and solid/liquid ratio) as the most statistically significant, with a fixed contact time (x_3) of 1 (Figure 2a), 5 (Figure 2b) and 9 h (Figure 2c), is showed in Figure 2.

The same trend is observed, in the graphs of Figure 2, where the best percentage of lactic acid sorption was obtained for the conditions of pH 4 and resin/solution ratio of 0.15 g/mL. Based on these results, it can be established that the highest lactic acid extraction was achieved for the highest solid/liquid ratio and the lower pH, regardless of the contact time.

Similar findings were reported by Luongo et al. [27]. The effect of pH on the lactic acid sorption was studied. The two strong anionic resins tested, IRA 900 and IRA 400, showed a similar trend, both effective at a pH above the pK_a (3.86) of lactic acid. At pH 5.0, the highest lactic acid removal efficiency was between 44 and 47% for IRA 900 and between 49 and 50% for IRA 400, respectively. However, the lactic acid removal efficiency did not change significantly for $pH > 5.0$. Otherwise, for the tertiary amine resins, IRA 96 and IRA 67, showed high selectivity at a pH below the lactic acid pK_a , reaching both the highest removal efficiency $> 99\%$ at pH 2.0. On the other hand, the contact time for lactic acid adsorption was established 20 min of operation, regardless of the initial concentration of lactic acid.

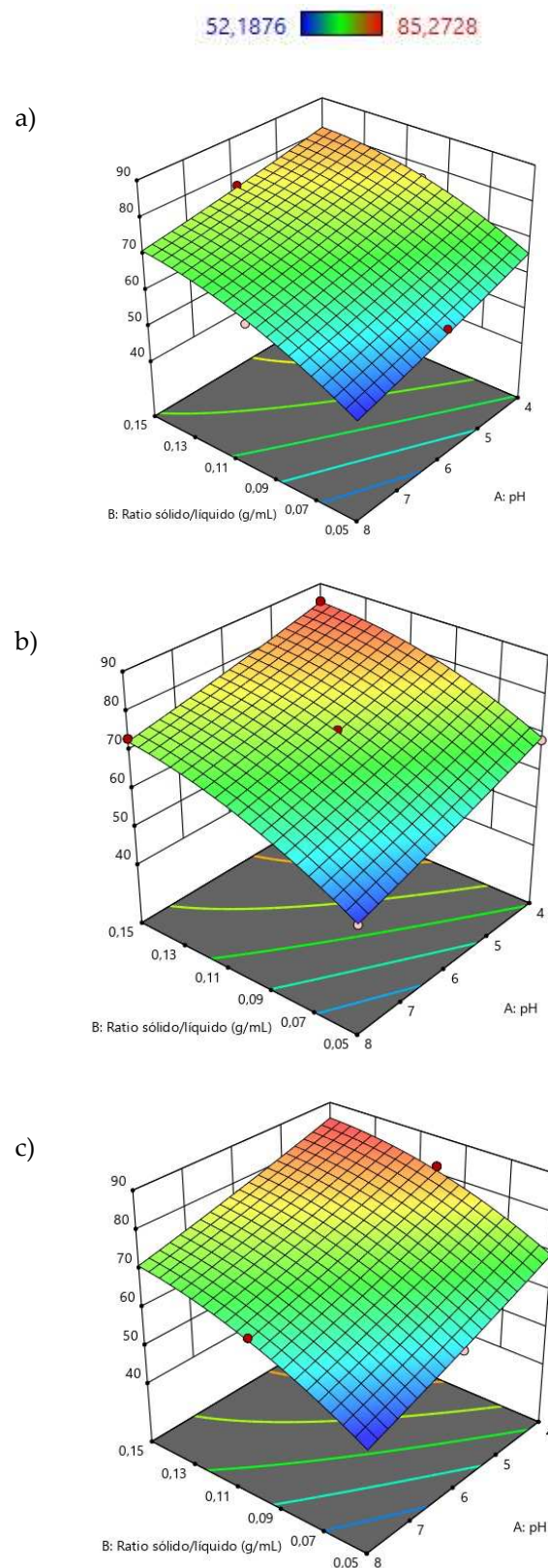


Figure 2. Lactic acid removal as an interaction between the solid/liquid ratio (x_2) and pH (x_1) setting time (x_3) at (a) 1 h, (b) 5 h and (c) 9 h for A100 resin.

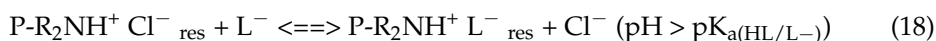
For a tertiary resin (A100), described for simplicity reasons as P-R₂N, where P is the polystyrene divinyl benzene structure and R are the alkyl chains of the tertiary amine group of the resin, the extraction of lactic acid (HL) could be described by a combination of

the reactions involving both the solute (Equation (17)) and the adsorbent (Equations (18) and (19)):

(a) Protonation of the tertiary amine group:



(b) Adsorption of lactic acid (HL) and lactate anion (L^-):



3.2.1. Lactic Acid Sorption Isotherms

Table 5 shows the equilibrium parameters for A100 tertiary resin, which were calculated by linear regression, for each isotherm (for average data).

Table 5. Comparison of equilibrium parameters for Langmuir, Freundlich, Dubinin–Radushkevich and Temkin isotherms.

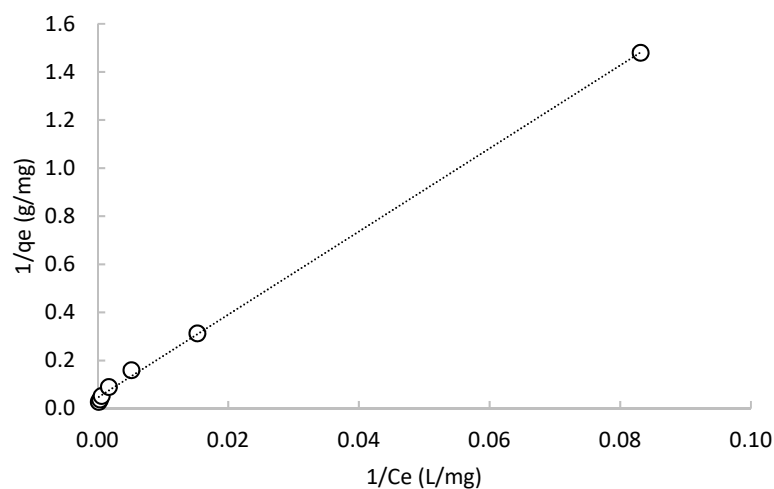
Langmuir Isotherm				Freundlich Isotherm		
r^2	q_m	k_L	R_L	r^2	n	k_F
0.999	(mg/g) 22.05	(mg/L) 0.003	0.035–0.770	0.984	(g/L) 1.572	(L/g) 0.182
Dubinin–Radushkevich Isotherm				Temkin Isotherm		
r^2	q_m	E	r^2	B_1	k_T	
0.662	(mg/g) 13.02	(mol ² /J ²) 76.771	(kJ/mol) 0.081	0.858	(J/mol) 5.599	(L/mg) 0.034

Additionally, Figure 3a shows the good concordance between the experimental and the theoretical data fitted by the Langmuir isotherm ($r^2 = 0.999$, error 1.7%). The R_L value obtained from the plot of $1/C_e$ against $1/q_e$ (between 0.035 and 0.770 for 1 to 10 g/L of lactic acid) indicates that the adsorption is favorable [55]. Moreover, the Freundlich isotherm is plotted in Figure 3b. The n value reached in this case is 1.572 g/L, which implies a beneficial adsorption process [56]. However, the r^2 value of 0.984 and an error of 19% show that the adsorption process can be explained by a monolayer adsorption process.

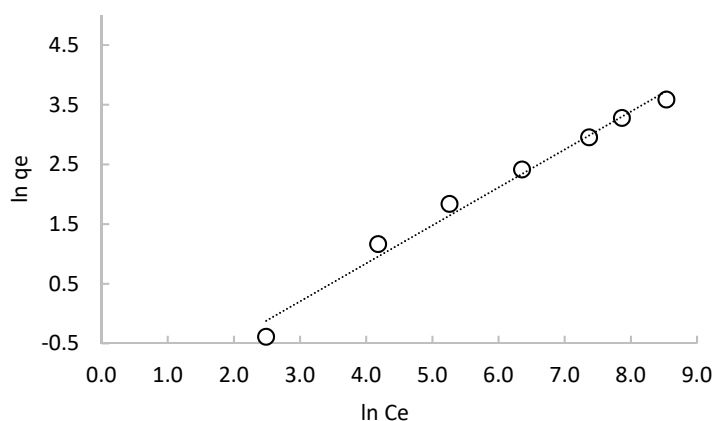
The experimental data were not well described with the Dubinin–Radushkevich and Temkin isotherms (see Table 5) since they yielded an r^2 value of 0.662 and 0.858, respectively. However, the apparent energy of adsorption obtained, 0.081 kJ/mol, indicates that the adsorption process is physically controlled [57] and the positive value of K_T (0.034 L/mg) indicates a favorable adsorption process. Therefore, considering the r^2 values and percentage errors of the studied models (Table 5), the adsorption of lactic acid into the A100 resin is described by the Langmuir isotherm.

Other authors have also obtained good fits of the lactic acid sorption with the Langmuir isotherm model [17,18,26,29]. For example, Moldes et al. [18] assessed mathematical models of lactic acid adsorption, using different anion exchange resins (IRA 900, IRA 400, IRA 96 and IRA 67). IRA 900 and IRA 400 are strong base resins, both based on quaternary ammonium groups, but in macroreticular and gel-type, respectively. Otherwise, IRA 96 and IRA 67 are free base resins, both with polyamine groups, also in macroreticular and gel-type, respectively. In all cases, good agreement was observed between the experimental and theoretical data predicted by equations for the different isotherms models used; with values of correlation coefficients (r^2) from 0.995 to 0.998. Regarding to adsorption capacity, IRA 400 provided the lowest value (161 mg/g), while IRA 67 achieved the maximum value (276 mg/g) for 125 g/L of lactic acid concentration at equilibrium. A similar finding is obtained in this work, where the adsorption capacity, by Langmuir model was, 22 mg/g

at 10 g/L (taking into account that in our work the initial lactic acid concentration was 10 times lower).



(a)



(b)

Figure 3. Equilibrium plots for the adsorption of lactic acid into the A100 resin: (a) Langmuir isotherm and (b) Freundlich isotherm.

3.2.2. Lactic Acid Sorption Kinetics

Results of the sorption kinetics, shown in Figure 4, indicates a very fast process. In less than 5 min more than 80% of the total equilibrium attainment was reached, and 20 min was time enough for achieving equilibrium attainment.

Table 6 includes the kinetic parameters obtained for the different models used in this work (for average data). Among the kinetic models tested, it was observed a good agreement between the experimental (5.45 mg/g) and theoretical (5.46 mg/g) adsorption capacity data predicted by the equations of the pseudo-second-order model; with a correlation coefficient (r^2) value of 1.000. Hence, it can be postulated that the adsorption process was well described by the pseudo-second-order kinetic model. Data were not well described by the Chien–Clayton kinetic model reaching the lowest correlation coefficient (r^2 value of 0.71). However, it can be observed that α value predicted (6×10^{20} mg/g·min), as a measure of the initial sorption rates [41], was very high.

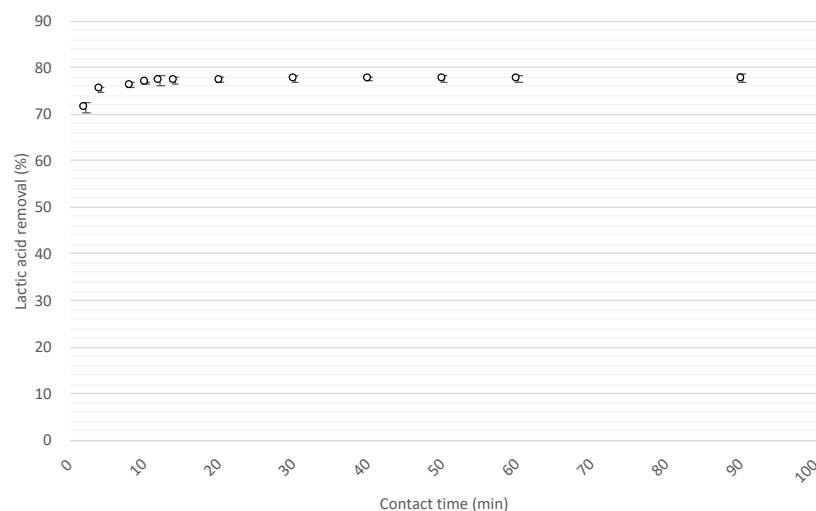


Figure 4. Variation of the lactic acid concentration on the A100 resin phase as a function of the contact time (1 g/L of lactic acid, resin/lactic acid ratio of 0.15 g/mL, pH 4).

Table 6. Comparison of kinetic parameters for pseudo-first-order, pseudo-second-order, Chien–Clayton and intraparticle diffusion kinetic models.

Pseudo-1st-Order Kinetic Model			
K_1 (L/g·min)	$q_e \text{ exp}$ (mg/g)	$q_e \text{ calc}$ (mg/g)	r^2
0.063	5.45	0.13	0.774
Pseudo-2nd-Order Kinetic Model			
K_2 (L/g·min)	$q_e \text{ exp}$ (mg/g)	$q_e \text{ calc}$ (mg/g)	r^2
1.470	5.45	5.46	1.000
Chien–Clayton Kinetic Model			
α (mg/g·min)	β (g/mg)	r^2	
6×10^{20}	9.81	0.705	
Intraparticle Diffusion Model			
K_P (mg/g·min ^{0.5})	C	r^2	
0.160	4.87	0.844	

The intraparticle diffusion model determines whether the adsorption process is controlled only by intraparticle diffusion or if it involves other phenomena, such as surface adsorption, ion exchange and complexation [58]. In regard with C value (4.87), obtained applying this model, it indicates that there are other phenomena, apart from the intraparticle diffusion (C values higher than 0) [41], implicated in the adsorption removal process of lactic acid (e.g., reactions Equations (17) to (19) proposed for the extraction mechanism).

Halilibrahimoğlu et al. [28] reported that the most favorable kinetic model for lactic acid recovery from water by Amberlite IRA 400 resin was also determined as pseudo-second-order kinetic model. Besides, the same results were reported by Zhang et al. [26] with a weak base anion gel-type resin.

3.3. Optimization of Desorption Process for Lactic Acid Recovery

Three type of regeneration solutions (NaOH, ethanol and a mixture of both) at three different concentrations (0.1, 0.5 and 1 M) were evaluated in the desorption process of lactic acid from the A100 tertiary resin. The use of ethanol was based on the search for a more biocompatible and environmentally friendly solution to regenerate resins, taking into account that this technology will be used to treat biocompounds. Additionally, the use of mixtures of aqueous/organic solvents is recommended for the desorption of organic

solutes from ion-exchange resins. Figure 5a shows the results obtained based on the desorption capacity. It can be observed that the best results were obtained with the mixture of NaOH/ethanol 0.5 M (4.75 ± 0.26 mg/g) and 0.1 M (4.61 ± 0.03 mg/g), followed by NaOH solutions (between 4.34 and 4.45 mg/g), and finally ethanol provided the lowest desorption capacities (<0.5 mg/g). This fact could be due to the fact that NaOH provides the necessary cations to regenerate the anionic exchange resin and release the lactate ion, while ethanol is a neutral molecule that is not able to perform the exchange properly. Similar results were obtained by other authors; for example, Cao et al. [17] tested organic solvents (methanol) to elute lactic acid adsorbed on Amberlite IRA 400 at pH 5, since methanol was a good solvent for washing step and it could reduce the product loss in washing step. The lactic acid recovery varied from 5.2%, using pure methanol, up to 54%, using 20% (*v/v*) methanol. However, Evangelista et al. [59] successfully used methanol as a regenerant and obtained a completely lactic acid recovery, but with a VI-15 resin. The VI-15 resin (Riedel-de-Haen, Seelze, Germany) is a copolymer of methylene-bis-acrylamide and imidazole groups (gel-type), whereas Amberlite IRA 400 is a strong basic gel-type anion exchange resin with quaternary ammonium groups and the matrix is a polystyrene divinylbenzene copolymer (macroreticular type). Therefore, different characteristics in the elution of lactic acid are expected when different types of resins were used.

In regard with the percentage of lactic acid recovery (based on the same average of adsorption capacity around 5.32 mg/g), it was possible to achieve 89% by using 0.5 M of the mixture NaOH/ethanol, followed by 87% with 0.1 M of the mixture NaOH/ethanol, and by the 0.5 M NaOH solution, recovering 86%. Taking into account an industrial point of view, Table 7 shows a brief economic study that was carried out to select the best regenerant for lactic acid recovery.

Table 7. Lactic acid recovery as a function of the regenerant type and concentration, as well as its price.

Type of Regenerant	Lactic Acid Recovery (%)	Regenerant Solution Cost * (€/L)
NaOH 0.1 M	84.0 ± 1.9	0.16
NaOH 0.5 M	85.6 ± 0.1	0.81
NaOH 1 M	82.3 ± 3.2	1.62
Ethanol 0.1 M	3.6 ± 0.5	0.24
Ethanol 0.5 M	3.8 ± 0.1	1.21
Ethanol 1 M	2.3 ± 0.7	2.42
Mixture NaOH/Ethanol 0.1 M	86.7 ± 0.7	0.31
Mixture NaOH/Ethanol 0.5 M	89.3 ± 2.5	1.57
Mixture NaOH/Ethanol 1 M	77.5 ± 2.3	3.13

* It is assumed a NaOH and ethanol price of 39.8 €/kg NaOH and 41.6 €/L ethanol, respectively according to a supplier company (e.g., Vidrafoc) at the lab-scale level.

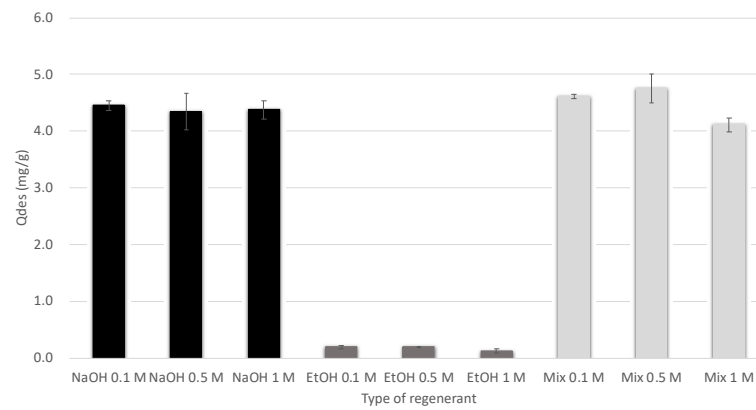
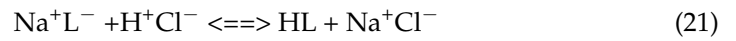
Among the three best lactic acid recoveries mentioned above, the one that provides the lowest cost (0.31 €/L) was the mixture of NaOH/ethanol at 0.1 M. However, it was observed that the lowest price of regenerant solution (0.16 €/L) was from using NaOH 0.1 M. For that reason, with this regenerant solution it could be saved twice for almost the same lactic acid recovery (84% vs. 87%). Therefore, the 0.1 M NaOH solution was selected as optimal for the following studies (contact time and solid/liquid ratio effect). This type of regenerant for lactic acid recovery is in agreement with other published works. For instance, Chen et al. [14] also used 0.1 M of NaOH solution as regenerant to recover lactic acid from fermentation of *Lactobacillus delbrueckii* by polyvinylpyridine resin (a weakly basic polymer). Additionally, the use of the NaOH cycle is the most efficient extraction and re-extraction route. However, in the desorption process with NaOH, sodium lactate is formed instead of lactic acid. The addition of HCl solution to convert the sodium lactate

in lactic acid is necessary. This conversion could be described by the following equations (Equations (20) and (21)):

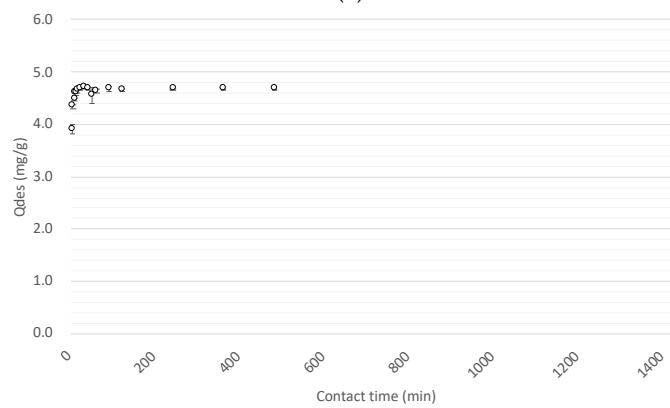
(a) Desorption of lactic acid (HL) with NaOH:



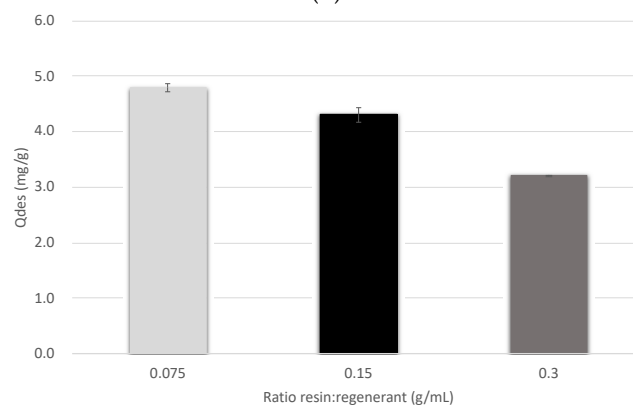
(b) Conversion of sodium lactate (NaL) to lactic acid (HL):



(a)



(b)



(c)

Figure 5. Effect of (a) type of regenerant, (b) contact time and (c) solid/liquid ratio in the desorption process of lactic acid by A100 resin.

Additionally, electrodialysis with bipolar membranes could also be used a downstream process to produce lactic acid solutions and if required latter being crystallized.

On the other hand, the desorption kinetic assay over 24 h is represented in Figure 5b. It can be seen that 30 min was sufficient time to achieve 4.62 mg/g as desorption capacity as well as the maximum lactic acid recovery (about 87%), using 0.1 M of NaOH as regenerant solution and a resin/regenerant ratio of 0.15 g/mL.

At the end, different resin/regenerant ratios were evaluated with 0.75, 1.5 and 3 g of resin fixing 10 mL of 0.1 M of NaOH as regenerant solution. These results are plotted in Figure 5c. It was observed that, for the same volume of regenerant solution, the use of less resin in the desorption process provided a slight increase in its capacity (being 4.8 mg/g the maximum). This value was not much higher when using the 0.15 g/mL ratio. Therefore, the latter is established as the optimum ratio for the desorption process.

This is a preliminary aiming to select the optimal resin and evaluate the behavior (isotherms and kinetics) with respect to an organic acid in order to apply it to a fermentative medium that contains competing ions. Therefore, ongoing research focuses on dynamic experiments, using real solutions.

In the global process of production of lactic acid, from fermentation broths in biotechnological reactors, ion-exchange should be considered as a stage with two main objectives: to selectively extract lactic acid and to reach the maximum concentration factor. It should be pointed out that that still not full-scale applications are described and then the identification of efficient ion-exchange resins are still needed. In addition, the integration of electrochemical membranes process in combination of crystallization could provide a promising train treatment for lactic acid recovery.

4. Conclusions

Lactic acid is a bioproduct worldwide used in the food, cosmetic and pharmaceutical sectors, but the bottleneck, from an industrial point of view, is its recovery from fermentation media. In this work, different anion exchange resins (A100, MN100, A200E and MP64) were evaluated for lactic acid downstream recovery. Among them, A100 resin, a weak base macroporous resin, provided the best results based on sorption capacity, lactic acid removal, desorption capacity and lactic acid recovery at two lactic acid concentrations (1 and 10 g/L). Afterwards, the sorption process was optimized by the Box–Behnken design, observing the maximum lactic acid removal value (85%) at pH 4, with a solid/liquid ratio of 0.15 g/mL and with a contact time of 1 h. Moreover, after analyzing the isotherm and kinetic parameters obtained for lactic acid sorption into A100 resin, it was observed that (i) the sorption process at equilibrium was well described by the Langmuir isotherm and was physically controlled; and (ii) the sorption process followed a pseudo-second-order kinetic model, with the existence of a high concordance between the experimental and theoretical sorption capacity. Finally, the desorption process optimization was as follows: resin/regenerant ratio of 0.15 g/mL, during 30 min, with 0.1 M of NaOH solution.

Author Contributions: Conceptualization, X.V., M.R., C.V. and J.L.C.; validation, X.V., M.R. and J.L.C.; formal analysis, X.V. and M.R.; investigation, X.V. and M.R.; resources, J.L.C.; data curation, X.V. and M.R.; writing—original draft preparation, X.V., M.R. and J.L.C.; writing—review and editing, X.V., M.R. and J.L.C.; visualization, X.V. and M.R.; supervision, X.V., M.R., C.V. and J.L.C.; project administration, J.L.C.; funding acquisition, J.L.C. All authors have read and agreed to the published version of the manuscript.

Funding: This research was funded by the R2MIT project (reference CTM2017-85346-R) financed by the Spanish Ministry of Economy and Competitiveness (MINECO) and the Catalan Government (reference 2017-SGR-312), Spain.

Institutional Review Board Statement: Not applicable.

Informed Consent Statement: Not applicable.

Data Availability Statement: The data presented in this study is available on request from the corresponding author.

Acknowledgments: X. Vecino acknowledges Spanish Ministry of Science and Innovation for her financial support under the project PID2019-103873RJ-I00. The authors would also like to acknowledge M. Parietti and J.M. Monge for their contribution to the project.

Conflicts of Interest: The authors declare no conflict of interest.

References

1. Komesu, A.; de Oliveira, J.A.R.; da Silva Martins, L.H.; Maciel, M.R.W.; Filho, R.M. Lactic Acid Production to Purification: A Review. *BioResources* **2017**, *12*, 4364–4383. [CrossRef]
2. Datta, R.; Tsai, S.P.; Bonsignore, P.; Moon, S.H.; Frank, J.R. Technological and Economic Potential of Poly(Lactic Acid) and Lactic Acid Derivatives. *FEMS Microbiol. Rev.* **1995**, *16*, 221–231. [CrossRef]
3. Gao, C.; Ma, C.; Xu, P. Biotechnological Routes Based on Lactic Acid Production from Biomass. *Biotechnol. Adv.* **2011**, *29*, 930–939. [CrossRef] [PubMed]
4. Alves de Oliveira, R.; Komesu, A.; Vaz Rossell, C.E.; Maciel Filho, R. Challenges and Opportunities in Lactic Acid Bioprocess Design—From Economic to Production Aspects. *Biochem. Eng. J.* **2018**, *133*, 219–239. [CrossRef]
5. De Oliveira, R.A.; Filho, R.M.; Rossell, C.E.V. High Lactic Acid Production from Molasses and Hydrolysed Sugarcane Bagasse. *Chem. Eng. Trans.* **2016**, *50*, 307–312. [CrossRef]
6. Hofvendahl, K.; Hahn-Hägerdal, B. Factors Affecting the Fermentative Lactic Acid Production from Renewable Resources. *Enzyme Microb. Technol.* **2000**, *26*, 87–107. [CrossRef]
7. Reddy, G.; Altaf, M.; Naveena, B.J.; Venkateshwar, M.; Kumar, E.V. Amylolytic Bacterial Lactic Acid Fermentation—A Review. *Biotechnol. Adv.* **2008**, *26*, 22–34. [CrossRef]
8. Gao, T.; Wong, Y.; Ng, C.; Ho, K. L-Lactic Acid Production by *Bacillus Subtilis* MUR1. *Bioresour. Technol.* **2012**, *121*, 105–110. [CrossRef]
9. Castillo Martinez, F.A.; Balciunas, E.M.; Salgado, J.M.; Domínguez González, J.M.; Converti, A.; de Oliveira, R.P.S. Lactic Acid Properties, Applications and Production: A Review. *Trends Food Sci. Technol.* **2013**, *30*, 70–83. [CrossRef]
10. Ouyang, J.; Ma, R.; Zheng, Z.; Cai, C.; Zhang, M.; Jiang, T. Open Fermentative Production of L-Lactic Acid by *Bacillus* Sp. Strain NL01 Using Lignocellulosic Hydrolyzates as Low-Cost Raw Material. *Bioresour. Technol.* **2013**, *135*, 475–480. [CrossRef]
11. Okano, K.; Tanaka, T.; Ogino, C.; Fukuda, H.; Kondo, A. Biotechnological Production of Enantiomeric Pure Lactic Acid from Renewable Resources: Recent Achievements, Perspectives, and Limits. *Appl. Microbiol. Biotechnol.* **2010**, *85*, 413–423. [CrossRef]
12. Abdel-Rahman, M.A.; Tashiro, Y.; Sonomoto, K. Recent Advances in Lactic Acid Production by Microbial Fermentation Processes. *Biotechnol. Adv.* **2013**, *31*, 877–902. [CrossRef] [PubMed]
13. López-Garzón, C.S.; Straathof, A.J.J. Recovery of Carboxylic Acids Produced by Fermentation. *Biotechnol. Adv.* **2014**, *32*, 873–904. [CrossRef] [PubMed]
14. Chen, C.C.; Ju, L.K. Adsorption Characteristics of Polyvinylpyridine and Activated Carbon for Lactic Acid Recovery from Fermentation of *Lactobacillus Delbrueckii*. *Sep. Sci. Technol.* **1998**, *33*, 1423–1437. [CrossRef]
15. Monteagudo, J.M.; Aldavero, M. Production of L-Lactic Acid by *Lactobacillus Delbrueckii* in Chemostat Culture Using an Ion Exchange Resins System. *J. Chem. Technol. Biotechnol.* **1999**, *74*, 627–634. [CrossRef]
16. Moldes, A.B.; Alonso, J.L.; Parajó, J.C. Resin Selection and Single-Step Production and Recovery of Lactic Acid from Pretreated Wood. *Appl. Biochem. Biotechnol. Part A Enzym. Eng. Biotechnol.* **2001**, *95*, 69–81. [CrossRef]
17. Cao, X.; Yun, H.S.; Koo, Y.M. Recovery of L-(+)-Lactic Acid by Anion Exchange Resin Amberlite IRA-400. *Biochem. Eng. J.* **2002**, *11*, 189–196. [CrossRef]
18. Moldes, A.B.; Alonso, J.L.; Parajó, J.C. Recovery of Lactic Acid from Simultaneous Saccharification and Fermentation Media Using Anion Exchange Resins. *Bioprocess Biosyst. Eng.* **2003**, *25*, 357–363. [CrossRef] [PubMed]
19. Gluszczyk, P.; Jamroz, T.; Sencio, B.; Ledakowicz, S. Equilibrium and Dynamic Investigations of Organic Acids Adsorption onto Ion-Exchange Resins. *Bioprocess Biosyst. Eng.* **2004**, *26*, 185–190. [CrossRef]
20. Tong, W.Y.; Fu, X.Y.; Lee, S.M.; Yu, J.; Liu, J.W.; Wei, D.Z.; Koo, Y.M. Purification of L-(+)-Lactic Acid from Fermentation Broth with Paper Sludge as a Cellulosic Feedstock Using Weak Anion Exchanger Amberlite IRA-92. *Biochem. Eng. J.* **2004**, *18*, 89–96. [CrossRef]
21. Dethlefsen, M.J.; Marathe, K.V.; Gaikar, V.G. Adsorption of Lactic Acid on Weak Base Polymeric Resins. *Sep. Sci. Technol.* **2006**, *41*, 2947–2971. [CrossRef]
22. John, R.P.; Nampoothiri, K.M.; Pandey, A. Acid Recovery from Cassava Bagasse Based Fermented Medium Using Anion Exchange Resins. *Braz. Arch. Biol. Technol.* **2008**, *51*, 1241–1248. [CrossRef]
23. Quintero, J.; Acosta, A.; Mejía, C.; Ríos, R.; Torres, A.M. Purification of Lactic Acid Obtained from a Fermentative Process of Cassava Syrup Using Ion Exchange Resins. *Rev. Fac. Ing.* **2012**, *65*, 139–151.
24. Bishai, M.; De, S.; Adhikari, B.; Banerjee, R. A Platform Technology of Recovery of Lactic Acid from a Fermentation Broth of Novel Substrate *Zizyphus Oenophlia*. *3 Biotech* **2015**, *5*, 455–463. [CrossRef]

25. Cui, S.; Zhao, J.; Zhang, H.; Chen, W. High-Density Culture of *Lactobacillus Plantarum* Coupled with a Lactic Acid Removal System with Anion-Exchange Resins. *Biochem. Eng. J.* **2016**, *115*, 80–84. [CrossRef]
26. Zhang, Y.; Qian, Z.; Liu, P.; Liu, L.; Zheng, Z.; Ouyang, J. Efficient in Situ Separation and Production of L-Lactic Acid by *Bacillus Coagulans* Using Weak Basic Anion-Exchange Resin. *Bioprocess Biosyst. Eng.* **2018**, *41*, 205–212. [CrossRef]
27. Luongo, V.; Palma, A.; Rene, E.R.; Fontana, A.; Pirozzi, F.; Esposito, G.; Lens, P.N.L. Lactic Acid Recovery from a Model of Thermotoga Neapolitana Fermentation Broth Using Ion Exchange Resins in Batch and Fixed-Bed Reactors. *Sep. Sci. Technol.* **2019**, *54*, 1008–1025. [CrossRef]
28. Halilibrahimoğlu, N.; İnci, İ.; Baylan, N. Lactic Acid Recovery from Water by Amberlite IRA-400. *Desalin. Water Treat.* **2019**, *172*, 190–198. [CrossRef]
29. Ahmad, A.; Othman, I.; Taher, H.; Banat, F. Lactic Acid Recovery from Date Pulp Waste Fermentation Broth by Ions Exchange Resins. *Environ. Technol. Innov.* **2021**, *22*, 101438. [CrossRef]
30. Purolite. *Purolite A100-Product Data Sheet*; Purolite: Barcelona, Spain, 2007.
31. Purolite. *Purolite MN100-Product Data Sheet*; Purolite: Barcelona, Spain, 2019.
32. Purolite. *Purolite A200E-Product Data Sheet*; Purolite: Barcelona, Spain, 2020.
33. Lewatit. *Lewatit MP 64-Product Data Sheet*; Lanxess: Cologne, Germany, 2011.
34. Box, G.E.P.; Behnken, D.W. Simplex-Sum Designs: A Class of Second Order Rotatable Designs Derivable from Those of First Order. *Ann. Math. Stat.* **1960**, *31*, 838–864. [CrossRef]
35. Ferreira, S.L.C.; Bruns, R.E.; Ferreira, H.S.; Matos, G.D.; David, J.M.; Brand, G.C.; Silva, E.G.P.; Reis, P.S.; Souza, A.S.; Santos, W.N.L. Box-Behnken Design: An Alternative for the Optimization of Analytical Methods. *Anal. Chim. Acta* **2007**, *597*, 179–186. [CrossRef] [PubMed]
36. Perez-Ameneiro, M.; Vecino, X.; Cruz, J.M.; Moldes, A.B. Physicochemical Study of a Bio-Based Adsorbent Made from Grape Marc. *Ecol. Eng.* **2015**, *84*, 190–193. [CrossRef]
37. Langmuir, I. The Adsorption of Gases on Plane Surfaces of Mica and Platinum. *J. Am. Chem. Soc.* **1918**, *40*, 1361–1403. [CrossRef]
38. Freundlich, H.M.F. Über Die Adsorption in Lösungen. *J. Phys. Chem.* **1906**, *57*, 385–470. [CrossRef]
39. Dubinin, M.M.; Zaverina, E.D.; Radushkevich, L.V. Sorption and Structure of Active Carbons. *J. Phys. Chem.* **1947**, *21*, 1351–1362.
40. Temkin, M.I.; Pyzhev, V. Kinetics of Ammonia Synthesis on Promoted Iron Catalysts. *Acta Physicochem* **1940**, *12*, 327–356.
41. Perez-Ameneiro, M.; Vecino, X.; Barbosa-Pereira, L.; Cruz, J.M.; Moldes, A.B. Removal of Pigments from Aqueous Solution by a Calcium Alginate-Grape Marc Biopolymer: A Kinetic Study. *Carbohydr. Polym.* **2014**, *101*, 954–960. [CrossRef]
42. Vecino, X.; Devesa-Rey, R.; Villagrasa, S.; Cruz, J.M.; Moldes, A.B. Kinetic and Morphology Study of Alginate-Vineyard Pruning Waste Biocomposite vs. Non Modified Vineyard Pruning Waste for Dye Removal. *J. Environ. Sci.* **2015**, *38*, 158–167. [CrossRef]
43. Lagergren, S. About the Theory of So-Called Adsorption of Soluble Substances. *Kungliga Svenska Vetenskapsakademiens. Handlingar* **1898**, *24*, 1–39.
44. Ho, Y.S.; McKay, G. Pseudo-Second Order Model for Sorption. *Process Biochem.* **1999**, *34*, 451–465. [CrossRef]
45. Chien, S.H.; Clayton, W.R. Application of Elovich Equation to the Kinetics of Phosphate Release and Sorption in Soils. *Soil Sci. Soc. Am. J.* **1980**, *44*, 265–268. [CrossRef]
46. Weber, W.J.; Morris, J.C. Advances in Water Pollution Research. In Proceedings of the First International Conference on Water Pollution Research, Jerusalem, Israel, 18–23 June 1962; p. 231.
47. Reig, M.; Vecino, X.; Hermassi, M.; Valderrama, C.; Gibert, O.; Cortina, J.L. Integration of Electrodialysis and Solvent-Impregnated Resins for Zn(II) and Cu(II) Recovery from Hydrometallurgy Effluents Containing As(V). *Sep. Purif. Technol.* **2019**, *229*, 115818. [CrossRef]
48. Cortina, J.L.; Meinhardt, E.; Røijals, O.; Martí, V. Modification and Preparation of Polymeric Adsorbents for Precious-Metal Extraction in Hydrometallurgical Processes. *React. Funct. Polym.* **1998**, *36*, 149–165. [CrossRef]
49. Jadbabaei, N.; Ye, T.; Shuai, D.; Zhang, H. Development of Palladium-Resin Composites for Catalytic Hydrodechlorination of 4-Chlorophenol. *Appl. Catal. B Environ.* **2017**, *205*, 576–586. [CrossRef]
50. Cortina, J.L.; Kautzmann, R.M.; Gliese, R.; Sampaio, C.H. Extraction Studies of Aurocyanide Using Macronet Adsorbents: Physico-Chemical Characterization. *React. Funct. Polym.* **2004**, *60*, 97–107. [CrossRef]
51. Pürschel, M.; Worch, E.; Ender, V. Uptake of NOM Fractions by Anion-Exchange Resins in Demineralization Plants. *Desalin. Water Treat.* **2014**, *52*, 2987–2995. [CrossRef]
52. Urbanowska, A.; Kabsch-Korbutowicz, M. The Efficiency of Macroporous Polystyrene Ion-Exchange Resins in Natural Organic Matter Removal from Surface Water. *E3S Web Conf.* **2017**, *22*. [CrossRef]
53. Zhang, L.; Li, A.; Wang, J.; Lu, Y.; Zhou, Y. A Novel Aminated Polymeric Adsorbent for Removing Refractory Dissolved Organic Matter from Landfill Leachate Treatment Plant. *J. Environ. Sci.* **2009**, *21*, 1089–1095. [CrossRef]
54. Urbanowska, A.; Kabsch-Korbutowicz, M. Isolation and Fractionation of Humic Substances Present in Water with the Use of Anion-Exchange Resins and Ultrafiltration. *Brazilian J. Chem. Eng.* **2018**, *35*, 1211–1217. [CrossRef]
55. McKay, G.; Blair, H.S.; Gardner, J.R. Adsorption of Dyes on Chitin. I. Equilibrium Studies. *J. Appl. Polym. Sci.* **1982**, *27*, 3043–3057. [CrossRef]
56. Kadirvelu, K.; Namasivayam, C. Agricultural By-Product as Metal Adsorbent: Sorption of Lead(II) from Aqueous Solution onto Coirpith Carbon. *Environ. Technol.* **2000**, *21*, 1091–1097. [CrossRef]

57. Sivakumar, P.; Palanisamy, P.N. Adsorption Studies of Basic Red 29 by a Non-Conventional Activated Carbon Prepared from *Euphorbia Antiquorum* L. *Int. J. ChemTech Res.* **2009**, *1*, 502–510.
58. Ndiaye, B.; Bustos, G.; Calvar, S.; Vecino, X.; Cruz, J.M.; Moldes, A.B.; Pérez-Cid, B. Selective Adsorption Capacity of Grape Marc Hydrogel for Adsorption of Binary Mixtures of Dyes. *Water. Air. Soil Pollut.* **2020**, *231*. [CrossRef]
59. Evangelista, R.L.; Nikolov, Z.L. Recovery and Purification of Lactic Acid from Fermentation Broth by Adsorption. *Appl. Biochem. Biotechnol. Part A Enzym. Eng. Biotechnol.* **1996**, *57–58*, 471–480. [CrossRef]

Article

Improvement of Phosphate Adsorption Kinetics onto Ferric Hydroxide by Size Reduction

Vicenç Martí ^{1,2,*} , Irene Jubany ², David Ribas ², José Antonio Benito ³ and Berta Ferrer ¹

¹ Barcelona Research Center in Multiscale Science and Engineering (EEBE), Department of Chemical Engineering, Technical University of Catalonia (UPC), Av. Eduard Maristany 16, 08019 Barcelona, Spain; bferrerorra@gmail.com

² Eurecat, Centre Tecnològic de Catalunya, Sustainability Area, Plaça de la Ciència 2, 08243 Manresa, Spain; irene.jubany@eurecat.org (I.J.), davidrrff@gmail.com (D.R.)

³ Department of Materials Science and Metallurgical (EEBE), Technical University of Catalonia (UPC), Av. Eduard Maristany 16, 08019 Barcelona, Spain; jose.a.benito@upc.edu

* Correspondence: vicens.marti@upc.edu; Tel.: +34-93-401-0957

Abstract: Ball milling and ultra-sonication size reduction procedures were applied to granular ferric hydroxide (GFH) to obtain two micro-sized adsorbents. These two adsorbents and GFH were investigated to improve the removal of phosphates from water. The size reduction procedures, using the milling method, allowed a reduction of size from 0.5–2 mm to 0.1–2 μm and total disaggregation of the GFH structure. Using an ultra-sonication method yielded a final size of 1.9–50.3 μm with partial disaggregation. The Langmuir model correlated well with the isotherms obtained in batch equilibrium tests for the three adsorbents. The maximum adsorption capacity (q_{max}) for the milled adsorbent was lower than GFH, but using ultra-sonication was not different from GFH. The equilibrium adsorption of two wastewater samples with phosphate and other anions onto the GFH corresponded well with the expected removal, showing that potential interferences in the isotherms were not important. Batch kinetics tests indicated that the pseudo second-order model fitted the data. Long-term adsorption capacity in kinetics (q_e) showed the same trend described for q_{max} . The application of milling and ultra-sonication methods showed 3.5- and 5.6-fold increases of the kinetic constant (k_2) versus the GFH value, respectively. These results showed that ultra-sonication is a very good procedure to increase the adsorption rate of phosphate, maintaining q_e and increasing k_2 .

Keywords: adsorption technology; ultra-sonication; phosphate removal; granular ferric hydroxide; micro-sized adsorbents

Citation: Martí, V.; Jubany, I.; Ribas, D.; Benito, J.A.; Ferrer, B.

Improvement of Phosphate Adsorption Kinetics onto Ferric Hydroxide by Size Reduction. *Water* **2021**, *13*, 1558. <https://doi.org/10.3390/w13111558>

Academic Editor: Cidália Botelho

Received: 10 May 2021

Accepted: 29 May 2021

Published: 31 May 2021

Publisher's Note: MDPI stays neutral with regard to jurisdictional claims in published maps and institutional affiliations.



Copyright: © 2021 by the authors. Licensee MDPI, Basel, Switzerland. This article is an open access article distributed under the terms and conditions of the Creative Commons Attribution (CC BY) license (<https://creativecommons.org/licenses/by/4.0/>).

1. Introduction

Several Circular Economy approaches applied to the adsorption of phosphate have been considered in the literature. These alternatives include the recovery of phosphorus and water from several wastewater streams [1–4], the use of low-cost products or recovered waste as sorbents [5–11], and the study of the re-use of phosphate-loaded sorbents [2,3,11–13]. To develop these strategies, it is paramount to optimize the performance of the sorption process.

Commercial granular ferric hydroxide (GFH) is formed by porous solids that have demonstrated a very good sorbent capacity for the recovery of phosphates from water in batch systems [1,12,14–17]. The adsorption of phosphates from aqueous solutions and wastewaters onto the GFH is usually performed in fixed-bed type contactors [18]. This system is easily operated, but multiple references show early breakthrough curves of phosphate in fixed-bed column assays [14,19,20]. This behavior is linked with sorbent capacities lower than in batch tests and is attributed to kinetic mass-transfer limitations [11,14,21]. Several ferric hydroxide sizes below the usual GFH size range (1 mm) have been used as promising materials to increase the kinetics and adsorption capacity of phosphate

in stirred batch tests, as it happens, for instance, in the case of activated carbon with micro-contaminants [22,23]. The procedures involved for size reduction of the adsorbent include sieving of GFH [24], grinding [1,17], or the synthesis and use of nano-sized materials [19,24–26]. From these references, only one study was centered in the role of reduced size particles obtained from the same bulk GFH on the adsorption of phosphate (equilibrium and kinetics) [17]. This specific study showed that all adsorbents exhibit similar adsorption capacities at equilibrium and that a reduction of sizes increased the kinetic constant of the initial sorbents up to 100-fold.

Top-down methods such as high energy ball milling are very effective alternatives that have been used for size reduction other water treatment materials such as nano-zero valent iron [27,28] and calcite [29]. Ultra-sonication is another top-down size reduction method able to produce microparticles and nanoparticles directly from some soft bulk material as hematitic/goethitic iron ore fines [30], talc [31], or TiO₂ [32]. Milling and ultra-sonication methods have the advantage that the chemistry of the particles will not be altered, hence bulk and particle adsorbents could be more directly comparable.

Within this context, the aim of this work is two-fold: (i) size reduction of one low-cost commercial GFH, using ball-milling and ultra-sonication, as a new method, to obtain low-size adsorbents; and (ii) the comparison of these materials of different sizes in terms of phosphate adsorption capacity and kinetic behaviour at the laboratory scale. Within this context, this study aims to understand the effects of size reduction on the improvement of sorption capacity and/or kinetics.

2. Materials and Methods

2.1. Adsorbent Preparation

The commercial GFH adsorbent used was Ferrosorp GW[®] (HeGo Biotec GmbH, Giessen, Germany) with sizes in the range of 0.5–2 mm. This kind of adsorbent mainly consists of Fe(OH)₃ and is obtained from an industrial low-cost product [12].

Two methods were used for the size reduction of the GFH solid.

The first method involved a two-step milling process, in which the first step consisted of dry milling, using a hammer mill (MF 10 basic microfine grinder drive, IKA-Werke GmbH, Staufen Germany) at 6000 rpm. Then, 250 g of the GFH sample was passed through this mill three times and sieved at 100 µm. In the second milling step, 6 g of this pre-milled sample was placed in a 250 mL carbon steel vial, alongside 200 g of S110 spherical high-carbon steel shots (Pometon S.p. A, Italy) and 150 mL of DI water. The material was milled at 250 rpm for 5 h using a Planetary ball mill (Fritsch GmbH, P-5, Mahlen und Messen, Germany). After milling, the slurry was separated from the steel grinding balls using a 75 µm sieve. The retained material was washed several times with DI water over the recovered slurry until reaching a final volume of 500 mL. The slurry was dried overnight in an oven at 100 °C (J.P. Selecta, Digiheat, Abrera, Spain) and the dry solid was disaggregated using an agate mortar. This milled solid is referred to as OF-M in the present work.

The second method used for the size reduction was disaggregation by ultrasonic waves. For this purpose, around 5 g of solid GFH was mixed with DI water in a 250–500 mL volumetric flask and sonicated for 5 min at 20 kHz in a lab ultrasonic cleaner (ATU Ultrasonidos, ATM40-2L-CD, Paterna, Spain). The suspension was centrifuged at 4000 rpm for 5 min to remove supernatant water. The solid was dried and disaggregated like in the milling method (see above). The dry particles obtained from this ultrasonic-based protocol are referred to as OF-U.

2.2. Characterization of Adsorbents

The content of total iron and calcium in the GFH sample was determined by sieving the dried solid below 40 µm and sampling 50 mg for acid digestion using HCl 30% Suprapure[®] (Supelco, Germany). After filtering the digested solid with a 0.45 µm filter, the total iron and calcium contents were obtained using an AAS instrument (Analytik Jena GmbH, contraAA 800, Jena, Germany).

The general morphology and individual particle size were studied by scanning electron microscopy (SEM) (Zeiss, Gemini ultra plus, Jena, Germany) equipped with energy-dispersive X-ray spectroscopy (EDS) (Oxford Instruments, X-MAX 50 mm², Abingdon, UK). Sample preparation involved two steps: (I) deposition and room evaporation over aluminium pins, and (II) sample metallization with Au-Pd 30 s at 18 mA (Quorum, Emitech SC7620 mini sputter, Laughton, UK).

The suspensions' granulometry was analysed using laser diffraction spectrometry for the OF-M samples (Beckman Coulter, LS 13320, Brea, CA, USA) and with a Malvern Panalytical Mastersizer 3000 (Malvern Panalytical Ltd., UK) for the OF-U samples in DI water.

The nitrogen Brunauer–Emmett–Teller (BET) specific surface area (SSA) was measured (Micromeritics ASAP 2020, Aachen, Germany). Degassing was carried out for several hours at a maximum temperature of 100 °C. Sample preparation for this analysis involved drying 1 g of the slurry. It was performed at 60 °C in a biological incubator (Raypa, Incuterm Digit, Terrassa, Spain) for 72 h. Thereafter, a dried cake was obtained, which was crushed to a fine powder using a manual agate mortar. The above-mentioned drying procedure was performed in a negative pressure lab cabinet to avoid exposure to nanopowder.

The zeta potential of 1 g/L suspensions of OF-M and OF-U was measured using 0.01 M analytical grade NaCl (Panreac, Spain) at equilibrium pH and dynamic light scattering detection (Brookhaven Instruments, NanoBrook Zeta Pals; Holtsville, NY, USA).

The pH of the point of zero charge (PZC) of GFH was evaluated via the immersion technique [33] using 25 g/L suspensions with an initial pH adjusted in the range of 3–12 with analytical grade hydrochloric acid (HCl) or sodium hydroxide (NaOH) (Panreac, Spain), as measured with a pH-meter (Crison, GLP 22, Alella, Spain).

2.3. Batch Adsorption Procedure

Phosphate test solutions were prepared by weighing K₂HPO₄ analytical grade (Scharlau, Spain). The dissolutions and dilutions were performed using deionized (DI) water (Merck-Millipore, Elix 70, Darmstadt, Germany). The pH was adjusted to 8.0 using HCl. This initial value of pH was chosen as a compromise between the buffer capacity of phosphate and the observed equilibrium pH. In this way, the theoretical predominant speciation of phosphate in all the synthetic samples was HPO₄²⁻. Phosphate equilibrium adsorption with GFH was also tested in two types of treated wastewater. The first wastewater (MR-1) was generated during the cleaning operation with phosphate products in a pig slaughterhouse and the treatment of water applied consisted of coarse and fine screening, homogenization, flotation, and nitrification-denitrification biological treatment. The second wastewater (MR-2) was obtained from a truck cover manufacturing textile company in which phosphate was associated with manufacturing process and cleaning operations. Treatment for MR-2 included physicochemical treatment, secondary biological treatment, and tertiary treatment with activated carbon.

Equilibrium and kinetic batch tests were performed by placing 50 mL of the phosphate dissolutions in Falcon tubes with different weighted amounts (Sartorius AG, Praxum 513-S, Göttingen, Germany) of each adsorbent at room temperature. Then, stirring at 8 rpm (Heidolph GmbH, REAX 20, Schwabach, Germany) was performed under dark conditions. After stirring the mixtures, the suspensions were centrifuged (J.P. Selecta, Centronic-BLT, Abrera, Spain) at 4000 rpm for 5 min. The supernatant solution was filtered with a regenerated cellulose (RC) 0.2 µm filter and analyzed using ion chromatography (Dionex, ICS 2100, Sunny Valley, OR, USA) with a 4 × 250 mm Ion Pac AS19 Column. The analysis method used 1 mL/minute of the generated KOH mobile phase with a gradient of 10–35 mM. The quantitation limit of the method was 0.5 mg PO₄³⁻/L. All masses of phosphate in the present work are expressed as mg PO₄³⁻.

The adsorption of phosphate onto the materials was calculated from the following mass balance equation:

$$q = \frac{(C_0 - C) \cdot V}{m} \quad (1)$$

where q is the amount of phosphate adsorbed onto the solid at time t (mg/g); C_0 and C are the phosphate concentrations at time zero and at time t (mg/L), respectively; V is the volume of dissolution in the batch experiment (L); and m is the mass of the solid adsorbent in the experiment (g).

The removal of phosphate, η (mass %), is given in Equation (2) and can also be expressed in terms of batch experiment conditions using Equation (1):

$$\eta = \frac{100 \cdot (C_0 - C)}{C_0} = \frac{100 \cdot m \cdot q}{V \cdot C_0} \quad (2)$$

Equilibrium batch tests were performed using replicate experiments of phosphate dissolutions (10, 20, 33, 50, 90, and 150 mg/L) with different weighed amounts of the three adsorbents (1, 2, and 3 g/L) for 120 h. The wastewater samples were filtered with a 0.45 μm nylon filter before the equilibrium experiment, which was performed with 2 and 3 g/L of GFH for 120 h and analyzed by ion chromatography, as mentioned before. Chloride, nitrate, and sulfate concentrations were also determined to check potential competition of these frequent anions with phosphates.

Freundlich (Equation (3)) and Langmuir (Equation (4)) isotherms were used to fit experimental equilibrium data C_e and q_e (obtained from the corresponding equilibrium using Equation (1)). These models have been originally applied in the literature [34,35].

$$q_e = K_F \cdot C_e^{1/n} \quad (3)$$

$$q_e = q_{\max} \cdot \frac{C_e \cdot b}{1 + b \cdot C_e} \quad (4)$$

where K_F ($\text{mg}^{1-1/n} \cdot (\text{L})^{1/n} / \text{g}$) and n are the constants of the Freundlich model that can be obtained by fitting $\log C_e$ versus $\log q_e$. In the Langmuir isotherm, q_{\max} is the maximum adsorption capacity (mg/g) and b is the binding constant (L/mg). Both parameters can be obtained by rearranging Equation (4):

$$\frac{C_e}{q_e} = \frac{1}{q_{\max} \cdot b} + \frac{C_e}{q_{\max}} \quad (5)$$

The theoretical calculation of phosphate removal was performed from the equilibrium concentration of GFH isotherm using Equations (1), (2), and (4), coded into a Microsoft Excel™ spreadsheet.

The kinetic behaviour of the three adsorbents was determined through duplicate kinetic batch tests with 2 g/L of the materials and 30 mg/L phosphate, which that is the minimum expected concentration in the wastewater to be analyzed. Test tubes were extracted after 1, 2, 3, 4, 5, 6, 22, 24, 27, 48, 52, 72, 75, 96, 144, and 168 h of contact time.

Pseudo first- (Equation (6)) and pseudo second-order (Equation (7)) models were employed to identify batch kinetics:

$$q = q_e \cdot (1 - \exp(-k_1 \cdot t)) \quad (6)$$

$$q = \frac{k_2 \cdot q_e^2 \cdot t}{1 + k_2 \cdot q_e \cdot t} \quad (7)$$

where k_1 is the first-order kinetic constant (h^{-1}) and k_2 is the second-order kinetic constant (g/mgh).

The corresponding linear forms of pseudo first- and pseudo second-order are as follows, respectively:

$$\text{Ln}(q_e - q) = \text{Ln}(q_e) - k_1 \cdot t \quad (8)$$

$$\frac{t}{q} = \frac{1}{k_2 \cdot q_e^2} + \frac{t}{q_e} \quad (9)$$

Pseudo second-order kinetics model (Equation (7)) could be linearized up to five different linear forms [36]. Regression using the linear form given in Equation (9) is the most used for phosphate kinetic studies [7–10,15]. This linear form could predict q_e very well, but several references [36–38] indicate that this linearization could be inappropriate to obtain a good value of k_2 and the initial adsorption rate value ($k_2 \cdot q_e^2$). In order to investigate this question, non-linear models using Equation (7) were applied [39]. The methodology used for non-linear regression consisted of the direct fitting of n data pairs (t_i, q_i) to Equation (7) using the values of q_e and k_2 that minimize the sum of squared errors, SS_{err} .

$$SS_{err} = \sum_{i=1}^n [q_i - q]^2 \quad (10)$$

The Solver function in Microsoft Excel™ software with the GRG Nonlinear solving method was used to minimize SS_{err} as the objective function to obtain the fitted q_e and k_2 . The q_e and k_2 results obtained in the linear model were used as a starting point for iteration.

2.4. Statistical Analysis

Two statistical methods were used to compare the fitting slopes parameters (m) used in linear models (Equations (5) and (9)) in order to investigate the effects of size reduction on q_{max} and q_e .

The first method was to obtain the 95% confidence interval (CI) for m , CI_m , which is given by the following:

$$CI_m = m \pm t_{(0.025, n-2)} \cdot s_e \quad (11)$$

where $t_{(0.025, n-2)}$ is the two-tailed Student's t -test value for a significance level of $\alpha = 0.05$ and $n - 2$ degrees of freedom (n is the number of fitting points), and s_e the standard error for the slope m . The extremes of this interval are the lower and the upper confidence levels (LCL and UCL, respectively). The comparison of these CI_m allows detecting the absence of overlap between the adsorbents, and thus confirming the difference between the slope fitting parameters (m).

The second method used was the comparison of the slope parameters of two experiments incorporating a dichotomous (dummy) independent variable, D , [40–43]. This D variable allows the combination of two sets of experimental data that correspond to the two categories (e.g., comparison of kinetics from GFH and OF-U adsorbents using Expression (9)), extending the linear model to a multilinear model in the following form:

$$Y_i = b_0 + b_1 \cdot X_i + b_2 \cdot D_i + b_3 \cdot D_i \cdot X_i + \text{error} \quad (12)$$

where Y_i and X_i are the linearized data values of the two sets of data (e.g., t_i/q_i and t_i for GFH and OF-U kinetics). The variable D_i takes the value of zero for the data points of the set of reference (e.g., GFH adsorbent) and the value of 1 for the other set of data points (e.g., OF-U).

Testing the statistical significance of b_3 parameter in this model, it is possible to know if the slopes of the two sets are equal. In the case where the CI of b_3 contains the zero, the hypothesis that the slopes of the two sets are equal cannot be rejected.

In both methods, the fitting calculations and statistical values were obtained using the LINEST function in Microsoft Excel™ software.

3. Results and Discussion

3.1. Characterization of Adsorbents

The total iron and calcium contents measured in dry GFH were 37.1% (weight to weight) and 6.3%, respectively. These values correspond to 71.0% $Fe(OH)_3$ and 15.6% $CaCO_3$, respectively. The sorbents used in the present paper are said to be formed by $Fe(OH)_3$ and calcite [12]. Therefore, these two compounds would explain more than 85% of the composition of the GFH.

SEM microphotographs of GFH show different superficial structures: big boulders in blue, flake crystal clusters in red, and intricate globular aggregates resembling broccoli in

green (Figure 1b). The structures of the granulated material are lost in the milled material with a size of approximately 100 nm (yellow circles in Figure 1c). Parent material structures are still maintained in the case of ultra-sonication, with sizes of a few microns (Figure 1d).

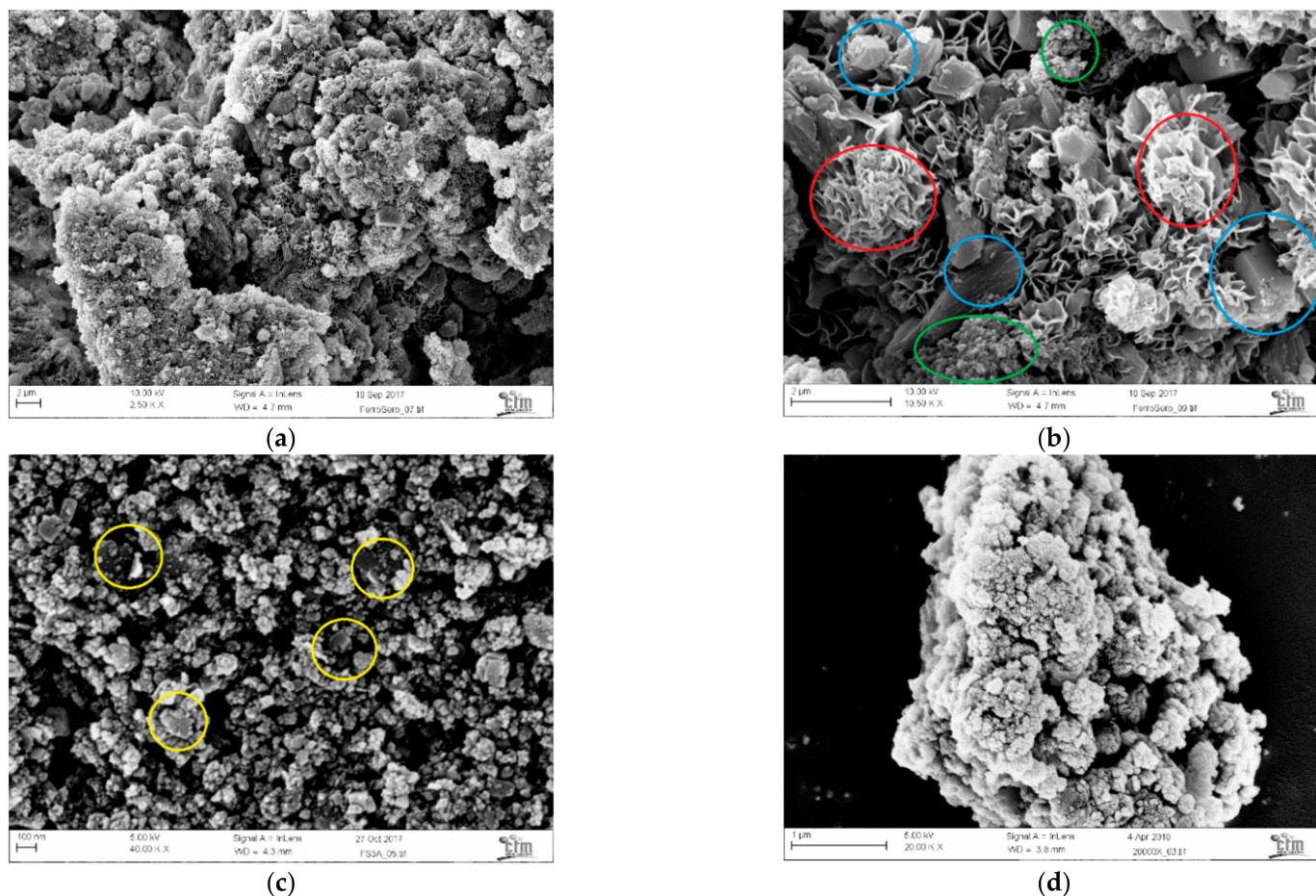


Figure 1. Scanning electron microscopy (SEM) microphotographs (a,b) granular ferric hydroxide (GFH), (c) OF-M (milled), and (d) OF-U (ultra-sonicated). See main text for explanation of coloured circles.

A summary of the other properties of the materials is shown in Table 1. More detail on the granulometry and BET measurements can be found in the Supplementary Materials (SM).

Table 1. Size, Brunauer–Emmett–Teller (BET) area, and zeta potential at equilibrium pH. GFH, granular ferric hydroxide.

	GFH	OF-M	OF-U
Size ¹ (μm)	500–2000 ²	0.1–2	1.9–50.3
BET Surface Area (m ² /g)	199.7	98.4	160.2
t-plot Micropore Area (m ² /g)	20.9	0	4.3
Zeta Potential ³ (mV)	−8.4 ± 2.8	−9.5 ± 1.0	−8.4 ± 1.9
Equilibrium pH	8.59	9.41	9.43

¹ Range p10 to p90 in volume, ² manufacturer information, ³ average ± standard deviation.

Size measurements of the OF-M and OF-U in suspension (Figure S1a,b in Supplementary Materials) using DLS (giving the size range between the 10th and 90th percentiles) showed that the milling system worked better for size reduction than the sonication system.

These DLS-based results were confirmed with SEM, although DLS showed possible agglomerations around 2 μm in the OF-M suspensions that were not found using SEM (Figure 1c).

The GFH BET surface area was within the same range as found in the literature (120–300 m^2/g) [1,14,15,17,18,44,45]. Comparing the three materials shows the destruction of the BET surface area with size reduction, including an important loss of micropore area, which is 100% in the case of the milled material. The adsorption isotherms of the three materials (Figure S2a–c, in Supplementary Materials) have a similar shape with an important hysteresis and sudden increase of adsorption at high pressures, indicating the presence of a significant amount of mesopores. These results are consistent with the SEM morphology (Figure 1) and indicate that, although milled particles (OF-U) were smaller, the change in surface area is linked to the loss of internal surface and not to an increase in surface area due to size [46].

The zeta potentials at equilibrium pH were very low and similar for all three materials, indicating a slight positive charge of the solid surface, matching the low stability of the suspension (easy sedimentation).

A plot of the change in pH (ΔpH) versus the initial pH for the PZC calculation of the GFH sample shows a very good linear relationship (Supplementary Materials, Figure S3).

pH_{PZC} , i.e., the pH that showed no variation of pH ($\Delta\text{pH} = 0$), was equal to 8.43. While these values are slightly higher than those reported for akaganeite, which fall within the range of 7.5–8 [14], pH_{PZC} in the GFH sample was very close to equilibrium for zeta potential measurement (see Table 1).

3.2. Effect of Particle Size on Adsorption Isotherm

While both the Langmuir and Freundlich models were able to produce acceptable fits to the data from all three adsorbents, the Langmuir model yielded a better overall fit (higher coefficient of determination, R^2) (Table 2 and Figure S4a,b in Supplementary Materials).

Table 2. Fitting parameters for the Freundlich and Langmuir models.

		GFH	OF-M	OF-U
Freundlich model				
R^2		0.8847	0.9554	0.9263
K_F	$(\text{mg}^{1-1/n} \cdot (\text{L})^{1/n} / \text{g})$	11.59	9.70	12.78
n	(-)	4.00	4.30	5.28
Langmuir model				
R^2		0.9481	0.9731	0.9358
q_{max}	(mg/g)	41.80	31.59	36.43
b	(L/mg)	0.1006	0.1051	0.0871

Taking the Langmuir model, Figure 2 shows the fitted isotherms for the adsorption data with the three tested adsorbents.

The fit of Figure 2 exhibits a possible loss of adsorption in q_{max} for the reduced materials. Figure S4,b also shows different slopes ($1/q_{\text{max}}$). The comparison of q_{max} for the three adsorbents could be performed by the two mentioned statistical analyses and is presented in Table 3.

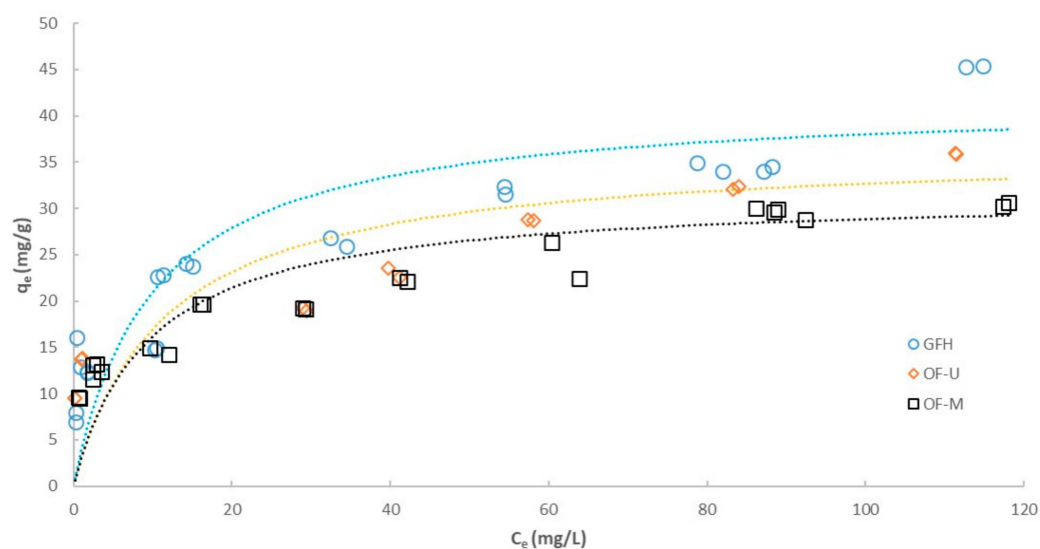


Figure 2. Fitted isotherms for the three tested adsorbents using the Langmuir model (dotted lines, see Table 2).

Table 3. 95% confidence interval (CI) for $1/q_{\max}$ and b_3 fitting parameters in the Langmuir model.

		GFH	OF-M	OF-U
Langmuir model CI				
Slope ($1/q_{\max}$)	(g/mg)	0.023925	0.031652	0.027449
Standard error	(g/mg)	0.001251	0.001177	0.002076
d.f. ¹	-	20	20	12
t-Student _{0.025}	-	2086	2086	2179
$1/q_{\max}$ UCL	(g/mg)	0.026536	0.034107	0.031971
$1/q_{\max}$ LCL	(g/mg)	0.021315	0.029196	0.022926
Dichotomous model comparison with GFH				
b_3 UCL ²	-	-	0.011198	-0.001109
b_3 LCL ²	-	-	0.004255	0.008156

¹ degrees of freedom ² See Supplementary Materials Table S1.

The first method is applied studying the slope of the linear fit, i.e., $1/q_{\max}$ and its associated CI (from Equation (10)) for the three adsorbents. Clearly, the resulting $1/q_{\max}$ UCL and $1/q_{\max}$ LCL differ for OF-M and GFH data because their CIs do not overlap. In the case of OF-U and GFH, there is an overlap of CIs. The second method uses the statistical analysis of the CI for b_3 using the dichotomous model (see also Table S1); it could be seen that the comparison of GFH and OF-M slopes showed significant differences, while the comparison of GFH and OF-U slopes resulted in not significant differences in $1/q_{\max}$ values. Consequently, the two statistical methods showed that there is a loss of maximum adsorption capacity in the milled solid (OF-M) compared with the GFH adsorbent. This may be partially owing to the loss of specific surface in the OF-M adsorbent because q_{\max} in OF-M decreases by around 24% and the loss in surface area is 50%, both with respect to GFH (see Table 1). This loss of adsorption capacity for phosphates using iron hydroxide could be related to the lower specific surface area, but this point is difficult to support for different origins of the adsorbents [24].

In the case of OF-U, $1/q_{\max}$ is statistically identical to the value obtained for GFH, despite a 20% loss in surface area. This result is supported by the fact that Ferrosorp adsorbent below 100 μm has already shown that the adsorption capacity for phosphates is maintained [17].

The values of q_{\max} in Table 2 are better than the typical values for other by-products and wastes such as brick waste [8], copper smelter slag [9], or carbon waste [10] that usually range from 0.04 to 5.35 mg PO_4^{3-} /g.

Red mud and commercial akaganeite [15,47], as well as commercial GFH [17,44], exhibit a similar range (26.8 to 39.6 mg PO_4^{3-} /g) as shown by the result of this study. Other studies using materials such as impregnated skin split waste [5], hybrid fibres [19], and synthetic materials [26] showed results within the range 66.4 to 220.8 mg PO_4^{3-} /g. Akaganeite also showed better results (51.8 to 71.5 mg PO_4^{3-} /g) in similar studies [1,24].

3.3. Removal of Phosphate from Wastewater

The initial phosphate concentration and GFH dosage for the two types of wastewater (MR-1 and MR-2) are shown in Table 4 (Initial Conditions). The initial phosphate concentrations strongly affect the theoretical (fitted) and experimental results for the two types of wastewater (MR-1 and MR-2).

Table 4. Adsorption results for wastewater using GFH for different initial phosphate concentrations, C_0 , and GFH doses.

Sample	Initial Conditions		Fitted Values ¹			Experimental Values ²		
	C_0 (mg/L)	m/V (g/L)	q_e (mg/g)	C_e (mg/L)	η (%)	q_e (mg/g)	C_e (mg/L)	η (%)
MR-1	3.1	2	1.38	0.34	89.1	>1.28	<0.5	>83.9
MR-1	3.1	3	0.96	0.23	92.5	>0.87	<0.5	>83.9
MR-2	41.6	2	17.3	6.98	83.2	17.8	5.55	86.6
MR-2	41.6	3	12.5	4.20	89.9	12.8	2.85	93.1

¹ Use of isotherm and mass balance for GFH and synthetic samples (see Figure S5); ² average of two values.

Despite the final phosphate concentration for MR-1 remains uncertain due to limitations of the chromatographic method, the experimental q_e and C_e values for the two samples are very close to the theoretical values calculated from the GFH isotherm (see Figure S5). Table S2 shows the initial ($t = 0$ h) and the equilibrium concentration ($t = 120$ h) of chlorides, nitrates, and sulfates for the same two samples of wastewater. As could be seen in Table S2, after 120 h of contact, the concentrations of chloride and nitrate remained constant and the concentration of sulfate increased with the dosage of GFH, which is linked to a leaching effect from GFH.

As the fit of the model (obtained with aqueous samples) to wastewater concentrations is very good and the main anions did not decrease with contact time, the potential interferences for adsorption isotherms can be neglected, and this adsorbent could be used for a similar kind of wastewater as those used in the study. The low effect of chloride, nitrate, and sulfate interferences has been reported with multicomponent samples in column experiments [1,19] and batch isotherms [48].

3.4. Effect of Particle Size on Kinetics

The adsorption kinetics for the three different materials are shown in Table 5 using the data points from Figure S6a,b. When comparing the pseudo first- and pseudo second-order fits (Equations (8) and (9)), the latter yielded a better correlation and less fitting error. Figure 3 shows the fitted kinetics for the three adsorbents using the pseudo second-order linear model (Equation (9) and Table 5). A detailed graphic of the same fitting in the first 6 h is also shown in the same figure.

Again, the fit of Figure 3 (asymptotic values) and Figure S6b (slopes) yielded a reasonable difference in q_e for milled adsorbents versus FGH and OF-U.

Table 6 lists the fitting parameters to perform the comparison of $1/q_e$ with the two statistical methods. The corresponding CIs for the three adsorbents show that the $1/q_e$ values for the OF-M kinetics fit differ from the slopes of the GFH and OF-U fits. The application of the dichotomous model (Table 5 and Table S3) shows a significant difference

in $1/q_e$ when GFH and OF-M were compared and no significant difference between GFH and OF-U.

Table 5. Fitting parameters for the pseudo first- and pseudo second-order adsorption kinetics models.

		GFH	OF-M	OF-U
Pseudo first-order (linear)				
R^2		0.6637	0.8764	0.7313
k_1	(h^{-1})	0.0189	0.0237	0.0260
$\ln(q_e)$	($\ln(\text{mg/g})$)	1.796	1.302	0.796
Initial rate ¹	($\text{mg/g}\cdot\text{h}$)	0.27	0.31	0.36
SS_{err} ¹		1055	931.1	1397
Pseudo second-order (linear)				
R^2		0.9915	0.9989	0.9997
q_e	(mg/g)	14.28	13.02	13.96
k_2	($\text{g/mg}\cdot\text{h}$)	0.0146	0.0322	0.0660
Initial rate ¹	($\text{mg/g}\cdot\text{h}$)	2.98	5.45	12.86
SS_{err} ¹		85.17	58.33	28.29
Pseudo second-order (non-linear)				
q_e	(mg/g)	13.66	12.21	13.52
k_2	($\text{g/mg}\cdot\text{h}$)	0.0257	0.0911	0.1437
Initial rate ¹	($\text{mg/g}\cdot\text{h}$)	4.80	13.58	26.27
SS_{err} ¹		53.34	11.47	5.88

¹ Calculated from the direct fitting of data to kinetic model with q_e and k_1 or k_2 .

Again, these results indicate a loss of adsorption capacity of OF-M compared with GFH and OF-U and the difference between the GFH and OF-U results is non-significant. The pattern for q_e is consistent with those for q_{max} . As a result, the GFH and OF-U isotherms can be considered similar, while OF-M differs when the equilibrium values are being considered.

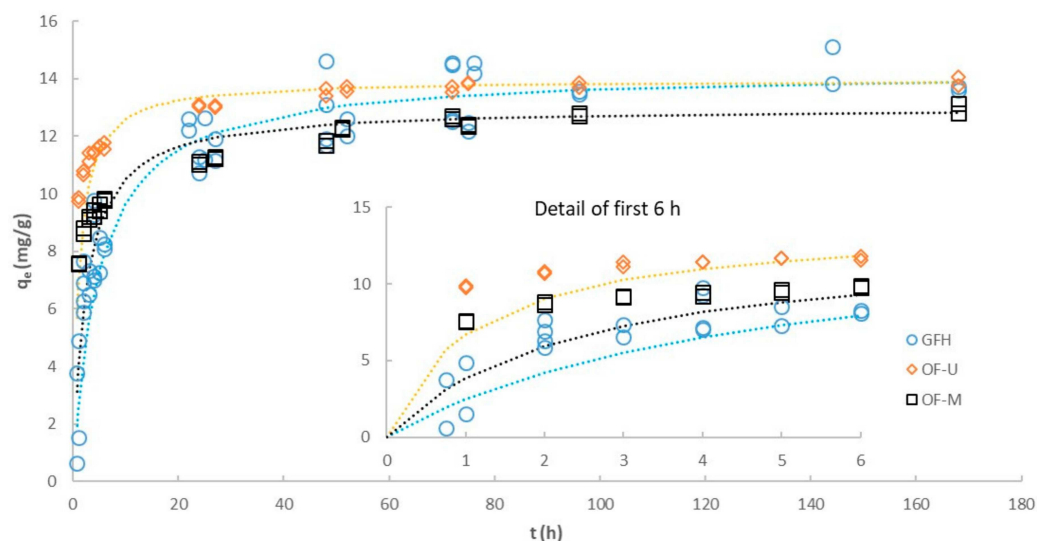


Figure 3. Adsorption kinetics for the three tested adsorbents with pseudo second-order fitted linear model (dotted lines, see Table 5).

Table 6. 95% confidence interval (CI) for $1/q_e$ and b_3 linear fitting parameters in second-order kinetics.

		GFH	OF-M	OF-U
Linear second-order model CI				
Slope ($1/q_e$)	(g/mg)	0.070023	0.076830	0.071627
Standard error	(g/mg)	0.00979	0.000492	0.000227
d.f. ¹	-	44	26	26
t-Student _{0,025}	-	2.015	2.056	2.056
$1/q_e$ UCL	(g/mg)	0.071996	0.077841	0.072095
$1/q_e$ LCL	(g/mg)	0.068049	0.075818	0.071160
Dichotomous model comparison with GFH				
b_3 UCL ²	-	-	0.009413	0.004121
b_3 LCL ²	-	-	0.004200	-0.000911

¹ Degrees of freedom ²; see Supplementary Materials Table S3.

The detailed kinetic data values of Figure 3 (6 first hours) clearly point to the idea that kinetics is faster for reduced materials than for GFH. The fitting of these initial hours using the second-order linear model of Figure 3 is very poor and underestimates the values of k_2 and initial slope. In order to improve this fitting for a better calculation of kinetic parameters, a second-order non-linear model (Equation (7)) with the same data was used. Table 5 compares the values of q_e , k_2 , and initial rate ($k_2 q_e^2$) for linear and non-linear second-order cases. It could be seen that SS_{err} is reduced when applying the non-linear model; therefore, the non-linear results describe the kinetics much better. Figure 4 shows the new fitting of kinetics to the same data shown in Figure 3, but with non-linear parameters with a visible improvement of the first 6 h.

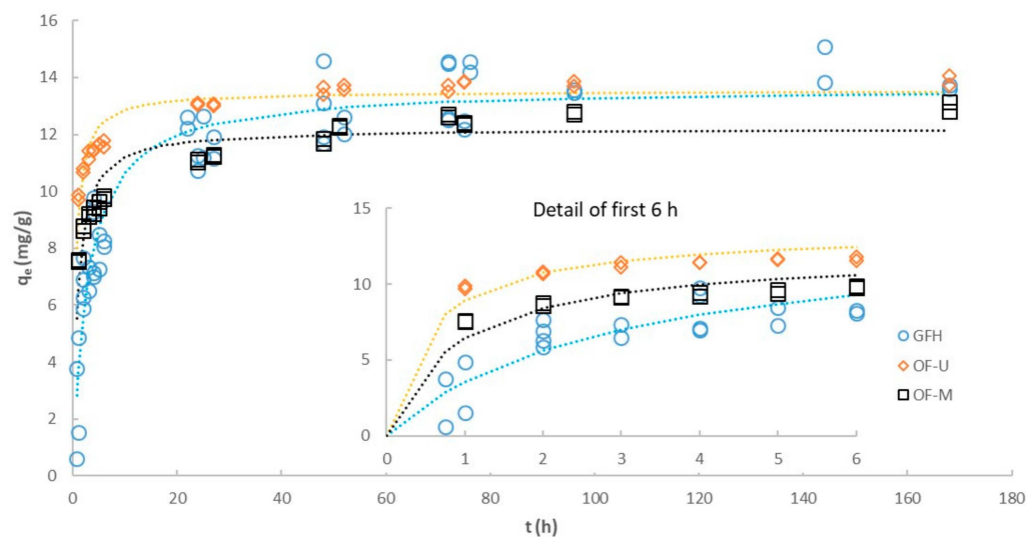


Figure 4. Adsorption kinetics for the three tested adsorbents with pseudo second-order fitted non-linear model (dotted lines, see Table 5).

Taking the linear values of k_2 and initial rate as a reference, it could be seen that k_2 and initial rate are underestimated by a factor of 2–3 times. Despite this difference, the results of Table 5 clearly indicate that q_e values are similar for linear and non-linear models. The calculated value of q_e from GFH Langmuir isotherm fitted values (Table 2 and Figure S5) applied to Equations (1) and (4) was 12.8 mg/g, which is closer to non-linear fitting q_e . For all these reasons, fitting values of non-linear kinetic model were chosen for discussion.

For small-sized adsorbents, the adsorption rate in the first few hours is higher compared with granular adsorbents (Figure 4). The values of k_2 of OF-M compared with GFH increased 3.5 times and the values of k_2 of OF-U compared with GFH increased 5.6 times.

Comparing the initial slope, the values of OF-M compared with GFH increased 2.8 times and the values of OF-U compared with GFH increased 5.5 times. As a final remark, the experimental results indicate that the solid OF-U performed better because the isotherm was similar to GFH and k_2 could be increased 5.6 times to reach the equilibrium value (q_e) in less time.

This trend linking size reduction and increment of kinetic rate was observed in three different GFH materials [17]. The key point highlighted in this reference was the importance of higher fraction of mesopores bigger than 10 nm for the enhancement of adsorption kinetics.

4. Conclusions

The present study investigated the potential of size reduction of a low-cost granular adsorbent using milling and ultra-sonication on the batch-scale adsorption of phosphate. While the milling procedure was more effective for size reduction, the total elimination of the initial GFH structure led to a notable decrease in the specific surface area and q_{\max} and q_e . Size-reduction using ultra-sonication partially eliminated the initial GFH structure and part of its specific surface area, but q_{\max} and q_e remained similar to the GFH. The effect in milled adsorbent could be linked to the high loss of specific surface area (50%) and, specifically, to the 100% loss of micropore area measured. The micropore area has been pointed to as an important contributor for phosphate adsorption in Ferrosorp material [17]. The use of ultra-sonication is linked to moderate size reduction and partial disaggregation, keeping part of the micropore area. Ferrosorp has shown, in other references [17], that the adsorption capacity of FGH is maintained after a moderate grinding process.

For the two size-reduced adsorbents, an important increase of the initial rate and k_2 was observed when compared with the GFH. This effect has also been reported for phosphates using Ferrosorp, and it is linked to the limitation of small pores' diffusion (below 10 nm) in the case of granular sorbents [17]. Kinetic mechanisms in granular adsorbents take place along the different transfer zones and include bulk fluid transport, film transport and intra-particle diffusion (or intra-pore), and physical attachment [49]. In the case of phosphates, similar mechanisms occur and film transport and intra-pore diffusion are the rate limiting steps [14]. Size reduction procedures decrease the intra-pore effect and increase the overall kinetics, which is measured as a pseudo-second order law.

Owing to this increase in rate, q values from kinetics will approach q_e and the isotherm will play a relevant parameter in the removal of phosphate. In the case of wastewater, the potential presence of interferences during adsorption also plays an important role. Future investigations open the possibility of developing a new strategy that could be applied to improve low-cost GFH quality adsorbents and enable the re-use of GFH phosphate-loaded adsorbents after its size reduction.

Supplementary Materials: The following are available online at <https://www.mdpi.com/article/10.3390/w13111558/s1>, Figure S1: Size distribution (a) OF-M (milled), (b) OF-U (ultra-sonicated); Figure S2: BET curves (a) GFH, (b) OF-M (milled), (c) OF-U (ultra-sonicated); Figure S3: Regression fitting for the calculation of pH_{PZC} (GFH); Figure S4. Linear regression fittings for the equilibrium models (a) Freundlich model, (b) Langmuir model; Table S1. 95% significance test for b_3 in Langmuir fitting parameters (a) comparison of GFH ($D = 0$) and OF-M ($D = 1$), (b) comparison of GFH ($D = 0$) and OF-U ($D = 1$); Table S2. Adsorption of main anions in wastewater; Figure S5. Theoretical phosphate removal from Langmuir isotherms (GFH) as a function of initial phosphate concentration and adsorbent concentration (dosage); Figure S6. Linear regression fittings for the kinetic models (a) pseudo first-order model, (b) pseudo second-order model; Table S3. 95% significance test for b_3 in second-order fitting parameters, (a) comparison of GFH ($D = 0$) and OF-M ($D = 1$), (b) comparison of GFH ($D = 0$) and OF-U ($D = 1$).

Author Contributions: Conceptualization, V.M. and I.J.; methodology, V.M. and J.A.B.; investigation, D.R. and B.F.; resources, V.M. and I.J.; writing—original draft preparation, V.M.; writing—review and editing, V.M. and I.J. All authors have read and agreed to the published version of the manuscript.

Funding: This research was funded by the Spanish Ministry of Science, Innovation, and Universities and Agencia Estatal de Investigación/European Regional Development Plan (grant CGL2017-87216-C4-3-R). Researchers from Eurecat were financially supported by the Catalan government through the grant ACCIÓ-Eurecat (Project PRIV2019-MICONANO).

Institutional Review Board Statement: Not applicable.

Informed Consent Statement: Not applicable.

Data Availability Statement: The data presented in this study is available on request from the corresponding author.

Acknowledgments: Authors wish to thank HeGo Biotec GmbH for supplying Ferrosorp GW[®] samples and Neus Bahí from EURECAT for the analysis of the samples. Editorial assistance, in the form of language editing and correction, was provided by XpertScientific Editing and Consulting Services.

Conflicts of Interest: The authors declare no conflict of interest. The funders had no role in the design of the study; in the collection, analyses, or interpretation of data; in the writing of the manuscript; or in the decision to publish the results.

References

- Genz, A.; Kornmüller, A.; Jekel, M. Advanced phosphorus removal from membrane filtrates by adsorption on activated aluminium oxide and granulated ferric hydroxide. *Water Res.* **2004**, *38*, 3523–3530. [CrossRef] [PubMed]
- Kalaitzidou, K.; Mitrakas, M.; Raptopoulou, C.; Tolkou, A.; Palasantza, P.A.; Zouboulis, A. Pilot-Scale Phosphate Recovery from Secondary Wastewater Effluents. *Environ. Process.* **2016**, *3*, 5–22. [CrossRef]
- Yogev, U.; Vogler, M.; Nir, O.; Londong, J.; Gross, A. Phosphorous recovery from a novel recirculating aquaculture system followed by its sustainable reuse as a fertilizer. *Sci. Total Environ.* **2020**, *722*, 137949. [CrossRef] [PubMed]
- Hermassi, M.; Valderrama, C.; Moreno, N.; Font, O.; Querol, X.; Batis, N.; Cortina, J.L. Powdered Ca-activated zeolite for phosphate removal from treated waste-water. *J. Chem. Technol. Biotechnol.* **2016**, *91*, 1962–1971. [CrossRef]
- Huang, X.; Liao, X.; Shi, B. Adsorption removal of phosphate in industrial wastewater by using metal-loaded skin split waste. *J. Hazard. Mater.* **2009**, *166*, 1261–1265. [CrossRef]
- Ren, J.; Li, N.; Zhao, L.; Li, L. Pretreatment of Raw Biochar and Phosphate Removal Performance of Modified Granular Iron/Biochar. *Trans. Tianjin Univ.* **2017**, *23*, 340–350. [CrossRef]
- López, R.; Antelo, J.; Fiol, S.; Macías-García, F. Phosphate adsorption on an industrial residue and subsequent use as an amendment for phosphorous deficient soils. *J. Clean. Prod.* **2019**, *230*, 844–853. [CrossRef]
- Edet, U.A.; Ifelebuegu, A.O. Kinetics, isotherms, and thermodynamic modeling of the adsorption of phosphates from model wastewater using recycled brick waste. *Processes* **2020**, *8*, 665. [CrossRef]
- Letshwenyo, M.W.; Sima, T.V. Phosphorus removal from secondary wastewater effluent using copper smelter slag. *Heliyon* **2020**, *6*, e04134. [CrossRef]
- Mekonnen, D.T.; Alemayehu, E.; Lennartz, B. Removal of phosphate ions from aqueous solutions by adsorption onto leftover coal. *Water* **2020**, *12*, 1381. [CrossRef]
- Hermassi, M.; Valderrama, C.; Font, O.; Moreno, N.; Querol, X.; Batis, N.H.; Cortina, J.L. Phosphate recovery from aqueous solution by K-zeolite synthesized from fly ash for subsequent valorisation as slow release fertilizer. *Sci. Total Environ.* **2020**, *731*, 139002. [CrossRef]
- Kunaschk, M.; Schmalz, V.; Dietrich, N.; Dittmar, T.; Worch, E. Novel regeneration method for phosphate loaded granular ferric (hydr)oxide-A contribution to phosphorus recycling. *Water Res.* **2015**, *71*, 219–226. [CrossRef]
- Suresh Kumar, P.; Ejerssa, W.W.; Wegener, C.C.; Korving, L.; Dugulan, A.I.; Temmink, H.; van Loosdrecht, M.C.M.; Witkamp, G.J. Understanding and improving the reusability of phosphate adsorbents for wastewater effluent polishing. *Water Res.* **2018**, *145*, 365–374. [CrossRef]
- Sperlich, A.; Schimmelpfennig, S.; Baumgarten, B.; Genz, A.; Amy, G.; Worch, E.; Jekel, M. Predicting anion breakthrough in granular ferric hydroxide (GFH) adsorption filters. *Water Res.* **2008**, *42*, 2073–2082. [CrossRef]
- Pepper, R.A.; Couperthwaite, S.J.; Millar, G.J. Re-use of waste red mud: Production of a functional iron oxide adsorbent for removal of phosphorous. *J. Water Process Eng.* **2018**, *25*, 138–148. [CrossRef]
- Streat, M.; Hellgardt, K.; Newton, N.L.R. Hydrous ferric oxide as an adsorbent in water treatment. Part 3: Batch and mini-column adsorption of arsenic, phosphorus, fluorine and cadmium ions. *Process Saf. Environ. Prot.* **2008**, *86*, 21–30. [CrossRef]
- Suresh Kumar, P.; Korving, L.; Keesman, K.J.; van Loosdrecht, M.C.M.; Witkamp, G.J. Effect of pore size distribution and particle size of porous metal oxides on phosphate adsorption capacity and kinetics. *Chem. Eng. J.* **2019**, *358*, 160–169. [CrossRef]

18. Asano, T. *Water Reuse: Issues, Technologies, and Applications*, 1st ed.; McGraw-Hill: New York, NY, USA, 2007; ISBN 9780071459273.
19. You, X.; Farran, A.; Guaya, D.; Valderrama, C.; Soldatov, V.; Cortina, J.L. Phosphate removal from aqueous solutions using a hybrid fibrous exchanger containing hydrated ferric oxide nanoparticles. *J. Environ. Chem. Eng.* **2016**, *4*, 388–397. [CrossRef]
20. Chittoo, B.S.; Sutherland, C. Column breakthrough studies for the removal and recovery of phosphate by lime-iron sludge: Modeling and optimization using artificial neural network and adaptive neuro-fuzzy inference system. *Chin. J. Chem. Eng.* **2020**, *28*, 1847–1859. [CrossRef]
21. Hand, D.W.; Crittenden, J.C.; Thacker, W.E. Simplified Models for Design of Fixed-Bed Adsorption Systems. *J. Environ. Eng.* **1984**, *110*, 440–456. [CrossRef]
22. Pan, L.; Nishimura, Y.; Takaesu, H.; Matsui, Y.; Matsushita, T.; Shirasaki, N. Effects of decreasing activated carbon particle diameter from 30 μm to 140 nm on equilibrium adsorption capacity. *Water Res.* **2017**, *124*, 425–434. [CrossRef] [PubMed]
23. Pan, L.; Takagi, Y.; Matsui, Y.; Matsushita, T.; Shirasaki, N. Micro-milling of spent granular activated carbon for its possible reuse as an adsorbent: Remaining capacity and characteristics. *Water Res.* **2017**, *114*, 50–58. [CrossRef] [PubMed]
24. Hilbrandt, I.; Shemer, H.; Ruhl, A.S.; Semiat, R.; Jekel, M. Comparing fine particulate iron hydroxide adsorbents for the removal of phosphate in a hybrid adsorption/ultrafiltration system. *Sep. Purif. Technol.* **2019**, *221*, 23–28. [CrossRef]
25. Han, J.; Ro, H.M. Interpreting competitive adsorption of arsenate and phosphate on nanosized iron (hydr)oxides: Effects of pH and surface loading. *Environ. Sci. Pollut. Res.* **2018**, *25*, 28572–28582. [CrossRef]
26. Li, N.; Ren, J.; Zhao, L.; Wang, Z.L. Fixed bed adsorption study on phosphate removal using nanosized FeOOH-modified anion resin. *J. Nanomater.* **2013**, *2013*, 1–5. [CrossRef]
27. Ribas, D.; Pešková, K.; Jubany, I.; Parma, P.; Černík, M.; Benito, J.A.; Martí, V. High reactive nano zero-valent iron produced via wet milling through abrasion by alumina. *Chem. Eng. J.* **2019**, *366*, 235–245. [CrossRef]
28. Ribas, D.; Cernik, M.; Martí, V.; Benito, J.A. Improvements in nanoscale zero-valent iron production by milling through the addition of alumina. *J. Nanoparticle Res.* **2016**, *18*, s11051–s12016. [CrossRef]
29. Hu, H.; Li, X.; Huang, P.; Zhang, Q.; Yuan, W. Efficient removal of copper from wastewater by using mechanically activated calcium carbonate. *J. Environ. Manage.* **2017**, *203*, 1–7. [CrossRef]
30. Donskoi, E.; Collings, A.F.; Poliakov, A.; Bruckard, W.J. Utilisation of ultrasonic treatment for upgrading of hematitic/goethitic iron ore fines. *Int. J. Miner. Process.* **2012**, *114–117*, 80–92. [CrossRef]
31. Katircioglu-Bayel, D. Effect of Combined Mechanical and Ultrasonic Milling on the Size Reduction of Talc. *Mining, Metall. Explor.* **2020**, *37*, 311–320. [CrossRef]
32. Fasaki, I.; Siamos, K.; Arin, M.; Lommens, P.; Van Driessche, I.; Hopkins, S.C.; Glowacki, B.A.; Arabatzis, I. Ultrasound assisted preparation of stable water-based nanocrystalline TiO₂ suspensions for photocatalytic applications of inkjet-printed films. *Appl. Catal. A Gen.* **2012**, *411–412*, 60–69. [CrossRef]
33. Fiol, N.; Villaescusa, I. Determination of sorbent point zero charge: Usefulness in sorption studies. *Environ. Chem. Lett.* **2009**, *7*, 79–84. [CrossRef]
34. Freundlich, H.M.F. Tiber die adsorption in losungen. *Z. Phys. Chem.* **1906**, *57*, 385–470. [CrossRef]
35. Langmuir, I. The constitution and fundamental properties of solids and liquids. *J. Am. Chem. Soc.* **1916**, *38*, 2221–2295. [CrossRef]
36. Kumar, K.V. Linear and non-linear regression analysis for the sorption kinetics of methylene blue onto activated carbon. *J. Hazard. Mater.* **2006**, *137*, 1538–1544. [CrossRef]
37. Zhang, L.; Du, C.; Du, Y.; Xu, M.; Chen, S.; Liu, H. Kinetic and isotherms studies of phosphorus adsorption onto natural riparian wetland sediments: Linear and non-linear methods. *Environ. Monit. Assess.* **2015**, *187*, s10661–s11015. [CrossRef]
38. Khambhaty, Y.; Mody, K.; Basha, S.; Jha, B. Pseudo-second-order kinetic models for the sorption of Hg(II) onto dead biomass of marine *Aspergillus niger*: Comparison of linear and non-linear methods. *Colloids Surfaces A Physicochem. Eng. Asp.* **2008**, *328*, 40–43. [CrossRef]
39. Draper, N.R. *Applied Regression Analysis/Norman R. Draper, Harry Smith*; John Wiley & Sons: New York, NY, USA, 1998; ISBN 0471170828.
40. Potthoff, R. On the Johnson-Neyman technique and some extensions thereof. *Psychometrika* **1964**, *29*, 241. [CrossRef]
41. Andrade, J.M.; Estévez-Pérez, M.G. Statistical comparison of the slopes of two regression lines: A tutorial. *Anal. Chim. Acta* **2014**, *838*, 1–12. [CrossRef]
42. Fox, J. *Applied Regression Analysis and Generalized Linear Models*; SAGE Publications: Los Angeles, CA, USA, 2016; ISBN 9781452205663.
43. Townend, J. *Practical Statistics for Environmental and Biological Scientists*; Wiley: Chichester, UK, 2002; ISBN 0471496650.
44. Pepper, R.A.; Couperthwaite, S.J.; Millar, G.J. Value adding red mud waste: Impact of red mud composition upon fluoride removal performance of synthesised akaganeite sorbents. *J. Environ. Chem. Eng.* **2018**, *6*, 2063–2074. [CrossRef]
45. Ilavsky, J.; Barloková, D. The use of granular iron -based sorption materials for nickel removal from water. *Polish J. Environ. Stud.* **2012**, *21*, 1229–1236.
46. Ghasemi, Y.; Emborg, M.; Cwirzen, A. Estimation of specific surface area of particles based on size distribution curve. *Mag. Concr. Res.* **2018**, *70*, 533–540. [CrossRef]

47. Lalley, J.; Han, C.; Mohan, G.R.; Dionysiou, D.D.; Speth, T.F.; Garland, J.; Nadagouda, M.N. Phosphate removal using modified Bayoxide® E33 adsorption media. *Environ. Sci. Water Res. Technol.* **2015**, *1*, 96–107. [CrossRef]
48. Geelhoed, J.S.; Hiemstra, T.; Van Riemsdijk, W.H. Phosphate and sulfate adsorption on goethite: Single anion and competitive adsorption. *Geochim. Cosmochim. Acta* **1997**, *61*, 2389–2396. [CrossRef]
49. LaGrega, M.D.; Buckingham, P.L.; Evans, J.C. *Hazardous Waste Management*, 2nd, ed.; McGraw-Hill: Boston, MA, USA, 2001; ISBN 0070393656.

Article

Hydroxyapatite Coatings on Calcite Powder for the Removal of Heavy Metals from Contaminated Water

Oriol Gibert ^{1,2,*}, César Valderrama ^{1,2} , María M. Martínez ^{1,2}, Rosa Mari Darbra ¹, Josep Oliva Moncunill ¹ and Vicenç Martí ^{1,2,3} 

¹ Chemical Engineering Department, EEBE, Technical University of Catalonia (UPC), Av. Eduard Maristany 16, 08019 Barcelona, Spain; cesar.alberto.valderrama@upc.edu (C.V.); maria.rosario.martinez@upc.edu (M.M.M.); rm.darbra@upc.edu (R.M.D.); josep.oliva@upc.edu (J.O.M.); vicens.marti@upc.edu (V.M.)

² Barcelona Research Center in Multiscale Science and Engineering, EEBE, Technical University of Catalonia (UPC), Av. Eduard Maristany 16, 08019 Barcelona, Spain

³ Eurecat-Centre Tecnològic de Catalunya, Sustainability Area, Pça. de la Ciència 2, 08243 Manresa, Spain

* Correspondence: oriol.gibert@upc.edu

Abstract: An approach for the remediation of heavy metal-contaminated wastewater that is gaining increasing attention is the application of hydroxyapatite (HAP)-based particles. HAP is conventionally synthesized through wet chemical precipitation of calcium and phosphate ions, although later studies have focused on HAP synthesis from solid calcite contacted with a phosphate solution under ambient conditions. This synthesis route can allow saving soluble Ca-chemicals and, thus, make the process more cost-efficient. The aim of this study was to coat natural calcite powder with a layer of HAP for the removal of Zn and Cu from contaminated water. For this purpose, a HAP layer was synthesized on calcite particles, characterized using several complementary techniques and evaluated for the removal of Zn and Cu from synthetic solutions. Sorption kinetics and equilibrium isotherms, as well as the effect of sonication of the synthesized sample on its sorption performance, were determined. The results showed that calcite particles were efficiently coated with a HAP layer with high capacity in removing Zn and Cu from acidic solutions, with a q_{\max} of 34.97 mg/g for Zn (increased to 37.88 mg/g after sonication of the sample) and 60.24 mg/g for Cu (which hardly varied with sonication). The mechanisms behind the sorption of Zn and Cu onto HAP, inferred from pH changes, the relation between metal uptake and Ca^{2+} release and XRD analysis, included surface complexation, ion exchange and precipitation of new Zn- and Cu-containing phases.

Keywords: hydroxyapatite; calcium carbonate; coating; heavy metal sorption; groundwater remediation

Citation: Gibert, O.; Valderrama, C.; Martínez, M.M.; Darbra, R.M.; Moncunill, J.O.; Martí, V.

Hydroxyapatite Coatings on Calcite Powder for the Removal of Heavy Metals from Contaminated Water.

Water **2021**, *13*, 1493. <https://doi.org/10.3390/w13111493>

Academic Editor: Laura Bulgariu

Received: 16 April 2021

Accepted: 23 May 2021

Published: 27 May 2021

Publisher's Note: MDPI stays neutral with regard to jurisdictional claims in published maps and institutional affiliations.



Copyright: © 2021 by the authors. Licensee MDPI, Basel, Switzerland. This article is an open access article distributed under the terms and conditions of the Creative Commons Attribution (CC BY) license (<https://creativecommons.org/licenses/by/4.0/>).

1. Introduction

Acidic metal-rich wastewater from mining and industrial processes represents an environmental problem worldwide due to its low pH and high content of heavy metals. It is well-known that heavy metals discharged into the environment may pose a serious hazard to all living beings because of their bioaccumulation and toxicity even at low concentrations [1,2]. Therefore, removal of heavy metals from this type of wastewater by an appropriate treatment becomes necessary.

When wastewater can be managed on the surface, above-ground engineered systems offer the opportunity to customize the operation conditions for an optimized performance. The removal of heavy metals in these systems can be achieved through several processes, with the most common ones being chemical precipitation, coagulation-flocculation, membrane filtration, ion-exchange, electrochemical processes and sorption. Chemical precipitation is the simplest and most employed approach, although it consumes large amounts of chemicals and can generate an excessive amount of sludge that requires further treatment [3,4]. Coagulation-flocculation also removes heavy metals from water with reduced time to settle suspended solids, but like chemical filtration, it produces huge amounts of

sludge that need to be handled and treated [3,5]. Membrane filtration (particularly nanofiltration and reverse osmosis) is recognized as a very efficient technology for the removal of dissolved heavy metals, although it usually requires high energy consumption and suffers from membrane fouling, posing difficulties in their operation and increasing operation costs [6,7]. Ion-exchange has also proved to be useful for the removal and recovery of heavy metals from water. It offers the advantages of selective removal and no sludge production, but on the other hand, ion-exchange resins are expensive and their regeneration can increase the cost even further. Moreover, successful removal by ion-exchange is applicable to only a limited number of metal cations [5,8]. Electrochemical methods are also an option to remove heavy metals from water, but they are usually associated to high costs and high electrical supply [3,7]. Finally, sorption arises as one of the most attractive methods thanks to its efficiency, versatility, simplicity in design and operation and low cost [5,9]. Sorption-based approaches are spreading as new sorbents and applications are researched. Within this context, the recent developments in micro- and nano-particles (MPs and NPs) with sorption capacity towards metals are gaining increased attention of researchers [2,10].

When contaminated water is groundwater (e.g., when mining acidic metal-rich streams known as acid mine drainage (AMD) percolate through the soil), the selection of the most suitable technology becomes more complicated. First, some of the above-mentioned processes (e.g., membrane filtration or ion-exchange) are technically impractical at depth and/or are cost-prohibitive when applied on surface after groundwater extraction. In these cases, in-situ remediation in the aquifer itself through the installation of a permeable reactive barrier (PRB) [11], the insertion into the subsoil of electrodes to promote electrochemical processes [12] or the introduction of reactive chemicals via injection wells [13] has become a matter of active research. Despite successful experiences, PRBs have shown to be restricted to shallow aquifers and often suffer from limited capture of the contaminated plume [11,14]. For their part, technologies based on in-situ-induced electrochemical processes are constrained by the limited metal removal and high energy consumption [12]. Another promising approach for in-situ remediation that is gaining increasing attention of researchers is the application of MPs and NPs in the subsoil able to immobilize, neutralize or decompose the contaminants present in groundwater, as the application of MPs and NPs allows reaching contaminants in deep aquifers not accessible by PRBs [10,15].

Many different materials have been evaluated for their application in the form of MPs and NPs [16,17]. For the removal of heavy metals, powders based on hydroxyapatite ($\text{Ca}_{10}(\text{PO}_4)_6(\text{OH})_2$, hereafter referred to as HAP) have been acknowledged as one of the most suitable reactants thanks to its high sorption capacity for heavy metals, low water solubility, availability and low cost, environmental compatibility and high stability under oxidizing and reducing conditions [18–20].

Properties (and thus performance) of a given HAP greatly depend on how it has been synthesized [21,22]. Among the conventional methods of producing HAP particles, the classical wet chemical precipitation (i.e., soluble Ca^{2+} and HPO_4^{2-} are precipitated in an aqueous solution at basic conditions) is often reported to be the most convenient one because, unlike more sophisticated strategies, it is not associated to high cost and energy use [23,24]. The final composition, morphology and properties of the synthesized HAP following the wet precipitation method depend on many variables, such as concentration and proportion of precursors, pH, temperature, presence of other ionic species or organic compounds and aging time [21,25,26]. Numerous studies have demonstrated that HAPs with high sorption capacity for metals can be synthesized over a wide range of values for these variables.

Modifications of the classical wet chemical precipitation of HAP have been investigated in other fields. HAP has been synthesized, under ambient conditions, from solid calcite contacted with a phosphate solution, on the basis that the solid calcite acts as a source of Ca^{2+} instead of externally adding it in the form of soluble Ca^{2+} . Under this

scheme, Ca^{2+} is supplied by dissolution of CaCO_3 and precipitated by the following overall reaction:



This approach has been applied for the synthesis of HAP from biogenic calcite (e.g., nacre, oyster shells, sea urchin spines or other natural osteo-inductive biomaterials) [20,26–28]. Further studies have compared the effect of using different orthophosphate sources in such a synthesis route [29]. In addition, under this scheme, studies aiming at protecting marble sculptures and monuments from acid rain have investigated the possibility of coating them with a film of HAP synthesized by using the marble itself as a Ca^{2+} source for the HAP [30–32]. Although these studies provide very promising results, further investigation is needed to fully understand HAP synthesis from solid CaCO_3 .

From a remediation perspective, preparing calcite particles coated by HAP for sorbing metals would allow saving huge amounts of soluble Ca-chemicals and, thus, make the process more cost-efficient and improve its competitiveness. Solid calcite, as one of the fifth most abundant biominerals in the Earth crust, has a very low cost and wide availability. However, to the best of our knowledge, there is a lack of studies from such a standpoint and only an attempt has been made to synthesize phosphatized dolomite as sorbent to be used for the treatment of metal-contaminated water [33].

Within this context, the aim of this bench-scale study was to coat natural calcite powders with a layer of HAP for the removal of heavy metal ions (Cu and Zn) from contaminated water. Zn and Cu ions were chosen as representative heavy metals, with wide presence in the environment caused mainly by human activity. The specific objectives were (1) to synthesize and characterize a layer of HAP on solid calcite particles, (2) to assess its sorption capacity toward Zn and Cu in single-metal solutions, determining the sorption kinetics and the equilibrium isotherms (and to compare them with those of commercial HAPs), (3) to evaluate the effect of sonicating the material on sorption performance and (4) to infer the mechanisms responsible for the removal of Zn and Cu.

2. Materials and Methods

2.1. Bare Calcite MPs and Chemical Reagents

The commercial calcite MPs were purchased from Reverté S.A. (Spain). The MPs were found to have an average particle size of 10 μm and exhibit a BET surface area of 0.87 m^2/g . The acid digestion of calcite MPs and analysis by ICP-OES showed a composition of 36.5% Ca and 0.17% Mg. Precursors $(\text{NH}_4)_2\text{HPO}_4$ (Scharlau $\geq 98\%$), CaCl_2 (Panreac $\geq 98\%$), NaOH (Panreac $\geq 98\%$) and ethanol (Scharlau $\geq 96\%$) were used for HAP synthesis. For sorption experiments, acidic Zn and Cu solutions were prepared from their ZnCl_2 and CuSO_4 salts (Panreac $\geq 98\%$) and HNO_3 (Panreac $\geq 96\%$). Performance of synthesized HAP was compared against commercial micro-HAP (Acros 35–40% in Ca) and nano-HAP (Merck $\geq 97\%$), labeled hereafter as mHAPcom and nHAPcom, respectively.

2.2. Synthesis Route of HAP Coatings on Calcite MPs

The synthesis route of the HAP coating consisted of a two-step procedure based on that applied by Graziani et al. for the coverage of marble with a HAP film [32]. First, 1 g of calcite MPs was placed in a plastic centrifuge tube and put into contact with 25 mL of a solution containing $(\text{NH}_4)_2\text{HPO}_4$ (0.1 M), CaCl_2 (0.1 M) and a pH of 8 in the presence of ethanol 0.5%, as ethanol has been found to improve the coverage of a calcite surface by a more uniform, crack-free and thinner layer of HAP [32]. The pH was adjusted by adding NaOH dropwise until the desired value was achieved. Second, a further precipitation of HAP following the same procedure and concentrations as described above but without ethanol was carried out.

For each step, the suspension was shaken in a rotary shaker (Heidolph GmbH, REAX 20, Schwabach, Germany) for 24 h. This time was chosen to allow possible precipitated intermediates (octacalcium phosphate, amorphous calcium phosphate, calcium-

deficient hydroxyapatite) to shift to HAP [23]. After 24 h, the synthesized solid (HAP-coated calcite MPs) was separated by centrifugation (J.P. Selecta, Centronic-BLT, Abrera, Spain) at 4000 rpm for 20 min, oven-dried (J.P. Selecta, Digiheat, Abrera, Spain) at 110 °C for 1.5 h and ground with a mortar before further use. This material was labelled “synt” (from synthesized).

In order to diminish the particle size of the selected material and thus potentially enhance its sorption capacity, a portion of it was subjected to sonication, as it is known that ultrasonic energy applied to a suspension can lead to breakage of agglomerated particles. Sonication of a sample of 4 g in 250 mL of deionized water was conducted in an ultrasonic cleaner (ATU Ultrasonidos, ATM40-2L-CD, Paterna, Spain) operating at a fixed frequency of 40 Hz for 30 min. The solid was then separated by centrifugation and dried as described above. The modified material was labelled “son” (from sonicated).

Performance of samples “synt” and “son” were compared against that of commercial HAP samples mHAPcom (micro-size) and nHAPcom (nano-size).

2.3. Characterization of the HAP-Coated MPs Samples

The synthesized material and its sonicated sub-sample were characterized using several complementary techniques. Functional groups were characterized employing a Fourier Transform Infrared (FTIR) spectrophotometer (Nicolet 6700, Madison, WI, USA) fitted with an Attenuated Total Reflectance (ATR) accessory (Smart Orbit). Mineralogical identity and crystallinity were analyzed by X-ray powder diffraction (XRD) recorded on a Bruker D8 Advance diffractometer. Morphology was viewed with a Focused Ion Beam–Scanning Electron Microscope (FIB-SEM) equipped with an energy dispersive spectrometer (EDS) for elemental analysis (Carl Zeiss Neon40, Jena, Germany). Samples were mounted on stainless-steel stubs using a double-sided adhesive carbon disc and sputter-coated with a thin layer of carbon to render them conductive for SEM observation. The specific BET surface area (S_{BET}) of the samples was measured by N_2 adsorption according to the Brunauer–Emmet–Teller method in a S_{BET} analyzer (Micromeritics ASAP 2020, Aachen, Germany). Degassing and heating was carried out at a maximum temperature of 250 °C. Particle size distribution (PSD) was determined using a Laser Diffraction Particle Size analyzer (Malvern Panalytical, MasterSizer 3000, Worcestershire, UK) with a Hydro EV wet dispersion unit. For calculations, the Mie theory was chosen, and refractive and absorption indices were 1.630 and 0.010, respectively. In order to obtain PSD of particles in the same conditions of the experiments, measurements were carried out with water and without application of ultrasounds. PSD curves provided by the instrument were given as volumetric PSD. The pH at the point zero charge (pH_{PZC}) was estimated through the immersion technique by putting an amount of solid material in contact with solutions at different initial pHs and measuring the change of pH (ΔpH) once equilibrium was reached [34].

2.4. Sorption Performance of the Synthesized HAP-Coated Material

2.4.1. General Procedure

All sorption experiments were carried out using standard batch methodology. Known volumes (50 mL) of prepared solutions of Zn and Cu (added in the form of ZnCl_2 and CuSO_4) at pH 4.6 were contacted with a weighted amount of sorbent in plastic centrifuge tubes and shaken in a rotatory shaker for 24 h at room temperature (21 ± 2 °C). For the kinetics study, the weighted amount was 0.05 mg, the Zn or Cu concentration was 50 mg/L and the supernatant solution samples were collected at predetermined time intervals (after 1, 2, 4, 6, 9, 12, 15, 25, 40, 60 min). For the equilibrium experiments, the weighted amounts of sorbent were 0.05 or 0.1 g, and the initial Zn or Cu concentrations were 5, 10, 20, 40, 60, 80, 100 and 120 mg/L. The ratio of aqueous phase volume (mL) to sorbent weight (mg) was varied as necessary to observe a measurable decrease in the concentration of Zn and Cu in the aqueous solution once the equilibrium was reached. No pH control was imposed during sorption experiments in order to mimic the subsoil conditions during the

remediation of contaminated groundwater. All centrifuge tubes were shaken in a rotary shaker at 50 rpm for 24 h, after which the supernatant solution was separated from the sorbent by centrifugation at 4000 rpm for 10 min, filtered (0.22 μm), acidified (1% HNO_3) and transferred to auto-sampler vials for analysis of the remaining Zn and Cu. The ions Ca^{2+} , HPO_4^{2-} and pH in the supernatant were also determined in separate aliquots.

2.4.2. Sorption Kinetics of Zn and Cu

The kinetics of the sorption of Zn and Cu onto the HAP was fitted using the pseudo first-order and the pseudo second-order kinetics models, whose linearized forms are, respectively:

$$\log(q_e - q) = \log q_e - \frac{k_1}{e} \times t \quad (1)$$

$$\frac{t}{q} = \frac{1}{k_2 \times q_e^2} + \frac{t}{q_e} \quad (2)$$

where q and q_e are the amounts of adsorbed metal per weight unit of adsorbent (mg/g) at equilibrium and at time t respectively, and k_1 and k_2 are the rate constants of pseudo first-order (min^{-1}) and pseudo second-order ($\text{g} \cdot \text{mg}^{-1} \cdot \text{min}^{-1}$), respectively.

The amount of adsorbed metal per weight unit of the adsorbent (q , in mg/g) was calculated from the following mass balance, also valid for the equilibrium:

$$q_e = \frac{V \times (c_i - c_e)}{w} \quad (3)$$

where c_i and c_e are the initial and equilibrium concentrations of the metal ion in the bulk solution (mg/L), V is the volume of the solution (L) and w is the weight of the sorbent (g).

2.4.3. Sorption Isotherms for Single-Metal Systems

Sorption equilibrium data are usually plotted as an isotherm displaying the content of the sorbed species on the sorbent (q_e) (in mg/g) versus the concentration of the remaining aqueous species (c_e) (in mg/L). The sorption data of this study were modeled taking into account the concentration of ions in both phases and according to the widely used Langmuir equations:

$$q_e = \frac{K_L \times q_{\max} \times c_e}{1 + K_L \times c_e} \quad (4)$$

where q_{\max} is the maximum adsorption capacity (mg/g) and K_L is the Langmuir binding constant, which is related to the energy of adsorption (L/mg). Experimental c_e and q_e data were used to determine the constants (q_{\max} , K_L) for each metal and sorbent from the linearized form of the Langmuir isotherm and using least-square regression analysis.

2.5. Water Analysis

Measurements of pH were made with a Hamilton combination pH electrode coupled to a Crison GLP22 pH meter. HPO_4^{2-} and Ca^{2+} in the supernatants in the sorption experiments were analyzed by ionic chromatography (IC) (Dionex, ICS-1000, Sunny Valley, ID, USA) equipped with cationic and anionic detectors (ICS-1000 and ICS-1100, respectively) and controlled by software Chromeleon[®] chromatographic. Ca, P and Mg (in the determination of the calcite composition), and Zn and Cu (in the sorption experiments) were analyzed by atomic absorption spectroscopy (AAS) (Varian, SpectraAA 50-B, Palo Alto, CA, USA) and inductively coupled plasma optical emission spectrometry (ICP-OES) (Perkin Elmer, Optima 8300, Waltham, MA, USA).

3. Results and Discussion

3.1. Characterization of the Synthesized Material

Figure 1 displays the FTIR spectra (a) and the XRD spectra (b) of the “synt” sample and, for comparison, calcite and a commercial HAP (mHAPcom).

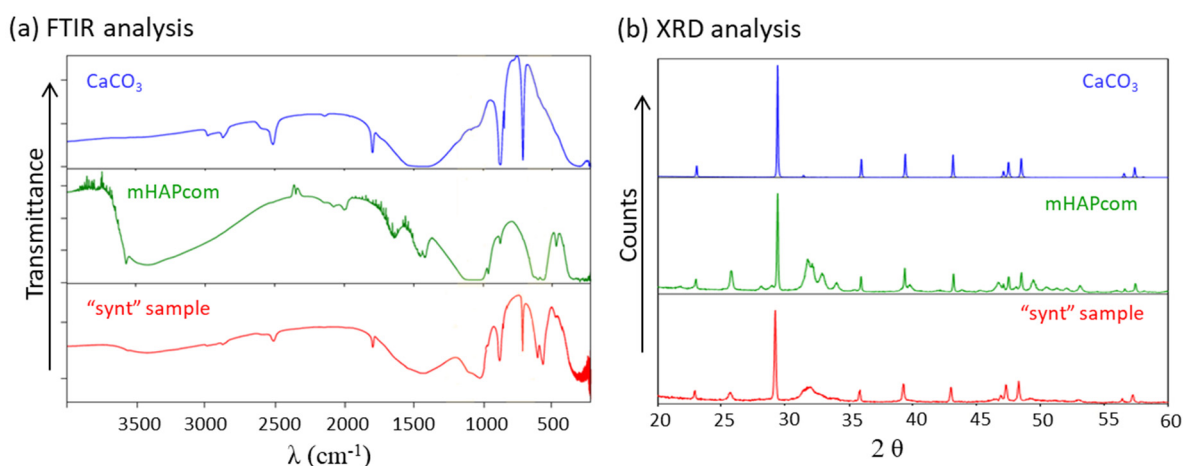


Figure 1. FTIR spectra (a) and the XRD spectra (b) of the selected synthesized material and, for comparison, calcite and a commercial HAP (mHAPcom).

The spectrum of the “synt” sample presented characteristic peaks and bands of HAP: a broad band centred at around 1030 cm⁻¹ (corresponding to asymmetric stretching mode ν_3 of the PO₄³⁻ group) and sharp peaks at 600 and 565 cm⁻¹ (ascribed to bending mode ν_4 of the PO₄³⁻ group). The slight shoulder observed at 964 cm⁻¹ may also be assigned to symmetric stretching mode ν_1 of the PO₄³⁻ group, as well as the broad band observed at 3420 cm⁻¹ which can be ascribed to the stretching vibrations ν (O-H) of the HAP (although it may also be of interstitial water) [35–38]. On the other hand, the characteristic peaks of CaCO₃ were also observed: a broad band centred at about 1440 cm⁻¹ (asymmetric stretching ν_3 of CO₃²⁻) and well-resolved peaks at 880 cm⁻¹ (out-of-plane bending ν_2 of CO₃²⁻) and 715 cm⁻¹ (symmetric in-plane bending ν_4 of CO₃²⁻). An additional slight peak at 1810 cm⁻¹ was also observed coming from stretching vibration ν (C=O), while the slight shoulder at 1060 cm⁻¹ can be ascribed to symmetrical stretching ν (C–O) [37,39]. The FTIR spectrum for the “son” sample resembled that of the “synt” sample (not shown).

The XRD spectrum of the “synt” sample presented characteristic diffraction peaks of HAP (e.g., 25.8° and 31.8°) together with those of its precursor CaCO₃ [26,31,40]. Again, the XRD spectrum for the “son” sample looked like that of the “synt” sample (not shown).

Figure 2 shows the SEM images of the sorbents used in sorption tests. SEM images of the “synt” sample showed that the surface of the calcite MPs was mostly covered by HAP, easily recognizable by its flower-like structure (Figure 2a) [41]. Consistently, EDS analysis confirmed that this layer was constituted by Ca, P and O. The layer visible by SEM did not display recognizable individual particles but a continuous coating of aggregated particles instead, making it difficult to assess an average particle size. Very occasional uncoated areas were also observed, exhibiting underlying calcite (with its characteristic layered terraces), as confirmed by EDS analysis (Figure 2b). These bare areas of calcite would help explain the loss of mass (10%) observed after the acid attack.

SEM images of the “son” sample seemed to indicate that sonication led to a detachment of HAP, yielding a surface with more bare areas of calcite and more cavities (Figure 2c). The “son” sample also exhibited a highly agglomerated structure. The associated EDS spectrum (not shown) resembled that of the uncovered areas of the “synt” sample (Figure 2b).

SEM images of the commercial macro- and nano-HAP (mHAPcom and nHAPcom, respectively) showed agglomerates of more rounded, smooth HAP particles with different size (of approximately 40 to 60 μ m) (Figure 2d,e, respectively).

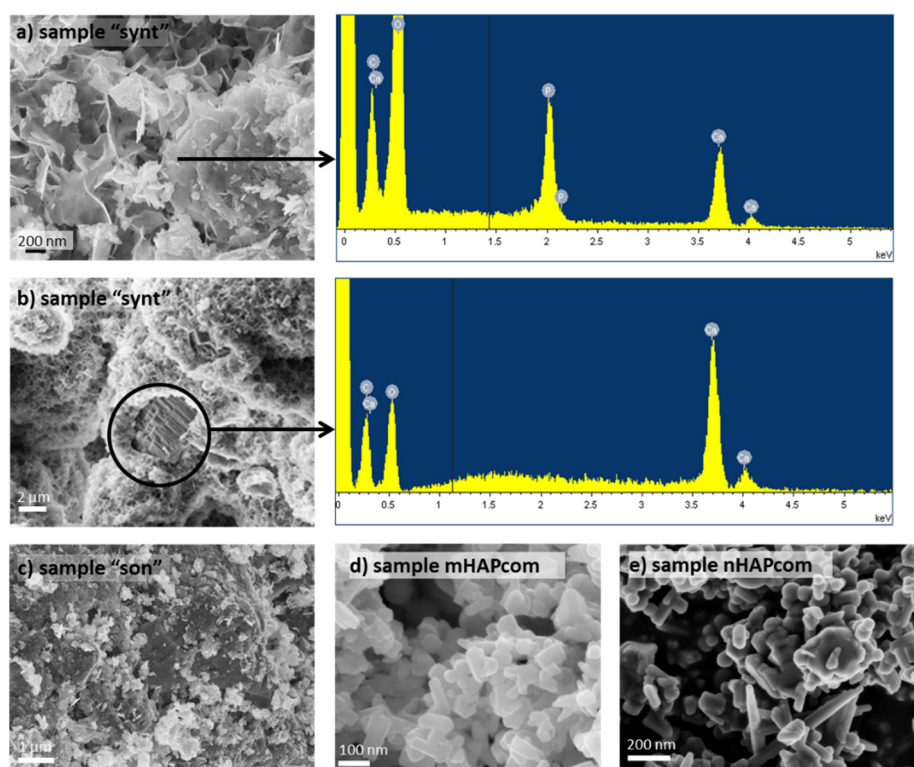


Figure 2. SEM images of the “synt” sample (a,b), “son” sample (c), mHAPcom (d) and nHAPcom (e).

BET results for all studied sorbents are summarized in Table 1. It is worth noting that a notorious specific surface area increment was obtained during the synthesis process from calcite to HAP. Measured values of S_{BET} surface areas for “synt” and “son” samples were 58.25 and 53.68 m^2/g , which were similar or slightly lower than that for the mHAPcom (60.77 m^2/g) and clearly higher than that for nHAPcom (18.93 m^2/g). The low value of the latter was probably related to its high crystallinity. The pore volumes of the synthesized HAPs were 0.0016 cm^3/g for the “synt” sample and 0.0013 cm^3/g for the “son” sample.

Table 1. Measured values of S_{BET} surface areas for all studied sorbents.

Sorbent	S_{BET} (m^2/g)
Initial calcite	0.87 ± 0.01
Synt	58.25 ± 0.08
Son	53.68 ± 0.16
mHAPcom	60.77 ± 0.20
nHAPcom	18.93 ± 0.11

Volumetric particle size distributions (PSD) of the studied samples are represented in Figure 3. The PSD curve of “synt” and “son” samples exhibited a similar symmetric single peak with distribution widths close to each other, with a shoulder or additional small peak on the right, suggesting that agglomeration of particles took place. However, the two PSDs differed in their mean diameter: 36 μm for “synt” and 23 μm for “son”. This seemed to prove that sonication resulted to some extent in a fracturing or breakage of the agglomerates. For mHAPcom, the PSD curve revealed a mean diameter of 10 μm , which was apparently smaller than that visualized in SEM analysis (Figure 2d). For nHAPcom, the PSD curve was non-uniform, which indicated that the sample contained particles with very different size (mean diameter of 6 μm). Differences in size between PSD and SEM measurements are usually attributed to agglomeration of particles or inaccuracies in the assumption of sphericity of particles measured in PSD.

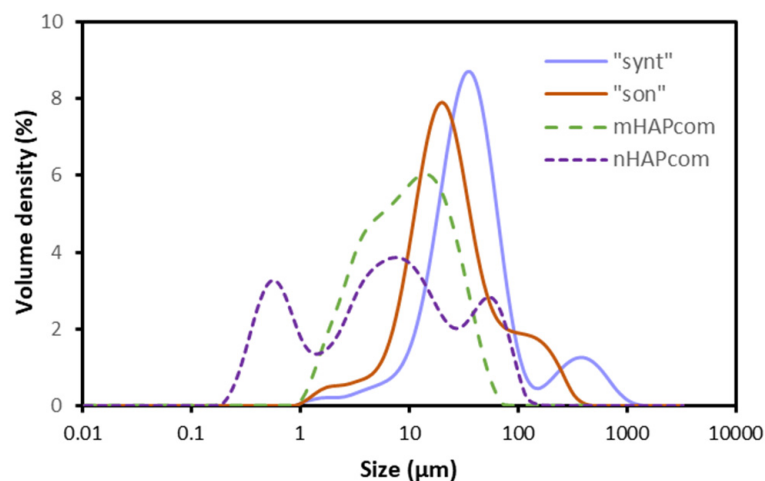


Figure 3. Volumetric particle size distributions (PSD) of samples “synt”, “son”, mHAPcom and nHAPcom.

The HAP particles synthesized in this study were hence presented as agglomerates of calcite cores coated with HAP of average size of 36 μm , with a large S_{BET} (58.25 m^2/g). Sonication of this sample caused some detachment of the HAP layer, resulting in slightly smaller agglomerates (of average size of 23 μm) and S_{BET} (53.68 m^2/g).

The pH_{PZC} was estimated by the immersion technique [34]. Figure 4 represents the change of pH (ΔpH) versus the initial pH. The pH_{PZC} was identified as the pH with no variation of pH ($\Delta\text{pH} = 0$) and quantified to be 7.7 for the “synt” sample and 8.2 for the mHAPcom sample. These values were comparable to reported pH_{PZC} for synthesized HAP (7.3–8.6) [25,41].

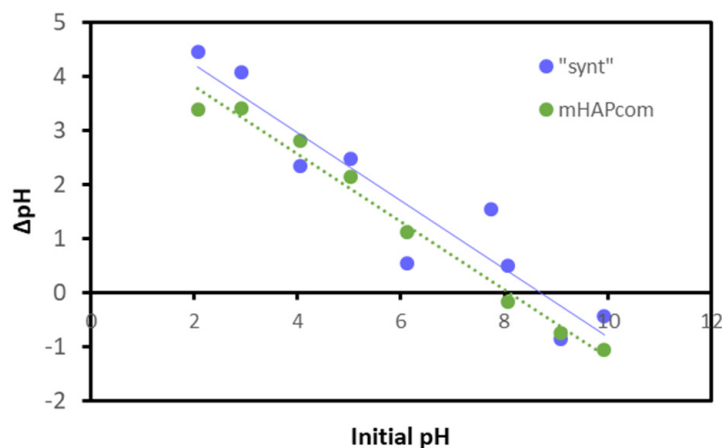


Figure 4. Experimental immersion technique curves corresponding to “synt” and mHAPcom samples for the determination of pH_{PZC} .

3.2. Adsorption Kinetics

Sorption of Zn and Cu onto the “synt” sample as a function of time is illustrated in Figure 5. It can be seen that, for both metals, equilibrium between the two phases was attained in approximately 40 min.

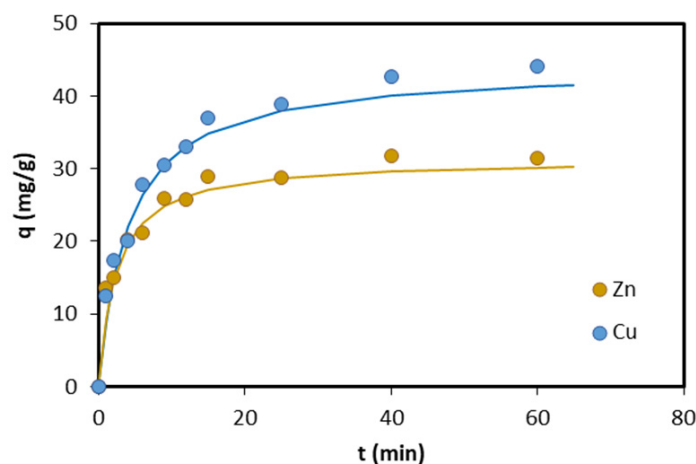


Figure 5. Sorption of Zn and Cu onto the synthesized material (“synt” sample) as a function of time. Symbols represent experimental data and fitting lines were plotted using the pseudo-second order kinetic model.

The experimental kinetic data were fitted with pseudo-first and pseudo-second order kinetic equations. The rate constants k_1 and k_2 , and q_e values were calculated from the interception and slope of the line obtained by plotting $\log(q_e - q)$ and t/q against t . The obtained values, together with regression coefficients, are shown in Table 2. The higher regression coefficients for the pseudo-second order kinetic model revealed that this model better described the kinetics of Zn and Cu sorption on HAP. The k_2 values were found in the range of published values for Zn (0.001–0.88 g/(mg·min)) [25,42] and Cu (0.001–0.076 g/(mg·min)) [36,42–44].

Table 2. Comparison of the pseudo-first and pseudo-second order kinetic models for the sorption of Zn and Cu onto the synthesized material (“synt” sample).

Metal	Pseudo-First Order Kinetic Model			Pseudo-Second Order Kinetic Model		
	q_e (mg/g)	k_1 (1/min)	R^2	q_e (mg/g)	k_2 g/(mg·min)	R^2
Zn	31.38	0.099	0.840	31.37	0.014	0.998
Cu	44.08	0.079	0.966	44.05	0.057	0.998

R^2 : correlation factor obtained from the linearized form of the kinetic models.

3.3. Adsorption Isotherms for Single-Metal Solutions

Figure 6 shows the experimental equilibrium data for the sorption of Zn and Cu in single-metal solutions onto “synt”, “son”, mHAPcom and nHAPcom materials. The fitting of the experimental c_e and q_e data to the Langmuir-type model gave rise to the values of the constants (q_{max} and K_L) provided in Table 3. The Langmuir curves generated with the obtained constants are plotted in Figure 6.

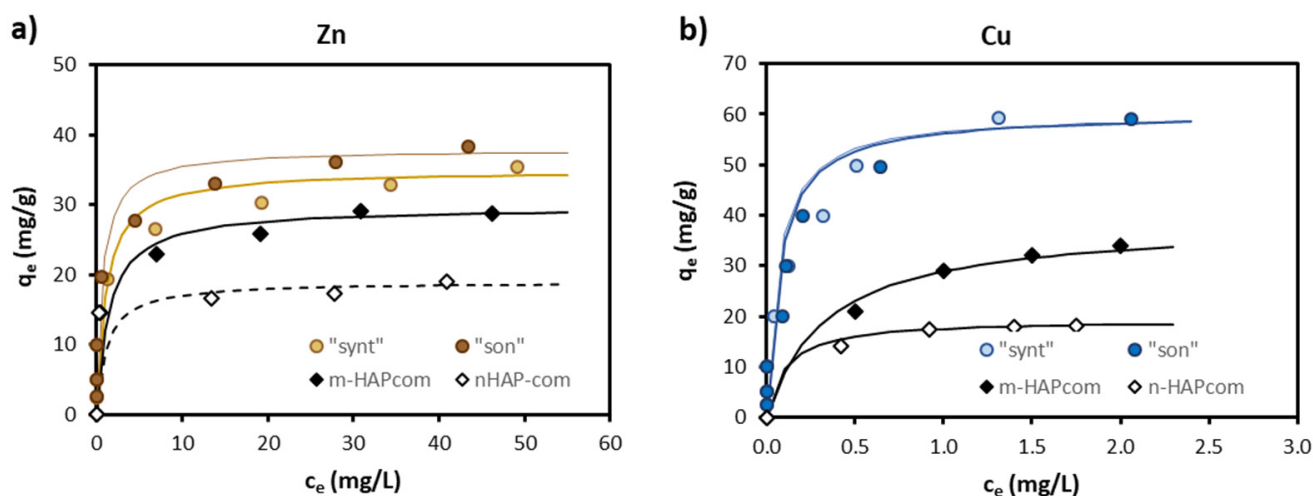


Figure 6. Sorption isotherms for Zn (a) and Cu (b) onto the sorbents evaluated in this study. Symbols represent experimental data and fitting lines are the isotherms derived from the Langmuir equations.

Table 3. Summary of obtained Langmuir adsorption parameters.

Metal	Sorbent	q_{\max}		K_L	R^2
		(mg/g)	(mg/m ²)	(L/mg)	
Zn	synt	34.97	0.600	0.91	0.9978
	son	37.88	0.706	1.47	0.9984
	mHAPcom	29.67	0.489	0.68	0.9985
	nHAPcom	18.98	1.003	0.85	0.9967
Cu	synt	60.24	1.034	15.09	0.9905
	son	60.24	1.122	13.83	0.9955
	mHAPcom	38.61	0.635	2.98	0.9997
	nHAPcom	19.27	1.018	9.88	0.9977

The “synt” and “son” materials were efficient in sorbing Zn ($q_{\max} = 34.97\text{--}37.88$ mg/g) and Cu ($q_{\max} = 60.24$ mg/g), with sorption capacities higher than those of commercial HAPs (Figure 5) (note that isotherms for Cu on both “synt” and “son” sorbents in Figure 6b superpose in the whole concentration range). Considering that sorption is a surficial process, q_{\max} were S_{BET} -normalized. As can be seen in Table 3, the obtained values were still higher for the synthesized materials (excepting for Zn on nHAPcom).

Table 4 compares q_{\max} obtained in this study with reported values in the literature. It must be kept in mind that sorption capacity of a given HAP largely depends on the conditions of its preparation and sorption experiments’ conditions. Therefore, Table 4 only compares studies on HAP synthesized through wet chemical precipitation and evaluated in batch sorption tests. As can be seen, values of q_{\max} in this study were comparable to published values. In general, more crystalline HAP yielded lower q_{\max} but also lower S_{BET} , so that S_{BET} -normalized q_{\max} remained almost constant, as also observed by Šljivić et al. [43].

Table 4. Comparison of Langmuir sorption parameters against previous studies with synthesized HAP through wet chemical precipitation.

HAP Synthesis and Characteristics				Adsorption					Ref
				Zn		Cu			
Precursors	pH	T	S _{BET} (m ² /g)	pH	q _{max} (mg/g)	q _{max} (mg/m ²)	q _{max} (mg/g)	q _{max} (mg/m ²)	
Ca(OH) ₂ + H ₃ PO ₄	n.r.	20	67	5.0	37.53	0.560	-	-	[25]
Ca(NO ₃) ₂ + (NH ₄)H ₂ PO ₄ (+Fe ₃ O ₄ /Fe ₂ O ₃)	11	90	142.5	5.0 ^(a)	140.6 ^(b)	0.99	-	-	[45]
Ca(OH) ₂ + H ₃ PO ₄	n.r.	100	76.6	6.0 ^(a) 5.5 ^(a)	102.04 37.27	1.332 0.750	- -	- -	[35]
Ca(NO ₃) ₂ + (NH ₄) ₂ HPO ₄	11	n.r.	n.r.	5.0 ^(a)	10.75	n.r.	-	-	[36]
commercial			77	6.0	37.14	0.482	-	-	[46]
commercial			50	6.6	95.89	1.92	76.49	1.53	[42]
CaCl ₂ + NH ₄ H ₂ PO ₄ + EtOH (+Fe ₃ O ₄)	11	20	101.2	5.0 ^(a)	-	-	48.78	0.482	[18]
Ca(OH) ₂ + H ₃ PO ₄	n.r.	n.r.	58	5.0	-	-	37.17	0.641	[43]
Ca(NO ₃) ₂ + H ₃ PO ₄ + NH ₄ ⁺ -salt	10	40	49.7	4.5 ^(a) 5.5 ^(a)	- -	- -	29.23 37.30	0.588 0.751	[44]
Calcite + (NH ₄) ₂ PO ₄ (+EtOH)			58.28	4.6	34.97	0.600	60.24	1.034	
Calcite + (NH ₄) ₂ PO ₄ (+EtOH) (+ sonication)	8	25	53.68	4.6	37.88	0.706	60.24	1.122	This study
Commercial (mHAPcom)			60.77	4.6	29.67	0.489	38.61	0.635	
Commercial (nHAPcom)			18.93	4.6	18.98	1.003	19.27	0.985	

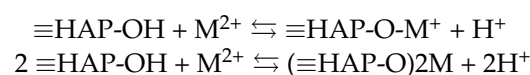
n.r.: not reported. ^(a) pH maintained constant. ^(b) Read from Figure 5 in Feng et al. [45].

Some authors have explained the difference in selectivity of HAP toward different metal cations on the basis of their hydrated ion radius and electronegativity [25]. The higher hydrated ion radius (4.30 Å) and lower electronegativity (1.60) of Zn than of Cu (4.19 and 1.90 Å, respectively) and their sorption extent observed in the present study seemed to support this theory.

3.4. Sorption Mechanisms

Figure 7 shows that Zn and Cu sorption was accompanied by a pH decrease (Figure 7a,c) and an increase of Ca²⁺ concentration in the solution (Figure 7b,d). Both were proportional to the amount of Zn and Cu sorbed onto HAP (q_e).

The pH decrease can be explained by the surface complexation reaction between Zn and Cu and deprotonated surface hydroxyls of HAP, summarized as follows [42,47]:



where M²⁺ stands for Zn²⁺ or Cu²⁺ ions. Decreases of pH by metal sorption on HAP have also been observed by other investigators [18,25,35,43]. In the absence of M²⁺, the pH in the present study increased from the initial pH 4.7 to 9.2. Unlike other studies, this increase was beyond pHPZC of HAP (in the range 6.1–8.3) [18,36,43], probably because calcite in bare areas of the HAP-coated calcite MPs dissolved and caused pH to rise to higher values than HAP alone would do. It is worth noting that as long as pH remained above pHPZC

(i.e., the HAP surface exhibited a negative charge), electrostatic forces between the HAP surface and the metal cation favored cation sorption [48].

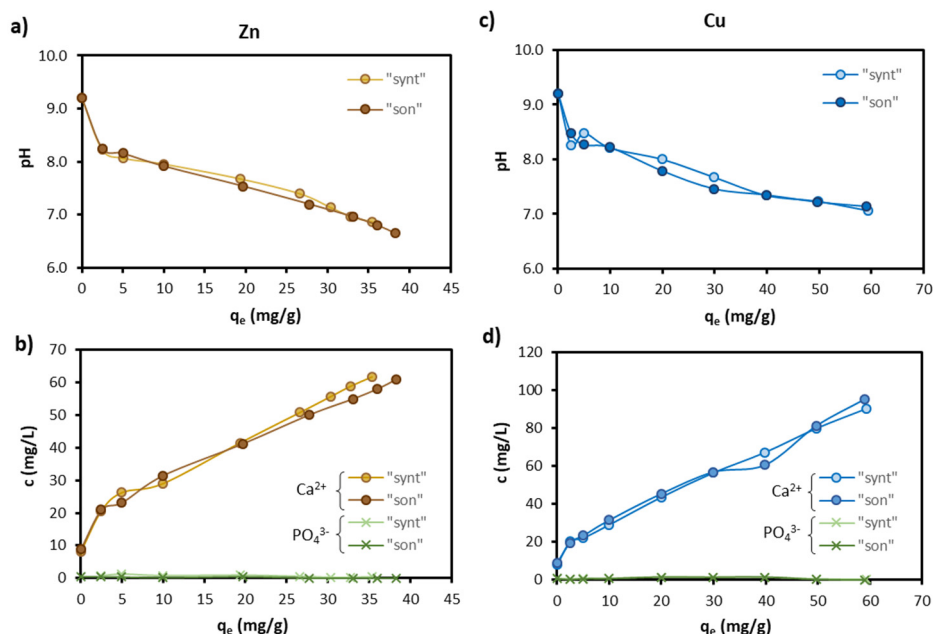
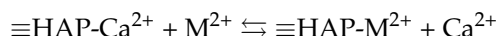


Figure 7. Variations in pH and Ca^{2+} and PO_4^{3-} concentrations following Zn sorption (a,b, respectively) and Cu (c,d, respectively) sorption.

However, the simple surface complexation process would not cause any Ca^{2+} concentration. The increase in Ca^{2+} concentration was fairly well-explained by an ion exchange process, whereby M^{2+} replaces a surface Ca^{2+} of the HAP, presented as follows:



Increases in Ca^{2+} concentration from ion exchange on HAP have previously been reported [18,25,42].

Figure 8 presents the relationship between the number of moles of released Ca^{2+} versus the number of moles of adsorbed Zn (Figure 8a) and Cu (Figure 8b). The relationship is linear with a slope very close to unity. A slope close to unity would suggest that Zn and Cu were removed solely by ion exchange.

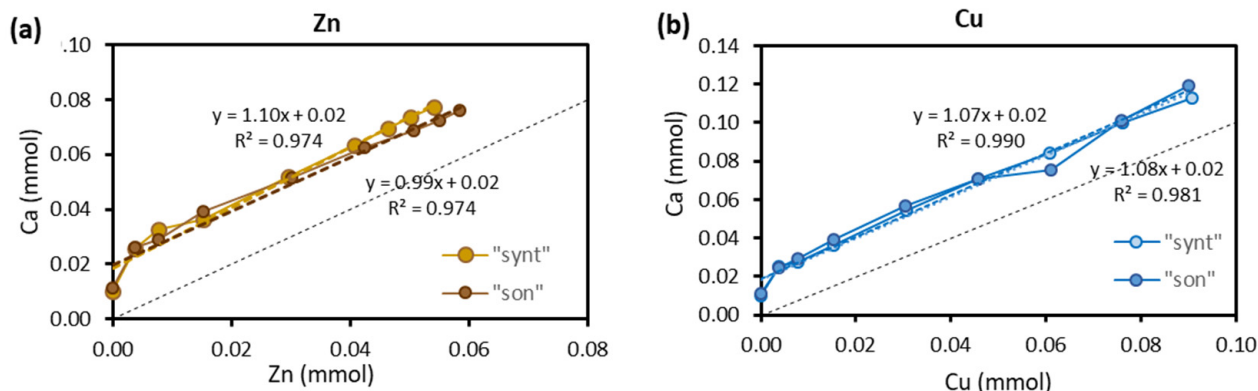


Figure 8. Relationship between the number of moles of released Ca^{2+} vs the number of moles of adsorbed Zn (a) and Cu (b).

Nevertheless, the decrease of pH seen above revealed that ion exchange could not be the unique mechanism behind the metal removal. Therefore, other mechanisms also

took place besides ion exchange that explained the Ca^{2+} release. Ca^{2+} release might also be due to exposed calcite dissolution, which was favored as pH decreased (from 9.2 to 7.0) as metal sorbed onto HAP (Figure 7). Ca concentration value on the y-axis (i.e., in the absence of metal sorption) would support this hypothesis. Another source that might contribute to the Ca^{2+} release (although to a limited extent) was HAP dissolution. Crystalline HAP dissolution is reported to occur generally at $\text{pH} < 5$, but non-crystalline and substituted with Ca^{2+} HAP (as it might be the case in this study as HAP was synthesized from calcite dissolution) may dissolve at higher pH [30,49]. Ca^{2+} concentrations in equilibrium with HAP have been reported to range from 1.4 mg/L for highly crystalline HAP to 7.5 mg/L for poorly crystalline HAP [49]. That being the case, the insignificant concentration of PO_4^{3-} (Figure 7) would indicate precipitation of PO_4^{3-} -bearing solid phases. Metal precipitation with PO_4^{3-} released from HAP dissolution has been observed [18,42,50].

Precipitation, and not only of PO_4^{3-} -bearing solid phases, is in fact a third mechanism that is expected to contribute to the overall removal of Zn and Cu. Speciation diagrams based on thermodynamic equilibria in Zn and Cu systems at $\text{pH} 6.5\text{--}8$ in the presence of CO_3^{2-} (from calcite) and PO_4^{3-} (from HAP) anticipate the formation of non-soluble phases such as $\text{Zn}_3(\text{PO}_4)_2 \cdot 4\text{H}_2\text{O}(\text{s})$ for Zn and $\text{Cu}_3(\text{PO}_4)_2(\text{s})$ and $\text{Cu}_2\text{CO}_3(\text{OH})_2(\text{s})$ for Cu (Figure 9).

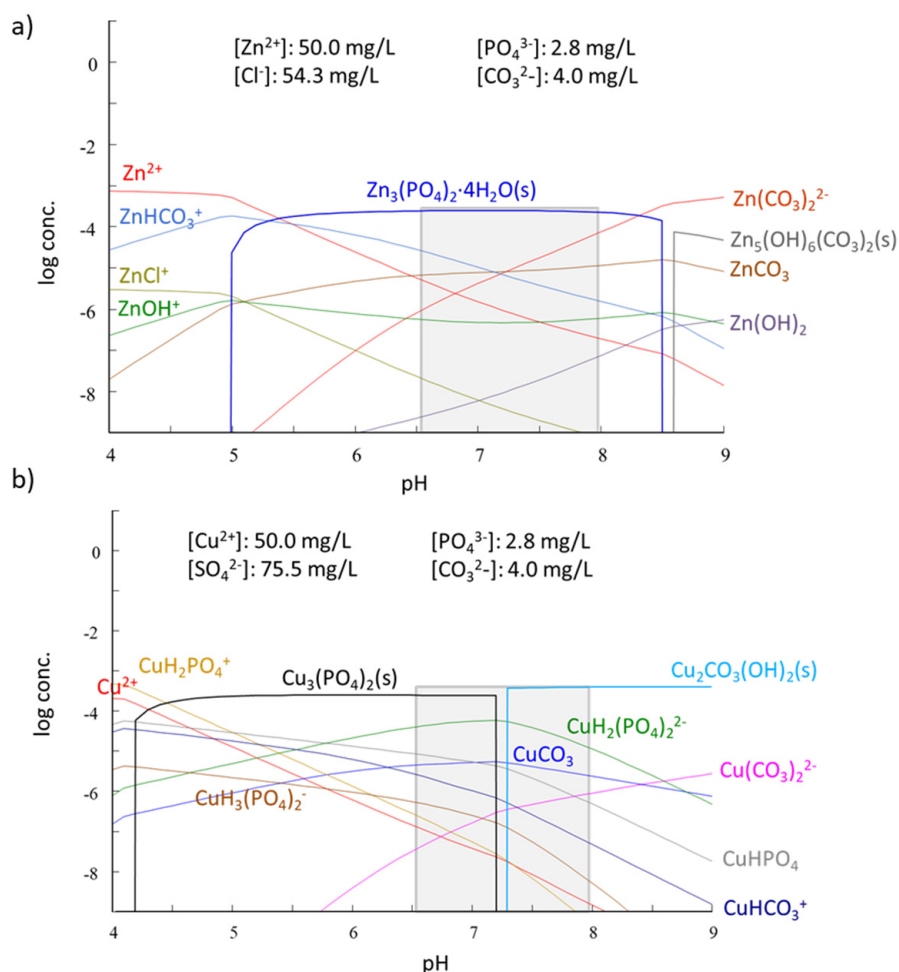


Figure 9. Species distribution diagram as a function of pH for (a) Zn and (b) Cu with a total metal concentration of 50 mg/L in a matrix representative of the supernatants containing the counter-ion in the metal salt (Cl^- for Zn and SO_4^{2-} for Cu), CO_3^{2-} and PO_4^{3-} . Minor species are not shown. The grey bars indicate the pH value of experiments. Distribution diagrams have been plotted using the software packages Hydra and Medusa [51].

XRD analysis performed on HAP loaded with Zn and Cu from the sorption experiments did not offer any peak attributable to new phases (not shown), probably due to their low crystallinity. However, XRD analysis of these samples after calcination at 700 °C for 3 h revealed the appearance of peaks associated to $\text{Zn}_3(\text{PO}_4)_2 \cdot 4\text{H}_2\text{O}$ (hopeite) for Zn, and to $\text{Cu}_3(\text{PO}_4)_2$ for Cu (Figure 10). The appearance of these peaks confirmed the precipitation of Zn and Cu in the form of phosphates (it must be kept in mind that calcination might have altered the precipitated new phases, e.g., decarbonation by loss of CO_2 , and that the observed phases by XRD can be only a part of the precipitated phases). Hopeite formation in sorption experiments of Zn onto HAP has also been observed by Stötzl et al. [50] and Sheha [35]. Although not in the present study, hydrozincite has also been detected by Sheha [35] and Meski et al. [36]. With regard to Cu, $\text{Cu}(\text{OH})_2$ and $\text{Cu}_2(\text{PO}_4)(\text{OH})$ (libethenite) have been detected by Šljivić et al. [43].

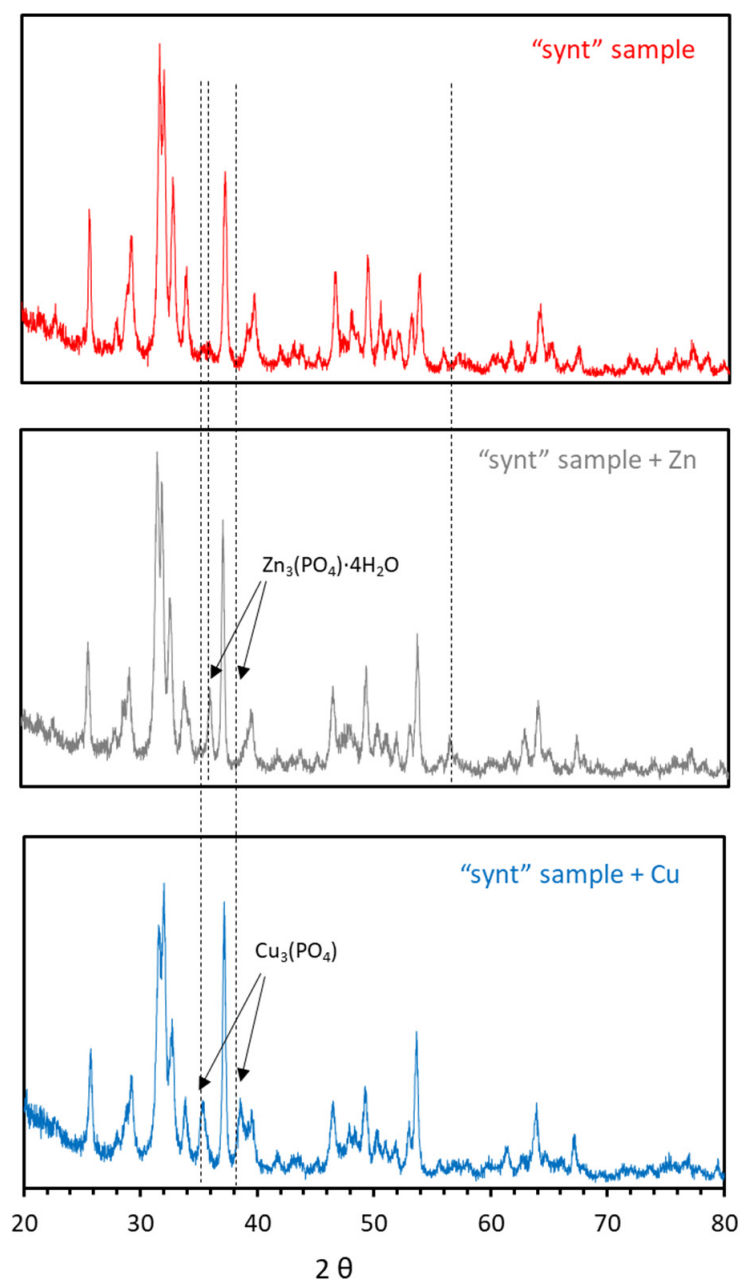


Figure 10. XRD patterns of the synthesized material after contact with Zn and Cu.

Further experiments were performed to experimentally confirm the occurrence of Zn and Cu precipitation in the studied conditions. With the purpose of isolating the eventual precipitation mechanism, HAP amounts (0.1 g) were weighted and equilibrated with deionized water (50 mL) at pH 4.25 for 24 h. Afterwards, the generated lixiviates were filtrated, and then, in the absence of HAP (i.e., without the possibility of sorption occurrence), Zn (or Cu) was added to achieve a final metal concentration of 50 mg/L. pH was adjusted to achieve different final values of 2.2, 6.7 and 8.0. Under these conditions, any disappearance of metal from the solution could only be attributed to precipitation. The analyses showed that at pH 2.2, neither Zn nor Cu were barely removed (<5%), but Zn was removed by 33% at pH 6.7 and by 99% at pH 8.0, while Cu was removed by 97% at pH 6.7 and >99% at pH 8.0. These findings were in agreement with the Zn and Cu speciation diagrams (Figure 9), except for Zn at pH 6.7, for which the observed removal was lower than the theoretical one.

4. Conclusions

Calcite MPs were efficiently coated with a HAP layer following a synthesis route based on two successive precipitations of HAP, with the first involving ethanol 0.5%. Since bare areas of calcite occurred, at pH 4.6 (that of the water to be treated), calcite partially dissolved, raising pH to values >9. The synthesized material showed high capacity in sorbing Zn and Cu from acidic solutions, making it potentially attractive for the removal of divalent heavy metals from contaminated water. The sorption isotherm was well fitted by the Langmuir model, with q_{\max} of 34.97 mg/g for Zn and 60.24 mg/g for Cu, indicating more affinity of HAP towards Cu than towards Zn. Sorption of Zn and Cu onto the synthesized HAP followed a pseudo-second order kinetics, with k_2 of 0.014 g/(mg·min) for Zn and 0.057 g/(mg·min) for Cu. On the other hand, sonication of the synthesized material seemed to lead to some breakage of agglomerated particles (decrease of mean diameter agglomerate from 36 to 23 μm), which resulted in a slight increase of q_{\max} for Zn (37.88 g/mg) without affecting that of Cu. The mechanisms behind the sorption of Zn and Cu onto HAP were diverse and mainly included surface complexation, ion exchange and precipitation of new Zn- and Cu-containing phases. These mechanisms acted together, and it was difficult to quantitatively estimate the contribution of each of them to the overall removal of Zn and Cu.

In view of this performance, we anticipate that the HAP-coated calcite MPs prepared in this study have the potential to remediate heavy metal-contaminated water in ex-situ and, more promisingly, in-situ treatments. When injected into the subsoil for in-situ treatment, these HAP-coated calcite MPs may avoid complications that other MPs and NPs aiming at the removal of heavy metals face, as reported by the relatively abundant fundamental research but also by the currently scarce experience in field applications. In fact, NPs based on carbonaceous materials do not always exhibit high metal sorption capacities unless they are functionalized, while zero-valent iron NPs have a strong tendency to aggregate, which hinders their migration through the contaminated plume, and to have their surface passivated by precipitated Fe-(oxy)hydroxide, which limits the reactivity of zero-valent iron. Despite this anticipated advantage of HAP-based particles, the limited availability of reports on their application for the removal of heavy metals from water makes further studies necessary, both at laboratory and field scales, before drawing major conclusions on the remediation constraints and environmental implications of their application.

On the other hand, it is acknowledged that one problem of NPs is the relatively high cost of synthesizing them. In this sense, and as an innovative aspect of the study, the synthesis route of HAP (based on solid calcite contacted with a phosphate solution instead of the conventional and widely employed wet chemical precipitation, which is based on the use of soluble Ca^{2+} -salts) can allow to save huge amounts of soluble Ca-chemicals and make the process more cost-efficient and improve its competitiveness.

Author Contributions: Conceptualization: O.G., V.M., C.V. and M.M.M.; Methodology: O.G. and V.M.; Formal analysis: V.M. and R.M.D.; Investigation: V.M. and M.M.M.; Resources: O.G. and V.M.; Data curation: O.G., V.M., C.V., M.M.M. and R.M.D.; Writing—Original draft preparation: O.G.; Writing—Review and editing: V.M., C.V. and J.O.M.; Supervision: V.M. and J.O.M.; Funding acquisition: V.M. All authors have read and agreed to the published version of the manuscript.

Funding: This work was funded by the Spanish Ministry of Science, Innovation and Universities and European Funds FEDER (AEI/FEDER) through the project NANOREMOV (CGL2017-87216-C4-3-R). Financial support was also received from the Agency for University Grants Administration and Research (AGAUR) of the Catalan Government through the Research Groups Support program (2014-SGR-050).

Institutional Review Board Statement: Not applicable.

Informed Consent Statement: Not applicable.

Data Availability Statement: The data presented in this study is available on request from the corresponding author.

Acknowledgments: The authors thank A. Marín, R. Ramos and A. Guillaumet for their laboratory assistance.

Conflicts of Interest: The authors declare no conflict of interest.

References

- Burri, N.M.; Weatherl, R.; Moeck, C.; Schirmer, M. A review of threats to groundwater quality in the Anthropocene. *Sci. Total Environ.* **2019**, *684*, 136–154. [CrossRef]
- Zhou, P.; Adeel, M.; Shakoor, N.; Guo, M.; Hao, Y.; Azeem, I.; Li, M.; Liu, M.; Rui, Y. Application of nanoparticles alleviates heavy metals stress and promotes plant growth: An overview. *Nanomaterials* **2021**, *11*, 26. [CrossRef]
- Vareda, J.P.; Valente, A.J.M.; Durães, L. Assessment of heavy metal pollution from anthropogenic activities and remediation strategies: A review. *J. Environ. Manag.* **2019**, *246*, 101–118. [CrossRef]
- Vidu, R.; Matei, E.; Predescu, A.M.; Alhalaili, B.; Pantilimon, C.; Tarcea, C.; Predescu, C. Removal of heavy metals from wastewaters: A challenge from current treatment methods to nanotechnology applications. *Toxics* **2020**, *8*, 101. [CrossRef]
- Carolin, C.F.; Kumar, P.S.; Saravanan, A.; Joshiba, G.J.; Naushad, M. Efficient techniques for the removal of toxic heavy metals from aquatic environment: A review. *J. Environ. Chem. Eng.* **2017**, *5*, 2782–2799. [CrossRef]
- Abdullah, N.; Yusof, N.; Lau, W.J.; Jaafar, J.; Ismail, A.F. Recent trends of heavy metal removal from water/wastewater by membrane technologies. *J. Ind. Eng. Chem.* **2019**, *76*, 17–38. [CrossRef]
- Kaushik, A.; Singh, A. Metal removal and recovery using bioelectrochemical technology: The major determinants and opportunities for synchronic wastewater treatment and energy production. *J. Environ. Manag.* **2020**, *270*, 110826. [CrossRef] [PubMed]
- Malik, L.A.; Bashir, A.; Qureashi, A.; Pandith, A.H. Detection and removal of heavy metal ions: A review. *Environ. Chem. Lett.* **2019**, *17*, 1495–1521. [CrossRef]
- Waheed, A.; Baig, N.; Ullah, N.; Falath, W. Removal of hazardous dyes, toxic metal ions and organic pollutants from wastewater by using porous hyper-cross-linked polymeric materials: A review of recent advances. *J. Environ. Manag.* **2021**, *287*, 112360. [CrossRef] [PubMed]
- Adeleye, A.S.; Conway, J.R.; Garner, K.; Huang, Y.; Su, Y.; Keller, A.A. Engineered nanomaterials for water treatment and remediation: Costs, benefits, and applicability. *Chem. Eng. J.* **2016**, *286*, 640–662. [CrossRef]
- Henderson, A.D.; Demond, A.H. Long-term performance of zero-valent iron permeable reactive barriers: A critical review. *Environ. Eng. Sci.* **2007**, *24*, 401–423. [CrossRef]
- Wen, D.; Fu, R.; Li, Q. Removal of inorganic contaminants in soil by electrokinetic remediation technologies: A review. *J. Hazard. Mater.* **2021**, *401*, 123345. [CrossRef] [PubMed]
- Xin, J.; Tang, F.; Yan, J.; La, C.; Zheng, X.; Liu, W. Investigating the efficiency of microscale zero valent iron-based in situ reactive zone (mZVI-IRZ) for TCE removal in fresh and saline groundwater. *Sci. Total Environ.* **2018**, *626*, 638–649. [CrossRef] [PubMed]
- Gibert, O.; Assal, A.; Devlin, H.; Elliot, T.; Kalin, R.M. Performance of a field-scale biological permeable reactive barrier for in-situ remediation of nitrate-contaminated groundwater. *Sci. Total Environ.* **2019**, *659*, 211–220. [CrossRef]
- Patil, S.S.; Shedbalkar, U.U.; Truskewycz, A.; Chopade, B.A.; Ball, A.S. Nanoparticles for environmental clean-up: A review of potential risks and emerging solutions. *Environ. Technol. Innov.* **2016**, *5*, 10–21. [CrossRef]
- Luo, J.; Yu, D.; Hristovski, K.D.; Fu, K.; Shen, Y.; Westerhoff, P.; Crittenden, J.C. Critical review of advances in engineering nanomaterial adsorbents for metal removal and recovery from water: Mechanism identification and engineering design. *Environ. Sci. Technol.* **2021**, *55*, 4287–4304. [CrossRef]
- Luo, J.; Fu, K.; Yu, D.; Hristovski, K.D.; Westerhoff, P.; Crittenden, J.C. Review of advances in engineering nanomaterial adsorbents for metal removal and recovery from water: Synthesis and microstructure impacts. *ACS EST Eng.* **2021**, *1*, 623–661. [CrossRef]

18. Thanh, D.N.; Novák, P.; Vejpravova, J.; Vu, H.N.; Lederer, J.; Munshi, T. Removal of copper and nickel from water using nanocomposite of magnetic hydroxyapatite nanorods. *J. Magn. Magn. Mater.* **2018**, *456*, 451–460. [CrossRef]
19. Cai, C.; Zhao, M.; Yu, Z.; Rong, H.; Zhang, C. Utilization of nanomaterials for in-situ remediation of heavy metal(loid) contaminated sediments: A review. *Sci. Total Environ.* **2019**, *662*, 205–217. [CrossRef]
20. Ou, M.-Y.; Ting, Y.; Ch'ng, B.-L.; Chen, C.; Cheng, Y.-H.; Chang, T.-C.; Hsi, H.-C. Using mixed active capping to remediate multiple potential toxic metal contaminated sediment for reducing environmental risk. *Water* **2020**, *12*, 1886–1900. [CrossRef]
21. Sadat-Shojai, M.; Khorasani, M.T.; Dinpanah-Khoshdargi, E.; Jamshidi, A. Synthesis methods for nanosized hydroxyapatite with diverse structures. *Acta Biomater.* **2013**, *9*, 7591–7621. [CrossRef]
22. Fihri, A.; Len, C.; Varma, R.S.; Solhy, A. Hydroxyapatite: A review of syntheses, structure and applications in heterogeneous catalysis. *Coordin. Chem. Rev.* **2017**, *347*, 48–76. [CrossRef]
23. Liu, C.; Huang, Y.; Shen, W.; Cui, J. Kinetics of hydroxyapatite precipitation at pH 10 to 11. *Biomaterials* **2001**, *22*, 301–3016. [CrossRef]
24. Wang, P.; Li, C.; Gong, H.; Jiang, X.; Wang, H.; Li, K. Effects of synthesis conditions on the morphology of hydroxyapatite nanoparticles produced by wet chemical process. *Powder Technol.* **2010**, *203*, 315–321. [CrossRef]
25. Smičiklas, I.; Onjia, A.; Raičević, S.; Janačković, Đ.; Mitrić, M. Factors influencing the removal of divalent cations by hydroxyapatite. *J. Hazard. Mater.* **2008**, *152*, 876–884. [CrossRef] [PubMed]
26. Marchegiani, F.; Cibej, E.; Vergni, P.; Tosi, G.; Fermani, S.; Falini, G. Hydroxyapatite synthesis from biogenic calcite single crystals into phosphate solutions at ambient conditions. *J. Cryst. Growth* **2009**, *311*, 4219–4225. [CrossRef]
27. Ni, M.; Ratner, B.D. Nacre surface transformation to hydroxyapatite in a phosphate buffer solution. *Biomaterials* **2003**, *24*, 4323–4331. [CrossRef]
28. Guo, Y.P.; Zhou, Y. Conversion of nacre powders to apatite in phosphate buffer solutions at low temperatures. *Mater. Chem. Phys.* **2007**, *106*, 88–94. [CrossRef]
29. Pham Minh, D.; Lyczko, N.; Sebei, H.; Nzihou, A.; Sharrock, P. Synthesis of calcium hydroxyapatite from calcium carbonate and different orthophosphate sources: A comparative study. *Mater. Sci. Eng. B* **2012**, *177*, 1080–1089. [CrossRef]
30. Naidu, S.; Scherer, G.W. Nucleation, growth and evolution of calcium phosphate films on calcite. *J. Colloid Interf. Sci.* **2014**, *435*, 128–137. [CrossRef]
31. Yang, F.; Liu, Y. Artificial hydroxyapatite film for the conservation of outdoor marble artworks. *Mater. Lett.* **2014**, *124*, 201–203. [CrossRef]
32. Graziani, G.; Sassonia, E.; Franzonia, E.; Scherer, G.W. Hydroxyapatite coatings for marble protection: Optimization of calcite covering and acid resistance. *Appl. Surf. Sci.* **2016**, *368*, 241–257. [CrossRef]
33. Ivanets, A.; Kitikova, N.; Shashkova, I.; Matrunchik, Y.; Kul'bitskaya, L.; Sillanpää, M. Non-acidic synthesis of phosphatized dolomite and its sorption behaviour towards Pb^{2+} , Zn^{2+} , Cu^{2+} , Cd^{2+} , Ni^{2+} , Sr^{2+} and Co^{2+} ions in multicomponent aqueous solution. *Environ. Technol. Innov.* **2016**, *6*, 152–164. [CrossRef]
34. Fiol, N.; Villaescusa, I. Determination of sorbent point zero charge: Usefulness in sorption studies. *Environ. Chem. Lett.* **2009**, *7*, 79–84. [CrossRef]
35. Sheha, R.R. Sorption behavior of Zn(II) ions on synthesized hydroxyapatites. *J. Colloid Interf. Sci.* **2007**, *310*, 18–26. [CrossRef]
36. Meski, S.; Ziani, S.; Khireddine, H.; Boudboub, S.; Zaidi, S. Factorial design analysis for sorption of zinc on hydroxyapatite. *J. Hazard. Mater.* **2011**, *186*, 1007–1017. [CrossRef]
37. Klinkaewnarong, J.; Utara, S. Ultrasonic-assisted conversion of limestone into needle-like hydroxyapatite nanoparticles. *Ultrason. Sonochem.* **2018**, *46*, 18–25. [CrossRef]
38. Lei, S.; Shi, Y.; Qiu, Y.; Che, L.; Xue, C. Performance and mechanisms of emerging animal-derived biochars for immobilization of heavy metals. *Sci. Total Environ.* **2019**, *646*, 1281–1289. [CrossRef]
39. Ramasamy, V.; Anand, P.; Suresh, G. Synthesis and characterization of polymer-mediated $CaCO_3$ nanoparticles using limestone: A novel approach. *Adv. Powder Technol.* **2018**, *29*, 818–834. [CrossRef]
40. Salimi, M.N.; Bridson, R.H.; Grover, L.M.; Leeke, G.A. Effect of processing conditions on the formation of hydroxyapatite nanoparticles. *Powder Technol.* **2012**, *218*, 109–118. [CrossRef]
41. Harding, I.S.; Rashid, N.; Hing, K.A. Surface charge and the effect of excess calcium ions on the hydroxyapatite surface. *Biomaterials* **2005**, *26*, 6818–6826. [CrossRef]
42. Corami, A.; Mignardi, S.; Ferrini, V. Copper and zinc decontamination from single- and binary-metal solutions using hydroxyapatite. *J. Hazard. Mater.* **2007**, *146*, 164–170. [CrossRef]
43. Šljivić, M.; Smičiklas, I.; Plečaš, I.; Mitrić, M. The influence of equilibration conditions and hydroxyapatite physico-chemical properties onto retention of Cu^{2+} ions. *Chem. Eng. J.* **2009**, *148*, 80–88. [CrossRef]
44. Wang, Y.J.; Chen, J.H.; Cui, Y.X.; Wang, S.Q.; Zhou, D.M. Effects of low-molecular-weight organic acids on Cu(II) adsorption onto hydroxyapatite nanoparticles. *J. Hazard. Mater.* **2009**, *162*, 1135–1140. [CrossRef]
45. Feng, Y.; Gong, J.L.; Zeng, G.M.; Niu, Q.Y.; Zhang, H.Y.; Niu, C.G.; Deng, J.H.; Yan, M. Adsorption of Cd (II) and Zn (II) from aqueous solutions using magnetic hydroxyapatite nanoparticles as adsorbents. *Chem. Eng. J.* **2010**, *162*, 487–494. [CrossRef]
46. Xu, Y.; Schwartz, F.W.; Trajna, S.J. Sorption of Zn^{2+} and Cd^{2+} on hydroxyapatite surfaces. *Environ. Sci. Technol.* **1994**, *28*, 1472–1480. [CrossRef]

47. Zhu, R.; Yu, R.; Yao, J.; Mao, D.; Xing, C.; Wang, D. Removal of Cd²⁺ from aqueous solutions by hydroxyapatite. *Catal. Today* **2008**, *139*, 94–99. [CrossRef]
48. Smičiklas, I.D.; Milonjić, S.K.; Pfenndt, P.; Raičević, S. The point of zero charge and sorption of cadmium (II) and strontium (II) ions on synthetic hydroxyapatite. *Sep. Purif. Technol.* **2000**, *18*, 185–194. [CrossRef]
49. Fulmer, M.T.; Ison, I.C.; Hankermayer, C.R.; Constantz, B.R.; Ross, J. Measurements of the solubilities and dissolution rates of several hydroxyapatites. *Biomaterials* **2002**, *23*, 751–755. [CrossRef]
50. Stötzel, C.; Müller, F.A.; Reinert, F.; Niederdraenk, F.; Barralet, J.E.; Gbureck, U. Ion adsorption behaviour of hydroxyapatite with different crystallinities. *Colloid Surface B* **2009**, *74*, 91–95. [CrossRef]
51. Chemical Equilibrium Software Hydra and Medusa. Inorganic Chemistry Department, Royal Institute of Technology: Stockholm, Sweden. Available online: <https://www.kth.se/che/medusa> (accessed on 3 February 2021).

Article

Adsorption of Malachite Green Dye onto Mesoporous Natural Inorganic Clays: Their Equilibrium Isotherm and Kinetics Studies

Sami Ullah ¹, Altaf Ur Rahman ², Fida Ullah ³, Abdur Rashid ⁴ , Tausif Arshad ¹ , Eva Viglašová ⁵ , Michal Galamboš ⁵ , Niyaz Mohammad Mahmoodi ⁶ and Haseeb Ullah ^{7,*} 

¹ Department of Civil Engineering, Mirpur University of Science and Technology, Mirpur 10250, Pakistan; eng.sami07@gmail.com (S.U.); tausif.ce@must.edu.pk (T.A.)

² Department of Physics, Riphah International University, Lahore 54000, Pakistan; altaf.urrahman@riphah.edu.pk

³ Department of Chemistry, Hazara University, Mansehra 21300, Pakistan; fida95229@gmail.com

⁴ Department of Environmental Sciences, Quaid-i-Azam University, Islamabad 45320, Pakistan; abdur.rashid@bs.qau.edu.pk

⁵ Department of Nuclear Chemistry, Faculty of Natural Sciences, Comenius University in Bratislava, Mlynská Dolina, Ilkovičova 6, 842 15 Bratislava, Slovakia; eva.viglasova@uniba.sk (E.V.); michal.galambos@uniba.sk (M.G.)

⁶ Department of Environmental Research, Institute for Color Science and Technology, Tehran 15119, Iran; mahmoodi@icrc.ac.ir

⁷ Department of Chemistry, Quaid-i-Azam University, Islamabad 45320, Pakistan

* Correspondence: chemist.ktk.06@gmail.com

Citation: Ullah, S.; Ur Rahman, A.; Ullah, F.; Rashid, A.; Arshad, T.; Viglašová, E.; Galamboš, M.; Mahmoodi, N.M.; Ullah, H.

Adsorption of Malachite Green Dye onto Mesoporous Natural Inorganic Clays: Their Equilibrium Isotherm and Kinetics Studies. *Water* **2021**, *13*, 965. <https://doi.org/10.3390/w13070965>

Academic Editor: Xanel Vecino

Received: 6 March 2021

Accepted: 30 March 2021

Published: 31 March 2021

Publisher's Note: MDPI stays neutral with regard to jurisdictional claims in published maps and institutional affiliations.

Abstract: Contamination of water with organic dyes is a major environmental concern as it causes serious life-threatening environmental problems. The present research was designed to evaluate the potential of three different natural inorganic clays (NICs) i.e., Pakistani bentonite clay (PB), bentonite purchased from Alfa Aesar (BT), and Turkish red mud (RM) for malachite green (MG) dye removal from an aqueous solution. Various analytical techniques, namely X-ray fluorescence spectrometry (XRF), X-ray diffractometry (XRD), Fourier transform infrared spectroscopy (FTIR), field emission scanning electron microscopy (FESEM), Brunauer–Emmett–Teller surface area measurement (BET), and thermogravimetric analysis (TGA), were used to investigate the physicochemical properties of the NICs samples. The effect of adsorption operational parameters such as contact time, aqueous phase pH, dye concentration, and amount of NICs on the adsorption behavior of MG onto NICs samples were investigated under the batch adsorption system. The equilibrium and kinetic inspection reflected the best description of MG adsorption behavior by the Langmuir isotherm model and pseudo-first-order kinetic model, respectively. The results indicated that the adsorption was favorable at higher pH. The maximum adsorption capacities calculated by Langmuir isotherm for PB, BT, and RM were found to be 243.90 mg/g, 188.68 mg/g, and 172.41 mg/g, respectively. It can be concluded that natural inorganic clays with a higher surface area can be used as an effective adsorbent material to remove the MG dye from an aqueous solution.

Keywords: clay; dye; adsorption; isotherm; kinetics



Copyright: © 2021 by the authors. Licensee MDPI, Basel, Switzerland. This article is an open access article distributed under the terms and conditions of the Creative Commons Attribution (CC BY) license (<https://creativecommons.org/licenses/by/4.0/>).

1. Introduction

In recent years, planners, environmental scientists, and decision-makers have been paying attention to sustainable resource development [1]. Within these resources, water is the most precious renewable natural resource, is the essential enabler, and a major source of survival of life [2,3]. Groundwater is the most important source of drinking water in the world [4]. Globally, groundwater accounts for about 43% of total irrigation use and provides potable water for about 1.5 billion people [5]. However, the rapid development of industrialization, manifold increase in the human population growth, and uncontrolled usage of

freshwater have imposed stress on groundwater resources, resulting in quality deterioration and quantity depletion [6,7]. It has been reported that more than 1.2 billion people around the world have no access to potable water, and around 663 million people are being affected by unsafe water [8,9]. Mainly, surface water and groundwater are contaminated due to the discharge of partially treated or untreated wastewater from various industries into the ecosystem. In particular organic dyes from industrial effluents such as textile, solar cells, leather, plastics, food, and paper cause serious health issues in humans and severe damages to the environment [10]. Over 1×10^5 types of dyes and more than 7×10^5 tons per year of pigments and dyestuff are produced and used in many industries, in which 12% is lost during the manufacturing process, and 20% of dyes enter freshwater resources as industrial effluents [11]. Due to their complex structures, organic dyes are mainly non-biodegradable and are resistant to environmental conditions such as heat, oxidizing agents, and light [12,13]. Moreover, most of the dyes are carcinogenic, mutagenic, and harmful to humans and aquatic biota [14]. In addition their high stability towards environmental conditions and resistance to the attack of microorganisms, the presence of organic dyes causes aesthetic problems, impedes penetration of light into receiving water bodies, and depletes dissolved oxygen, thereby disturbing the ecological aquatic systems [15,16].

Malachite green (MG) dye is an organic compound of triphenylmethane, widely used as a colorant [17], biocide in the aquacultural industry [18], therapeutic agent, anthelmintic, and medical disinfectant [19,20]. Despite its wide application, several reports describe its carcinogenic and hazardous effects. It acts as a tumor-promoting agent in mammalian liver cells [21]. Therefore, the detection of MG in foodstuff, fishes, and animal milk used by humans is of great concern [22].

Several techniques have been applied for the decontamination of wastewater containing organic dyes such as adsorption [23], photocatalysis [24], biological treatment [25], chemical oxidation [26], coagulation/flocculation [27], membrane filtration [28], and ozonation [29]. Among different methods, adsorption is a more suitable and prime treatment method, because of the simplicity of design, inexpensiveness, ease of operation, and high efficiency [30]. Initially, activated carbons were the most commonly used adsorbent [31], but the regeneration difficulties and high production cost tend to limit its use as a potential adsorbent [32]. These limitations have encouraged scientists to explore abundant, cheaper, and highly efficient adsorbents such as bio-sorbents, natural materials, and waste materials [33–35].

The utilization of clays and clay minerals as an alternative adsorbent has many advantages, such as environmental friendliness, low cost, higher surface area, abundance and ease in availability, chemical stability, and a high potential for chemical modification [36–38]. Mainly, clays have layered structures and adsorb harmful substances between their layer spaces [39]. Depending on the target pollutants, clays can be used as an adsorbent both in natural and/or modified form [40]. Among the various types of clay, bentonite is the most utilized clay material, mainly composed of at least 50% smectite, and more precisely montmorillonite. Bentonite represents a 2:1 phyllosilicate, consisting of an octahedral alumina sheet sandwiched between two tetrahedral silica sheets [41]. The overall negative charge on the bentonite clay, being caused by the isomorphous substitution of Al^{+3} for Si^{+4} in the tetrahedral layer and Mg^{+2} for Al^{+3} in the octahedral layer, is balanced by the exchangeable cations located in the interlayer spaces, such as Na^+ , K^+ , and Ca^{+2} [42].

The objective of the current research work was to assess the ability of mesoporous natural inorganic clays (NICs) for the removal of MG dye from an aqueous solution. The influence of adsorption time, aqueous phase pH, MG concentration, and the amount of NICs on the decolorization capabilities of NICs were evaluated. The obtained adsorption results were analyzed by different kinetic and isotherm models.

2. Materials and Methods

2.1. Materials

The NICs adsorbents were obtained: bentonite from Pakistan (PB), bentonite purchased from Alfa Aesar (BT), and red mud from Turkey (RM). The NICs samples were

ground and washed with boiled distilled water followed by a filtration process to remove the soluble impurities. After that, NICs samples were then dried in an oven for 24 h at 80 °C and ground. Sodium hydroxide, hydrochloric acid, and malachite green is a water-soluble cationic dye that belongs to the triphenylmethane category (chemical formula: $C_{23}H_{25}ClN_2$, color index number = 42,000, molar mass: 364.91 g/mol, abbreviated as MG) were obtained from Sigma Aldrich, and used without further pre-treatment. The structure of the MG is shown in Figure 1.

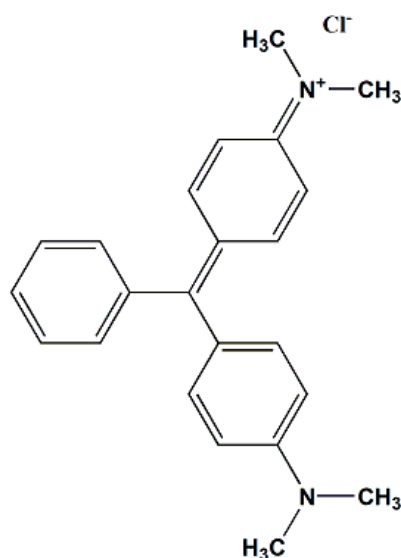


Figure 1. Chemical structure of MG dye.

2.2. Pretreatment of NICs Samples

All of the NICs samples were pretreated as follows: the NICs samples were suspended in distilled water for 4 h and cleaned many times with freshly prepared distilled water. The clean NICs were then oven-dried for 24 h at 105 °C. Finally, the dried NICs materials were stored in sealed jars for further use, without any further physical or chemical treatment.

2.3. Characterization of NICs

To evaluate the mechanism of dye adsorption, it is imperative to examine the characteristics of the adsorbent materials. Therefore, the physicochemical characterizations of the adsorbent materials were analyzed by using various analytical techniques. The chemical composition and elemental analysis of NICs were determined by X-ray fluorescence spectroscopy (XRF) using Bruker Tiger S8 XRF Spectrometer. The X-ray diffraction (XRD) patterns using Bruker D-2 Phaser, Cu $K\alpha$ radiation over a 2θ interval of 4°–40° were performed to investigate the crystallinity and phase composition of the NICs adsorbents. A Fourier transform infrared spectroscopic (FTIR) analysis was performed by using Bruker-Tensor-27 between 400 to 4000 cm^{-1} for the examination of surface functional groups of NICs. A field emission scanning electron microscopic (FESEM) analysis was performed to determine the NICs adsorbent morphologies using FESEM-EDS (Zeiss Ultra Plus). The Brunauer–Emmett–Teller (BET) nitrogen physisorption measurements were performed using a BET Micromeritics ASAP 2020 instrument for the calculations of pore sizes and specific surface area of the NICs adsorbents. The thermogravimetric analysis (TGA) measurements were carried out using the TGA Q500 model instrument, a nitrogen atmosphere (60 mL/min of N_2), and the samples were heated at 10 °C per minute rise over the temperature range of 25–800 °C.

2.4. Batch Adsorption Studies

To evaluate the adsorption abilities of NICs adsorbents, batch adsorption experiments were performed using 250 mL conical flasks containing 100 mL of working solutions. The influence of operating parameters such as time (10–120 min), NICs amount (0.1–0.5 g), dye concentration (100–350 mg/L), and pH (3–11) on MG dye remediation was investigated in batch studies. Typically, 0.1 g of NICs and MG solution (100 mL) with the desired pH and concentration were added to a 250 mL conical flask and stirred continuously. At pre-determined intervals, the NICs samples were separated. The remaining concentration of MG in the filtrate was spectrophotometrically measured by a UV-vis spectrophotometer (Shimadzu UV1700 Japan).

The adsorbed amount of MG (mg/g) was calculated using the following equations:

$$q_e = \frac{(C_0 - C_e) \times V}{M} \quad (1)$$

where V (L) represents the volume of MG solution, C_0 (mg/L) is the initial MG concentration, C_e (mg/L) is the concentration at equilibrium, and M (g) is the amount of NICs.

3. Result and Discussion

3.1. Characterization of NICs

The XRF analysis was carried out to investigate the chemical compositions of the NICs used adsorbents. Table 1 shows that PB and BT clays are mainly composed of alumina and silica, while the major components of the RM clay are iron oxide, alumina, and silica, with other oxides present in trace amount in all of the NICs samples. Figure 2 shows the major chemical constituents present in NICs samples.

Table 1. Chemical composition of NICs clay.

Parameter	Chemical Composition (%)		
	PB Clay	BT Clay	RM Clay
Al ₂ O ₃	56.3	60.7	18.7
SiO ₂	18	16.4	15.3
Fe ₂ O ₃	10.5	5.54	44.34
CaO	4.41	4.68	1.36
K ₂ O	3.51	1.1	0.38
MgO	3.1	3.4	0.47
Na ₂ O	1.6	6.8	12
TiO ₂	1.21	0.63	6.27

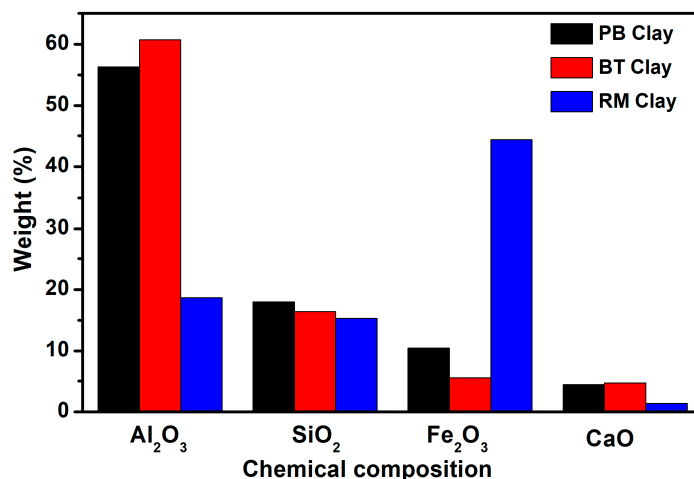


Figure 2. Major chemical constituents of the natural inorganic clays (NICs) adsorbents.

XRD analysis was employed to examine the mineralogical composition and crystalline nature of the NICs samples, as shown in Figure 3. The results indicate that PB and BT clay has the following mineral phases: illite, kaolinite, quartz, and calcite. The dominant diffraction peaks for the PB and BT clays were found at Bragg's angle (2θ) = $\sim 9^\circ$, $\sim 12.5^\circ$, $\sim 27^\circ$, $\sim 28^\circ$, and $\sim 29^\circ$ which corresponds to illite, kaolinite, quartz, feldspars, and calcite, respectively [43,44]. According to the XRD data, RM is mainly composed of hematite, with other minerals such as gibbsite, diaspore, and calcite being present as minor constituents [45].

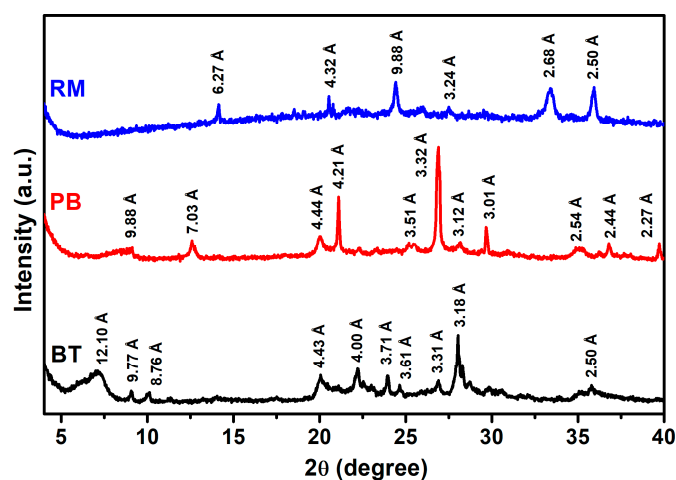


Figure 3. XRD patterns of bentonite purchased from Alfa Aesar (BT), Pakistani bentonite clay (PB), and Turkish red mud (RM) adsorbent.

The surface functional groups of NICs investigated by the accomplishment of FTIR analysis are shown in Figure 4. The results indicated the presence of characteristic absorption bands of NICs at 3696 cm^{-1} belonging to the O-H stretching vibrations of the inner surface hydroxyl group and $3612\text{--}3616\text{ cm}^{-1}$ belonging to the O-H stretching vibrations of the structural hydroxyl [46]. The broadbands $3386\text{--}3422\text{ cm}^{-1}$ were due to the stretching vibration of H-O-H of hydrogen-bonded inter-layer water molecules [47], while the bands of OH deformation mode of coordinated water molecules appeared at $1632\text{--}1641\text{ cm}^{-1}$ [48]. The strong bands at $970\text{--}998\text{ cm}^{-1}$ were referred to as the Si-O-Si stretching vibrations [49]. The Si-O bending vibration and Si-O-Mg, Si-O-Si, and Si-O-Al stretching vibrations of the NICs adsorbents were found in the range of $415\text{--}796\text{ cm}^{-1}$ [50,51].

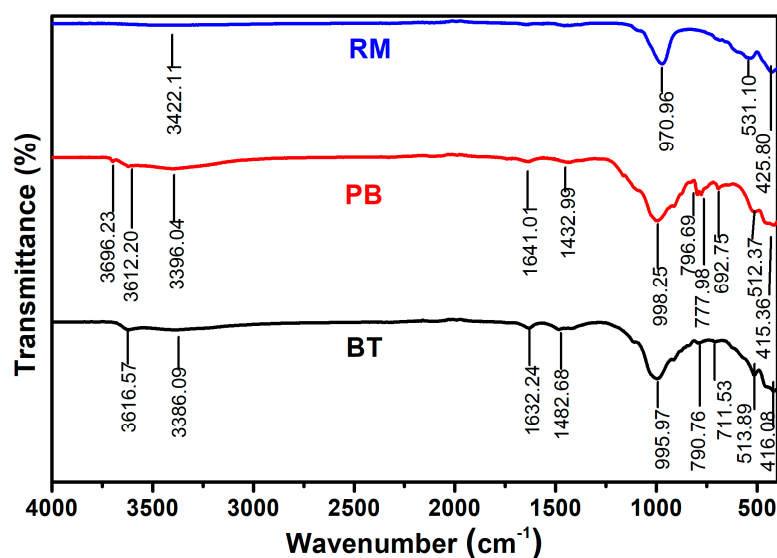


Figure 4. FTIR spectra of RM, PB, and BT adsorbent.

The NICs adsorbent morphologies were analyzed by SEM analysis (Figure 5). It was observed that PB and BT clays have quite a rough porous surface with blunt edges due to the agglomeration of small particle size, while the RM clay has a smooth surface compared to the other two clays and a fluffy appearance because of the closely packed flakes.

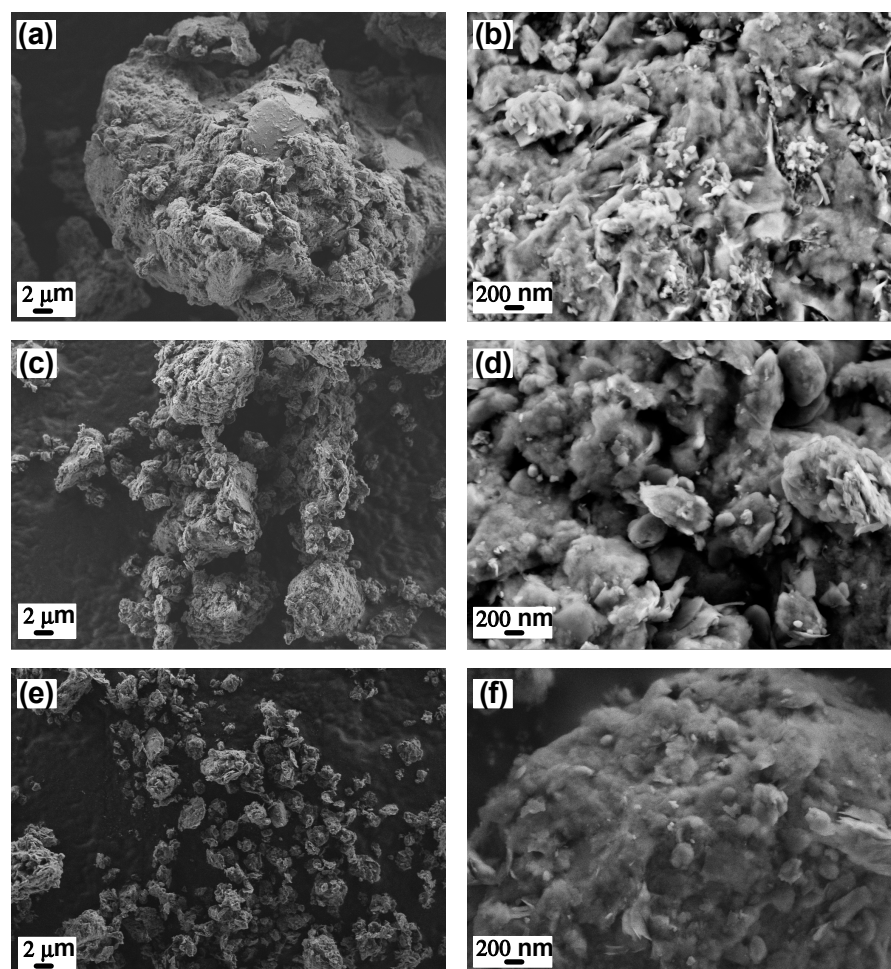


Figure 5. SEM images of (a,b) BT, (c,d) PB, and (e,f) RM adsorbent.

The pore size distribution and surface area of the NICs materials were determined by BET N_2 sorption isotherm analysis. Figure 6 shows that the observed sorption isotherms are of type IV with an H3 type of hysteresis loops. The results confirm the mesoporous nature of the used NICs adsorbents [52]. Both the adsorption-desorption isotherms completely overlapped at low relative pressure $P/P_0 < 0.4$, but showed a distinct hysteresis loop at relatively high pressure ($P/P_0 > 0.4$), which is the typical characteristics of layered materials. The calculated pore sizes and surface area derived from BET N_2 sorption isotherm of the NICs are given in Table 2. The thermal behaviors of NICs were studied by TG analysis.

Table 2. Surface and pore characteristics of the NICs adsorbents.

Parameter	Unit	PB Clay	BT Clay	RM Clay
Surface Area	m^2/g	115.99	38.306	16.796
Pore Volume	cm^3/g	0.1527	0.0711	0.0656
Pore Size	nm	9.6055	19.168	25.834

It is clear from Figure 7 that a continuous weight loss was observed for all the clay minerals in the test temperature range. A two-step weight loss of 9.8%, 8.7%, and 7.5%

was observed for PB, BT, and RM adsorbents, respectively. The first weight loss due to the dehydration of adsorbed water occurred over the 30 °C to 160 °C temperature range, while the second weight loss over the 200 °C to 650 °C temperature range occurred due to the loss of hydrated cations on the exchangeable sites and interlayer water dehydration of the NICs adsorbents.

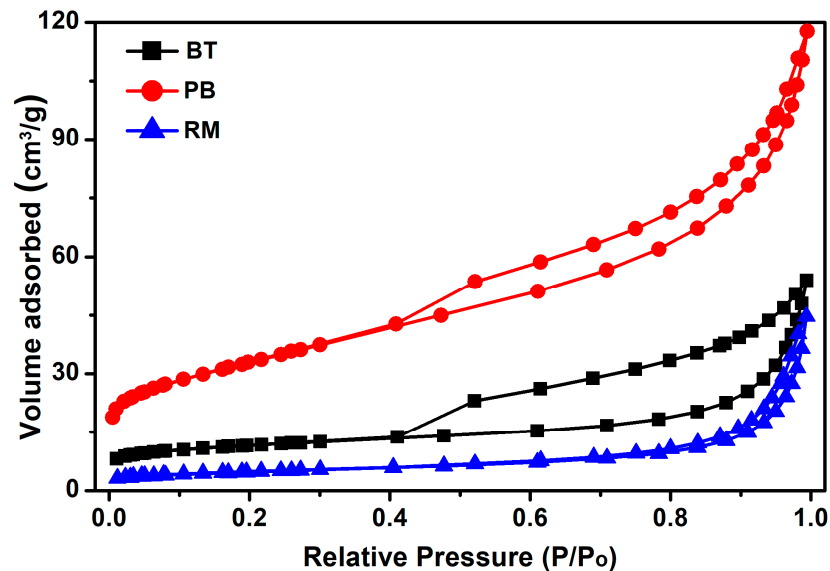


Figure 6. Brunauer–Emmett–Teller (BET) N₂ adsorption-desorption isotherms plot of the NICs sorbent.

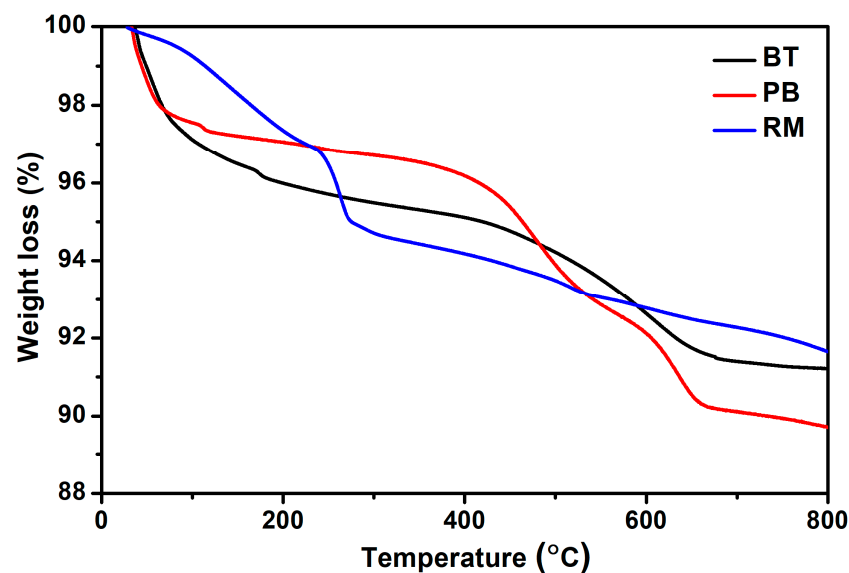


Figure 7. Thermogravimetric analysis (TGA) of BT, PB, and RM adsorbent.

3.2. Adsorption Studies of MG Dye

The adsorption behaviors of the NICs were examined to assess their potential applications in the decontamination of wastewater containing organic dyes. The influence of adsorption time, aqueous phase pH, MG concentration, and the amount of NICs on the decolorization capabilities of NICs were evaluated under batch conditions.

The adsorption uptake of MG by the NICs under varied periods of adsorption contact time (10 to 120 min) is shown in Figure 8. During the experiments, the adsorption capacities increased with the increase in the adsorption contact time. Initially, the rate of dye uptake was high, and afterward, a gradual decrease was observed until the equilib-

rium was attained [53]. This trend of variation in the MG uptake rates was related to the availability of adsorbent surface active sites. In the beginning, the faster adsorption rates were attributed to the abundant surface-active sites that saturated over time and opposed further adsorption [54,55].

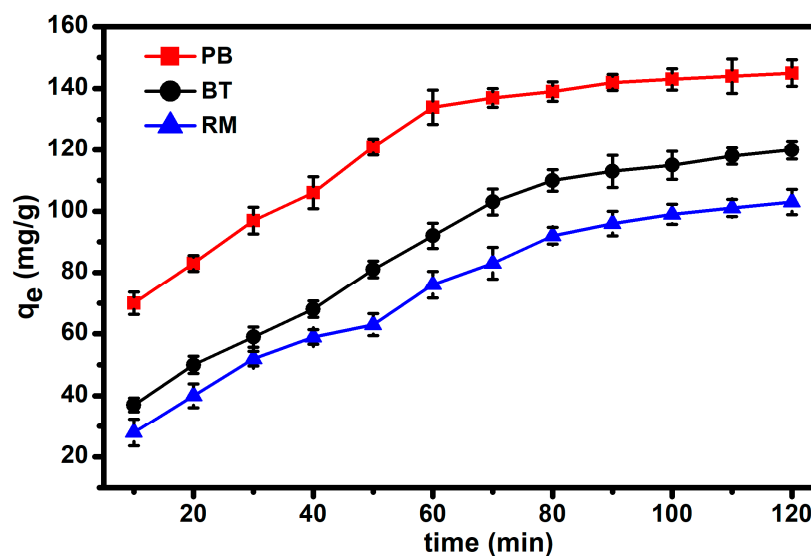


Figure 8. Effect of contact time on malachite green (MG) adsorption.

The initial solution pH is a foremost significant controlling parameter in the process of dye adsorption, as it can directly influence the adsorbent surface charges, the solute's dissociation, and as the adsorption mechanism [56]. It is also associated with the structural changes and color intensities of dye molecules and is directly related to the competitive adsorption process between the MG molecules and hydrogen ions [57]. The influence of initial pH on the adsorption characteristics of MG by NICs adsorbents was examined in the pH range of 3–11. According to the results (Figure 9), the adsorption capacities of NICs adsorbents increased from 45.6 to 130.8 mg/g for RM, 62.4 to 142.8 mg/g for BT, and 82.8 to 170.6 mg/g for PB, with the increase of pH of MG solution from 3 to 11, respectively. In an alkaline environment, the surface functional groups (Si-OH and Al-OH) of the NICs were deprotonated by $-OH$, due to which the surface became negatively charged; as a result, the electrostatic interaction between anionic NICs surfaced and cationic MG molecules increased [1], whereas at low solution pH, the H^+ ions concentration was very high, thus competing intensely with the cationic dye to occupy the adsorption site, therefore causing a reduction in the adsorption of MG dye [58].

It is essential to analyze the effect of the adsorbent amount, to optimize and select the best-required dose of an adsorbent for scaling-up and designing large-scale equipment [59]. The influence of adsorbent dosage on dye adsorption is presented in Figure 10. The obtained results show that increasing the NICs dose from 0.1 to 0.5 g resulted in decreases in the adsorption capacities from 76 to 23.4 mg/g for RM, 92 to 27.4 mg/g for BT, and 134 to 29.6 mg/g for PB. The resulted decrease in adsorption capacities is due to the increasing NICs dose (0.1 to 0.5 g), while the number of MG molecules remained fixed ($C_e = 100$ mg/L). Hence, at a higher NICs dose, some of the surface-active sites of the NICs remained empty [60].

To determine the influence of the initial MG concentration on the adsorption capacities, the experiments were performed by changing the concentration in the range of 100–350 mg/L, keeping other conditions constant. The results are shown in Figure 11. It was determined that the adsorption capacities of MG onto NICs adsorbents increased from 92 to 223 mg/g for PB, 69 to 149 mg/g for BT, and 57 to 125 mg/g for RM as the initial concentration increased from 100 to 350 mg/L. Moreover, at higher concentrations, the adsorption uptake rate was also higher due to the higher concentration gradient [61].

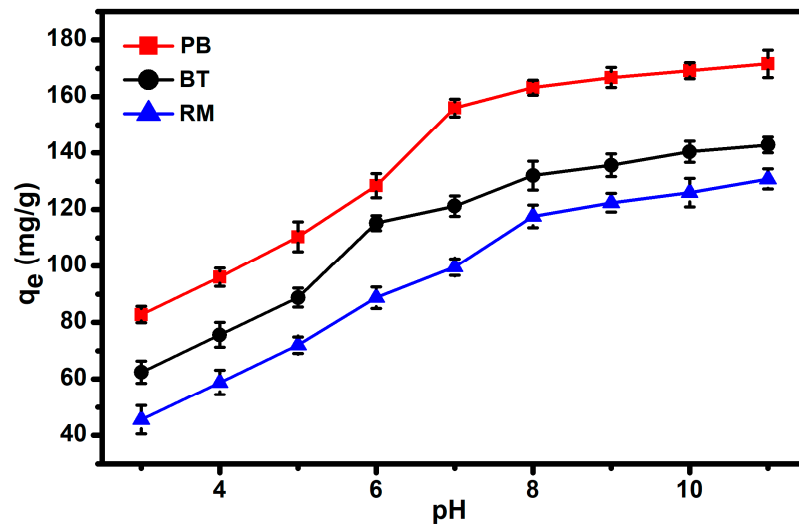


Figure 9. Effect of pH on MG adsorption.

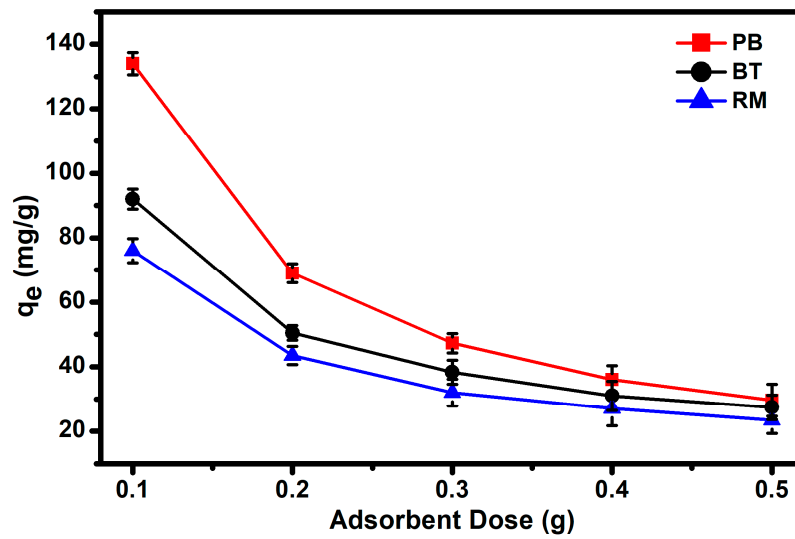


Figure 10. Effect of adsorbent dose on MG adsorption.

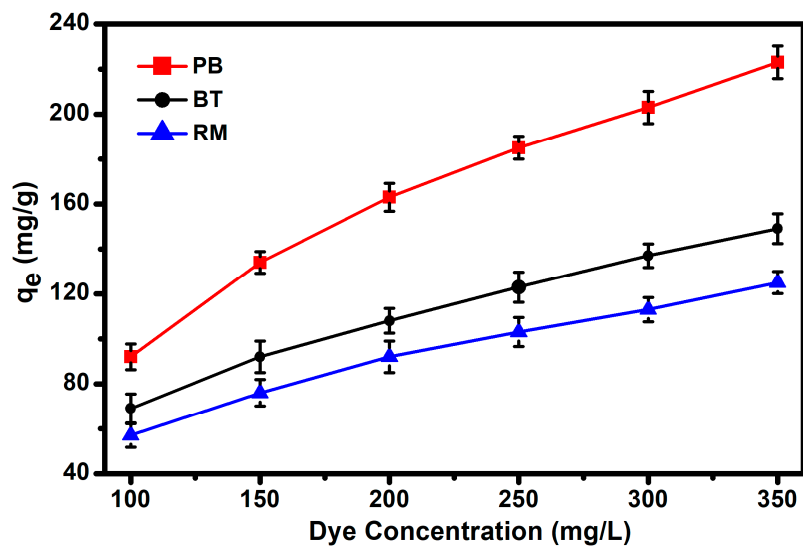


Figure 11. Effect of initial dye concentration on MG adsorption.

By taking into account the above experimental data and analysis, a mechanism for the electrostatic interactions between the MG and NICs was proposed, as illustrated in Figure 12.

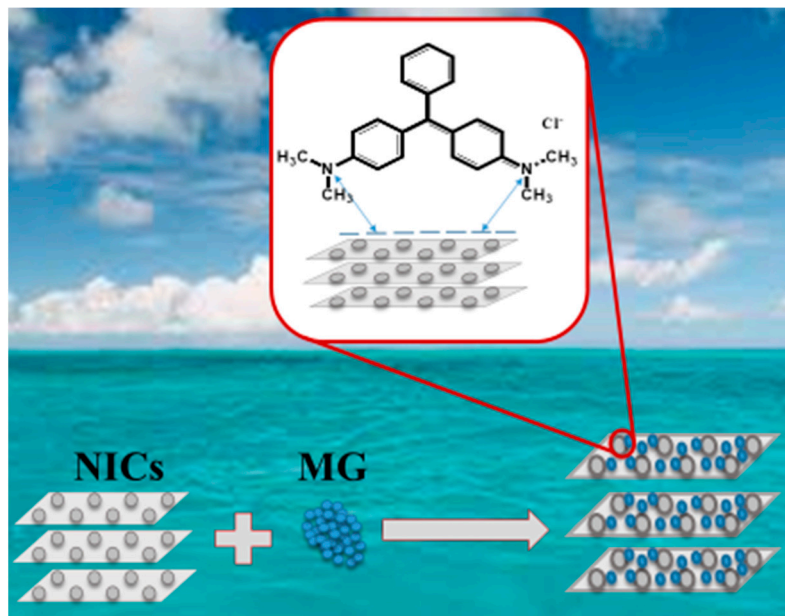


Figure 12. The adsorption mechanism of MG onto NICs.

3.3. Adsorption Kinetics

Adsorption kinetics analysis was carried out to describe the rate of adsorbate uptake and evaluate the adsorption mechanism. The adsorption process occurs mainly in three steps; (i) the external mass transfer of the adsorbate molecules from the bulk solution to the external adsorbent surface, (ii) transfer of adsorbed molecules to the adsorption sites, (iii) and finally, retention via sorption itself [62]. Therefore, the experimental data were inspected by the two different kinetic models, namely the pseudo-first-order and pseudo-second-order kinetics model.

The pseudo-first-order kinetic model can be represented as follows [55]:

$$\log(q_e - q_t) = \log q_e - \frac{k_1}{2.303} t \quad (2)$$

where k_1 (min^{-1}) is the pseudo-first-order rate constant, q_e and q_t are the adsorption capacities (mg/g) at equilibrium and at any time t (min), respectively.

The empirical equation for the pseudo-second-order kinetic model is [63]:

$$\frac{dq_t}{dt} = k_2(q_e - q_t)^2 \quad (3)$$

Integrating and rearranging Equation (3), we received

$$\frac{t}{q_t} = \frac{1}{k_2 q_e^2} + \frac{1}{q_e} t \quad (4)$$

where k_2 ($\text{g/mg} \cdot \text{min}$) is the pseudo-second-order model rate constant.

The linear fitting kinetic results are presented in Figure 13a,b and the calculated kinetic parameters are given in Table 3. When the regression coefficients (R^2) values of the used models were compared, it was found that they have almost the same values for R^2 . However, the experimental (q_{exp}) values of the pseudo-first-order model were found close

to the calculated (q_e) as compared to the pseudo-second-order model, which confirms that the adsorption of MG was followed by the pseudo-first-order model.

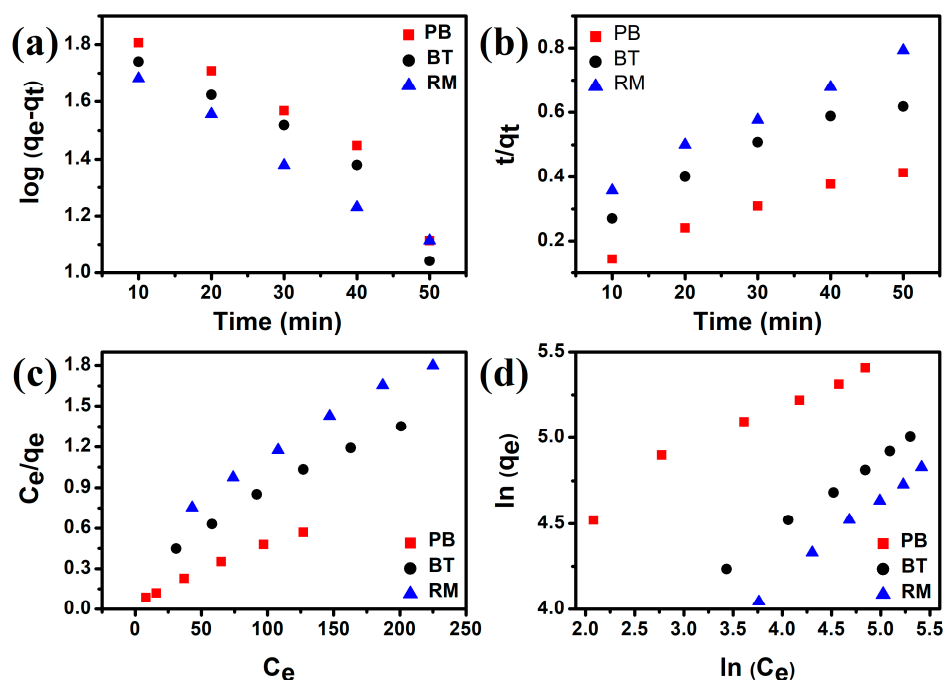


Figure 13. (a) Pseudo-first-order and (b) pseudo-second-order kinetic models; (c) Langmuir isotherm and (d) Freundlich isotherm model for MG adsorption onto NICs adsorbents.

Table 3. Kinetic data predicted by pseudo-first-order and pseudo-second-order kinetic models for the adsorption of MG onto NICs adsorbents.

Adsorbent	Dye	Pseudo-First Order				Pseudo-Second Order		
		$q_{(exp)}$ (mg/g)	$q_{e (calc)}$ (mg/g)	K_1 (min^{-1})	R^2	$q_{e (calc)}$ (mg/g)	K_2 (mg/g)	R^2
PB clay	MG	134	105.22	0.01645	0.935	147.06	0.007	0.975
BT clay	MG	92	89.74	0.01641	0.928	113.63	0.009	0.953
RM clay	MG	76	67.70	0.01460	0.996	95.24	0.010	0.992

3.4. Adsorption Isotherm

The adsorption isotherm studies provide helpful information to understand the nature of the interaction between the adsorbed matter and adsorbent, and to evaluate the efficiency of the adsorbent material used for adsorption. The experimental data were evaluated by two commonly used adsorption isotherm models, namely the Freundlich and Langmuir models. According to the Langmuir model, adsorption of analyte takes place on the homogenous sites the adsorbent with the monolayer formation [63], and can be expressed as:

$$\frac{C_e}{q_e} = \frac{1}{K_L q_m} + \frac{C_e}{q_m} \tag{5}$$

where K_L (L/mg) represents the adsorption equilibrium constant for the Langmuir model and is related to the adsorption energy, q_e and q_m are the equilibrium adsorption amount of adsorbate and monolayer adsorption capacity of adsorbents in the experiments (mg/g), respectively, and C_e (mg/L) is equilibrium adsorbate concentration.

The Freundlich isotherm, applied to non-ideal and reversible adsorption, is valid for multilayer adsorption of analyte and can be expressed as:

$$l_n q_e = l_n K_F + \frac{1}{n_F} l_n C_e \quad (6)$$

where K_F (mg/g) represents the Freundlich constant and $1/n$ is the heterogeneity factor.

All of the correlation coefficients and constants obtained from the used adsorption isotherm models were summarized in Table 4. The results show that both of the isotherms have very high R^2 ; however, experimental maximum adsorption capacities are close to the q_m calculated from the Langmuir isotherm model. The results show that adsorption of MG onto the surface of NICs adsorbents occurs via monolayer formation.

Table 4. Langmuir and Freundlich parameters for the adsorption of MG onto NICs adsorbents.

Adsorbent	Dye	$q_{(exp)}$ (mg/g)	Langmuir			Freundlich			
			q_m (mg/g)	K_L (L/mg)	R^2	R_L	n_F	K_F (mg/g)	R^2
PB clay	MG	223	243.90	0.064	0.994	0.135	3.373	53.83	0.968
BT clay	MG	149	188.68	0.016	0.990	0.382	2.462	17.30	0.998
RM clay	MG	125	172.41	0.011	0.993	0.481	2.153	10.15	0.995

A direct comparison of the adsorption capacities obtained in this study and earlier reported in the literature is difficult due to the varying experimental conditions employed in those studies. However, from Table 5, it can be concluded that the NICs used in this study provide better results for MG adsorption than the others reported in the literature.

Table 5. Comparison of the maximum adsorption capacities of some adsorbents used for MG dye.

Adsorbent	Isotherm	q_m (mg/g)	References
Kaolin	Langmuir	52	[64]
Clayey soil	Langmuir	78.57	[65]
Diatomite	Langmuir	23.64	[66]
Rattan sawdust	Langmuir	62.71	[67]
Wood apple shell	Langmuir	34.56	[68]
Walnut shell	Langmuir	90.8	[69]
Conch shell powder	Langmuir	92.25	[70]
Sea shell powder	Langmuir	42.33	[21]
PB clay	Langmuir	223	This study
BT clay	Langmuir	149	This study
RM clay	Langmuir	125	This study

4. Conclusions

In the current study, three different mesoporous natural clays were used as an environment-friendly, efficient, easily available, and low-cost material for the adsorption of cationic MG dye from an aqueous environment. The chemical composition, mineralogical composition, and texture of NICs were determined by using XRF, XRD, FESEM, FTIR, BET, and TGA analysis. It was observed that PB clay has a quite rough surface with blunt edges and higher surface area as compared to the BT clay and RM clay. The experimental results indicated that adsorption removal of MG was highly dependent on the adsorption contact time, aqueous pH, NICs dose, and MG concentration. The adsorption capacities of MG onto NICs increased with the increase in the adsorption contact time, pH, and MG concentration, while it decreased with the increase in NICs dose. Furthermore, the kinetics data fitted the pseudo-first-order model well. The isotherm data illustrated the suitability of employing the Langmuir isotherm model. The adsorption capacity of PB clay (223 mg/g) was found higher than the BT clay (149 mg/g) and RM clay (125 mg/g). The adsorption of MG dye was more correlated to the BET surface area and available binding sites of the

adsorbent material. Conclusively, naturally occurring mesoporous clays can be efficiently applied for the removal of cationic dyes from contaminated environs.

Author Contributions: Conceptualization, H.U.; methodology, S.U., A.R., and F.U.; investigation, S.U., A.U.R., F.U., A.R., T.A., and E.V.; writing—original draft preparation, S.U. and F.U.; writing—review and editing, H.U., M.G., and N.M.M.; supervision, H.U.; funding acquisition, H.U. All authors have read and agreed to the published version of the manuscript.

Funding: This research was funded by the department of chemistry, Quaid-i-Azam University, Islamabad, Pakistan.

Institutional Review Board Statement: Not applicable.

Informed Consent Statement: Not applicable.

Data Availability Statement: The data presented in this study are available in the main text of the article.

Conflicts of Interest: The authors declare no conflict of interest.

References

- Gamoudi, S.; Srasra, E. Adsorption of organic dyes by HDPy+-modified clay: Effect of molecular structure on the adsorption. *J. Mol. Struct.* **2019**, *1193*, 522–531. [CrossRef]
- Garg, D.; Kumar, S.; Sharma, K.; Majumder, C. Application of waste peanut shells to form activated carbon and its utilization for the removal of Acid Yellow 36 from wastewater. *Groundw. Sustain. Dev.* **2019**, *8*, 512–519. [CrossRef]
- Rashid, A.; Khan, S.; Ayub, M.; Sardar, T.; Jehan, S.; Zahir, S.; Khan, M.S.; Muhammad, J.; Khan, R.; Ali, A. Mapping human health risk from exposure to potential toxic metal contamination in groundwater of Lower Dir, Pakistan: Application of multivariate and geographical information system. *Chemosphere* **2019**, *225*, 785–795. [CrossRef]
- Amarasooriya, A.; Kawakami, T. Removal of fluoride, hardness and alkalinity from groundwater by electrolysis. *Groundw. Sustain. Dev.* **2019**, *9*, 100231. [CrossRef]
- Adebayo, T.B.; Abegunrin, T.P.; Awe, G.O.; Are, K.S.; Guo, H.; Onofua, O.E.; Adegbola, G.A.; Ojadiran, J.O. Geospatial mapping and suitability classification of groundwater quality for agriculture and domestic uses in a Precambrian basement complex. *Groundw. Sustain. Dev.* **2021**, *12*, 100497. [CrossRef]
- Ahmed, M.; Mashkoor, F.; Nasar, A. Development, characterization, and utilization of magnetized orange peel waste as a novel adsorbent for the confiscation of crystal violet dye from aqueous solution. *Groundw. Sustain. Dev.* **2020**, *10*, 100322. [CrossRef]
- Priya, K.; Aswin, K.; Indu, M.; Adarsh, S. Assessment of hydrogeochemical processes in the aquifers of Coimbatore city, India with special reference to nickel contamination. *Groundw. Sustain. Dev.* **2020**, *11*, 100393. [CrossRef]
- Bolisetty, S.; Peydayesh, M.; Mezzenga, R. Sustainable technologies for water purification from heavy metals: Review and analysis. *Chem. Soc. Rev.* **2019**, *48*, 463–487. [CrossRef] [PubMed]
- Pillai, P.; Dharaskar, S.; Shah, M.; Sultania, R. Determination of fluoride removal using silica nano adsorbent modified by rice husk from water. *Groundw. Sustain. Dev.* **2020**, *11*, 100423. [CrossRef]
- Hou, M.-F.; Ma, C.-X.; Zhang, W.-D.; Tang, X.-Y.; Fan, Y.-N.; Wan, H.-F. Removal of rhodamine B using iron-pillared bentonite. *J. Hazard. Mater.* **2011**, *186*, 1118–1123. [CrossRef]
- Chu, H.; Liu, X.; Liu, B.; Zhu, G.; Lei, W.; Du, H.; Liu, J.; Li, J.; Li, C.; Sun, C. Hexagonal 2H-MoSe₂ broad spectrum active photocatalyst for Cr (VI) reduction. *Sci. Rep.* **2016**, *6*, 1–10. [CrossRef] [PubMed]
- Saeed, M.; Munir, M.; Nafees, M.; Shah, S.S.A.; Ullah, H.; Waseem, A. Synthesis, characterization and applications of silylation based grafted bentonites for the removal of Sudan dyes: Isothermal, kinetic and thermodynamic studies. *Microporous Mesoporous Mater.* **2020**, *291*, 109697. [CrossRef]
- Sarma, G.K.; Gupta, S.S.; Bhattacharyya, K.G. *RETRACTED: Adsorption of Crystal Violet on Raw and Acid-Treated Montmorillonite, K10, in Aqueous Suspension*; Elsevier: Amsterdam, The Netherlands, 2016.
- Hou, H.; Zhou, R.; Wu, P.; Wu, L. Removal of Congo red dye from aqueous solution with hydroxyapatite/chitosan composite. *Chem. Eng. J.* **2012**, *211*, 336–342. [CrossRef]
- Tsai, W.; Chang, C.; Lin, M.; Chien, S.; Sun, H.; Hsieh, M. Adsorption of acid dye onto activated carbons prepared from agricultural waste bagasse by ZnCl₂ activation. *Chemosphere* **2001**, *45*, 51–58. [CrossRef]
- Raghu, M.; Kumar, K.Y.; Prashanth, M.; Prasanna, B.; Vinuth, R.; Kumar, C.P. Adsorption and antimicrobial studies of chemically bonded magnetic graphene oxide-Fe₃O₄ nanocomposite for water purification. *J. Water Process Eng.* **2017**, *17*, 22–31. [CrossRef]
- Crini, G.; Peindy, H.N.; Gimbert, F.; Robert, C. Removal of CI Basic Green 4 (Malachite Green) from aqueous solutions by adsorption using cyclodextrin-based adsorbent: Kinetic and equilibrium studies. *Sep. Purif. Technol.* **2007**, *53*, 97–110. [CrossRef]
- Tsai, W.-T.; Chen, H.-R. Removal of malachite green from aqueous solution using low-cost chlorella-based biomass. *J. Hazard. Mater.* **2010**, *175*, 844–849. [CrossRef] [PubMed]

19. Saha, P.; Chowdhury, S.; Gupta, S.; Kumar, I.; Kumar, R. Assessment on the removal of malachite green using tamarind fruit shell as biosorbent. *Clean Soil Air Water* **2010**, *38*, 437–445. [CrossRef]
20. Srivastava, S.; Sinha, R.; Roy, D. Toxicological effects of malachite green. *Aquat. Toxicol.* **2004**, *66*, 319–329. [CrossRef] [PubMed]
21. Chowdhury, S.; Saha, P. Sea shell powder as a new adsorbent to remove Basic Green 4 (Malachite Green) from aqueous solutions: Equilibrium, kinetic and thermodynamic studies. *Chem. Eng. J.* **2010**, *164*, 168–177. [CrossRef]
22. Nethaji, S.; Sivasamy, A.; Thennarasu, G.; Saravanan, S. Adsorption of Malachite Green dye onto activated carbon derived from *Borassus aethiopicum* flower biomass. *J. Hazard. Mater.* **2010**, *181*, 271–280. [CrossRef] [PubMed]
23. Duan, Y.; Song, Y.; Zhou, L. Facile synthesis of polyamidoamine dendrimer gel with multiple amine groups as a super adsorbent for highly efficient and selective removal of anionic dyes. *J. Colloid Interface Sci.* **2019**, *546*, 351–360. [CrossRef]
24. Kheirabadi, M.; Samadi, M.; Asadian, E.; Zhou, Y.; Dong, C.; Zhang, J.; Moshfegh, A.Z. Well-designed Ag/ZnO/3D graphene structure for dye removal: Adsorption, photocatalysis and physical separation capabilities. *J. Colloid Interface Sci.* **2019**, *537*, 66–78. [CrossRef]
25. Yuan, Y.-J.; Chen, D.; Yu, Z.-T.; Zou, Z.-G. Cadmium sulfide-based nanomaterials for photocatalytic hydrogen production. *J. Mater. Chem. A* **2018**, *6*, 11606–11630. [CrossRef]
26. Fu, J.; Yu, J.; Jiang, C.; Cheng, B. g-C₃N₄-Based heterostructured photocatalysts. *Adv. Energy Mater.* **2018**, *8*, 1701503. [CrossRef]
27. SMoghaddam, S.; Moghaddam, M.A.; Arami, M. Coagulation/flocculation process for dye removal using sludge from water treatment plant: Optimization through response surface methodology. *J. Hazard. Mater.* **2010**, *175*, 651–657. [CrossRef] [PubMed]
28. Chen, X.; Zhao, Y.; Moutinho, J.; Shao, J.; Zydney, A.L.; He, Y. Recovery of small dye molecules from aqueous solutions using charged ultrafiltration membranes. *J. Hazard. Mater.* **2015**, *284*, 58–64. [CrossRef]
29. Ikhtlaq, A.; Brown, D.R.; Kasprzyk-Hordern, B. Catalytic ozonation for the removal of organic contaminants in water on alumina. *Appl. Catal. B Environ.* **2015**, *165*, 408–418. [CrossRef]
30. Jayanthi, S.; Eswar, N.K.; Singh, S.A.; Chatterjee, K.; Madras, G.; Sood, A. Macroporous three-dimensional graphene oxide foams for dye adsorption and antibacterial applications. *RSC Adv.* **2016**, *6*, 1231–1242. [CrossRef]
31. Bentahar, S.; Dbik, A.; el Khomri, M.; el Messaoudi, N.; Lacherai, A. Adsorption of methylene blue, crystal violet and congo red from binary and ternary systems with natural clay: Kinetic, isotherm, and thermodynamic. *J. Environ. Chem. Eng.* **2017**, *5*, 5921–5932. [CrossRef]
32. Basaleh, A.A.; Al-Malack, M.H.; Saleh, T.A. Methylene Blue removal using polyamide-vermiculite nanocomposites: Kinetics, equilibrium and thermodynamic study. *J. Environ. Chem. Eng.* **2019**, *7*, 103107. [CrossRef]
33. Alkan, M.; Doğan, M.; Turhan, Y.; Demirbaş, Ö.; Turan, P. Adsorption kinetics and mechanism of maxilon blue 5G dye on sepiolite from aqueous solutions. *Chem. Eng. J.* **2008**, *139*, 213–223. [CrossRef]
34. Chakraborty, S.; Chowdhury, S.; Saha, P.D. Adsorption of crystal violet from aqueous solution onto sugarcane bagasse: Central composite design for optimization of process variables. *J. Water Reuse Desalin.* **2012**, *2*, 55–65. [CrossRef]
35. Mittal, A.; Mittal, J.; Malviya, A.; Kaur, D.; Gupta, V. Adsorption of hazardous dye crystal violet from wastewater by waste materials. *J. Colloid Interface Sci.* **2010**, *343*, 463–473. [CrossRef] [PubMed]
36. Chen, H.; Zhao, J.; Zhong, A.; Jin, Y. Removal capacity and adsorption mechanism of heat-treated palygorskite clay for methylene blue. *Chem. Eng. J.* **2011**, *174*, 143–150. [CrossRef]
37. De Queiroga, L.N.F.; Franca, D.B.; Rodrigues, F.; Santos, I.M.; Fonseca, M.G.; Jaber, M. Functionalized bentonites for dye adsorption: Depollution and production of new pigments. *J. Environ. Chem. Eng.* **2019**, *7*, 103333. [CrossRef]
38. Vimonses, V.; Lei, S.; Jin, B.; Chow, C.W.; Saint, C. Kinetic study and equilibrium isotherm analysis of Congo Red adsorption by clay materials. *Chem. Eng. J.* **2009**, *148*, 354–364. [CrossRef]
39. Olusegun, S.J.; Lima, L.F.d.; Mohallem, N.D.S. Enhancement of adsorption capacity of clay through spray drying and surface modification process for wastewater treatment. *Chem. Eng. J.* **2018**, *334*, 1719–1728. [CrossRef]
40. Munir, M.; Nazar, M.F.; Zafar, M.N.; Zubair, M.; Ashfaq, M.; Hosseini-Bandegharai, A.; Khan, S.U.-D.; Ahmad, A. Effective Adsorptive Removal of Methylene Blue from Water by Didodecyldimethylammonium Bromide-Modified Brown Clay. *ACS Omega* **2020**, *5*, 16711–16721. [CrossRef]
41. Brito, D.F.; Filho, E.C.d.; Fonseca, M.G.; Jaber, M. Organophilic bentonites obtained by microwave heating as adsorbents for anionic dyes. *J. Environ. Chem. Eng.* **2018**, *6*, 7080–7090. [CrossRef]
42. Javed, S.H.; Zahir, A.; Khan, A.; Afzal, S.; Mansha, M. Adsorption of Mordant Red 73 dye on acid activated bentonite: Kinetics and thermodynamic study. *J. Mol. Liq.* **2018**, *254*, 398–405. [CrossRef]
43. Elmoubarki, R.; Mahjoubi, F.; Tounsadi, H.; Moustadraf, J.; Abdennouri, M.; Zouhri, A.; el Albani, A.; Barka, N. Adsorption of textile dyes on raw and decanted Moroccan clays: Kinetics, equilibrium and thermodynamics. *Water Resour. Ind.* **2015**, *9*, 16–29. [CrossRef]
44. Chaari, I.; Fakhfakh, E.; Medhioub, M.; Jamoussi, F. Comparative study on adsorption of cationic and anionic dyes by smectite rich natural clays. *J. Mol. Struct.* **2019**, *1179*, 672–677. [CrossRef]
45. Agatzini-Leonardou, S.; Oustadakis, P.; Tsakiridis, P.; Markopoulos, C. Titanium leaching from red mud by diluted sulfuric acid at atmospheric pressure. *J. Hazard. Mater.* **2008**, *157*, 579–586. [CrossRef] [PubMed]
46. Makhoukhi, B.; Djab, M.; Didi, M.A. Adsorption of Telon dyes onto bis-imidazolium modified bentonite in aqueous solutions. *J. Environ. Chem. Eng.* **2015**, *3*, 1384–1392. [CrossRef]
47. Madejová, J. FTIR techniques in clay mineral studies. *Vib. Spectrosc.* **2003**, *31*, 1–10. [CrossRef]

48. Toor, M.; Jin, B.; Dai, S.; Vimonses, V. Activating natural bentonite as a cost-effective adsorbent for removal of Congo-red in wastewater. *J. Ind. Eng. Chem.* **2015**, *21*, 653–661. [CrossRef]
49. Jawad, A.H.; Abdulhameed, A.S. Mesoporous Iraqi red kaolin clay as an efficient adsorbent for methylene blue dye: Adsorption kinetic, isotherm and mechanism study. *Surf. Interfaces* **2020**, *18*, 100422. [CrossRef]
50. Hassanien, M.M.; Abou-El-Sherbini, K.S.; Al-Muaiikel, N.S. Immobilization of methylene blue onto bentonite and its application in the extraction of mercury (II). *J. Hazard. Mater.* **2010**, *178*, 94–100. [CrossRef]
51. Ahmadi, A.; Foroutan, R.; Esmaili, H.; Tamjidi, S. The role of bentonite clay and bentonite clay@ MnFe₂O₄ composite and their physico-chemical properties on the removal of Cr (III) and Cr (VI) from aqueous media. *Environ. Sci. Pollut. Res.* **2020**, *27*, 1–14. [CrossRef]
52. el Ouardi, M.; Laabd, M.; Oualid, H.A.; Brahmi, Y.; Abamrane, A.; Elouahli, A.; Addi, A.A.; Laknifli, A. Efficient removal of p-nitrophenol from water using montmorillonite clay: Insights into the adsorption mechanism, process optimization, and regeneration. *Environ. Sci. Pollut. Res.* **2019**, *26*, 19615–19631. [CrossRef] [PubMed]
53. Marrakchi, F.; Khanday, W.; Asif, M.; Hameed, B. Cross-linked chitosan/sepiolite composite for the adsorption of methylene blue and reactive orange 16. *Int. J. Biol. Macromol.* **2016**, *93*, 1231–1239. [CrossRef]
54. Bentahar, S.; Dbik, A.; el Khomri, M.; el Messaoudi, N.; Lacherai, A. Removal of a cationic dye from aqueous solution by natural clay. *Groundw. Sustain. Dev.* **2018**, *6*, 255–262. [CrossRef]
55. Ullah, H.; Nafees, M.; Iqbal, F.; Awan, S.; Shah, A.; Waseem, A. Adsorption Kinetics of Malachite green and Methylene blue from aqueous solutions using surfactant-modified Organoclays. *Acta Chim. Slov.* **2017**, *64*, 449–460. [CrossRef] [PubMed]
56. Doğan, M.; Özdemir, Y.; Alkan, M. Adsorption kinetics and mechanism of cationic methyl violet and methylene blue dyes onto sepiolite. *Dye. Pigment.* **2007**, *75*, 701–713. [CrossRef]
57. Munagapati, V.S.; Yarramuthi, V.; Nadavala, S.K.; Alla, S.R.; Abburi, K. Biosorption of Cu (II), Cd (II) and Pb (II) by *Acacia leucocephala* bark powder: Kinetics, equilibrium and thermodynamics. *Chem. Eng. J.* **2010**, *157*, 357–365. [CrossRef]
58. Fil, B.A. Isotherm, kinetic, and thermodynamic studies on the adsorption behavior of malachite green dye onto montmorillonite clay. *Part. Sci. Technol.* **2016**, *34*, 118–126. [CrossRef]
59. Ghanizadeh, G.; Asgari, G. Adsorption kinetics and isotherm of methylene blue and its removal from aqueous solution using bone charcoal. *React. Kinet. Mech. Catal.* **2011**, *102*, 127–142. [CrossRef]
60. Rehman, M.S.U.; Munir, M.; Ashfaq, M.; Rashid, N.; Nazar, M.F.; Danish, M.; Han, J.-I. Adsorption of Brilliant Green dye from aqueous solution onto red clay. *Chem. Eng. J.* **2013**, *228*, 54–62. [CrossRef]
61. Karim, A.B.; Mounir, B.; Hachkar, M.; Bakasse, M.; Yaacoubi, A. Removal of Basic Red 46 dye from aqueous solution by adsorption onto Moroccan clay. *J. Hazard. Mater.* **2009**, *168*, 304–309. [CrossRef] [PubMed]
62. Bhatti, H.N.; Zaman, Q.; Kausar, A.; Noreen, S.; Iqbal, M. Efficient remediation of Zr (IV) using citrus peel waste biomass: Kinetic, equilibrium and thermodynamic studies. *Ecol. Eng.* **2016**, *95*, 216–228. [CrossRef]
63. Ullah, R.; Iftikhar, F.J.; Ajmal, M.; Shah, A.; Akhter, M.S.; Ullah, H.; Waseem, A. Modified clays as an efficient adsorbent for brilliant green, ethyl violet and allura red dyes: Kinetic and thermodynamic Studies. *Pol. J. Environ. Stud.* **2020**, *29*, 3831–3839. [CrossRef]
64. Tehrani-Bagha, A.; Nikkar, H.; Mahmoodi, N.; Markazi, M.; Menger, F. The sorption of cationic dyes onto kaolin: Kinetic, isotherm and thermodynamic studies. *Desalination* **2011**, *266*, 274–280. [CrossRef]
65. Saha, P.; Chowdhury, S.; Gupta, S.; Kumar, I. Insight into adsorption equilibrium, kinetics and thermodynamics of Malachite Green onto clayey soil of Indian origin. *Chem. Eng. J.* **2010**, *165*, 874–882. [CrossRef]
66. Tian, L.; Zhang, J.; Shi, H.; Li, N.; Ping, Q. Adsorption of malachite green by diatomite: Equilibrium isotherms and kinetic studies. *J. Dispers. Sci. Technol.* **2016**, *37*, 1059–1066. [CrossRef]
67. Hameed, B.; El-Khaiary, M. Malachite green adsorption by rattan sawdust: Isotherm, kinetic and mechanism modeling. *J. Hazard. Mater.* **2008**, *159*, 574–579. [CrossRef]
68. Sartape, A.S.; Mandhare, A.M.; Jadhav, V.V.; Raut, P.D.; Anuse, M.A.; Kolekar, S.S. Removal of malachite green dye from aqueous solution with adsorption technique using *Limonia acidissima* (wood apple) shell as low cost adsorbent. *Arab. J. Chem.* **2017**, *10*, S3229–S3238. [CrossRef]
69. Dahri, M.K.; Kooh, M.R.R.; Lim, L.B. Water remediation using low cost adsorbent walnut shell for removal of malachite green: Equilibrium, kinetics, thermodynamic and regeneration studies. *J. Environ. Chem. Eng.* **2014**, *2*, 1434–1444. [CrossRef]
70. Chowdhury, S.; Das, P. Mechanistic, kinetic, and thermodynamic evaluation of adsorption of hazardous malachite green onto conch shell powder. *Sep. Sci. Technol.* **2011**, *46*, 1966–1976. [CrossRef]

MDPI
St. Alban-Anlage 66
4052 Basel
Switzerland
Tel. +41 61 683 77 34
Fax +41 61 302 89 18
www.mdpi.com

Water Editorial Office
E-mail: water@mdpi.com
www.mdpi.com/journal/water



MDPI
St. Alban-Anlage 66
4052 Basel
Switzerland

Tel: +41 61 683 77 34
Fax: +41 61 302 89 18

www.mdpi.com



ISBN 978-3-0365-3925-6